

Tactile 3D probing system for measuring MEMS with nanometer uncertainty : aspects of probing, design, manufacturing and assembly

Citation for published version (APA):

Bos, E. J. C. (2008). *Tactile 3D probing system for measuring MEMS with nanometer uncertainty : aspects of probing, design, manufacturing and assembly*. [Phd Thesis 1 (Research TU/e / Graduation TU/e), Mechanical Engineering]. Technische Universiteit Eindhoven. <https://doi.org/10.6100/IR633124>

DOI:

[10.6100/IR633124](https://doi.org/10.6100/IR633124)

Document status and date:

Published: 01/01/2008

Document Version:

Publisher's PDF, also known as Version of Record (includes final page, issue and volume numbers)

Please check the document version of this publication:

- A submitted manuscript is the version of the article upon submission and before peer-review. There can be important differences between the submitted version and the official published version of record. People interested in the research are advised to contact the author for the final version of the publication, or visit the DOI to the publisher's website.
- The final author version and the galley proof are versions of the publication after peer review.
- The final published version features the final layout of the paper including the volume, issue and page numbers.

[Link to publication](#)

General rights

Copyright and moral rights for the publications made accessible in the public portal are retained by the authors and/or other copyright owners and it is a condition of accessing publications that users recognise and abide by the legal requirements associated with these rights.

- Users may download and print one copy of any publication from the public portal for the purpose of private study or research.
- You may not further distribute the material or use it for any profit-making activity or commercial gain
- You may freely distribute the URL identifying the publication in the public portal.

If the publication is distributed under the terms of Article 25fa of the Dutch Copyright Act, indicated by the "Taverne" license above, please follow below link for the End User Agreement:

www.tue.nl/taverne

Take down policy

If you believe that this document breaches copyright please contact us at:

openaccess@tue.nl

providing details and we will investigate your claim.

Tactile 3D probing system for measuring MEMS with nanometer uncertainty.

**Aspects of probing, design,
manufacturing and assembly.**

Edwin Johannes Cornelis Bos

Tactile 3D probing system for measuring MEMS with nanometer uncertainty.

**Aspects of probing, design,
manufacturing and assembly.**

PROEFSCHRIFT

ter verkrijging van de graad van doctor
aan de Technische Universiteit Eindhoven,
op gezag van de Rector Magnificus, prof.dr.ir. C.J. van Duijn,
voor een commissie aangewezen door
het College voor Promoties
in het openbaar te verdedigen
op dinsdag 8 april 2008 om 16.00 uur

door

Edwin Johannes Cornelis Bos

geboren te Eindhoven

Dit proefschrift is goedgekeurd door de promotoren:

prof.dr. A.H. Dietzel

en

prof.dr.ir. P.H.J. Schellekens

Copromotor:

dr.ir. F.L.M. Delbressine

Cover photo: Bart van Overbeeke

Printed in the Netherlands by Ponsen & Looijen

Copyright © 2007 by E.J.C. Bos

All rights reserved. No part of the material protected by this copyright notice may be reproduced or utilized in any form or by any means, electronic or mechanical, including photocopying, recording or by any information storage and retrieval system, without prior written permission of the author.

A catalogue record is available from the Eindhoven University of Technology Library

ISBN: 978-90-386-1216-4

This research was funded by the Dutch Ministry of Economic Affairs (SenterNovem).

I often say that when you can measure what you are speaking about and express it in numbers, you know something about it; and when you cannot measure it; when you cannot express it in numbers, your knowledge is meager and of unsatisfactory kind.
It may be the beginning of knowledge, but you have scarcely, in your thought, advanced to the stage of science, whatever the matter be.
Lord Kelvin, 1886

Tactile 3D probing system for measuring MEMS with nanometer uncertainty - Summary

Measurement underpins manufacturing technology, or in more popular terms: when you cannot measure it, you cannot manufacture it. This is true on *any* dimensional scale, so for micro- and nanotechnology to deliver manufactured products it must be supported by reliable metrology. Component miniaturization in the field of precision engineering and the development of micro electromechanical systems (MEMS) thus results in a demand for suitable measurement instruments for complex three-dimensional components with feature dimensions in the micrometer region and associated dimensional tolerances below 100 nm.

As will be discussed in the first chapter of this thesis, several ultra precision coordinate measuring machines (CMMs) are developed. These CMMs are suitable for measuring complex three-dimensional products, like MEMS and other miniaturized components. From a discussion on available probe systems in the first chapter it is apparent that, with respect to measurement uncertainty and applicability of measurements on MEMS and other miniaturized components, the performance of ultra precision CMMs is currently limited by the performance of available *probe systems*.

The main reason is that the measurement using a probe system is not purely influenced by work piece topography, but also by *interaction physics* between probe tip and work piece. As the dimensional scale of the measurement decreases, the problems associated with this interaction become increasingly apparent. Typical aspects of this interaction include the influence of contact forces on plastic deformations in the contact region, surface forces and geometric and thermal effects. The influence of these aspects on the measurement result is discussed in the second chapter. This chapter will combine results from literature, simulation and experimental results to discuss the aspects that influence the measurement result in tactile probes. From these results it will become apparent that these aspects underlie the limitation for precision measurements on miniaturized components using tactile CMM metrology.

As a result, these interaction aspects are the main challenge when designing ultra precision probes. The analysis of the interaction physics is used in the design of a *novel silicon probing system* with integrated piezo resistive strain gauges to measure a displacement of the probe tip. The result is a probe system with a colliding mass of 34 mg and an isotropic stiffness at the probe tip with a stiffness down to 50 N/m. The measurement range of the probing system is 30 μm , but in most measurements a range of 10 μm is used which slightly improves the signal to noise ratio.

Calibration results using the planar differential laser interferometer setup as discussed in chapter 1 show a standard deviation of 2 nm over 2000 measurement points taken in a 6 hour time frame over a repeated 5.5 μm displacement. The *combined 3D uncertainty* of the probing system is estimated to be 17.4 nm.

In order to measure micrometer scale structures, including holes and trenches, the probing system

can be equipped with *micrometer scale probe tips*. The main limitation is the relative stiffness between the stylus and the suspension of the probing system. By design optimization, a ratio between the length and radius of the measurement part of the stylus of 50 can be obtained, making the probing system *highly* suitable for measuring these micrometer scale structures. So far, probe tips with a radius of 25 μm have been manufactured and work is being done to decrease this radius even further.

The probing system is implemented on a high-accuracy coordinate measuring machine and is suitable for three-dimensional tactile measurements on miniaturized components with nanometer uncertainty.

A *main limitation* when manufacturing the probe is assembly of the probe tip, stylus and chip which is discussed in chapter 4. Assembly of the probe is investigated in a series of experiments on an automated assembler. Based on these results, the design of the probe is optimized for assembly and the automated assembler is made suitable for assembly of the probe by implementation of a novel suction gripper. This resulted in an improvement in placement uncertainty at the tip by a factor of 10 and an increase in yield during assembly from 60 - 80% initially, to over 95%.

In chapter 5 several experimental results with the probe system are discussed, including a quantification of the effects of surface forces on tactile measurements. It is shown that these effects are highly repeatable and result in an attraction of 40 μN and 60 μN in the xy - and z -direction, respectively. Moreover, it is shown that the influence of surface forces on a measurement in the xy -plane can be observed for a separation of 500 μm or less. Finally, conclusions and recommendations for further research are discussed in chapter 6.

Contents

1	Introduction	1
1.1	Dimensional metrology	1
1.2	Measurement tasks	2
1.3	Low uncertainty coordinate measuring machines	4
1.3.1	F25 by Zeiss	4
1.3.2	NanoCMM by Van Seggelen	6
1.3.3	Ruijl's CMM	7
1.4	3D tactile probes for micro components	9
1.4.1	PTB membrane probe	9
1.4.2	Fiber probes	9
1.4.3	Metas probe	12
1.4.4	NPL capacitive probe	12
1.4.5	Vibrating probe	14
1.5	Probe by Pril	15
1.6	Calibration methods for tactile 3D probes	16
1.6.1	Calibration on a separate setup	17
1.6.2	Calibration on the CMM	18
1.6.3	Probe tip calibration	19
1.7	Research objectives and outline of this thesis	22
2	Aspects of probing	25
2.1	Forces during tactile probing	25
2.1.1	Hard probes, touch-trigger probes and measuring probes	25
2.1.2	Probing strategy	26
2.1.3	Impact force	28
2.1.4	Over travel force	31
2.1.5	Overlap between collision and over travel forces	33
2.1.6	Contact of rough spheres	36
2.1.7	Surface forces	38
	Overview of surface forces	40
	Comparison of surface forces to gravitational forces	42
	Effect of the surface forces on static and dynamic friction	43
	Experimental results	46
	Reduction of surface forces	48
2.1.8	Scanning measurement	48
2.1.9	Dynamic excitations	51
2.1.10	Synchronization between probe and CMM	56
2.2	Contact effects	58
2.2.1	Tip rotations during single point probing	58
2.2.2	Micro-friction in normal contact	62
2.2.3	Micro-friction in rolling contact	64
2.2.4	Vibrating styli	64

2.2.5	Wear of the probe tip and work piece	67
2.2.6	Probe tip cleaning	68
2.3	Geometric effects for tactile probes	69
2.3.1	Finite stiffness effects of the probe	69
2.3.2	Finite stiffness effects of the CMM	73
2.3.3	Finite stiffness effects of the object	73
2.3.4	Radius of the probe tip	75
2.3.5	Release distance of the probe tip	76
2.3.6	Anisotropic effects	78
2.4	Thermal effects in probe	81
2.5	Assembly and hysteresis	85
2.5.1	Deviations in assembly	85
2.5.2	Hysteresis	86
2.6	Conclusions	91
3	Probe Development	93
3.1	General Design Considerations	93
3.1.1	Specifications	93
3.1.2	Sensitivity of the probe	94
3.1.3	Supply voltage and signal amplification	96
3.2	Layout of the chip	97
3.2.1	Anisotropic effects	101
3.2.2	Center platform and stylus	103
3.2.3	Micro spherical tips	105
3.3	Probe holder	107
3.3.1	Electronics	108
3.3.2	Clamping of the chip	109
3.3.3	Connection to measurement machine	112
3.4	Conclusion	113
4	Suction gripper for micro assembly	115
4.1	Introduction	116
4.2	Assembly techniques	116
4.3	Influence of contact forces	117
4.4	Grippers for micro assembly	119
4.5	Design of the gripper	120
4.6	Experimental results	123
4.7	Assembly of the probe	125
4.8	Conclusions	128
5	Experimental results	129
5.1	Probe calibration	129
5.2	Probe repeatability	130
5.3	Effect of surface forces during measurements	131
5.4	Frequency analysis	133
5.5	Drift of the probing system	136
5.6	Uncertainty evaluation of the probing system	136
5.7	Conclusions	138
6	Conclusions and recommendations	139
6.1	Conclusions	139
6.2	Recommendations	140

A	Original probe by W. Pril	141
A.1	Specifications	141
A.2	Probe calibration	142
A.3	Measurement results	143
B	Contact of nominally flat rough surfaces	147
C	Surface forces	153
C.1	Van der Waals force	153
C.2	Electrostatic attraction	156
C.3	Hydrostatic adhesion	159
C.4	The influence of relative humidity on hydrostatic adhesion	161
D	Stiffness and characteristics of the suspension	165
D.1	Introduction	165
D.2	Stiffness matrix for a slender rod	166
D.3	Mechanical behavior of single crystalline silicon	167
D.4	Stiffness model of the sensor	167
D.5	Stiffness model of the suspension	172
D.6	Stresses in the slender rods	175
D.7	Conversion matrix	176
E	Design considerations	179
E.1	Fundamentals of determinism	179
E.2	Exact-constraint design	180
E.3	Thermal design considerations	181
E.4	Dynamic and thermal considerations	184
F	Von Mises equivalent stress	189
G	Hertz contact mechanics	191
G.1	Introduction	191
G.2	Elastic deformation	191
G.3	Elastic-plastic deformation	192
G.4	Energy	194
H	Uncertainty evaluation of the setup	197
H.1	Traceability in length measurement	197
H.2	Refractive index of air	198
H.3	Dead path length	199
H.4	Wavelength instability	201
H.5	Periodic deviations	201
H.6	Mechanical misalignments	202
	Bibliography	205

List of symbols

Symbols

Symbol	Description	Unit
α	Angle	rad
	Coefficient of linear thermal expansion	K^{-1}
β	Angle	rad
γ	Surface tension	N/m
δ	Indentation	m
	Displacement	m
ε	Strain	—
ζ	Damping coefficient	—
θ	Angle	rad
λ	Wavelength	m
	Coefficient of thermal conductivity	W/mK
μ	Coefficient of friction	—
ν	Poisson ratio	—
ξ	Creep ratio	—
ρ	Specific mass	kg/m ³
σ	Surface roughness	m
	Surface charge	V
	Stress	Pa
$\sigma_{0.2}$	Yield strength	Pa
χ	Ratio	—
ω	Angular frequency	rad/sec
A	Transformation matrix	m/V

Symbol	Description	Unit
a	Acceleration	m/s ²
	Contact radius	m
A	Area	m ²
c	Stiffness	N/m
d	Distance	m
E	Young's modulus	Pa
f	Frequency	Hz
F	Force	N
F_b	Buckling force	N
F_{imp}	Force due to impact	N
F_{ovt}	Force due to over travel	N
G	Shear modulus	Pa
	Gradient	K/m
	Gauge factor	—
h	Offset	m
H	Hardness	Pa
	Hamaker constant	—
	Hysteresis percentage	—
I	Second moment of area	m ⁴
l	Length	m
m	Measurement signal	V
	Measured distance	m
	Mass	kg
M	Moment	Nm
O	Circumference	m
p	Position	m
	Pressure	Pa
P	Power	W
r	Radius	m
	Radial position	m
R	Electrical resistance	Ω
	Rotation	rad
S	Sensitivity	m/V
t	Time	sec
	Thickness	m
T	Temperature	K
v	Speed	m/s
V	Voltage	V
	Volume	m ³
V_o	Applied voltage	V
V_m	Measured voltage	V
w	Width	m
	Force per unit length	N/m
x	Position along x -axis	m
	Distance	m
y	Position along y -axis	m
z	Position along z -axis	m

Subscript	Refers to
0	Nominal value
c	Center, e.g. of a sphere
l	Leg of the center platform in the probe chip
r	Slender rod connecting the center platform to the edge of the chip
st	Stylus, connecting the probe tip to the center platform of the chip
t	Probe tip
w	Edge of a wall or plane
x	x -direction
y	y -direction
z	z -direction

Chapter 1

Introduction

There is an increasing need for 3D measurements on MEMS and other miniaturized components with low uncertainty. Several ultra precision coordinate measuring machines are developed which are suitable for this task. Currently, the applicability of this method and the measurement uncertainty that can be achieved is limited as a result of the effects that influence the interaction between the probe tip and work piece on a micro scale.

Measurement underpins manufacturing technology, or in more popular terms: when you cannot measure it, you cannot manufacture it. This is true on any dimensional scale, so for micro- and nanotechnology to deliver manufactured products it must be supported by reliable metrology [Leach 01]. Different metrological techniques are available [Danzebrink 06, Hansen 06, Hocken 05, Lonardo 02, Vorburger 97], and therefore in section 1.1 the advantages and limitations of measurements using a coordinate measuring machine (CMM) are briefly discussed.

There is an ongoing trend of component miniaturization in the field of precision engineering and the development of micro electromechanical systems (MEMS). This trend results in a demand for suitable measurement instruments for complex three-dimensional components with feature dimensions in the micrometer region and associated dimensional tolerances below 100 nm. The use of a coordinate measuring machine in this market will become apparent when discussing several typical products in section 1.2.

However, conventional coordinate measuring machines (CMMs) lack the required level of measurement uncertainty. In recent research efforts, the three-dimensional measurement uncertainty of CMMs is therefore decreased to less than 100 nm, making them suitable for dimensional measurements on miniaturized components. Several suitable CMMs are discussed in section 1.3.

Currently, the applicability of this method and the measurement uncertainty that can be achieved is limited by the available probing systems. Several probe systems are therefore briefly discussed in sections 1.4 and 1.5, including the probe system developed by Pril [Pril 02] at the Eindhoven University of Technology. Advantages and limitations of these probes will become apparent when discussing the aspects of probing in the next chapter.

1.1 Dimensional metrology

No instrument measures topography alone [Franks 91]. A mechanical instrument will also respond to changes in the mechanical properties of the surface, e.g. Young's modulus and hardness, an

optical probe will respond to reflectivity and optical constants, a scanning tunneling microscope (STM) responds to electrical properties of the surface, etc. The influence of surface properties on a measurement becomes increasingly apparent in the micro- and nanometer region [Leach 01].

Different methods thus have different advantages and limitations. Coordinate measuring machines (CMMs) allow high-accuracy measurements on complex three-dimensional components. This measurement method is flexible and fast, as it allows an operator to form a quick three-dimensional picture of an object even when its shape and nominal tolerance is not known in advance. Scanning measurements, where the probe tip is moved along the work piece surface, can be used to obtain detailed information about the work piece surface. Figure 1.1 shows several measurement tasks which are difficult or impossible using other methods.

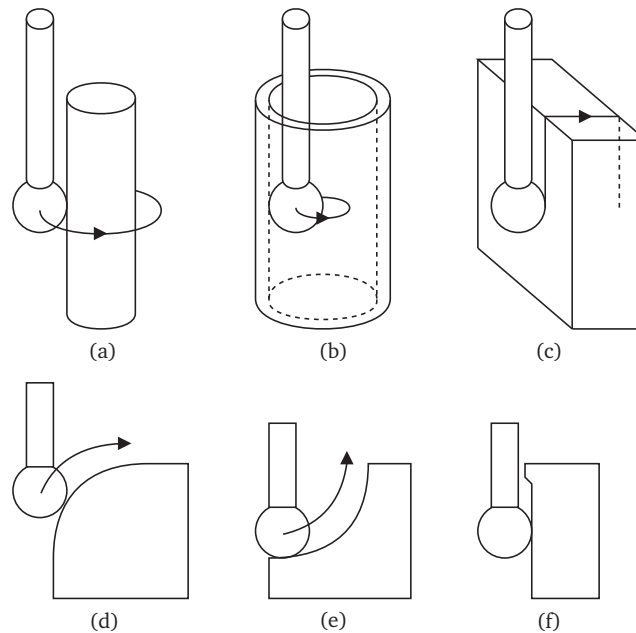


Figure 1.1: Some typical measurement tasks of coordinate measuring machines: (a, b): shape, diameter and cylindricity on varying heights, (c): orthogonality of planes, (d, e): radius of edge and (f): measurement under burr.

Movement of the probe by the coordinate measuring machine is typically done along three axis. These axis can be of the rotary type, but typically three mutually orthogonal linear axis are used, as shown in figure 1.2. Each axis consists of a guide way, for the y -axis indicated by (2), and a carriage, for the y -axis indicated by (1). The three linear axis position the probe housing (4) in such a way that the probe tip contacts the work piece (6). When contact is detected by the probe, the position of the x -, y - and z -carriage of the CMM is recorded. For a measuring probe, as discussed in section 2.1.1, the deflection of the probe tip relative to its housing is added to this position. Using software compensation the probe tip dimension is corrected for [Li 03, Weckenmann 98]. The direction of contact can be obtained from either the probe system, by interpolation of at least three points in the neighborhood of the measurement point or by estimation, e.g. from a CAD model [Weckenmann 04].

1.2 Measurement tasks

As mentioned at the start of this chapter, a clear ongoing trend of component miniaturization can be observed in industry and science. As a result, uncertainty requirements on manufacturing and measurement equipment also increases. This is indicated by the famous Taniguchi graph [Taniguchi 83], as shown in figure 1.3, which even today is a good indication of current state of the art in precision engineering [Hansen 06, Pril 02, Schellekens 98].

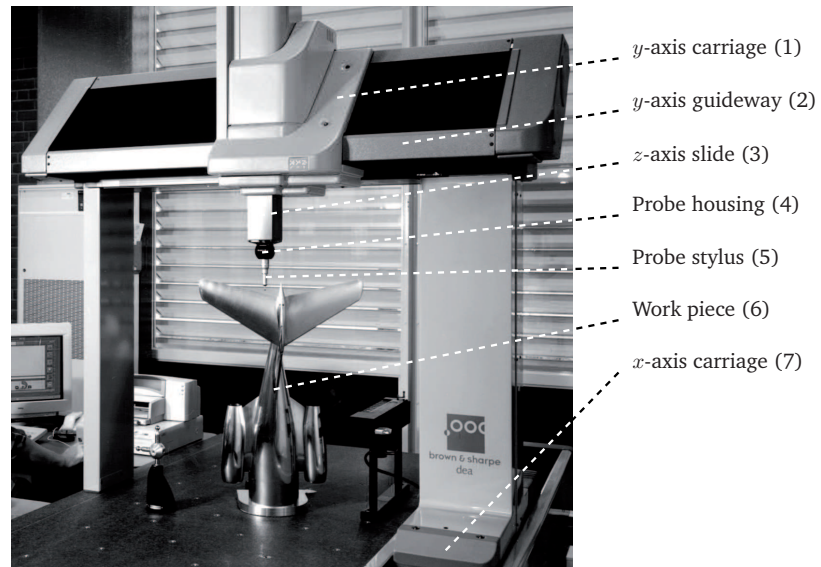


Figure 1.2: Photo of bridge-type coordinate measuring machine (CMM).

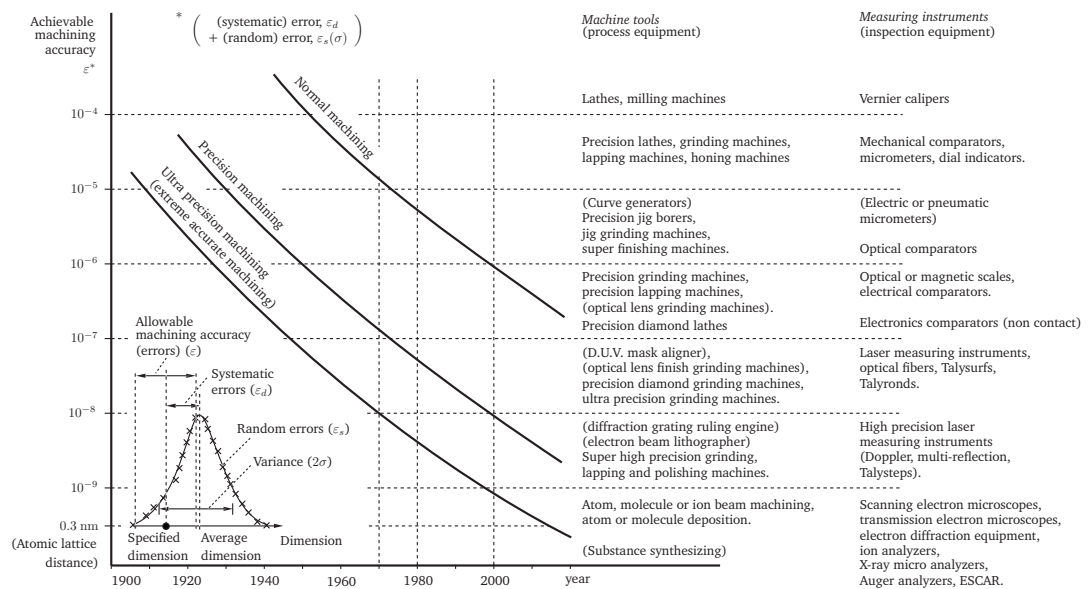


Figure 1.3: Taniguchi graph predicting current and future manufacturing and measurement uncertainty [Taniguchi 83].

A second result of component miniaturization is the decreasing features size of components being measured. Hole diameters and 3D structures in a component of $100\text{ }\mu\text{m}$ or less are common. As a result, the measurement instrument should be able to handle these small dimensions. As will be discussed in the next chapter, the probe tip diameter, which contacts the work piece, is a limiting factor for measuring smaller features using a coordinate measuring machine. Figure 1.4 shows several example products that could be measured using a precision coordinate measuring machine.



Figure 1.4: Example products: (a) commercially available mini hard drive, (b) inside of a precision wrist watch, (c) array of micro-needles, each with a height of approximately $130\text{ }\mu\text{m}$ and (d) fuel injection nozzles with an inner diameter of approximately $100\text{ }\mu\text{m}$.

1.3 Low uncertainty coordinate measuring machines

As discussed in the previous section component miniaturization results in a demand for 3D measurements on product features as small as several tens of micrometers with an uncertainty of 100 nm or less. Application of precision design principles [Corbett 00, Hale 99, Schellekens 98, Slocum 92, Vermeulen 99] resulted in the development of several CMMs with an uncertainty of 100 nm or less which are now commercially available. An important design principle in coordinate measuring machines (CMMs) is the Abbe principle. The Abbe principle states that the distance to be measured should be a straight line extension of the graduations on the scale that serves as a reference, as will be discussed in section 2.5.1.

1.3.1 F25 by Zeiss

The first system is commercialized by Zeiss under the name F25, as shown in figure 1.5 (a). The prototype of the F25 CMM is developed by Vermeulen [Vermeulen 99] at the Eindhoven University of Technology. Abbe deviations in the xy -plane are minimized by aligning the graduated rulers

of two 1D optical encoders to the probe tip center at all positions in the xy -plane, as shown schematically in figure 1.6. Air bearings (4) allow two intermediate bodies (5) to translate over a stationary guide (3). This allows the top intermediate body (5) to translate in x -direction and the right intermediate body to translate in y -direction.



Figure 1.5: Photo of the F25 precision 3D coordinate measuring machine.

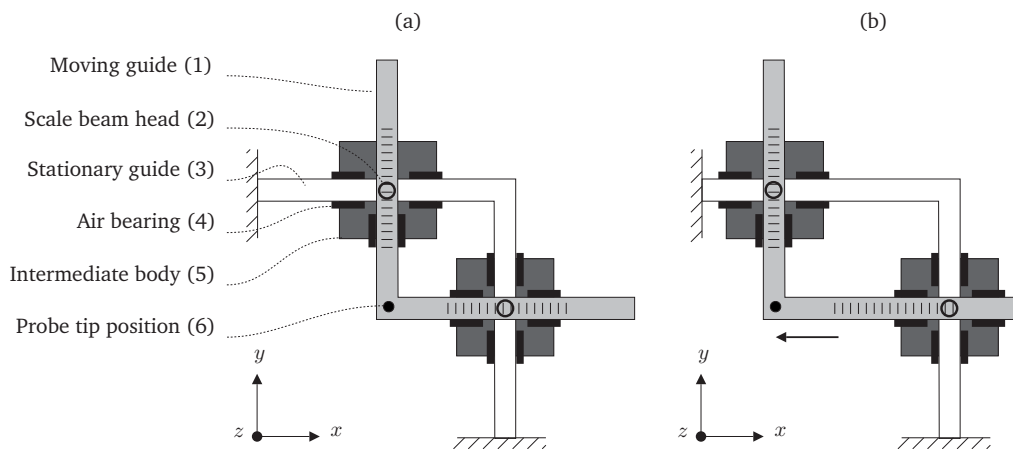


Figure 1.6: Schematic of measurement in xy -plane with the NanoCMM, (a) guides are in their mean position, (b) moving guide with scale beams and probe has moved in negative x -direction.

A second set of air bearings (4) on the intermediate body (5) allows a moving guide (1) to translate with respect to the intermediate body. A translation of the moving guide (1) in x -direction will therefore result in an equal translation of the top intermediate body in x -direction, while the position of the right intermediate body remains unaffected. This is shown in figure 1.6 (b).

Two sets of scale beams are mounted on top of the moving guide (1). The scale beams are aligned to the probe tip center (6). A relative displacement between the moving guide and intermediate body is recorded by the scale beam head (2) which is mounted onto the intermediate body. In this layout, the scale beams are aligned to the functional measurement point, i.e. the probe tip center, regardless of the position of the moving guide in the xy -plane. This will ideally result in zero Abbe offset, as discussed in section 2.5.1. As a result Abbe deviations resulting from a CMM translation in the xy -plane, which are a main source of measurement deviations in conventional CMMs, can

be neglected.

The z -axis is mounted on top of moving guide (1) and carries the probe. In the F25, the z -stroke is 100 mm and is guided by air bearings. The Abbe principle in the F25 is satisfied when the z -axis is in its neutral position. When the z -axis moves, the graduated rulers for the x - and y -direction are not aligned with the probe tip center, resulting in an Abbe deviation with an Abbe arm equal to the displacement in z -direction from its neutral position. The contribution of the resulting Abbe deviation to the total measurement deviation is reduced by using precision air bearings, which decreases straightness deviations in the guides. This results in a 3D position uncertainty of 250 nm in a measuring volume of 140 x 140 x 100 mm. It should be noted that the measurement uncertainty improves for measurements with a limited z -displacement. Since these measurements can be performed around the neutral z -position, the contribution of the Abbe deviation can be reduced. Therefore, the position uncertainty on miniaturized components is expected to be around 100 nm. It is noted that the contribution of the probing system is not included in the positional uncertainty budget of the CMM.

1.3.2 NanoCMM by Van Seggelen

The NanoCMM, developed by Van Seggelen [Seggelen 05, Seggelen 07], is shown in figure 1.7. The measurement system in the xy -plane of the NanoCMM is similar to the system developed by Vermeulen [Vermeulen 99] as discussed in the previous section. A main difference is a reduced design specification for the z -axis of 4 mm. As a result the Abbe arm is reduced to a maximum of plus minus 2 mm, making it feasible to use elastic guides for the z -stroke and improving position uncertainty of the machine.

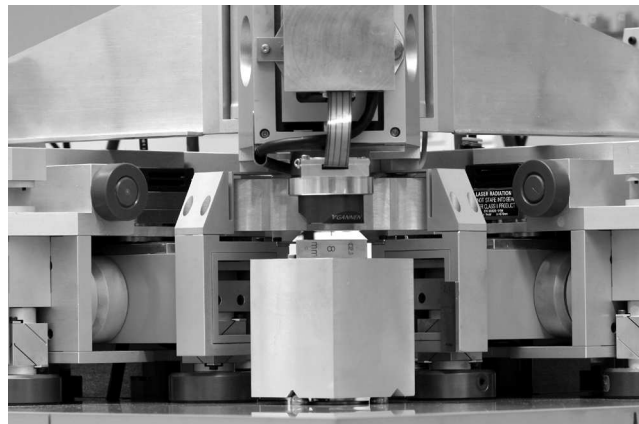


Figure 1.7: Photo of NanoCMM by van Seggelen.

A schematic of the mechanism used to create a z -translation is shown in Figure 1.8. The probe holder (5) is mounted on a body (1) that translates in z -direction guided by two leaf springs (11). When one set of leaf springs is used, a displacement in z -direction also results in a small displacement in x -direction. This displacement in x -direction is counteracted by displacement Δx_a in x -direction of an auxiliary body (10) with the same magnitude, but opposite direction. A lever (6) with rotary point (8) is used to assure that the z -displacement of body (1) is twice that of the auxiliary body (10). This assures that the displacements in x -direction of the body (1) and auxiliary body (10) are equal in magnitude, resulting in a pure translation of the body (1) in z -direction.

Leaf springs (11) not only have a stiffness in x -direction, i.e. their length direction, but also in z -direction. The force as a result of this stiffness needs to be supplied by the z -actuator. To reduce actuator power consumption a spring (9) is used that applies a force on the body (1). When the body (1) translates in z -direction, the spring (9) endpoint is translated by the same amount, thus effectively rotating the spring. This results in a force component in z -direction, which partly

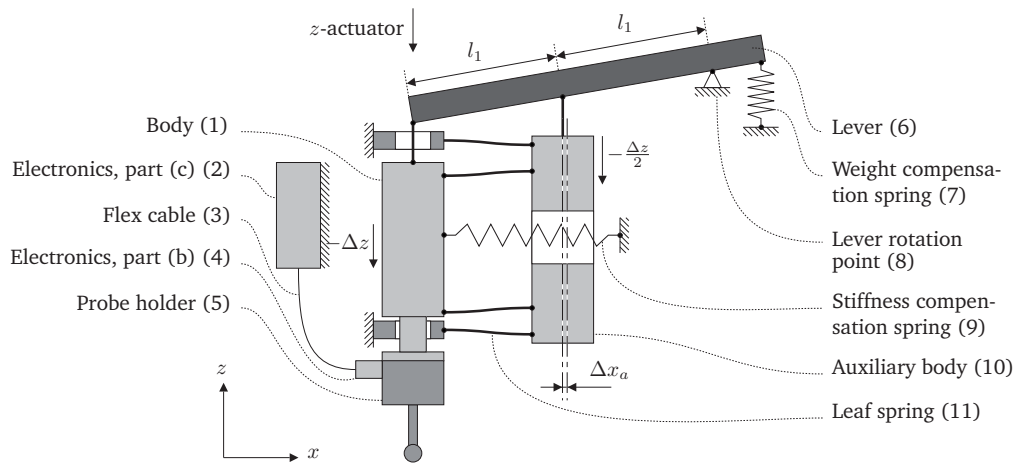


Figure 1.8: Schematic of guide along z -axis in the NanoCMM.

compensates the force due to the stiffness in z -direction of the leaf springs. By adjusting the preload force of the stiffness compensation spring (9) power consumption in the z -actuator, required to overcome the leaf spring stiffness when translating the body (1) in z -direction, is minimized.

The CMM Abbe point is obtained when the body (1) is in its zero position, i.e. $z_1 = 0$. Gravity forces on the elements of the z -axis, including the probe holder (5), pull the body (1) from this position. To compensate for the effects of gravity a weight compensation spring (7) is used, which assures that without actuation the body (1) is kept in its zero position. It is noted that when the body (1) moves from its zero position, the scale beams on the xy -stage are no longer aligned with the probe tip. This results in an Abbe offset, equal to the displacement from the zero position. Since the Abbe offset is limited to 2 mm, half the z -stroke, and by using precision guides, the contribution of Abbe deviation to measurement uncertainty is limited to a few nanometers [Seggelen 07]. The 3D position uncertainty of the NanoCMM is estimated by Van Seggelen [Seggelen 07] to be 25 nm in a measuring volume of 50 x 50 x 4 mm.

1.3.3 Ruijl's CMM

Finally, the CMM developed by Ruijl [Ruijl 01] at Philips Applied Technologies is discussed, as shown in figure 1.9. The metrology frame of this CMM is shown schematically in figure 1.10. The probe (1) is kept stationary and its position is measured using three orthogonal laser interferometer systems (3, 6) which intersect at the probe tip center. The work piece (5) is mounted on a movable mirror table (4) which positions the work piece relative to the probe (1). The mirror table reflects the laser interferometer beams, thus minimizing the Abbe offset regardless of the mirror table position.

A separate metrology frame (2) is used to connect the laser interferometer heads (3, 6) to the probe (1). To reduce measurement deviations due to thermal variations the mirror table is made from Zerodur[®] and the metrology frame is made from Invar. Furthermore, an aluminum shielding is applied around the metrology frame to reduce fluctuations and thermal gradients. The measurement range of the Ruijl CMM is 100 x 100 x 40 mm and the estimated volumetric position uncertainty is 27 nm [Ruijl 01].

Other low uncertainty CMMs include the VideoCheck UA 400 by Werth Messtechnik, the Nanocord by Mitutoyo, UA3P by Panasonic and NMM-1 by SIOS Meßtechnik. The NMM-1 concept is similar to the concept of the Ruijl CMM, shown in figure 1.10, with three orthogonal laser interferometers in a Zerodur[®] metrology frame [Hausotte 02].

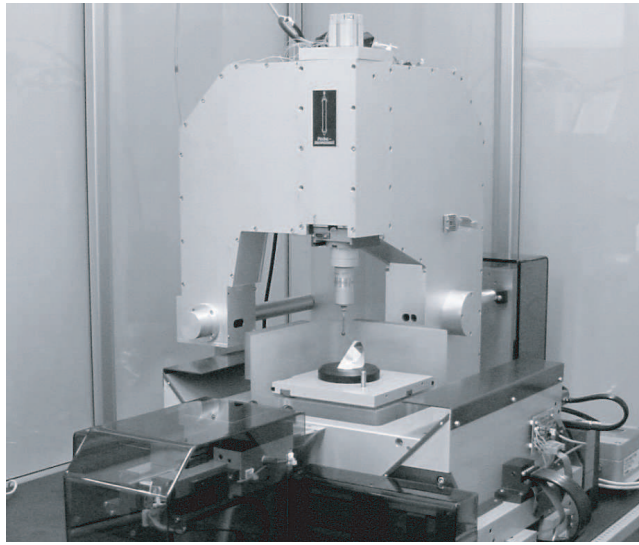


Figure 1.9: Photo of CMM by Ruijl.

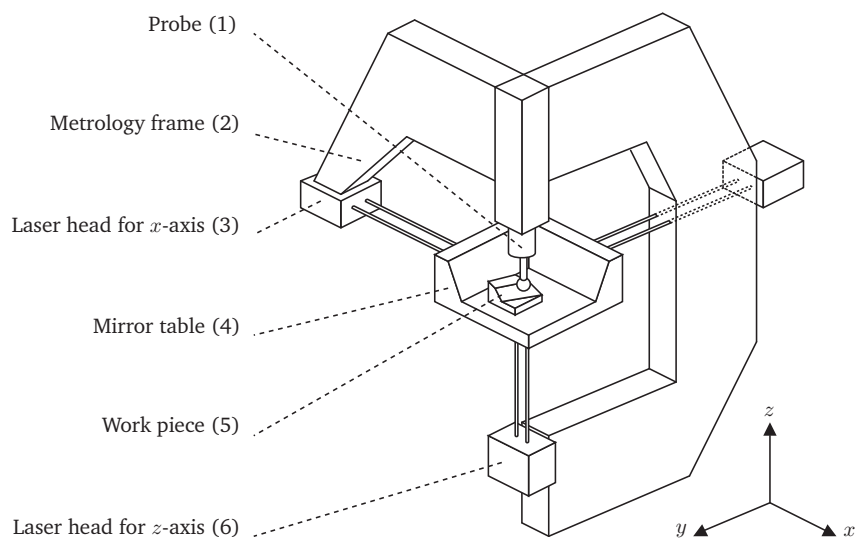


Figure 1.10: Measurement principle of CMM by Ruijl.

1.4 3D tactile probes for micro components

As mentioned in the previous section several high-accuracy CMMs have been developed. The probe system used in combination with the CMM is a critical factor for the measurement uncertainty and applicability of these machines. In order to operate effectively these probes should be able to measure a three-dimensional displacement with an uncertainty well below that of the CMM and preferably with a measurement range larger than the CMM over travel range. This section will discuss several probes that are developed for high-accuracy CMM metrology [Weckenmann 04].

1.4.1 PTB membrane probe

The probe by the Physikalisch-Technische Bundesanstalt (PTB) consists of a membrane with integrated piezo resistive strain gauges, as shown in figure 1.11. A stylus with probe tip is attached to the center of the membrane using epoxy adhesive. The strain gauges are used to detect deformations of the membrane and can thus be used to measure a displacement of the probe tip.

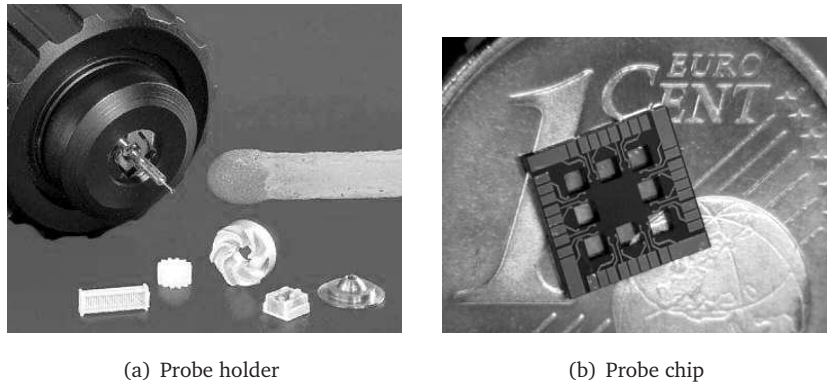


Figure 1.11: Silicon tactile 3D probing system as developed at the PTB [Brand 02, Pornnoppadol 02]: (a) probe holder with example products, (b) silicon chip with strain gauges.

As discussed in section E.2 a membrane suspension is overdetermined, which may result in internal stresses when the membrane is deformed. Consequently, the length of the membrane has to increase when the probe tip is moved. This will increase the stiffness of the suspension and result in a non linear stiffness. For a membrane length between stylus and edge of 1 mm, a thickness of 30 μm and a stylus length of 5 mm the stiffness is approximately 2000 N/m in the xy -plane and 48000 N/m in z -direction [Brand 02, Cao 02].

Probing forces can be reduced by creating holes in the membrane, referred to as a stripe membrane system, as shown in figure 1.11 (b). The calculated stiffness of a stripe membrane probe is 160 N/m in the xy -plane and 800 N/m in z -direction [Pornnoppadol 02, Pornnoppadol 04]. The anisotropic stiffness at the probe tip influences the measurement behavior of the probe, as discussed in section 2.3.6. The measurement uncertainty of the membrane probe could not be obtained from literature but is estimated to be between 50 - 100 nm.

1.4.2 Fiber probes

Both the Physikalisch-Technische Bundesanstalt (PTB) and the National Institute of Standards and Technology (NIST) have developed a tactile probe using an optical fiber as stylus. Two CCD-camera's are used to detect a 3D displacement of the tip. First, the opto-tactile fiber probe developed at the PTB is discussed [Guijun 98, Schwenke 01]. Initially, this probe was equipped with a single CCD camera, as schematically shown in figure 1.12.

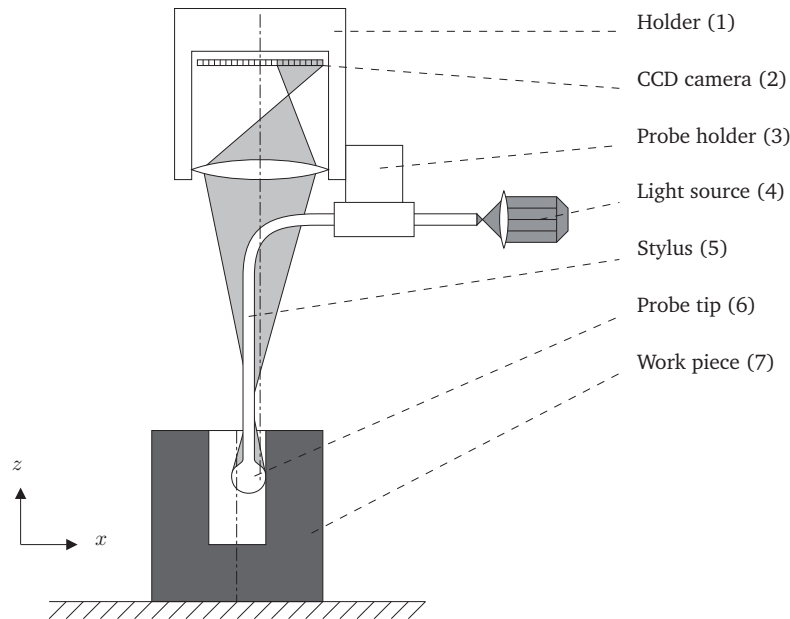


Figure 1.12: Schematic of 2D fiber probe with CCD camera as developed by the PTB.

The probe stylus (5) and tip (6) are illuminated using a LED light source (4). The backscattered light from the probe tip (6) is imaged on a CCD camera (2). The position of this image on the CCD is therefore a measure for the xy -position of the probe tip. Measurement of a tip displacement in z -direction, e.g. by analyzing the size of the image on the CCD, is relatively inaccurate. As a result this probe is essentially 2D [Schwenke 01].

For single point repeatability in xy -direction the standard deviation is approximately 50 nm. It is noted that the measurement uncertainty is influenced by the quality of the imaged light spot. Reflected light from the probe tip on the work piece surface may reduce the contrast in the CCD image or result in a mirror image [Schwenke 01]. Probing uncertainties in the range of 0.2 - 0.5 μm can be obtained, depending on the measurement task, probe tip diameter, illumination and depth of measurement, e.g. in a hole [Weckenmann 05].

A main advantage of this method is that the CCD camera directly measures the probe tip position. Finite stiffness effects of the stylus, as discussed in section 2.3.1, therefore do not influence probe resolution. As a result this method allows the measurement part of the stylus¹ to consist of a thin, e.g. radius < 10 μm , and long, e.g. measurement length up to 20 mm, fiber.

It is noted however, that typically the stiffness of a fiber stylus is low in comparison to surface forces between tip and work piece, as discussed in section 2.1.7. As a result the release distance and stick-slip during scanning increases, as discussed in sections 2.3.5 and 2.1.8. This limits the practical use of highly compliant, i.e. long and thin, styli. Methods to improve the scanning behavior include vibrating the probe tip and the use of a stroboscopic light source. However, this also increases measurement uncertainty.

The design of the 2D probe, as schematically shown in figure 1.12, can be extended to a 3D system, as schematically shown in figure 1.13. To improve the measurement uncertainty in z -direction, a second sphere (9) is attached to the stylus. The image of this target sphere (9) is reflected on a second CCD camera (2) using a mirror (8). The distance between probe tip (6) and target sphere (9) thus determines the maximum depth when measuring high aspect ratio structures, e.g. holes.

For a pure translation in z -direction it is assumed that the measurement part of the stylus, i.e. the thin part of the stylus on which the probe tip is mounted, is straight and that its length direction is

¹When small probe tips are used the stylus typically consists of a support part with a relatively large diameter for handling and a measurement part on which the probe tip is mounted to be able to measure small structures, as shown in section 3.2.3.

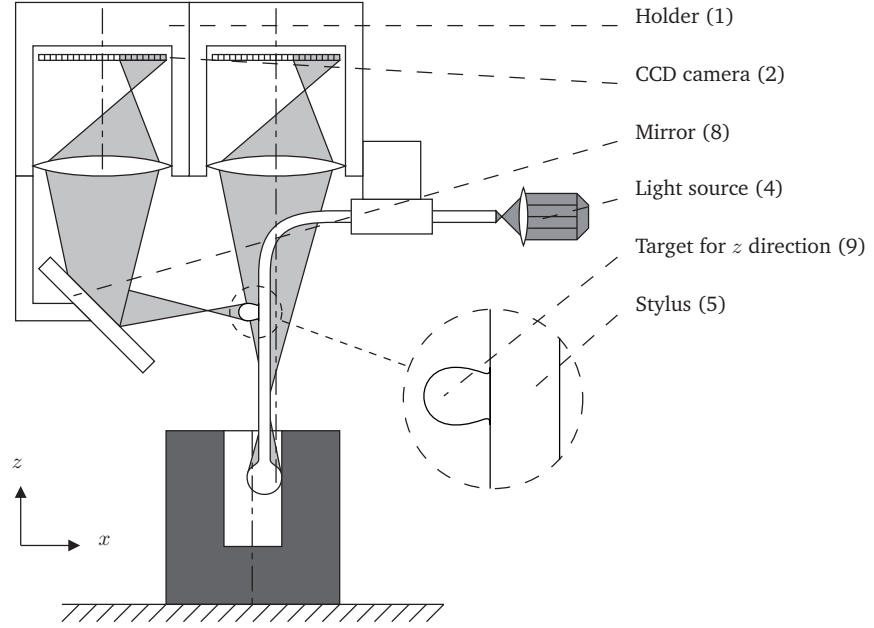


Figure 1.13: Schematic of 3D PTB fiber probe.

aligned with the force vector. The stiffness c_{zz} is then given by:

$$c_{zz} = \frac{EA}{l} \quad (1.1)$$

For a stylus with measurement length $l = 5$ mm, radius $r = 10$ μm and Young's modulus $E = 70$ GPa, the cross sectional area $A = 3 \cdot 10^{-10}$ m^2 , resulting in a stiffness c_{zz} of 4.4 kN/m. When probing in z -direction, the part of the stylus between probe tip and target for z -direction is therefore considered rigid with respect to the horizontal part of the optical fiber [Schwenke 01]. Some deflection will occur during 3D probing however, and the 3D tip position is therefore calculated by combining the evaluations of both camera images.

Another system using a fiber stylus and CCD camera to detect tip displacement has been developed at NIST [Muralikrishnan 04, Stone 05], as shown in figure 1.14. When the probe tip contacts the work piece in x - or y -direction, the stylus bends as a result of the contact force. In the z -direction, the contact force results in buckling of the stylus. Deformations of the stylus are recorded using two CCD camera's, or a single CCD camera when the field of view is split, mounted orthogonal to the length direction of the stylus.

By looking at the stylus on a certain position above the probe tip optical disturbances by backscattering of the probe tip in a hole or other structures is reduced. Also, no additional sphere is required for the detection of displacements in z -direction. However, limitations of this approach include that z -displacements are detected by buckling, which is not stable and may be hard to predict in true 3D measurements. Also, the part of the fiber between probe tip and the point of detection is included in both the metrology and structural loop between probe tip and work piece and adds to the measurement uncertainty.

Assuming that one end of the stylus is fixed and the other one pinned, the buckling force F_b is given by²:

$$F_b = \frac{\pi^2 EI}{0.7^2 l^2} \quad (1.2)$$

²It is noted that in practical applications the stylus will not be perfectly straight. As a result buckling will be more reproducible and the buckling force will be lower than the theoretical value.

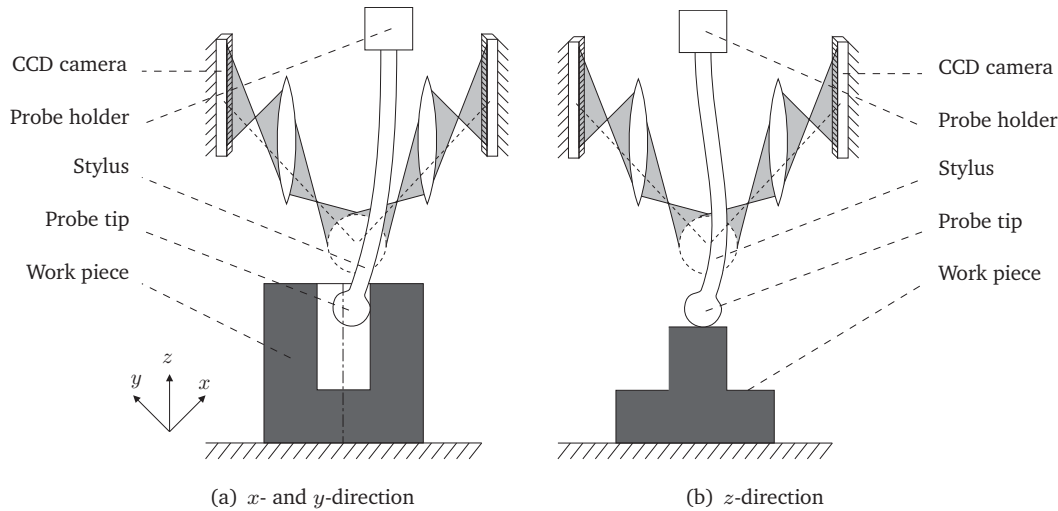


Figure 1.14: Schematic operation of the NIST fiber probe: (a) in xy -direction bending of the stylus is detected, (b) in z -direction buckling of the stylus is detected.

Where I is the second moment of area of the measurement part of the stylus, i.e. $I = \frac{\pi r^4}{2}$.

For a stylus with a measurement length $l = 20$ mm, radius $r = 25$ μm and Young's modulus $E = 70$ GPa the buckling force F_b can be calculated to be 2 mN. Decreasing stylus stiffness also increases the release distance and stick-slip during scanning, as discussed in sections 2.3.5 and 2.1.8. The measurement uncertainty with the NIST fiber probe was not found in literature but is estimated to be approximately 0.2 - 0.5 μm .

1.4.3 Metas probe

A 3D probe based on elastic hinges [Küng 05, Meli 03, Meli 04] is commercialized by Metas, as shown in figure 1.15. All axis are inclined by 45 degrees, resulting in an equivalent orientation with respect to gravity when the probe is mounted on a CMM. Sagging due to gravity is compensated for by an adjustable system using permanent magnets. All three axis are manufactured from a single piece of aluminum by milling and electro discharge manufacturing (EDM).

The flexure hinges have a wall thickness of 60 μm resulting in an isotropic stiffness of 26 N/m independent on stylus length. The equivalent mass at the probe tip is approximately 7 gram, which is relatively high and may result in plastic work piece deformation, as discussed in section 2.1.3. To reduce the influence of the colliding mass an elastic element with an isotropic stiffness of 2 kN/m is used, as shown in figure 1.15 (b). The first eigen frequency of the probe is approximately 11 Hz [Fracheboud 02].

A displacement of the probe tip is measured using three inductive sensors, mounted on the probe housing. During single point probing, probe deflections are recorded at different indentation positions to obtain a force-distance curve for the measurement point. The force-distance curve, based on all measurement points, is extrapolated to zero deflection where also the contact force is zero. Using this method in a single point repeatability test a standard deviation of 5 nm was obtained over 5 consecutive measurement points [Meli 03]. The 3D measurement uncertainty with this probe is not found in literature but is estimated to be approximately 50 nm.

1.4.4 NPL capacitive probe

The National Physical Laboratory (NPL) has developed a capacitive probe with a suspension consisting of three flexures in a triangular arrangement [Leach 01, Leach 04A, Leach 04B, Peggs 99],

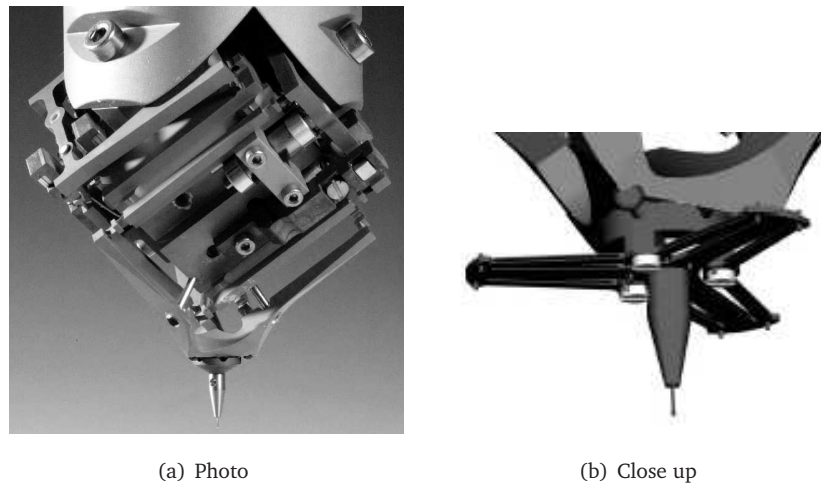


Figure 1.15: Metas probe: (a) photo, (b) schematic close up of the elastic element used as a mechanical filter.

as shown in figure 1.16. The three slender rods are manufactured from a $50\text{ }\mu\text{m}$ thick beryllium-copper sheet. The rods are connected to the stylus via a frame consisting of three tungsten carbide tubes and a central disk. The equivalent mass and stiffness at the probe tip when probing in z -direction are approximately 370 mg and 10 N/m , respectively. By choosing an appropriate stylus length the probe stiffness can be made isotropic.

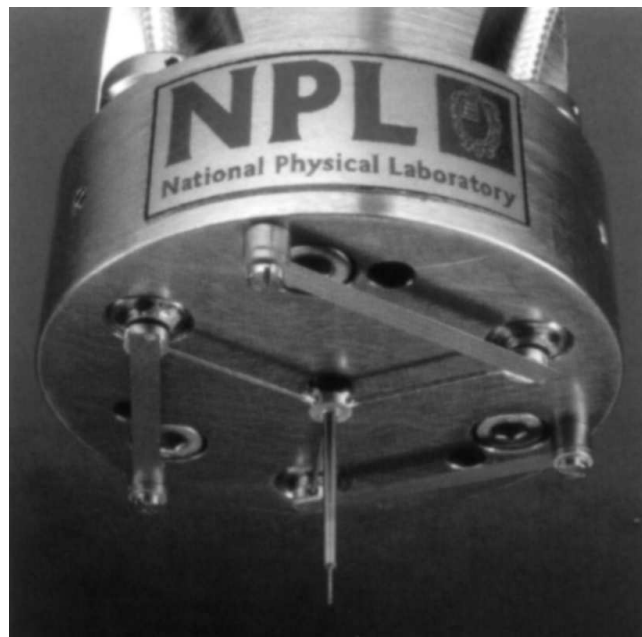


Figure 1.16: Photo of NPL capacitive probe.

The sensing elements of the probe are three miniature capacitance gauges, mounted in the probe holder. Three aluminum target disks of 3 mm in diameter are mounted on the junction of the flexures with the tungsten carbide tubes. A displacement of the probe tip results in a translation and/or rotation of the center tungsten-carbide body, which is suspended on the three flexures. As a result of these translations and/or rotations the gaps between one or more capacitance gauges and aluminum target disks change. By recording each gap, the position of the probe tip can be calculated.

The maximum range of the probe is limited by the gap between the capacitance gauges and target disks, which is approximately $20\text{ }\mu\text{m}$. When the target disks are mounted on the center tungsten-carbide body they are hand polished to be coplanar. The resolution of the capacitance gauges with a $20\text{ }\mu\text{m}$ gap is 3 nm .

When the probe tip is displaced in z -direction the effective length of the rods will decrease, resulting in a small parasitic displacement of the probe tip, as discussed in section 2.2.1. The 3D measurement uncertainty with this probe is not found in literature but is estimated to be between $50 - 100\text{ nm}$.

1.4.5 Vibrating probe

Vibrating probes were originally developed for measurements on the profile of ink-jet and fuel injection nozzles [Weckenmann 04]. In most cases these probes were essentially 1D systems in which changes in resonant frequency were used as a sensing mechanism [Bauza 05, Kim 96, Kim 99, Lebrasseur 00, Masuzawa 93, Takaya 04, Takaya 05].

Mitutoyo commercializes a vibrating probe system [Hidaka 06, Nishimura 01], as shown schematically in figure 1.17. The glass probe tip used is formed into a spherical shape by utilizing surface tension in the melting state, similar to the manufacturing process of the borosilicate tip as described in section 3.2.3. The Ni-Cr stylus is glued on the surface of a lead zirconate titanate (PZT) component. This bulk-PZT is divided into a driving and a sensing electrode. The stylus is vibrated in its longitudinal resonant state at approximately 349 kHz by the driving electrode.

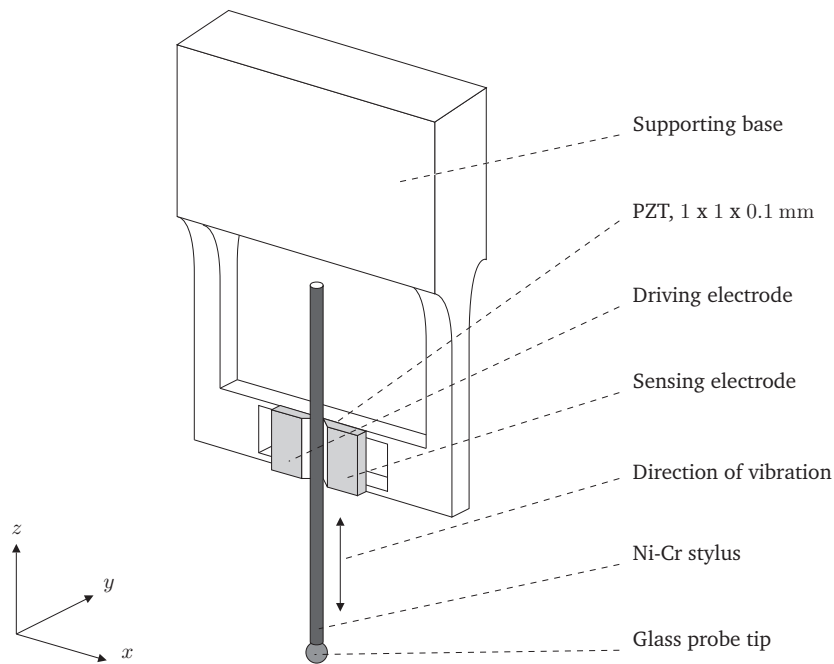


Figure 1.17: Schematic of UMAP Ultrasonic probe.

Contact between the probe tip and work piece can be detected by a change in the vibrational amplitude, phase or resonant frequency, as discussed in section 2.2.4. The probe system registers a single measurement quantity and is thus considered a 1D sensor. However, the system is sensitive to 3D displacements of its tip and can thus be used in 3D measurements when the direction of approach and the nominal shape of the work piece are known. The optimum sensitivity with this system is obtained when the length direction of the stylus is aligned with the probing direction.

An important advantage of the probe is the high aspect ratio, up to 100, between the length of the stylus measurement part and the tip ball diameter. Measurements with a $20\text{ }\mu\text{m}$ diameter Ni-Cr stylus with a length of 3 mm and a $30\text{ }\mu\text{m}$ diameter glass probe tip show a measurement uncertainty in the micrometer region.

Contact forces with this system are highest when probing in the length direction of the stylus, i.e. along the z -axis. Using equation 1.1 the stiffness in the length direction of the stylus for a Young's modulus E of 200 GPa is calculated to be 21 kN/m. For a CMM over travel of 7 μm , as discussed in section 2.1.4, equation 2.10 results in a contact force of 0.15 N. This value exceeds the buckling force of 3.5 mN, as calculated using equation 1.2, which would result in buckling of the stylus during a measurement.

As discussed in appendix G, a tip diameter of 30 μm loaded with 3.5 mN will result in plastic deformation. It is therefore assumed that the contact force is reduced by control, by adding additional compliance to the system, by decreasing approach speed or a combination of these. For the xy -direction, the contact force during a measurement is reported to be 0.15 μN [Hidaka 06].

A second point of interest is that the point of contact between probe tip and stylus is influenced by bending of the stylus. Therefore surface forces, as discussed in section 2.1.7, and other sources that cause the stylus to deform during a measurement will influence the probe measurement uncertainty. Hidaka and Schellekens [Hidaka 06] believe that it may be expected that after careful calibration and the implementation of error compensation sub-micrometer uncertainty may be obtained with this probe.

1.5 Probe by Pril

From section 1.3 and 1.4 it may be concluded that the probe system and not the coordinate measuring machine is currently the limiting factor with respect to the measurement uncertainty that can be achieved with this method. This is especially true for probe systems with a low contact force, like the fiber probes and the vibrating probes discussed in the previous section. Probing systems that are designed for optimum measurement uncertainty, close to that of precision coordinate measuring machines, have much higher contact forces and are limited with respect to their application on micro components. Therefore a new low uncertainty probe system is developed, as will be discussed in this thesis.

The original probe prototype, as shown in figure 1.18, is developed at the Eindhoven University of Technology by Pril [Pril 02]. This section briefly discusses the design of this probe. Additional information, including probe calibration and measurement results, can be found in appendix A.

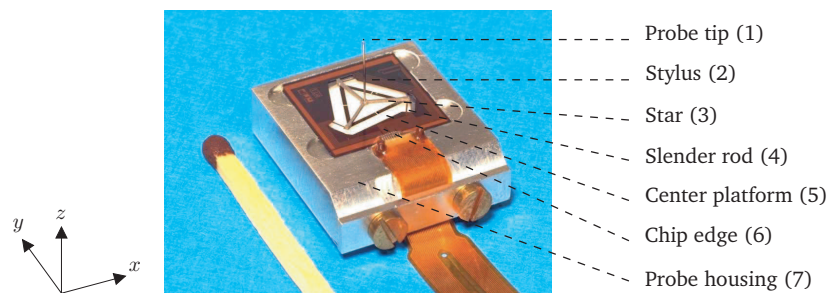


Figure 1.18: Tactile 3D probing system developed by Pril [Pril 02] showing the holder and chip design.

The probe consists of a stylus (2) with a ruby sphere (1). It is attached to a silicon chip (4-6) via a three-legged star (3) using epoxy glue. The edge of the chip (6) is connected to the probe housing (7). The center platform (5), slender rods (4) and edge of the chip are manufactured from a single piece of silicon. The center platform is connected to the edge of the chip using these three slender rods. This allows the probe tip to translate in z -direction and make pseudo translations in x - and y -direction due to a rotation of the center platform around the y - and x -axis respectively. The remaining degrees of freedom are fixed. For reasons of thermal and mechanical stability the rods are oriented in a triangular fashion, as discussed in section E.2.

Since the edge of the chip (6) is fixated, a displacement of the probe tip results in a deformation of the slender rods. This deformation is detected using four piezo resistive strain gauges ($R_1 - R_4$),

deposited on each rod in a Wheatstone bridge configuration [Pril 02], as shown in Figures 1.19 and 1.20.

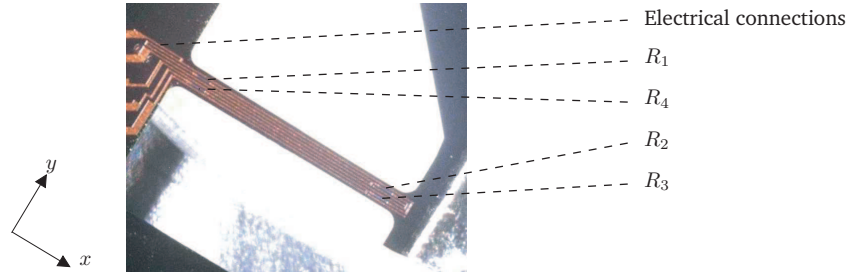


Figure 1.19: Closeup of the slender rods with electrical connections and piezo resistive strain gauges.

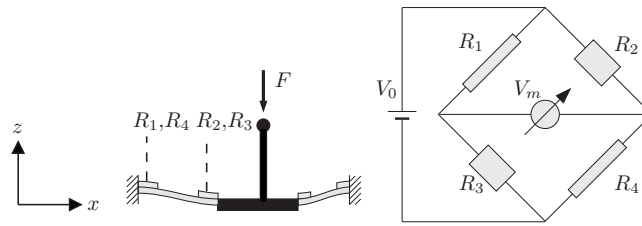


Figure 1.20: A displacement of the probe tip results in a deformation of the slender rods. As a result R_1 and R_4 are stretched, increasing their resistance, and R_2 and R_3 are compressed. As a result of the Wheatstone bridge configuration this results in a change in the voltage V_m .

A voltage V_0 across the bridge results in a measurement signal V_m when the resistance of R_1 and R_4 changes relative to R_2 and R_3 . This results in one measurement signal for each slender rod in the suspension. The position of the probe tip should be determined for three degrees of freedom, i.e. translation in z and pseudo translations in x - and y -direction, and three measurement signals are recorded (one for each slender rod). The relation between the tip displacement $[\Delta x \ \Delta y \ \Delta z]'$ and measurement signals $[\Delta m_1 \ \Delta m_2 \ \Delta m_3]'$ is given by sensitivity matrix \mathbf{A} according to:

$$\begin{bmatrix} \Delta x \\ \Delta y \\ \Delta z \end{bmatrix} = \begin{bmatrix} s_{1x} & s_{2x} & s_{3x} \\ s_{1y} & s_{2y} & s_{3y} \\ s_{1z} & s_{2z} & s_{3z} \end{bmatrix} \begin{bmatrix} \Delta m_1 \\ \Delta m_2 \\ \Delta m_3 \end{bmatrix} = \mathbf{A} \begin{bmatrix} \Delta m_1 \\ \Delta m_2 \\ \Delta m_3 \end{bmatrix} \quad (1.3)$$

Here s_{1x} is the sensitivity of the strain gauges on rod 1 for a displacement of the probe tip in direction x . The sensitivity matrix \mathbf{A} thus gives the relation between the displacement of the probe tip and the signal from the strain gauges of the three slender rods. When the sensitivity matrix is known it is possible to calculate the displacement of the probe tip using the measured output voltages from the slender rods.

1.6 Calibration methods for tactile 3D probes

Calibration of the probes is essential to determine their uncertainty with respect to the standard of length, i.e. traceability. For several probes, including the probe by Pril, the setup used to determine the uncertainty of the probe can also be used to characterize its behavior. For the probe by Pril, the characterization is necessary to determine the sensitivity matrix \mathbf{A} , as discussed in section 1.5. Important parameters for the tactile 3D probes discussed above are the diameter and roundness of its tip. For conventional systems the uncertainty of the measurement is large in comparison

to the uncertainty in tip diameter. However, for current low uncertainty probes, the influence of the tip diameter and roundness on the total uncertainty can become a dominant factor. Therefore calibration and compensation of this effect becomes a necessity.

In the next section the method of calibrating a probing system on a separate setup is discussed. An example 1D setup is discussed, which is used to calibrate the probe system as discussed in this thesis. The probing system can also be calibrated when mounted on a CMM, which will be briefly discussed in section 1.6.2. Finally, some methods to calibrate the probe tip are described.

1.6.1 Calibration on a separate setup

The advantage of a separate setup to calibrate the behavior of a probe system is that it can be designed for optimum uncertainty. Since such a setup is typically much smaller than a CMM it can easily be isolated from environmental disturbances. Typically, the probe is calibrated in a single direction on such a setup. By reorienting the probe on the setup the response to a probe tip displacement can be measured in any direction. This allows a 3D calibration of the probe using a 1D calibration setup. Most displacement measurements with the tactile 3D probing system, discussed in this thesis, are performed using a 1D calibration setup. This setup will be discussed in the remainder of this section.

A schematic view of the plane mirror differential laser interferometer setup [Pril 02, Loon 97] is shown in figure 1.21. The probe to be calibrated (1) is attached to a bracket (2) and placed on top of the setup. The probe tip is brought into contact with a measurement mirror (4). The measurement mirror is guided in z -direction using elastic hinges (not shown). A ring shaped reference mirror (3) is rigidly connected to the setup housing (6). The position of the measurement mirror relative to the reference mirror is controlled using a piezo actuator (5).

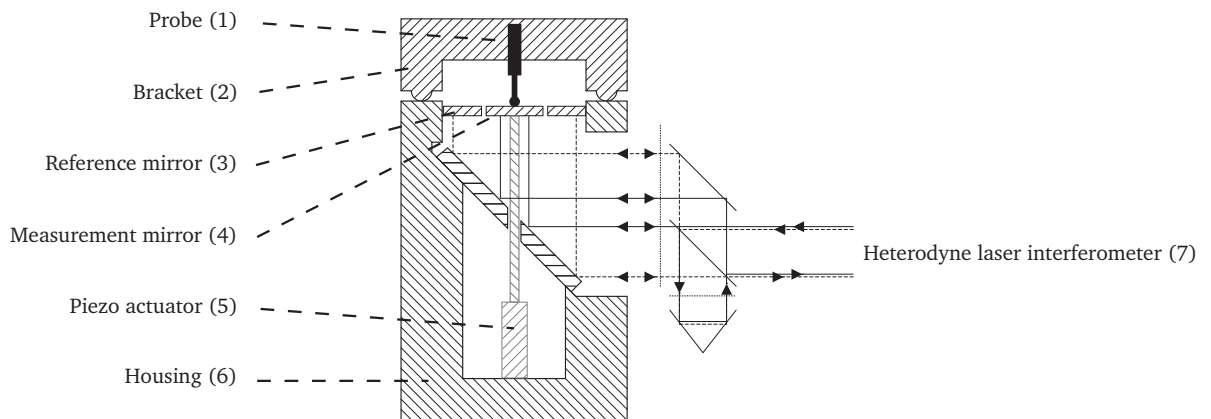


Figure 1.21: Schematic view of the plane mirror differential laser interferometer setup used to measure the behavior of the probe.

Thus a displacement of the measurement mirror results in a displacement of the probe tip. The measurement signal from the probe as a result of this displacement is recorded. Simultaneously, the displacement of the measurement mirror relative to the reference mirror is measured using a heterodyne laser interferometer (7). The measurement is repeated for several positions of the measurement mirror.

As mentioned, the behavior of the probe can be measured for only one direction at a time with this setup. Therefore three V-shaped grooves are made on the top and on a side of the bracket (2). The probe housing, (7) in figure 1.18, has three spheres, which match the position of the V-shaped grooves. This connection is commonly referred to as a Kelvin clamp [Hale 01] and allows an operator to rotate the probe around its z -axis, see figure 1.18, with respect to the bracket by 120 and 240 degrees respectively.

The merits of the differential laser interferometer are listed below [Pril 02]:

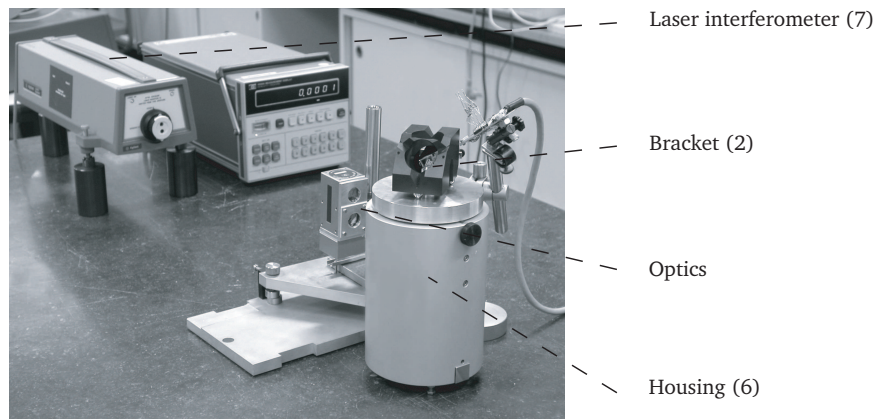


Figure 1.22: Photo of calibration setup with heterodyne laser interferometer.

- The two mirrors can be close to each other which decreases the thermal loop of the calibrator;
- The reference and measurement mirror can be positioned symmetrically around the measurement axis which preserves the cylindrical symmetry of the calibrator;
- The mass of the measurement mirror can be small, improving the dynamical properties of the calibrator;
- The light beam from the heterodyne later interferometer (7) is split into a measurement beam and a reference beam using a polarizing beam splitter. Both beams reflect two times at the reference (3) or measurement (4) mirror causing a double pass and hence double sensitivity compared to an interferometer setup with two corner cubes;
- Both beams travel equal distances through the concerning media (air and glass), provided that the measurement (4) and reference (3) mirror lie in the same plane. A change in refractive index, e.g. due to a homogeneous temperature or pressure variation, will effect both beams equally and will therefore not influence the measurement uncertainty.

The range of the calibrator is 30 micrometers. The uncertainty of the calibrator is influenced by [Pril 02, Loon 97]: the uncertainty of the interferometer system, which is 1 nm, the uncertainty due to mechanical tolerances of the parts and alignment of the beams, which leads to a relative error of 0.1%, and an expected worst case thermal drift of 5.2 nm for a temperature change of 100 mK

1.6.2 Calibration on the CMM

Using an artifact the probe can be calibrated on the CMM itself. An important advantage of this method is that the alignment between the probe and CMM is included in the calibration measurement. Deviations due to the finite stiffness of the CMM, as discussed in section 2.3.2, and the connection and alignment between probe and CMM are thus partially compensated for. Using a calibrated spherical artifact, i.e. a master ball, the calibration of the probe tip can also be performed on the CMM, as discussed in the next section.

An important limitation of this method is that the uncertainty of the CMM is included in the probe calibration. Coefficients of the sensitivity matrix \mathbf{A} are typically taken as an average sensitivity, e.g. using a least squares fit procedure, over a large number of measurement values. As a result, random deviations of probe and CMM are partially compensated for.

1.6.3 Probe tip calibration

Tactile 3D probes typically use a spherical probe tip to make contact with a work piece. During a measurement the position of the probe tip center point is determined by the measurement system of the coordinate measuring machine. For a perfect sphere the point of contact on the work piece can easily be calculated once the radius of the probe tip and the direction from the probe tip center point to the point of contact are known [Li 03]. The direction during probing can be obtained from the probing system, by interpolation over at least three points near the contact point or by estimation, e.g. from a CAD model of the work piece [Weckenmann 04].

Unfortunately, probe tips are not perfectly spherical. For traditional CMMs the stage position uncertainty is usually much larger than the typical roundness deviation of probing spheres, around 40 - 80 nm for precision spheres, and is included in the measurement uncertainty of the CMM [Haitjema 96, Küng 07]. For precision probing systems, as discussed in this thesis, the effects of roundness and radius of the tip can be a major contribution to the measurement uncertainty and thus needs to be compensated for.

In order to compensate for the form and radius of the tip it needs to be calibrated. A direct way of measuring a sphere is the use of a Michelson interferometer [Bray 97, Griesmann 04, Jansen 06, Nicolaus 96, Nicolaus 97]. A Michelson interferometer produces an interference pattern over the measurement pattern which can be used to create a surface map of an object. For the measurement of spheres a spheric Michelson interferometer, as shown in figure 1.23, is often used.

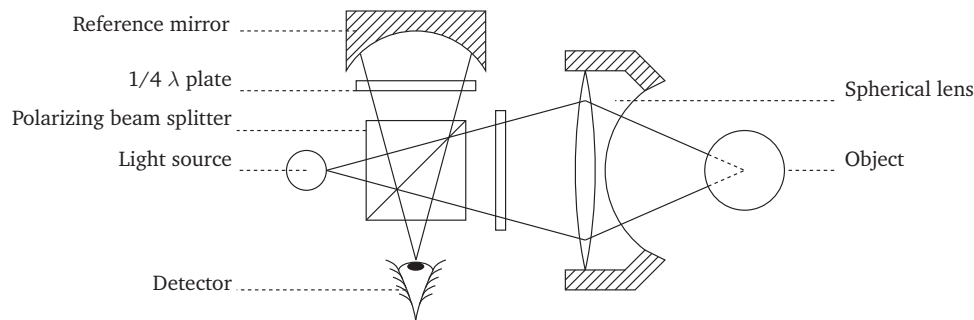


Figure 1.23: Schematic of a spheric Michelson interferometer.

The interference pattern produced by the Michelson interferometer does not cover the entire surface of the probe tip. Measurements at several angles are therefore combined using stitching [Jansen 06] to produce a complete image. By using a second spheric Michelson interferometer both the topography and the diameter can be measured [Nicolaus 96, Nicolaus 97].

The measurement uncertainty depends on several parameters, including the material of the object and the alignment of the measurement setup [Schmitz 01, Schmitz 02, Selberg 92]. Uncertainty levels of a few nanometers can be obtained with this method [Jansen 06]. However, for spheres with a diameter below 1 mm the applicability of this method is limited and the measurement uncertainty increases.

A second direct method of tip calibration is proposed by Chen [Chen 07] who used an optical microscope with CCD camera to acquire contour images of a probe tip. A back light projector with intensity feedback control is used along with a time-averaged image processing strategy. Using a x50 optical objective and sub-pixel edge detection a measurement uncertainty of about 0.5 μm has been obtained with this system. The measurement uncertainty is therefore currently insufficient for ultra precision probes. However, the method is applicable for micro spherical tips as it allows calibration of probe tips with a diameter of only a few tens of micrometers.

Finally, a mechanical direct method of tip calibration is discussed. The roughness and roundness of a probe tip can be measured using a turntable- or stylus-type instrument where 360° traces of the tip are made. An uncertainty below 10 nm is possible with this type of measurement [Gao 96, Haitjema 96, Meli 02, Neugebauer 01, Thalmann 05]. However, roundness measurements become more complex as the diameter of the probe tip decreases. Deviations of the instrument, including

its setting precision and transducer alignment, are such that the measurement uncertainty will be significantly degraded for spheres with a diameter of 2 mm or below [Chetwynd 87]. The method can be combined with a comparator measurement [Koenders 03, Küng 07, Neugebauer 97] to improve the uncertainty in the tip diameter calibration. A limitation of a direct mechanical measurement is that the interaction may, especially for fragile probe systems, damage the probe. Damage to the probe suspension can be prevented by fixating it during the measurement. However, this remains a difficult task to do correctly.

As discussed in the previous paragraphs, a direct measurement of a spherical probe tip with a diameter below 2 mm is in most cases not practical or even possible. An alternative method is to use a calibrated spherical artifact and calibrate the probe tip on the CMM. By measuring the artifact, as shown schematically in figure 1.24, the shape and diameter of the probe tip can be obtained from the measurement results.

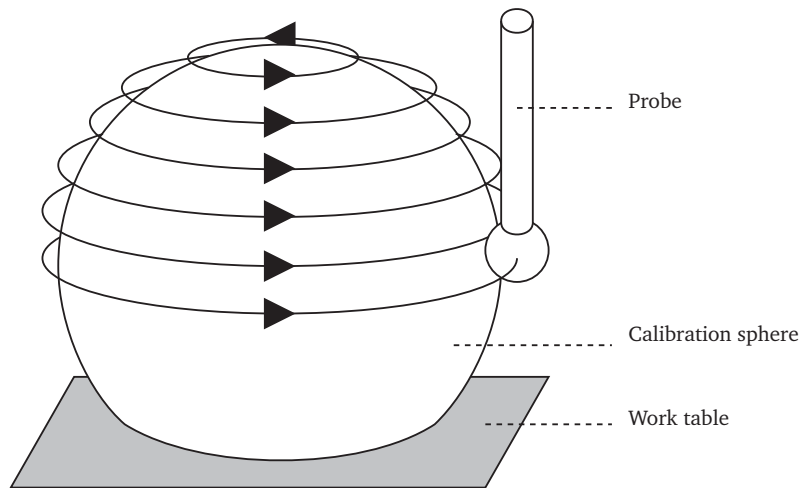


Figure 1.24: Schematic of tip calibration on a CMM using a spherical artifact.

If the alignment of the artifact on the CMM is not known with sufficient uncertainty before the measurement, error separation techniques can be used. This technique consists of a series of measurements, similar to figure 1.24, for several orientations of the artifact relative to the probe tip. By analyzing the variation in the measured profiles, the contribution of the probe tip and artifact to this profile, i.e. their shape, can be determined. In its simplest form this technique requires two orientations, as schematically shown in figure 1.25, and is often referred to as the reversal method [Chetwynd 76, Chetwynd 87, Donaldson 72B, Evans 96].

By using error separation techniques it is also possible to use a non-calibrated spherical artifact to obtain the roundness deviations of the probe tip and artifact. However, the diameter of the probe tip and spherical artifact cannot be obtained from error separation using only two spheres. For this reason Küng *et al.* [Küng 05, Küng 07] used a third sphere in their measurements, as schematically shown in figure 1.26.

The measured distance between the centers of spheres 1 and 2, $m_{12}(\alpha)$, at angle α in figure 1.26 (a) is a function of the local radii $r_1(\alpha)$ and $r_2(\alpha)$ of spheres 1 and 2, respectively. To be able to measure all three spheres relative to each other it should be possible to use at least one sphere as both a reference artifact and as a probe tip. In the example of figure 1.26 (a) this results in three simple equations:

$$\begin{aligned} m_{12}(\alpha) &= r_1(\alpha) + r_2(\alpha) \\ m_{13}(\alpha) &= r_1(\alpha) + r_3(\alpha) \\ m_{23}(\alpha) &= r_2(\alpha) + r_3(\alpha) \end{aligned} \tag{1.4}$$

The system can easily be solved for any sphere, e.g. for sphere 1 the radius $r_1(\alpha)$ is given by:

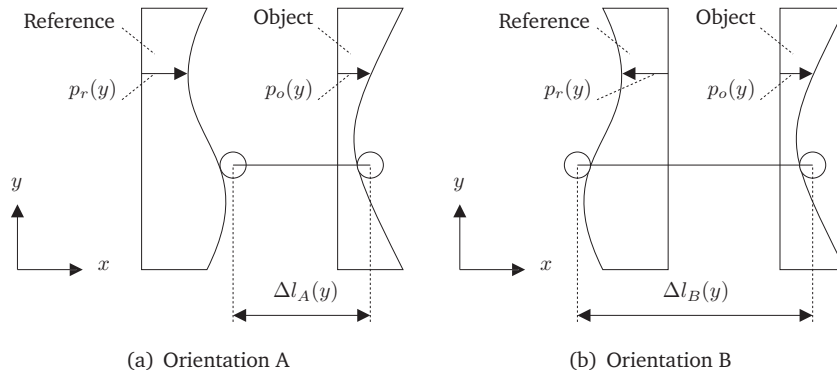


Figure 1.25: Schematic of the reversal method, (a): the contribution of the reference shape $p_r(y)$ at position y is subtracted from the measured length variation, i.e. $\Delta l_A(y) = p_o(y) - p_r(y)$, (b): the contribution of the reference is added, i.e. $\Delta l_B(y) = p_o(y) + p_r(y)$.

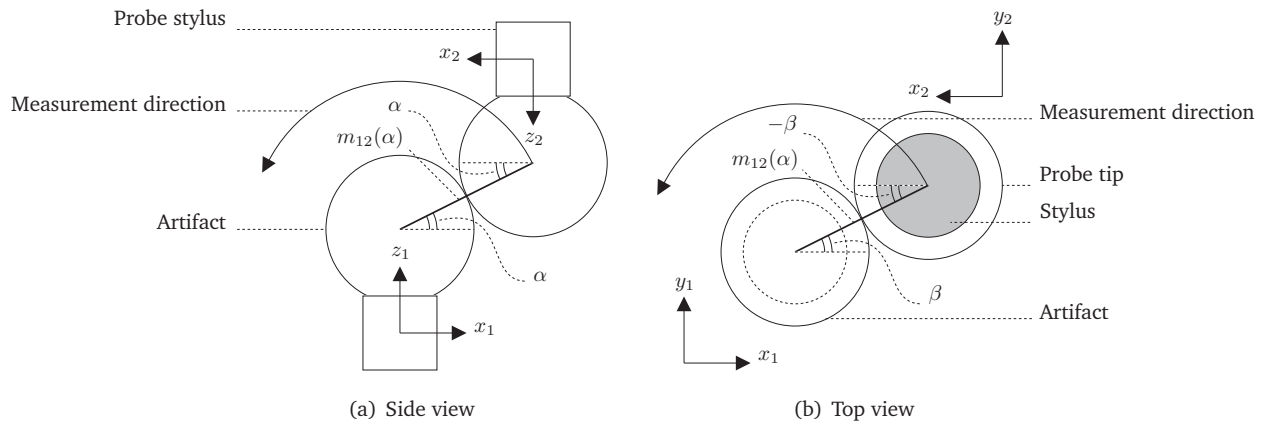


Figure 1.26: Schematic of side and top view of two spheres in contact.

$$r_1(\alpha) = \frac{m_{12}(\alpha) + m_{13}(\alpha) - m_{23}(\alpha)}{2} \quad (1.5)$$

For the measurement around the z -axis, as shown in figure 1.26 (b), the method is more complicated as the local coordinate systems of the spheres are mirrored. As shown in this figure, the contact point on the artifact is at an angle β relative to the local x -axis for sphere 2, x_2 , while the contact point on the probe tip is at an angle of $-\beta$ relative to its local x -axis, x_1 . As a result, this system requires the use of error separation techniques, as discussed before, to be able to do a three dimensional calibration [Küng 05, Küng 07]. A main drawback of this method is the time needed to perform the calibration and that it cannot be used in combination with most low uncertainty probing systems as discussed in section 1.4.

Another possibility to obtain the diameter of the probe tip is by using it to scan a sharp well defined edge [Morel 2006, Spaan 06]. Commercial available diamond blades have a sharpness radius down to about 10 nm. The edge radius can be neglected if it is smaller than the required calibration uncertainty and the measured diameter can then be regarded as the diameter of the probe tip. Figure 1.27 shows the result of a scanning measurement of a diamond blade with a 10 nm edge radius using a prototype version of the probe as discussed in this thesis.

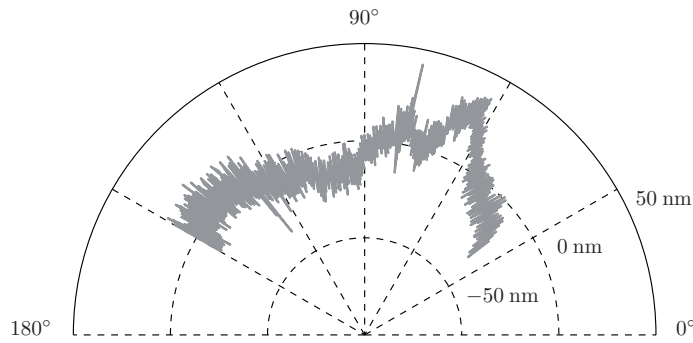


Figure 1.27: Residual of a scanning measurement on a diamond cutting blade with 10 nm tip radius after subtraction of a best-fitting sphere with radius 500.04 μm [Spaan 06].

The deviation of indirect methods of probe tip calibration, as discussed in this section, can be 20 nm or less [Küng 07], depending on the method of measurement and the combined uncertainty of probe and CMM used. It should be clear that probe tip calibration becomes increasingly complicated for decreasing tip diameters.

1.7 Research objectives and outline of this thesis

As discussed in the introduction of this thesis there is an increasing need for 3D measurements on MEMS and other miniaturized components with low uncertainty. Several ultra precision coordinate measuring machines are developed which are suitable for this task. Currently, the applicability of this method and the measurement uncertainty that can be achieved is limited as a result of the effects that influence the interaction between the probe tip and work piece on a micro scale.

The main goal for the research as presented in this thesis is getting a better insight in the aspects that influence tactile probing on a micro scale and the development of a probing system suitable for three-dimensional measurements on micro scale features with a repeatability below 20 nm.

The probing systems which are currently available, as discussed in section 1.4, offer low uncertainty but are not suitable for measuring small components, often due to high contact forces during probing as a result of a high colliding mass or stiffness of the probing system. Several probing systems are available that are suitable for measuring small components, but these lack the required measurement uncertainty of 100 nm or less.

Probing systems which are currently available are therefore not suitable for low uncertainty 3D metrology on miniaturized components. The next chapter will therefore focus on the interaction physics between probe tip and work piece. It will become apparent that the interaction is influenced by the dimensional scale of the measurement and is a main reason of the limitations of 3D metrology on miniaturized components.

The results from chapter 2 will be used in the design of a new ultra precision 3D tactile probing system. The design of this system is discussed in chapter three. The probing system has a colliding mass of 34 mg, an isotropic stiffness down to 50 N/m at the probe tip and is suitable for measuring miniaturized components.

A main challenge in the manufacturing process of the probing system is assembly, since it incorporates the handling of small, e.g. tip diameters down to 120 μm , and fragile components. Chapter 4 discusses the design and experimental results of a suction gripper suitable from handling these small and fragile components.

Experimental results with the tactile 3D probing system are discussed in chapter 5 and finally, in chapter 6, concluding remarks and recommendations for further research are given.

Chapter 2

Aspects of probing

Measurement instruments are sensitive to more than one physical quantity. When measuring the topography of a work piece, the measurement result will therefore always be influenced by the environment and (local) variations in the work piece itself. A mechanical probe will respond to both topography and changes in the mechanical properties of the surface, e.g. elastic modulus and hardness. An optical probe is influenced by the reflectivity and optical constants of the work piece, a scanning tunneling microscope (STM) responds to the electrical properties of the work piece and so on [Franks 91].

As the scale of the measurement decreases, the problems associated with the surface-probe interactions become increasingly apparent [Leach 01]. The focus of this thesis is on the mechanical probing of a work piece to determine its dimensional parameters. The effects associated with measurements on a micro-scale are discussed in this chapter.

2.1 Forces during tactile probing

The forces during probing are greatly influenced by the type of probe system used and the measurement strategy. Therefore, in the first section the three main types of probes are discussed and the measurement strategy is discussed in section 2.1.2.

2.1.1 Hard probes, touch-trigger probes and measuring probes

Mechanical probes are used to detect the surface of the work piece to be measured by means of physical contact between a probe tip and the work piece. Mechanical probes can be categorized in hard probes, touch-trigger probes and measuring probes [Cauchick-Mighel 98, Lu 82, Pril 02, Roth 83, Vliet 96, Weckenmann 04].

Hard probes do not have their own suspension and hence the probe tip is rigidly connected to the measuring head of the Coordinate Measuring Machine (CMM), as shown in figure 2.1 (a). Compared to touch-trigger probes and measuring probes this method results in a high stiffness of the loop between probe tip and work piece and a large colliding mass. As discussed in sections 2.1.3 to 2.1.5, this results in high forces and deviations during the measurement.

Touch-trigger probes have a suspension, as shown in figure 2.1 (b), which greatly reduces the forces during a measurement in comparison to hard probes. A touch trigger probe produces a

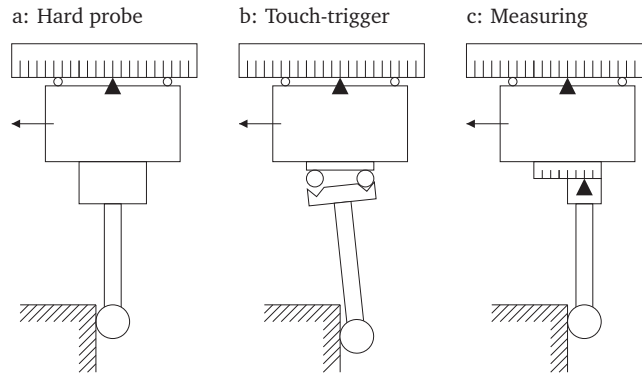


Figure 2.1: Schematic representation of three main types of mechanical probes: (a) hard probe, (b) touch-trigger probe, (c) measuring probe.

boolean signal to indicate whether the probe tip is in contact with the work piece or not. The position of the CMM measuring head is recorded when a trigger signal is generated by the touch-trigger probe. This trigger signal may be generated upon contact between tip and work piece, when the contact is broken or both.

A measuring probe has its own suspension and measurement system, as shown in figure 2.1 (c). Therefore it is able to provide quantitative information about the position of the tip ball with respect to the reference point. This improves the measurement uncertainty and is needed to perform a scanning measurement, as will be discussed in the next section.

2.1.2 Probing strategy

The probing strategy greatly affects the aspects that influence the measurement. Therefore in this section two probing strategies are discussed, single or discrete point probing and scanning.

During single point probing, the position of only one point on a work piece is measured during a probing operation. The position of other points on the work piece are measured in subsequent probing operations, as shown in figure 2.2.

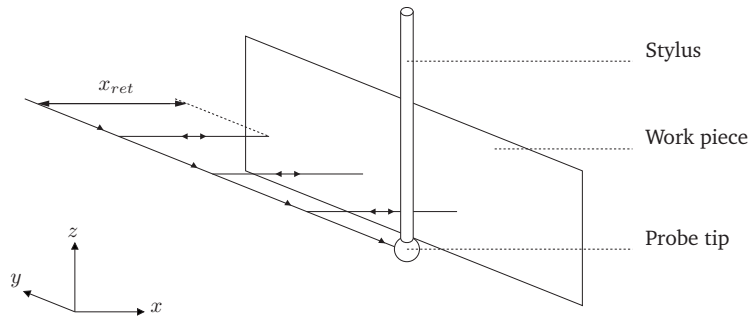


Figure 2.2: Schematic representation of sequential single point probing operations on a work piece. Between measurement points the probe is retracted by x_{ret} .

A schematic of a single point probing operation is shown in figure 2.3. At time $t = t_0$ the CMM with probe approaches the work piece with a speed of v_0 m/s. When the probe tip collides with the surface of the work piece at $t = t_1$ the kinetic energy at the probe tip is absorbed by the deformation of the probe tip and work piece, which results in an impact force F_{imp} .

When the contact is registered by the probe a signal is supplied to the CMM controller, which reacts at time t_2 with deceleration of the CMM movement. At time t_3 the CMM movement has ended.

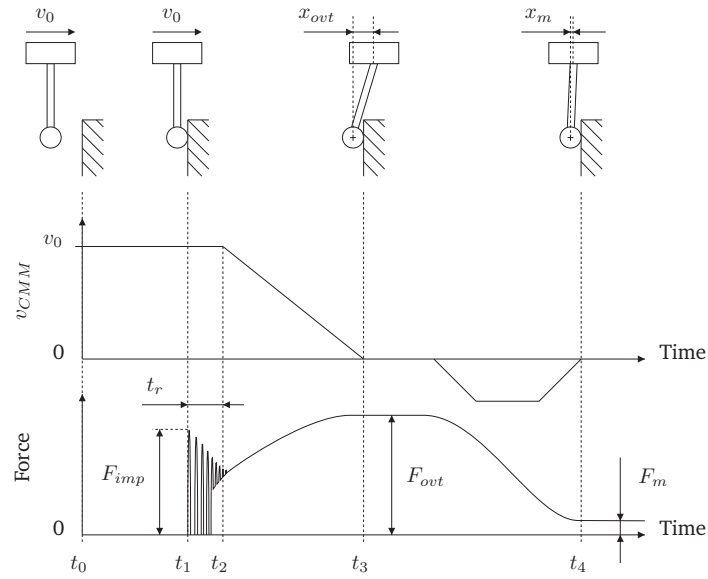


Figure 2.3: Schematic representation of the speed of the CMM and forces during single point probing.

The distance traveled between the point of initial contact of probe tip and work piece at t_1 and the point where the movement of the CMM ends at t_3 is hereafter referred to as the over travel distance x_{ovt} . The over travel distance x_{ovt} results in an over travel force F_{ovt} due to the stiffness of the loop between probe tip and work piece through the CMM.

When the probe is of the measuring type, as discussed in the previous section, a low force probing strategy can be used. Here, the CMM will gradually retract the probe using the probe signal as feedback until a preset distance x_m or a preset contact force F_m is obtained at t_4 . After the CMM comes to a standstill a measurement point is taken by adding the displacement of the probe tip, relative to its rest position, to the position of the scales. During the measurement or in post processing, the measurement results need to be corrected for the probe tip radius, indentation of the work piece and the probe tip, roundness deviations of the probe tip and other factors that influence the measurement, as will be discussed in the remainder of this chapter.

A disadvantage of the low force probing strategy is the time it takes to retract the probe. To speed up the measurement, a measurement can also be taken at t_3 after the CMM comes to a standstill. However, the measurement force F_m now equals the over travel force F_{ovt} , which increases the deformation and indentation of the work piece and probe at the measurement position, relative to the low force probing strategy.

An important advantage of a single point probing strategy is that the CMM comes to a complete standstill before taking a measurement. As a result, dynamic effects like bouncing of the probe tip on the work piece, as shown in figure 2.3 and discussed in section 2.1.3 are reduced and a more stable situation is reached before each measurement.

A second advantage is that multiple measurement values can be taken at each point. Averaging of the measurement results decreases the contribution to the measurement uncertainty of deviations that are non-systematic during the measurement, e.g. noise in the electronics. For these deviations, an estimate of the experimental standard deviation on the average value of the measurand s_m is given by [Walpole 06]:

$$s_m = \frac{s}{\sqrt{n}} \quad (2.1)$$

Here s is the experimental standard deviation of these effects and n is the number of measurement points.

For a measuring probe, operating at 1 kHz, 100 measurements can be taken in 10 ms, which re-

duced the contribution to the measurement uncertainty of these effects by a factor of 10.

Naturally, when using a touch-trigger probe only 2 measurement points can be taken per probing operation, as discussed in the previous section. Increasing the number of measurement points for a touch-trigger probe thus requires repeating the measurement procedure and is therefore time consuming.

A disadvantage of the sequential single point probing method is that the process of approaching the surface and withdrawing the probe is repeated for each point to be measured. When a large number of points needs to be measured this procedure is therefore time consuming. For these tasks a scanning measurement procedure can be used. Here, the tip of the probe is brought into contact with the work piece and is then guided on a line along the surface. The tip of the probe remains in contact with the surface and a set of coordinates is sampled in a time sequence [Destefani 01]. As a result many more points per unit time can be measured, which reduces the total measurement time considerably.

A disadvantage of scanning is the measurement uncertainty introduced by dynamic effects during scanning, as discussed in section 2.1.8, the triggering of the signal from the probe with the CMM measurement and the limited number of measurement values that can be used to measure the tip position at a certain point. Also, stick slip effects during scanning influence the measurement, as will be discussed in section 2.1.8.

Scanning measurements are not feasible with touch-trigger probes. However, a pseudo scanning mode can be performed by moving the probe along the surface with intermitted contact. The data capture rate is much smaller than with measuring probes [Weckenmann 04].

The term pseudo scanning is also used by several manufacturers with respect to measuring probes and consists of a series of single point probing operations, similar to figure 2.2. The points of contact are often not known in advance, but are calculated from previous measurements [Hidaka 06] as shown in figure 2.4. Since contact is intermitted, pseudo scanning is considered as a series of single point probing operations for the purpose of this thesis.

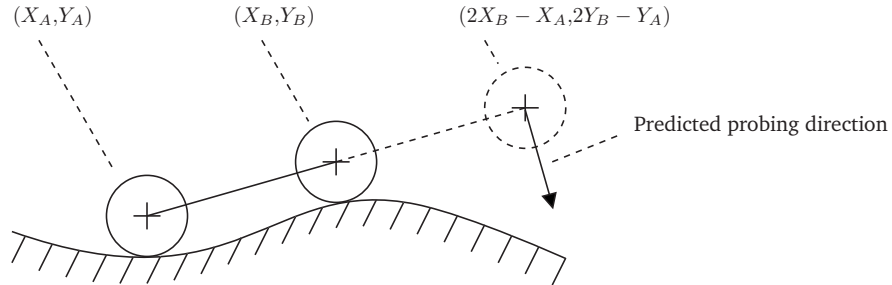


Figure 2.4: Simple control algorithm for pseudo scanning.

2.1.3 Impact force

During a collision between the tip of the probe and the work piece the kinetic energy at the probe tip is absorbed by the deformation of the probe tip and work piece:

$$\frac{1}{2}m_t\Delta v^2 = \int_0^\delta F_{Hz}(\delta)d\delta = \frac{8}{15}\sqrt{r_t}E_{red}\delta^{\frac{5}{2}} \quad (2.2)$$

Here, δ is the indentation of work piece and probe tip in m, Δv is the relative speed between the probe tip and work piece at the point of contact in m/s, r_t is the radius of the probe tip in m and m_t is the equivalent mass of the collision, which is here defined as the mass that is 'felt' when accelerating the probe tip. The Hertz contact force F_{Hz} and the reduced Young's modulus E_{red} are calculated using equations G.3 and G.5, respectively, as discussed in appendix G.

Material	E in GPa	ν	$\sigma_{0.2}$ in MPa	$\sqrt{(\frac{\sigma_{0.2}^5}{E_{red}^4})}$
Aluminum	70	0.33	280	0.3
Invar	145	0.3	483	0.4
Steel	200	0.3	885	1.17

Table 2.1: Ratio $\sqrt{(\frac{\sigma_{0.2}^5}{E_{red}^4})}$ for several materials.

It is noted that material properties depend on the scale of the contact. As the contact region size approaches the grain size of the work piece material the effective Young's modulus usually increases [Meli 07]. Also, mechanical properties at the surface of a bulk material may be influenced by surface segregation and oxide layers.

Using equation G.2, the impact force F_{imp} can be calculated:

$$F_{imp} = \sqrt[5]{\frac{125}{36} m_t^3 \Delta v^6 E_{red}^2 r_t} \quad (2.3)$$

Using equation G.7, the maximum admissible relative speed Δv , based on the onset of plastic deformation, between the probe tip and work piece can be calculated:

$$\Delta v = \sqrt{\frac{(1.61\pi)^5}{30} \frac{r_t^3 \sigma_{0.2}^5}{E_{red}^4 m_t}} \quad (2.4)$$

Where $\sigma_{0.2}$ is the yield strength of the work piece material.

The ratio $\sqrt{(\frac{\sigma_{0.2}^5}{E_{red}^4})}$ depends on the work piece material and is a measure for the kinetic energy a material can absorb until plastic deformation begins. This ratio for aluminum, Invar and steel in contact with sapphire is shown in table 2.1.

In order to prevent plastic deformation when probing an aluminum work piece with a 1 mm/s approach speed and a sapphire probe tip, the equivalent mass at the probe tip should be below 161 mg for a 250 μm tip radius and below 35 mg for a 150 μm tip radius. This can also be seen from figure 2.5 where the admissible equivalent mass is shown as a function of the radius of the probe tip. The equivalent mass of the 3D tactile probe, discussed in chapter 3, is approximately 9 mg in x - and y - direction and 34 mg in z -direction. The impact force F_{imp} in this situation corresponds to approximately 1.1 mN in x - and y -direction and 2.7 mN in z -direction. It is noted that most commercial styli with a 150 μm or 250 μm tip radius have a mass of 300 mg or more. Thus it may be expected that plastic deformation occurs when probing an aluminum work piece with a 1 mm/s approach speed with these styli.

A second effect during the collision of the probe tip with the work piece is bouncing of the probe tip. During the initial collision between the work piece and probe the relative speed is v_0 , as shown in figure 2.3. The kinetic energy of the probe tip, as a result of the relative speed of the probe and work piece Δv , is absorbed by the deformation of the probe tip and work piece, as shown in equation 2.2.

Energy is dissipated in the contact between probe tip and work piece, e.g. due to friction or plastic deformation as described by equation G.14. To describe this effects a factor e is introduced, where e^2 is the part of the energy stored in the deformation of probe tip and work piece which is converted back into kinetic energy:

$$\frac{1}{2} m_t \Delta v_2^2 = e^2 \int_{\delta}^0 F_{Hz}(\delta) d\delta \quad (2.5)$$

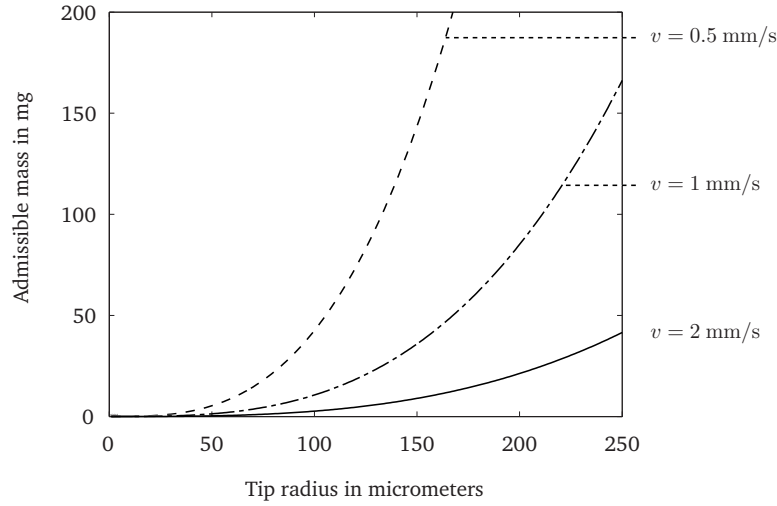


Figure 2.5: Admissible mass at the probe tip in order to prevent plastic deformation due to impact forces of a planar aluminum work piece. The admissible mass is shown as a function of the radius of the probe tip and for different approach speeds.

Where Δv_2 is the relative velocity between the probe tip and the work piece after the collision. Assuming a probe that is initially at rest, $v_1 = 0$, and a CMM that moves a work piece with a constant speed v_0 , the velocity v_2 of the probe tip after the collision is given by:

$$v_2 = (1 + e) v_0 \quad (2.6)$$

The velocity x'_t and position x_t of the probe tip during vibration in its eigen frequency after the collision are¹ [Dekkers 02]:

$$\begin{aligned} x'_t &= (1 + e) v_0 \cos(\omega_0 t) \\ x_t &= \frac{(1 + e) v_0}{\omega_0} \sin(\omega_0 t) \approx \frac{(1 + e) v_0}{\omega_0} \left(\omega_0 t - \frac{\omega_0^3 t^3}{6} \right) \end{aligned} \quad (2.7)$$

Here t is the time in seconds and ω_0 is the eigen frequency, often referred to as natural frequency, of the probe in the direction of velocity v_0 .

The response time t_r of a high accuracy CMM, as shown in figure 2.3, is typically 2 ms [Ruijl 01, Seggelen 07, Vermeulen 99]. When the eigen frequency f_e of the probe is between 100 and 140 Hz or higher, depending on the energy loss during the collision and damping of the probe, the CMM has not started decelerating at the time of the second collision between the probe tip and the work piece. The speed of the CMM during the second collision will therefore be v_0 and the position of the work piece x_t equals $v_0 t$. Using equation 2.7, the bouncing time t_b between the first and second collision can be calculated:

$$t_b = \frac{\sqrt{6}}{\omega_0} \sqrt{\frac{e}{1 + e}} \quad (2.8)$$

Which for a fully elastic collision, $e^2 = 1$, results in $t_b = \frac{\sqrt{3}}{\omega_0}$.

The relative velocity during the second collision is given by:

¹The Taylor series for a sine function is an entire function. The maximum deviation in the approximation used is $(\omega_0^5 t^5) / 120$.

$$\Delta v = v_0 \left(1 - (1 + e) \cos \left(\sqrt{\frac{6e}{1+e}} \right) \right) \quad (2.9)$$

Which for a fully elastic collision results in $\Delta v = v_0 - 2v_0 \cos(\sqrt{3}) \approx 1.32v_0$.

To prevent an increase of the relative speed during the second collision, the kinetic energy of the probe must be dissipated. From equation 2.9, it can be seen that Δv during the second collision equals v_0 when $e < 0.68$. In other words, when 54% of the kinetic energy of the probe tip is absorbed by friction and plastic deformation of the work piece, the relative speed during the second collision will be the same as the relative speed during the first collision. This is shown in figure 2.6 where the position of the work piece and probe tip of the probe are shown as a function of the dimensionless time.

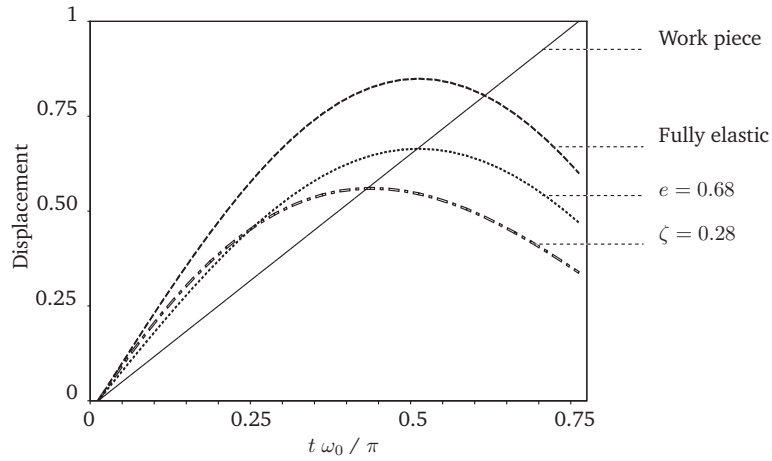


Figure 2.6: Position of the work piece, solid line, and probe tip, dotted lines, after the initial collision.

A second important dissipation process is damping of the movement of the probe tip. It can be shown that for a damping factor ζ of 0.28 or higher, the relative speed during consecutive bounces does not increase.

The eigen frequency f_e of the 3D tactile probe, discussed in section 3, is approximately 1100 Hz in x - and y -direction and 550 Hz in z -direction. The z direction corresponds to the length direction of the stylus, as shown in figure 2.2. The bouncing of the tip of this probe on an aluminum work piece in x -direction is simulated using simulink, as shown in figure 2.7 and figure 2.8. The bouncing effect is emphasized by assuming a low damped probe, with $\zeta = 0.01$, and no energy loss due to friction and plastic deformation in the contact between the probe tip and work piece, i.e. $e^2 = 1$.

It can be seen in this model that the relative speed during consecutive collisions increases from 1 mm/s during the first collision to 2.2 mm/s after 2 ms. The maximum contact force after 2 ms, 3.2 mN, is almost a factor of 3 higher than the contact force during the first collision, 1.1 mN. It is noted that, due to movement of the CMM, the force after 2 ms is a combination of the impact force and over travel force, as discussed in the next two sections.

2.1.4 Over travel force

The second force to consider while probing a work piece is the over travel force F_{ovt} , as discussed in section 2.1.2. The force F_{ovt} depends on the over travel x_{ovt} of the CMM and the stiffness c between the probe tip and work piece, i.e. the stiffness of the loop through the probe, CMM and work piece:

$$F_{ovt} = x_{ovt}c \quad (2.10)$$

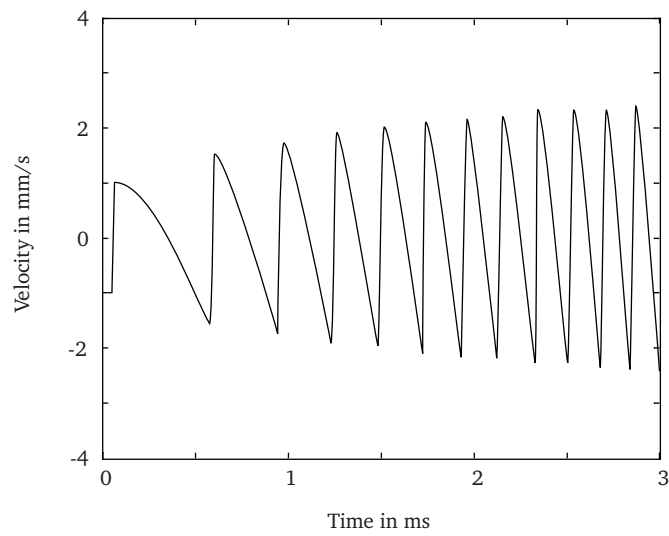


Figure 2.7: Simulated relative speed between probe tip and work piece during single point probing.

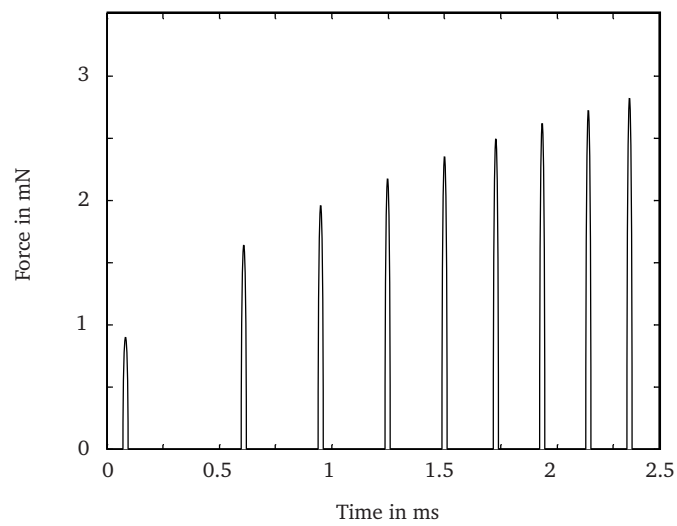


Figure 2.8: Simulated force between probe tip and work piece during single point probing.

Typically the stiffness of the CMM is an order of magnitude higher than the stiffness of the probe suspension. Since the stiffness of the work piece is unknown and varies from measurement to measurement, for the purpose of calculating the over travel force F_{ovt} we will assume that c equals the stiffness of the probe at its tip c_t in the measurement direction.

The over travel mainly depends on the dynamics of the CMM and the probing speed. It is assumed that after a reaction time t_r the CMM will start to decelerate with a constant negative acceleration a_{CMM} . The admissible speed v_{ovt} based on the onset of plastic deformation, equation G.7, due to over travel forces is given by:

$$v_{ovt} = -t_r a_{CMM} + \sqrt{t_r^2 a_{CMM}^2 + \frac{(1.61\pi)^3}{3} \frac{r_t^2 \sigma_{0.2}^3}{c_t E_{red}^2} a_{CMM}} \quad (2.11)$$

The response time t_r of a high accuracy CMM and its deceleration a_{CMM} are typically 2 ms and 0.1 m/s² [Ruijl 01, Seggelen 07, Vermeulen 99]. For an approach speed of 1 mm/s this results in an over travel distance x_{ovt} of 7 μ m. For a planar aluminum work piece, probed by a sapphire probe tip with a speed of 1 mm/s, the stiffness c_t should be less than 985 N/m for a 250 μ m tip radius and 354 N/m for a 150 μ m tip radius to prevent plastic deformation. This can also be seen from figure 2.9, where the admissible stiffness c_t at the probe tip is shown as a function of the radius r_t of the probe tip.

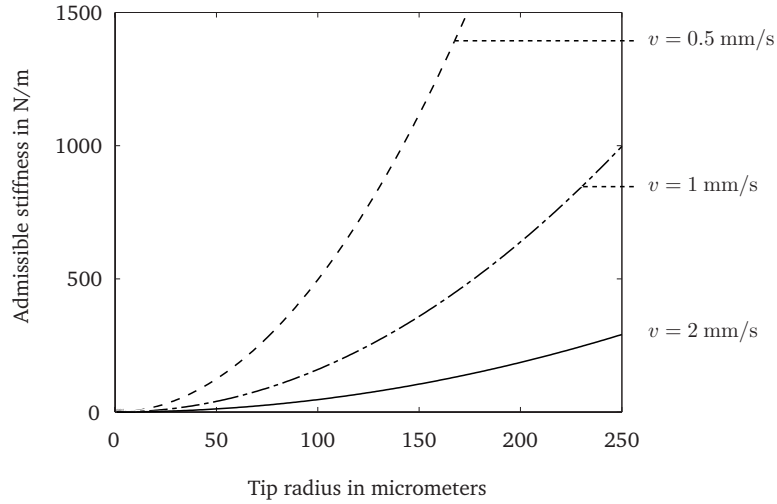


Figure 2.9: Admissible stiffness at the probe tip in order to prevent plastic deformation due to over travel forces of a planar aluminum work piece. The admissible stiffness is shown as a function of the radius of the probe tip for different approach speeds.

The stiffness at the probe tip of the 3D tactile probe, discussed in section 3, is optimized for the radius of the probe tip, as discussed in appendix D. For a 250 μ m radius of the probe tip a rod thickness of 30 μ m is used, which results in a stiffness of 480 N/m. For a probe with a tip radius of 25 μ m the rod thickness is reduced to 10 μ m, which results in a stiffness at the probe tip of 20 N/m.

2.1.5 Overlap between collision and over travel forces

When the probe collides with the work piece for a second time within the reaction time t_r of the CMM and the relative speed between the probe tip and work piece increases in consecutive bounces, as discussed in section 2.1.3, it is likely that the maximum contact force is a combination of the impact force F_{imp} and the over travel force F_{ovt} . The over travel force after 2 ms, the reaction time t_r of the CMM, for this probe is given by $v_0 t_r c_t$, which corresponds to approximately 1 mN.

This effect is illustrated using the simulink model from section 2.1.3. Bouncing of the probe tip on the surface is emphasized using a low damping coefficient of the probe suspension, $\zeta = 0.08$, and no energy loss due to friction and plastic deformation in the contact between the probe tip and work piece, i.e. $e^2 = 1$. The solid black line in figure 2.10 is the over travel force. The solid gray line is the force between the probe tip and the work piece, which is the sum of the impact force and the over travel force.

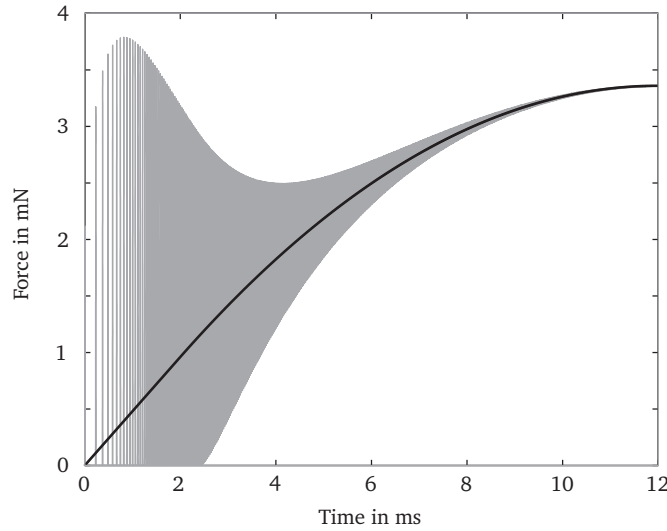


Figure 2.10: Force between probe tip and work piece when probing in x direction with a 1 mm/s approach speed. The equivalent mass m_t in this direction is 8 mg and the stiffness c_t and damping coefficient ζ are 480 N/m and 0.08, respectively.

It would be of interest to analyze the maximum force that occurs during the collision. Figure 2.11 shows the ratio χ_c between the contact force during the first collision between probe tip and work piece and the maximum contact force. The ratio χ_c is calculated as a function of ζ for an equivalent mass of the probe of 8, 29 and 100 mg, respectively. Similar to the results from section 2.1.3, the maximum contact force is approximately 3 times as high as the initial contact force for a low damped probe.

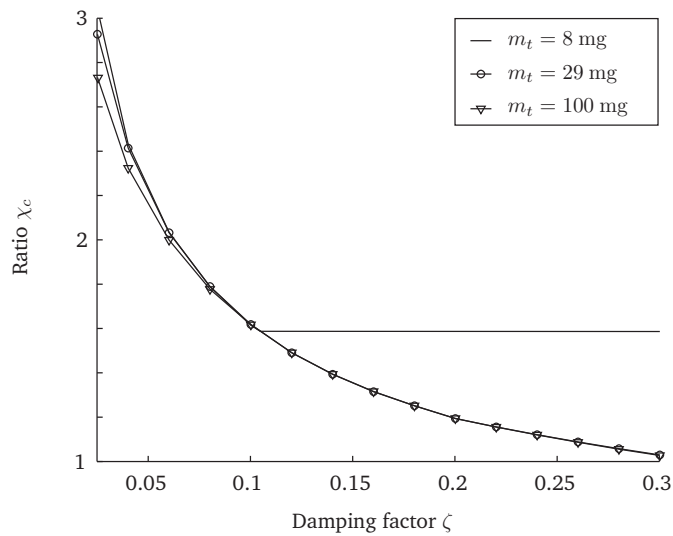


Figure 2.11: Ratio χ_c between the contact force during the first collision and the maximum contact force.

From this figure it can be seen that the ratio χ_c between the initial contact force and the maximum

contact force is only influenced by ζ , and not by the eigen frequency f_e of the probe. However, this only holds when the maximum contact force is reached during the reaction time t_r of the CMM. In the model a reaction time of 2 ms is used, after which the CMM starts to decelerate. The speed of the CMM during a collision with the probe tip after t_r will therefore be reduced, reducing the collision force. This effects can be observed in figure 2.11 for $\zeta = 0.025$ and $\zeta = 0.05$. Here, the maximum contact force is reached after t_r for $m_t = 29$ mg and $m_t = 100$ mg, decreasing the ratio χ_c .

Finally, it can be seen in this picture that the ratio χ_c between the initial contact force and the maximum contact force becomes a constant for the probe with $m_t = 8$ mg when $\zeta > 0.11$. For this value, the maximum contact force arises from the maximum over travel force F_{ovt} of the CMM.

The second point of interest is the settling time t_s of the probe, defined as the time needed for the vibration amplitude to decrease to a set percentage of its initial value. For a simple 1 degree of freedom mass-damper system, the settling time t_s is proportional to [Tongue 96]:

$$t_s \propto \frac{1}{\zeta \omega_n} \propto \frac{t_b}{\zeta} \quad (2.12)$$

Here, ω_n is the natural frequency of the probe and t_b is the bouncing time of the probe, equation 2.8.

For the purpose of this work, it is of interest to analyze the time needed for the vibrational amplitude to decrease to less than 5 nm. For optimum throughput, the time needed should be less than 12 ms, the time required by the CMM to end its motion after the first collision, as discussed in section 2.1.4. The influence of the damping coefficient ζ on the required time is shown in figure 2.12 for several values of the equivalent mass at the probe tip.

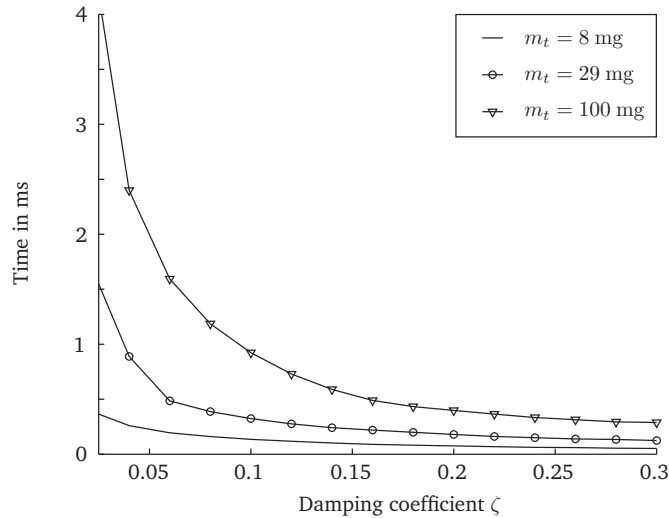


Figure 2.12: Time needed for the vibrational amplitude of the probe to decrease to less than 5 nm after the initial collision between probe tip and work piece during single point probing.

From the previous sections it may be concluded that in order to prevent plastic deformation when probing a flat aluminum work piece with a 1 mm/s approach speed and using a sapphire tip with a radius of 150 μm , the equivalent mass at the probe tip should be 35 mg or less. Also, the stiffness at the probe tip should be below 354 N/m to prevent plastic deformation due to the over travel of the CMM. It is noted that the maximum force due to bouncing of the probe tip on the work piece surface during probing is influenced by the damping factor of the probe. For low damped probes the maximum impact force during single point probing may be a factor of 2 - 3 higher then the contact force during the initial collision.

2.1.6 Contact of rough spheres

In previous sections, the contact surface of the probe tip and work piece were assumed to be perfectly smooth. Using this assumption, the admissible force between a smooth sapphire sphere with a tip radius $r_t = 250 \mu\text{m}$ and a smooth planar aluminum work piece is 7 mN, as calculated in section 2.1.4.

However, as discussed in appendix B, plastic deformation can never be avoided completely in the contact between rough surfaces. In this section the contact between rough spherical parts, e.g. the probe tip and work piece, will be discussed. When analyzing the spherical contact of rough surfaces two problems at different scales need to be taken into account:

- The bulk or macro-scale compression of the objects;
- The deformation of asperities on the surface of the objects.

When calculating the contact force and indentation of a rough spherical contact on a micro scale, the influence of the fluid layer between the structures should be taken into account. Two additional assumptions are made:

1. The pressure in the adsorbed water layer between the surfaces is homogeneous;
2. The influence on the deformation of asperities due to lubrication of the contact as a result of the adsorbed water layer can be neglected.

The first assumption states that water molecules can move between the asperities to create an homogeneous pressure. Therefore there is no local pressure buildup in the fluid layer, e.g. as a result of trapped water molecules.

Using the above assumptions the main influence of the water layer, adsorbed on the surface, when calculating the indentation due to a static force is an increase in the contact force due to surface tension, as discussed in section 2.1.7. This can be taken into account when calculating the indentation depth between rough spherical parts, as discussed in section 2.1.7.

Several authors presented models to describe the spherical contact between rough surfaces. Most notable are the publications by Greenwood & Tripp [Greenwood 67], Mikic [Mikic 74A], Mikic & Roca [Mikic 74B] and Bahrami et al. [Bahrami 04, Bahrami 05]. Kagami et al. [Kagami 83] developed a numerical model to describe the spherical contact of rough surfaces. By comparison with experimental data, they found that the effect of the deformation mode of the asperities, i.e., elastic, plastic, or elasto-plastic on the results of their analysis was small in the practical range.

Asperities in spherical contact act as a compliant layer on the surface of the objects. Compared to perfectly smooth surfaces the contact area is therefore extended, resulting in a reduced contact pressure for a given load. This is shown in figure 2.13 for a force F of 50 N, a reduced Young's modulus E_{red} of 112.1 GPa, a hardness H of 4 GPa and a sphere radius r_t of 25 mm.

Here, the pressure p is shown as a function of radial position r . To obtain non dimensional variables, the pressure p and radial position r are divided by the maximum Hertz contact pressure $p_{0,H}$ and Hertz contact radius a_H , respectively. It can be seen that as the surface roughness σ_z increases, the maximum pressure p_0 in the contact decreases and is distributed over a larger area.

Since the effect of surface roughness is modeled using a Gaussian distribution, the pressure distribution asymptotically approaches zero. The contact radius a_l is therefore defined as the radius r where the normalized pressure is 0.01 or less:

$$\frac{p(r = a_l)}{p_0} < 0.01 \quad (2.13)$$

Where p_0 is the maximum contact pressure, $p_0 = p(r = 0)$.

For the spherical contact between rough surfaces, the general pressure distribution p is [Bahrami 04]:

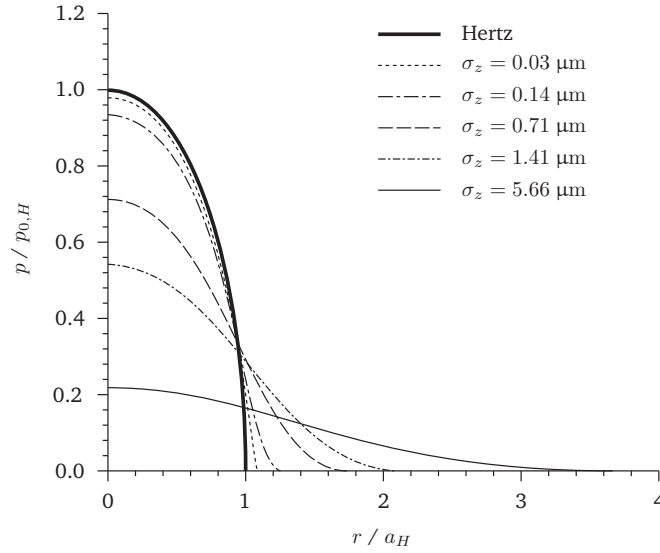


Figure 2.13: Effect of surface roughness on the pressure distribution between a sphere and a plane [Bahrami 05, Greenwood 67, Kagami 83].

$$p\left(\frac{r}{a_l}\right) = p_0 \left(1 - \left(\frac{r}{a_l}\right)^2\right)^\gamma \quad (2.14)$$

Where r is the radial position and:

$$\gamma = 1.5 \frac{p_0}{p_{0,H}} \left(\frac{a_l}{a_H}\right)^2 - 1 \quad (2.15)$$

Here, a_H and $p_{0,H}$ are the Hertz contact radius, equation G.1, and the maximum Hertz pressure in the contact, equation G.4, respectively.

Bahrami [Bahrami 04] used a numerical model to predict the pressure distribution. He compared the results from his numerical model to experimental results and literature [Bahrami 05] and found good agreement. Using a curve-fitting approach he obtained the following relationships for the non-dimensional maximum contact pressure p_0^* and the non-dimensional contact radius a^* :

$$p_0^* = \frac{p_0}{p_{0,H}} = \frac{1}{1 + 1.37 \frac{\alpha}{\tau^{0.075}}} \quad (2.16)$$

$$a^* = \frac{a_l}{a_H} = \begin{cases} \frac{1.605}{\sqrt{p_0^*}} & 0.01 \leq p_0^* \leq 0.47 \\ 3.51 - 2.51 p_0^* & 0.47 \leq p_0^* \leq 1 \end{cases} \quad (2.17)$$

Equations 2.16 and 2.17 depend on the non-dimensional roughness parameters α , published by Greenwood et al. [Greenwood 84], and τ [Bahrami 05]:

$$\alpha = \frac{\sigma r_t}{a_H^2} = \sigma \left(\frac{16 r_t E_{red}^2}{9 F_c^2} \right)^{\frac{1}{3}} \quad (2.18)$$

$$\tau = \frac{r_t}{a_H} = \left(\frac{4 E_{red} r_t^2}{3 F_c} \right)^{\frac{1}{3}} \quad (2.19)$$

Where F_c is the contact force, a_H the Hertz contact radius, σ is the root-mean-square roughness and r_t is the radius of the probe tip.

When the pressure distribution is known, the method presented in appendix B can be used to calculate the number and mode of deformed asperities at a given position. By integration over the contact surface the deformation of all asperities in contact and the elastic deformation of the half-space can be calculated, as shown in e.g. [Bahrami 05, Greenwood 67, Mikic 74B].

Another factor of interest is the mutual approach of distant points in the probe tip and work piece, hereafter referred to as compliance. The compliance δ between rough spherical bodies as a function of the radial position r is given by [Kagami 83]:

$$\delta = \delta_a(r) + \delta_b(r) + \frac{r^2}{2r_t} \quad (2.20)$$

Where $\delta_a(r)$ and $\delta_b(r)$ are the deformation of asperities and the bulk deformation at radial position r , respectively. In the vicinity of the contact the profile of the probe tip, with radius r_t , can be approximated by a paraboloid, $u(r) = u_0 - r^2/2r_t$, the third part of equation 2.20.

Assuming that the deformation of asperities at the edge of the contact is zero [Bahrami 04], equation 2.20 can be written as:

$$\delta = \delta_b(a_l) + \frac{a_l^2}{2r_t} \quad (2.21)$$

Using a numerical approach, Bahrami et al. [Bahrami 05] obtained an analytical solution for the bulk deformation at the edge of the contact:

$$\delta_b(a_l) = \frac{4p_0 a_l}{\pi E_{red} \left(4.79 - 3.17 (p_0^*)^{3.13} \right)} \quad (2.22)$$

The non-dimensional compliance δ^* is obtained by combining equations 2.17, 2.21 and 2.22:

$$\delta^* = \frac{\delta}{\delta_H} = 0.5 (a^*)^2 + \frac{8p_0^* a^*}{\pi^2 \left(4.79 - 3.17 (p_0^*)^{3.13} \right)} \quad (2.23)$$

Where $\delta_H = a_H^2/r_t$ is the compliance between a perfectly smooth sphere, with radius r_t , and a perfectly flat work piece using Hertz theory.

Bahrami et al. [Bahrami 05] estimated the maximum deviation of this method to be 5% in the range of $0.01 \leq p_0^* \leq 1$.

Figure 2.14 shows the non dimensional compliance δ^* between a planar aluminum work piece and a sapphire spherical probe tip, with a radius of 10, 100 and 1000 micrometers, respectively, for a contact force F_c of 1 mN as a function of surface roughness.

Figure 2.15 shows the calculated compliance δ as a function of surface roughness for a contact force of 1 mN. The compliance between a perfectly smooth work piece and a perfectly smooth sphere δ_H is calculated using Hertz theory. This constant value is shown in figure 2.15 as a reference.

It can be concluded that compared to the Hertz theory for perfectly smooth surfaces, the compliance between probe tip and work piece can easily be an order of magnitude higher when the effects of surface roughness are taken into account.

2.1.7 Surface forces

The relative importance of adhesion forces, often referred to as surface forces, with respect to gravity increases as the dimensions of a component decrease [Elwenspoek 01]. This is especially

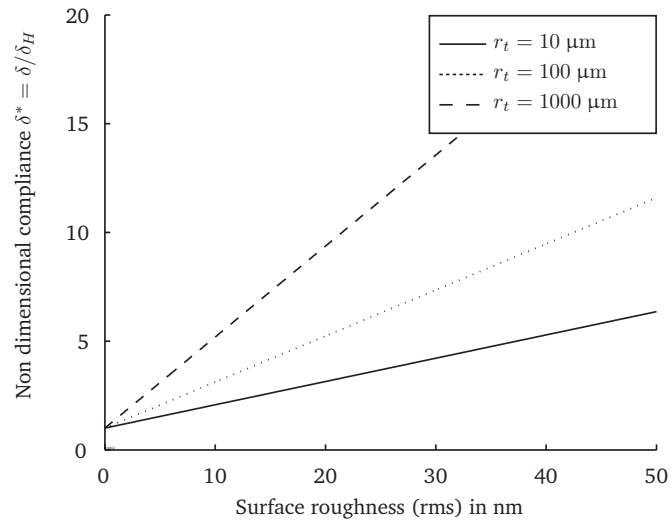


Figure 2.14: Non dimensional compliance δ^* as a function of surface roughness between a plane and a sphere with a radius of 10, 100 and 1000 micrometers, respectively.

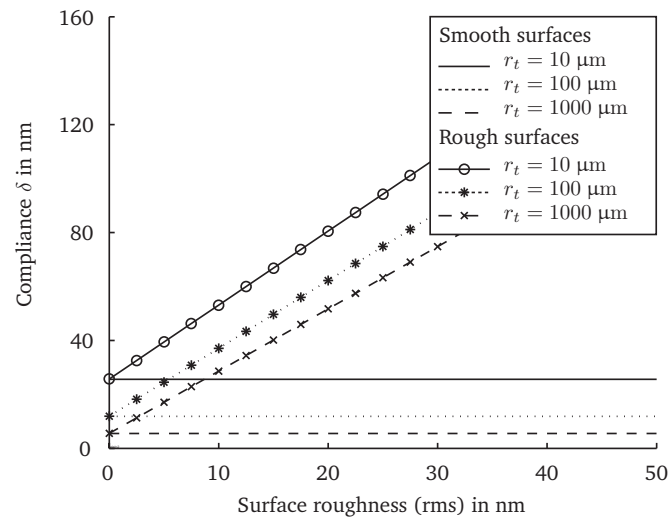


Figure 2.15: Effect of surface roughness on the compliance between a sphere and planar work piece for a sphere with a radius of 10, 100 and 1000 micrometers, respectively.

Material	Hamaker constant H_{12} for contact with sapphire
Gold	26.1
Silver	24.9
Aluminum	23.6
Germanium	21.6
Copper	21.0
Diamond	21.0
Silicon	19.9
Carbon	18.3
Iron	18.1
Sapphire	15.5
Water	8.2

Table 2.2: Hamaker constants for the contact between sapphire and several materials. All values are given in 10^{-20} J.

important when performing measurements on small components and when handling them, e.g. during micro assembly [Arai 95, Bowling 88, Brussel 00, Fearing 95, Feddema 01, Maboudian 97, Tas 96]. In this section the simplified mathematics of these surface forces are discussed and verified using the experimental setup discussed in section 1.6.1. Since these forces are, in most cases, not controlled in terms of magnitude and direction they are often disturbing. Therefore the section will conclude with measures to reduce these forces during a measurement.

The adhesive forces arise primarily from van der Waals forces, electrostatic attraction and surface tension. The balance between these forces depends on the environmental conditions, such as humidity, temperature, surrounding medium, surface condition, material and relative motion. The van der Waals forces, electrostatic attraction and surface tension are also discussed in appendix C.

Overview of surface forces

First, calculation of the van der Waals force, which is discussed in appendix C.1, is briefly described in this section. Hamaker [Hamaker 37] determined the van der Waals force F_{vdw} between a sphere and an infinite half space:

$$F_{vdw} = \frac{2Hr_1^3}{3d_{ww}^2(d_{ww} + 2r_1)^2} \quad (2.24)$$

Where d_{ww} is the distance between the wall and the edge of the sphere, r_1 is the sphere radius and H is the Hamaker constant. The Hamaker constant for the contact between a work piece and a sapphire sphere is given in table 2.2.

As an example, the van der Waals force between an aluminum half space and a sapphire sphere with a radius of $250 \mu\text{m}$ is now calculated. From table 2.2 a Hamaker constant of $23.6 \cdot 10^{-20}$ J is obtained. Using equation 2.24 and assuming a distance between the edge of the sphere and wall d_{ww} of 0.4 nm [Arai 95] a van der Waals attraction force F_{vdw} of $61.5 \mu\text{N}$ is obtained.

An important influence factor for the van der Waals forces is the surface roughness of both parts. A rough estimate for this effect is given by equation C.6 in appendix C.1. Assuming a peak-to-peak surface roughness R_t of 5 nm , a van der Waals force F_{vdw} of $1.17 \mu\text{N}$, or 2% of $61.5 \mu\text{N}$, is obtained.

Finally, it is noted that the contact force between the objects will likely result in a local plastic deformation of the roughness peaks. This permanent deformation increases the effective contact area. The adhesion force between the surfaces thus increases for an increasing contact force [Jones 03].

The second surface force under consideration is the Casimir force [Casimir 48A, Casimir 48B]. The Casimir force is the attraction of two uncharged material bodies due to modification of

the zero-point energy associated with the electromagnetic modes in the space between them [Lamoreaux 05].

The Casimir force F_C between two parallel plates of area A is given by [Bressi 02, Lamoreaux 97, Lamoreaux 05]

$$F_C = \frac{\pi^2 \hbar c}{240 d^4} A \quad (2.25)$$

Where \hbar is the reduced Planck constant, i.e. $\hbar = h/(2\pi) = 1.0546 \cdot 10^{-34}$ Js, c is the speed of light in vacuum, i.e. $c = 299792458$ m/s $\approx 300 \cdot 10^6$ m/s, and d is the distance between the plates.

The Casimir force between a sphere with radius r and a flat surface is given by [Buks 01, Chan 01, Lamoreaux 97, Mohideen 98]:

$$F_C = \frac{r \pi^3 \hbar c}{360 d^3} \quad (2.26)$$

For a sphere with a radius r of 250 μm and a distance d of 1 nm the Casimir force is calculated to be 0.7 mN. When the separation d is 0.2 μm or higher the Casimir force $F_C \leq 85$ pN and is generally considered to be neglectable.

The third surface force under consideration is electrostatic attraction, as discussed in appendix C.2. The electrostatic force F_{e2} between two spheres with homogeneous surface charge σ can be calculated using [Arai 95]:

$$F_{e2} = \frac{4\pi\sigma_1\sigma_2r_1^2r_2^2}{\epsilon_0 d_{cc}^2} \quad (2.27)$$

Where r_1 and r_2 are the radii of sphere 1 and 2, respectively, d_{cc} is the distance between the sphere centers and ϵ_0 is the permittivity in vacuum, i.e. $\epsilon_0 = 8.85 \cdot 10^{-12}$ C²/(Nm²).

A rough estimate is given for the force between an aluminum sphere with a radius r_1 of 250 μm and a silicon wall. Using a charge density on the sphere σ_1 of $1.5 \cdot 10^{-7}$ C/m², as discussed in appendix C.2, and letting r_2 go to infinity, equation 2.27 results in a force due to the contact potential difference between the sphere and wall of 8.3 pN.

However, significant amounts of charge may be generated by friction forces and differences in contact potential [Fearing 95]. The charge acquired by an insulator from a contact with a metal or other insulator depends on the nature of the insulator material and on the type and duration of the contact [Cottrell 78, Davies 67, Medley 53]. At atmospheric pressure and a gap in the order of centimeters the maximum charge density is limited to about $3 \cdot 10^{-5}$ C/m², due to the breakdown strength of air, which is about $3 \cdot 10^6$ V/m [Brussel 00, Koyano 96, Lowell 80]. Using the same approach as before with this value, a force due to the charge as a result of friction between a silicon sphere and an aluminum wall of 80 μN is obtained.

Finally, a brief overview of hydrostatic attraction is given, as discussed in more detail in appendices C.3 and C.4. Hydrostatic adhesion is often the dominant force in micro structures [Brussel 00, Tsuchitani 94] and is increased by a high humidity, large radii of curvature, long contact times and hydrophilic surfaces.

The hydrostatic force F_s is given by:

$$F_s = \pi r_2^2 \gamma \left(\frac{1}{r_1} + \frac{1}{r_2} \right) + 2\pi r_2 \gamma \quad (2.28)$$

Where the radii of the meniscus r_1 and r_2 , the radius of the sphere r_t , the separation distance d , the surface tension of the liquid γ and the contact angles θ_1 and θ_2 , depicted in figure C.4, are connected via simple equations, as discussed in appendix C.3.

	Contact angle in degrees
Teflon	95°
Polyethylene	88°
Polyimide	60°
Aluminum Nitride	45°
Sapphire	35°
Glass	0°

Table 2.3: Contact angle of water on several materials [Liang 96].

Table 2.3 gives typical values of the contact angle of water on several materials. It is noted that the contact angle is very sensitive to contaminants and to physical modifications of the surface [de Gennes 85, Mittal 06].

For the contact between a spherical probe tip with radius r_t and a plane, equation 2.28 is often simplified to [Bowling 88, Fearing 95, Tori 94]:

$$F_s \approx 4\pi r_t \gamma \quad (2.29)$$

The Kelvin radius r_k is a measure of the size of the meniscus that forms between two surfaces and is a function of radii of the meniscus r_1 and r_2 :

$$\frac{1}{r_k} = \left(\frac{1}{r_1} + \frac{1}{r_2} \right) = \frac{RT}{\gamma V} \ln \frac{p_0}{p_w} \quad (2.30)$$

Where T is the absolute temperature, V the molar volume, R the universal gas constant, $R \approx 8314.5 \text{ J/kmol} \cdot \text{K}$, p_0 the partial pressure of water vapor in the air and p_w the vapor pressure of water.

The Kelvin radius r_k is used as a measure for the minimum distance that should be kept between the surfaces to prevent the formation of a stable layer of water between the objects [Brussel 00].

As discussed in appendix C.4 the adsorption of water on the surface of an object will naturally depend upon the partial pressure of water vapor, the temperature of the system and the affinity of the objects for water molecules. The thickness of the water layer is typically between a tenth and several tens of nanometers [Grigg 92, Heim 96, Hooton 04, Hu 95A, Hu 95B, Patel 97]. Also, especially for hydrophobic surfaces, water droplets may appear on the surface [Freund 99].

Most literature references, including [Christenson 88, Cleaver 04, Fisher 81, Harnby 96, Sugawara 93, Zimon 82], conclude that the hydrostatic adhesion increases monotonically with an increasing relative humidity RH . Another factor of influence is the surface roughness of the contact area. The effects of the surface roughness and relative humidity has been discussed by several authors, including [Harnby 96, McFarlane 50, Rabinovich 02]. The hydrostatic attraction is generally shown to decrease when the surface roughness increases.

As an example, the hydrostatic attraction between a sapphire sphere with a radius of $250 \mu\text{m}$ and an aluminum plane is calculated. For the calculation we assume a relative humidity RH of 60%, an absolute temperature T of 293.15 K and a molar volume of water V of $18 \cdot 10^{-6} \text{ m}^3/\text{mol}$. Using equation 2.30 with $R = 8.3145 \text{ J/mol} \cdot \text{K}$ and $\gamma = 0.073 \text{ N/m}$ a Kelvin radius r_k of 1 nm is obtained. Since $r_t \gg r_k$, equation 2.29 is used, which gives a total hydrostatic attraction F_s of 0.23 mN.

Comparison of surface forces to gravitational forces

Especially for micro assembly operations, the relative magnitude of the separate surface forces with respect to gravity is of interest. When surface forces prevail over gravity, the component may

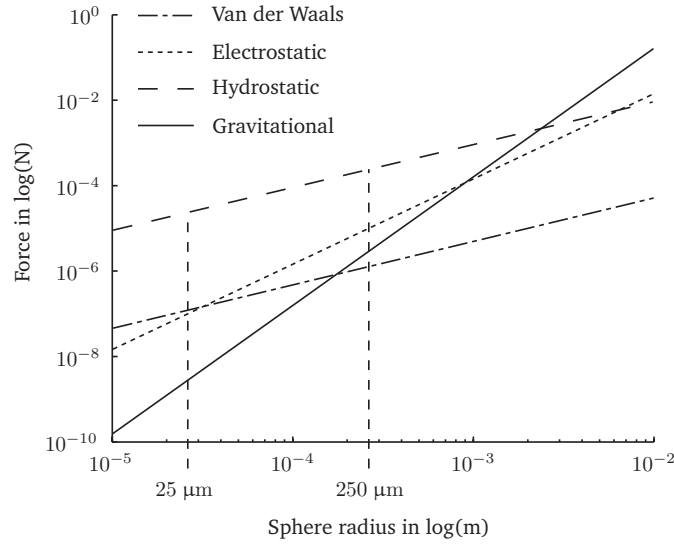


Figure 2.16: Comparison of the magnitude of the separate surface forces between a sapphire sphere and a planar half space as a function of the sphere radius.

be more difficult to handle. Figure 2.16 shows the van der Waals, Electrostatic and Hydrostatic attraction force between a sphere and a planar half space, as a function of the radius of the sphere.

For the calculation of the electrostatic force, a charge density σ of $1 \cdot 10^{-5} \text{ C/m}^2$ is used. The calculation of the other forces follows the same approach as used in the previous sections. It can be seen that for this example, gravity prevails over the sum of the surface forces when the sphere radius is larger than 2.8 mm.

For a tip radius of 250 μm , the sum of the surface forces in figure 2.16 is 0.24 mN, which is an order of magnitude below the impact and over travel forces of the probe discussed in this thesis, as calculated in section 2.1.3 and 2.1.4. However, for other probes the magnitude of the surface force can be substantially higher than the impact and over travel forces, as discussed in section 2.3.5. The effects on the measurement is discussed later in this chapter.

Effect of the surface forces on static and dynamic friction

The static friction between a sphere and a plane is influenced by the force component F_N orthogonal to the plane and the coefficient of friction between the sphere and plane. The forces during the probing of micro components need to be small to minimize plastic deformation of the probe tip and work piece, as discussed in sections 2.1.3 and 2.1.4. As a result, the magnitude of surface forces is often in the same order as the forces during probing. Since surface forces typically increase the force component F_N they may have a significant influence on the static friction force. This was investigated by Tian *et al.* [Tian 92, Tian 93] for the static friction force between the head and disk interface of a magnetic recorder. The coefficient χ_{sf} , which is a measure for the relative magnitude of the static friction forces, is shown in figure 2.17 as a function of the relative humidity for different thicknesses of the lubricant film.

It can be seen in this figure that the static friction force increases for an increasing relative humidity and thickness of the lubricant film. This is caused by the increase in hydrostatic attraction when the thickness of the water and lubricant layer increases, as discussed in the previous section. A point of interest is the graph for the contact without lubrication (thickness 0.0 nm). The static friction force at 2% RH is slightly higher than the force at 50% RH. Most likely this is caused by electrostatic adhesion [Wan 92], as will be discussed later in this section.

A similar increase of the static friction force with an increasing relative humidity for the head - disk interface in a magnetic recorder was also observed by Li *et al.* [Li 90]. They also observed an

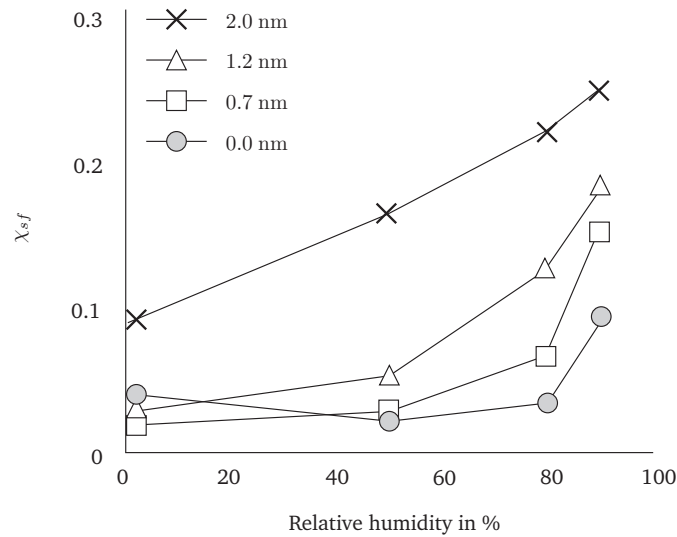


Figure 2.17: χ_{sf} versus relative humidity for different lubricant thicknesses [Tian 92].

increase in the friction force for an increasing dwell time, especially at high levels of the relative humidity, as shown in figure 2.18. This is caused by film mobility and the fact that the presence of the probe tip on the surface will promote the localized condensation of water [Dey 00]. Finally, the electrostatic adhesion at a low relative humidity was observed to decrease for an increasing dwell time.

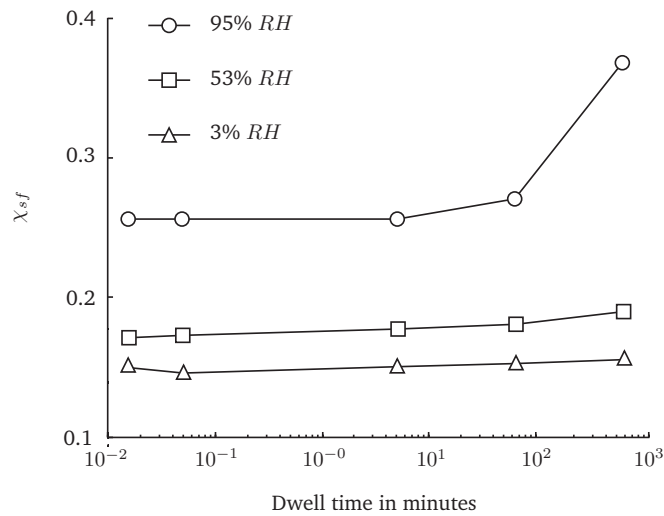


Figure 2.18: χ_{sf} as a function of dwell time for different relative humidities [Li 90].

The decrease in electrostatic adhesion with relative humidity and dwell time results from the adsorbed water layer on the surface. When the relative humidity increases, the thickness of the adsorbed water layer increases, which results in a decrease of the surface resistivity [Dorda 60, Sharma 03]. This in turn decreases the half life of the charge decay, as shown in figure 2.19 [Shashoua 58, Shashoua 63].

For the dynamic friction case the adsorbed water layer on a hydrophilic surface acts as a lubricant, reducing the coefficient of friction at a relative humidity > 70% [Binggeli 94, Cleaver 04]. No reduction in friction coefficient was observed for the hydrophobic carbon surface. The authors explain this by the relative absence of water molecules on the surface. Figure 2.20 shows the dynamic friction force as a function of the applied load for several values of the relative humidity.

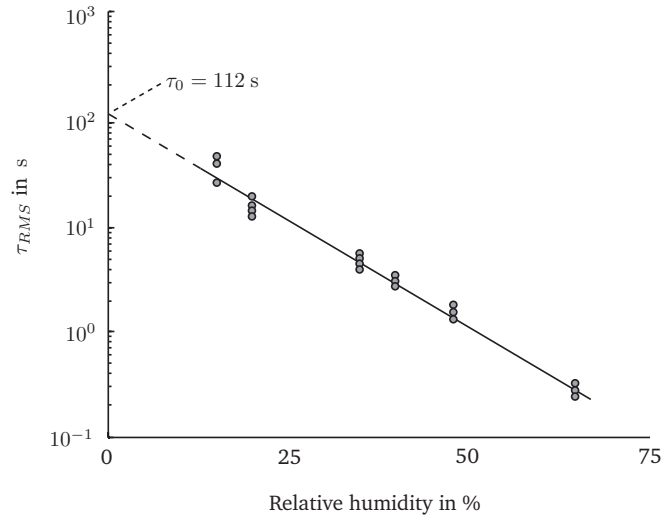


Figure 2.19: Dependence of the root mean square half life of charge decay on the relative humidity for a cellulose film [Shashoua 58].

The linear relation between the measurements indicate that the friction coefficient is constant at a given value of relative humidity. It can also be seen that the friction coefficient decreases for increasing relative humidity.

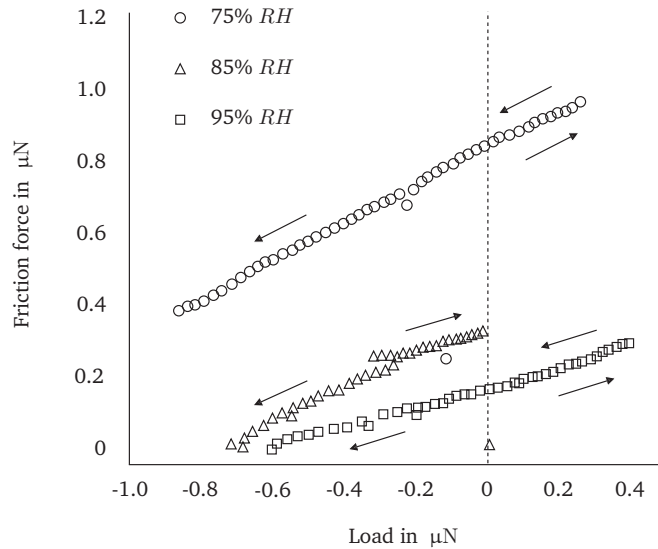


Figure 2.20: Friction force between an AFM tip and a silicon oxide surface on an Si(100) wafer as a function of the applied load for several values of the relative humidity. The arrows indicate whether the load is increasing or decreasing [Binggeli 94].

Another factor of influence with respect to dynamic friction is charge generated by friction forces, as discussed in section C.2. This sliding friction electrification is investigated by Kumar *et al.* [Kumar 92] for the contact between an aluminum cylinder and a low-density polyethylene (LDPE) plane, and an aluminum cylinder on a polypropylene (PP) plane. The surface potential was shown to increase linearly with the sliding velocity in the range of 0.33 to 0.75 m/s. Higher velocities increase the number of contacts, which increases the transfer of charge [Fabish 79, Elsdon 76, Yu 89].

The surface charge also showed a square-root dependence on the contact force up to 6.5 N. This is caused by plastic deformation of the asperities, which increases the contact area [Elsdon 76, Wahlin 74]. Finally, Kumar *et al.* investigated the relation between the surface charge and charging time, as shown in figure 2.21. It can be seen that between 20 and 120 s of charging, the surface potential increases linearly with charging time, similar to the results by [Elsdon 76, Fabish 79, Giacometti 99, Yu 89].

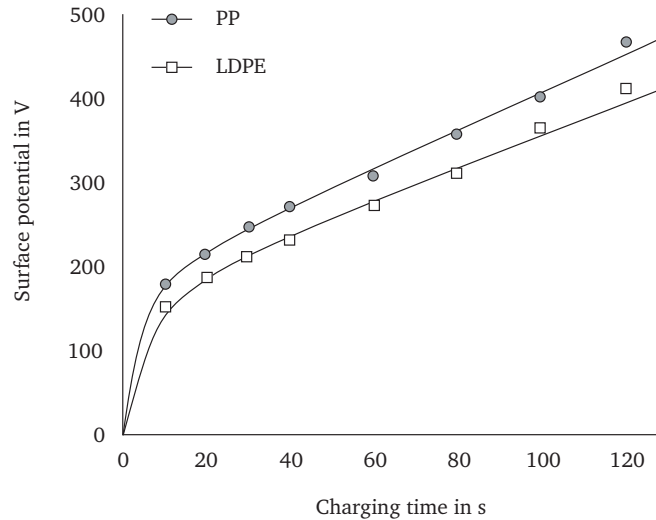


Figure 2.21: Surface potential as a function of the charging time at a sliding velocity of 0.44 m/s and a contact force F_N of 5.5 N between an aluminum cylinder and a polymer plane [Kumar 92].

In summary, it can be stated that the relative humidity should be above 10% to decrease the build up of electrostatic charge and below 60% to decrease hydrostatic adhesion. As a guideline for precision tactile probing the relative humidity should therefore be around 30 - 40% RH. In section 2.1.7 other measures to decrease surface forces are discussed. Some of these, like using ionized air, are designed to minimize the build up of electrostatic charge, which could justify a lower relative humidity. However, it should be clear, also from section C.3, that the optimum value of the relative humidity will always depend on the combination of probe and work piece.

A complete review of friction is beyond the scope of this thesis and the reader is referred to [Bengisu 97, Martins 90, Oden 85, Rabinowicz 04, Tabor 81].

Experimental results

The effect of surface forces during a single point probing operation, as discussed in section 2.1.2 and figure 2.2, is measured using the setup discussed in section 1.6.1. When the object approaches the probe tip a 'snap in' effect of approximately 15 nm can be observed, as shown in figure 2.22. A similar 'snap in' effect also occurs in AFM measurements [Heinz 99]. The effect is caused by forces between the tip of the probe and the object prior to contact.

After contact, the movement of the object continues until the probe tip is deflected by 1.5 μm . Similar to a single point probing operation, the object is then retracted. Due to surface forces the object will stick to the work piece, as shown in figure 2.22. After a certain displacement, the forces due to the deformation of the probe suspension will prevail over the sum of the surface forces between the probe tip and object and a 'snap out' effect can be observed, as also discussed in section 2.3.5.

The magnitude of the 'snap out' effect is investigated using an aluminum, sapphire and steel measurement object, as shown in figure 2.23. The measurements are performed using the probe developed by Pril, as discussed in appendix A, and hence the stiffness is direction dependent. The maximum deflection and the corresponding force are shown in table 2.4.

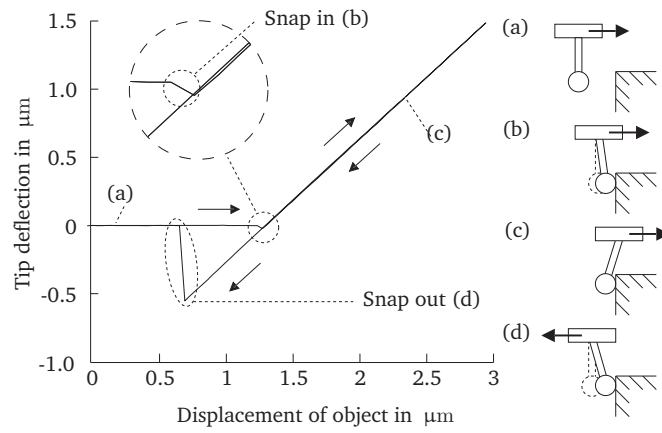


Figure 2.22: Measurement of the effects of surface forces during a single point probing operation.



Figure 2.23: Measurement objects used in the surface force measurements. From left to right: Aluminum, sapphire and steel.

	Direction b		Direction c		Direction d	
	Δx_s	F_s	Δx_s	F_s	Δx_s	F_s
Aluminum	0.35	67	0.15	26	0.45	78
Sapphire	0.6	114	0.7	121	0.9	156
Steel	0.2	38	0.08	14	0.15	26

Table 2.4: Maximum deflection Δx_s in μm and associated force F_s in μN due to surface forces between a sapphire probe tip and different work piece materials [Widdershoven 04]. The measurement directions **b**, **c** and **d** are schematically shown in figure A.1.

Some handling is required to replace the samples in the test setup. This has to be done manually and hence the conditions of the measurement vary. This accounts for the differences in the 'snap out' force of the measurements. However, the measured forces are in the same order of magnitude as the calculated values from the previous sections.

Reduction of surface forces

As discussed at the start of section 2.1.7, the influence of surface forces is especially important when performing measurements on small components and during micro assembly. Therefore, in this section we will briefly discuss several measures to reduce the magnitude of surface forces during these operations. Measures to reduce surface forces are derived from the above discussion on surface forces and from literature [Abe 95, Arai 95, Brussel 00, Fearing 95, Mastrangelo 00]:

- The relative humidity influences both the electrostatic adhesion, via the surface charge, and the hydrostatic adhesion. A relative humidity above 10% reduces the build up of electrostatic charge and improves the decay of surface charge. To reduce the hydrostatic adhesion, a relative humidity below 60% should be used. For micro assembly, electrostatic and surface tension effects can be eliminated by performing the handling and assembly operations while immersed in a fluid [Yeh 94].
- The use of hydrophobic coatings reduces hydrostatic adhesion. When the contact angle, indicated in figure C.4 by θ_1 and θ_2 , between the objects and liquid is made larger than 90 degrees, capillary forces push the objects apart.
- Free charges such as in ionized air can combine with and neutralize exposed surface charges.
- Use conductive materials which do not easily form highly insulating native oxides. By grounding the conductors the electrostatic charge can be drained off.
- Use materials with a small contact potential difference to minimize the contact electrification.
- High contact pressures, caused by the adhesion forces, can cause local deformations at the contact site [Bowling 88]. This deformation will increase the contact area and hence the net adhesive force. Therefore, hard materials are preferable.
- Keep the contact area small. Therefore, a contact between spherical objects is preferred over the contact between planar objects. For assembly operations, the contact area can also be reduced by increasing the surface roughness. This will considerably reduce the van der Waals forces.

It is important to note that in most applications the attraction forces are dominated by hydrostatic attraction, as discussed in section 2.1.7 and appendix C. The items in the above list are arranged to first reduce hydrostatic attraction, then electrostatic attraction and finally van der Waals forces. However, it should be clear that this arrangement is somewhat system specific.

2.1.8 Scanning measurement

During scanning the tip of the probe is in continuous contact with the work piece. Due to this contact the play of forces differs from a single point probing operation. This results in a stick-slip effect during scanning and a deformation of the structural loop. Also the tip may loose contact with the work piece if the direction of contact changes, e.g. when scanning a peak at high scanning speed. Finally, as the probe is not at rest at the time of the measurement, the measurement result is influenced by dynamics, predominantly those of probe, work piece and CMM.

First, the play of forces during scanning is discussed, as shown in figure 2.24. The main contributions to the force F_N between the probe tip and work piece normal to the contact area are the CMM scanning forces and surface forces. Calculation of the scanning force is comparable to the

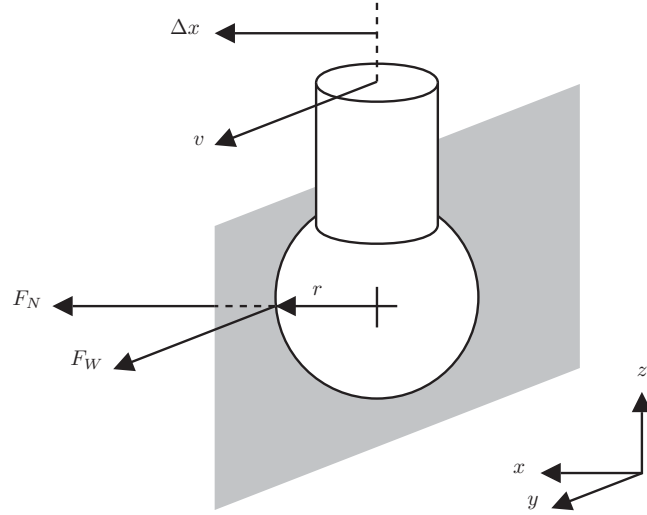


Figure 2.24: Schematic of the forces during a scanning measurement.

calculation of the over travel force, discussed in section 2.1.4. It results from the displacement Δx of the probe tip relative to its housing during scanning in y direction, as shown in figure 2.24.

The relative displacement Δx of the probe tip during the scanning measurement is controlled by the coordinate measuring machine. Assuming a relative displacement between 1 and 2 μm and a stiffness c_t at the probe tip of 480 N/m, see appendix D, results in a scanning force of 0.5 and 1 mN, respectively. From section 2.1.7 a surface force F_S of 0.24 mN is assumed for a probe with a tip radius r of 250 μm . The force F_N between probe tip and work piece is therefore assumed to be $0.74 \leq F_N \leq 1.24$ mN.

The friction force F_W between the probe tip and work piece is a function of the contact force F_N and the coefficient of friction μ between the tip and work piece, $F_W = F_N \mu$. Assuming a coefficient of friction μ of 0.15, a maximum friction force F_W of 0.19 mN is obtained.

The force in y -direction, F_y , results from the movement Δy of the probe tip in y direction relative to its zero position and the stiffness c_t at the probe tip in y direction, $F_y = c_t \Delta y$. When $F_y < F_W$ friction dominates and the probe tip sticks to the work piece. Slip of the probe tip over the work piece occurs when $F_y > F_W$. The maximum displacement in y direction Δy_{max} before the probe tip slips is then given by:

$$\Delta y_{max} = \mu \left(\Delta x + \frac{F_S}{c_t} \right) \quad (2.31)$$

It can easily be seen from equation 2.31 that the influence of surface forces during scanning is increased for a decreasing stiffness at the probe tip. Using $\Delta x = 1$ μm , $\mu = 0.1$ and F_S of 0.24 mN a maximum displacement Δy_{max} of 0.15 μm is obtained when $c_t = 480$ N/m, 0.58 μm when $c_t = 50$ N/m and 24.1 μm when $c_t = 1$ N/m.

It should be clear that the stick-slip effect can be large during tactile scanning of micro products with a low stiffness probe. By looking at equation 2.31, there are several options to improve the scanning behavior of tactile probes. First, the coefficient of friction μ can be reduced, e.g. by using a vibrating probe tip [Hidaka 06]. A second option is to optimize the suspension stiffness c_t for a given tip radius. And finally, surface forces can be reduced, as discussed in section 2.1.7.

The friction force F_W also results in a moment M_z around the z -axis, where $M_z = F_W r$. For a tip radius r of 250 μm this results in a moment M_z of 47.5 nNm, which causes a deformation of the structural loop between probe tip and work piece.

The suspension of the probe, discussed in this thesis, consists of three slender rods. A deformation of these strain gauges is detected by a change in resistance of four piezo resistive strain gauges,

deposited on each rod, in a Wheatstone bridge configuration. Ideally, an elongation or shortening of the slender rods in the probe suspension therefore results in an equivalent change in the resistance of the piezo resistive strain gauges and does not contribute to the measurement uncertainty of the probe. Therefore, the main contribution to the measurement uncertainty due to the moment on the probe tip results from torsion of the slender rods, forces on the rods when the probe tip is not in its zero position, manufacturing tolerances and assembly tolerances. These are second order effects, which can be neglected.

However, there is also a rotation of the probe tip as a result of the moment M_z . The rotational stiffness of the probe, discussed in section 3, around the z axis is 0.03 Nm/rad in its zero position. A moment of 47.5 nNm thus results in a rotation of $1.63 \text{ } \mu\text{rad}$, which corresponds to a displacement at the point of contact of 0.4 nm for a tip radius r of $250 \text{ } \mu\text{m}$.

The second effect, discussed in this section, is the loss of contact during a scanning measurement. As mentioned earlier in this section, the force F_N between probe tip and work piece is assumed to be between 0.74 and 1.24 mN .

The maximum acceleration of the probe tip a_{max} as a result of this force is given by:

$$a_{max} = \frac{F_N}{m_{eq}} = \frac{c_t \Delta x + F_s}{m_{eq}} \quad (2.32)$$

Where m_{eq} is the equivalent mass at the probe tip and F_s is the sum of surface forces.

Scanning of a peak on the surface is modeled using the simple model shown in figure 2.25. Using a constant scanning speed v_{scan} and assuming that both the probe tip and work piece are rigid, the height $h(t)$ of the probe tip at time t is given by:

$$h(t) = \sqrt{r_{tot}^2 - x_0^2 + 2x_0 v_{scan} t - v_{scan}^2 t^2} - r_{tot} + h_p \quad (2.33)$$

Here, r_{tot} is the distance between the center of the probe tip and the peak, $r_{tot} = r_t + r_p$ and x_0 is the horizontal distance at initial contact:

$$x_0 = \sqrt{r_{tot}^2 - (r_{tot} - h_p)^2} \quad (2.34)$$

Double differentiation of equation 2.33 results in the acceleration $a(t)$ during the scanning of a peak:

$$a(t) = \frac{-(2x_0 v_{scan} - 2v_{scan}^2 t)^2}{4(r_{tot}^2 - x_0^2 + 2x_0 v_{scan} t - v_{scan}^2 t^2)^{\frac{3}{2}}} - \frac{v_{scan}^2}{\sqrt{r_{tot}^2 - x_0^2 + 2x_0 v_{scan} t - v_{scan}^2 t^2}} \quad (2.35)$$

The maximum acceleration a_{max} of the probe tip when scanning of a peak occurs during the initial contact, $t = 0$. Using equations 2.34 and 2.35 now yields:

$$a_{max} = \frac{v_{scan}^2 r_{tot}^2}{(r_{tot} - h_p)^3} \quad (2.36)$$

Combining equations 2.32 and 2.36 yields the maximum speed while scanning a peak without loss of contact between probe tip and work piece:

$$v_{max} = \frac{(r_{tot} - h_p)^{\frac{3}{2}} \sqrt{c_t \Delta x + F_s}}{r_{tot} \sqrt{m_{eq}}} = 2\pi f_e \frac{(r_t + r_p - h_p)^{\frac{3}{2}}}{r_t + r_p} \sqrt{\Delta x + \frac{F_s}{c_t}} \quad (2.37)$$

It can easily be seen from equation 2.37 that the maximum admissible scanning speed v_{max} without loss of contact decreases as the radius of the probe tip decreases. Assume that $F_s = 0$, $\Delta x = 1 \text{ } \mu\text{m}$ and the peak height h_p and top radius r_p are $2 \text{ } \mu\text{m}$ and $1 \text{ } \mu\text{m}$, respectively. When this peak is

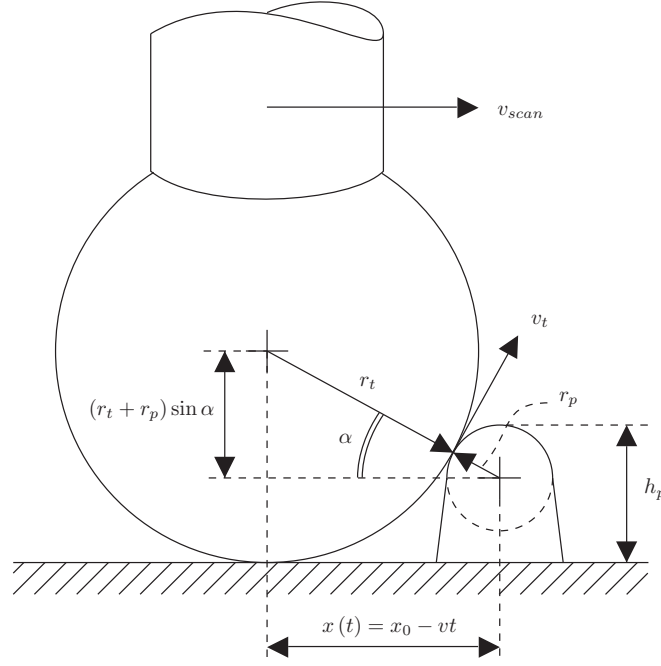


Figure 2.25: Schematic model for the contact between probe tip and a peak during scanning.

scanned by a probe with a stiffness c_t of 480 N/m, an equivalent mass m_{eq} of 8 mg and a tip radius r_t of 10 μm , the maximum scanning speed v_{max} using equation 2.37 is 35 mm/s. Note that for a probe with an equivalent mass of 10 g and a stiffness c_t of 50 N/m the admissible scanning speed is 0.3 mm/s for the same profile.

It is noted that the scanning speed v_{scan} is influenced by stick-slip in the contact. Therefore the scanning speed will be higher than the nominal scanning speed of the CMM in the slip-region of the contact.

Finally, the centrifugal force F_c during scanning is discussed and is given by:

$$F_c = \frac{m_{eq} v_{scan}^2}{r_p} \quad (2.38)$$

Where r_p is the radius of the circular path followed by the probe tip. Using the same values as before the maximum speed when scanning a circular path with $r_p = 0.1$ mm without loss of contact is $v_{scan} = 77$ mm/s for the probing system as discussed in this thesis, i.e. $m_{eq} = 8$ mg and $c_t = 480$ N/m. For a probe with an equivalent mass of 10 g and a stiffness c_t of 50 N/m the admissible scanning speed is 0.7 mm/s for the same radius.

2.1.9 Dynamic excitations

Vibrations may result in a deformation in the metrology loop between probe tip and work piece. The deformations due to vibrations in the metrology loop are hard to compensate for, and therefore contribute to the uncertainty of the measurement if they are not recorded by the probing system and CMM². An example with respect to the probe, as discussed in this thesis, are deformations of the stylus due to vibrations, as these are not recorded by the probing system. The deformations in this part of the metrology loop should therefore be minimized as they contribute to the measurement uncertainty.

²When a vibration in the metrology loop is measured by both the probing system and CMM it can be compensated for. However, this is influenced by the synchronization between probing system and CMM, as discussed in the next section.

Criterion	Vibration velocity in $\mu\text{m}/\text{sec}$ (rms)
Workshop (ISO)	800
Office (ISO)	400
Residence, computer systems (ISO)	200
BBN criterion A Bench microscope up to 400x magnification, coordinate measuring machine, probe testing equipment, precision balance	50
BBN criterion B Bench microscope at >400x magnification, micro surgery, eye surgery, optical equipment on isolation table	25
BBN criterion C Electron microscope up to 30000x magnification, microtomes, magnetic resonance imager	12.5
BBN criterion D Electron microscope at >30000x magnification, mass spectrometer, cell implant equipment	6
BBN criterion E Not isolated laser and optical research systems	3

Table 2.5: Vibration criteria [Amick 91, Ungar 90].

When the probe is suspended on a CMM these vibrations also result in a vibration of the probe tip, and hence positional noise. This positional noise is recorded by the probe and therefore does not influence the measurement uncertainty directly. However, the positional noise does influence the trigger level and thereby the over travel distance and force, as discussed in section 2.1.4.

The main sources of dynamic excitation of the probe in a typical measurement are:

- floor vibrations
- acoustic excitation
- vibrations due to the measurement instrument, e.g. the coordinate measuring machine

In this section first the influence of floor vibrations is discussed. Several criteria can be used to describe floor vibrations [Amick 91, Bessason 99, Gordon 99]. In this section the BBN criterion is used [Dekkers 02, Ungar 90, Visscher]. The BBN criterion is based on 1/3-octave band analysis and specifies vibration levels for several equipment classes, as shown in table 2.5. As a worst case scenario BBN criterion A is used in the analysis, as shown in figure 2.26. The root-mean-square (rms) floor vibration velocity v_{rms} is given by the square root of the integral of the power spectral density (PSD) of the frequency band from $\omega_{i,1}$ to $\omega_{i,2}$ [Howard 02]:

$$v_{rms,i} = \sqrt{\int_{\omega_{i,1}}^{\omega_{i,2}} \text{PSD}(\omega) d\omega} \quad (2.39)$$

The amplitude of the floor vibration z_{rms} is calculated by integration of the velocity v_{rms} .

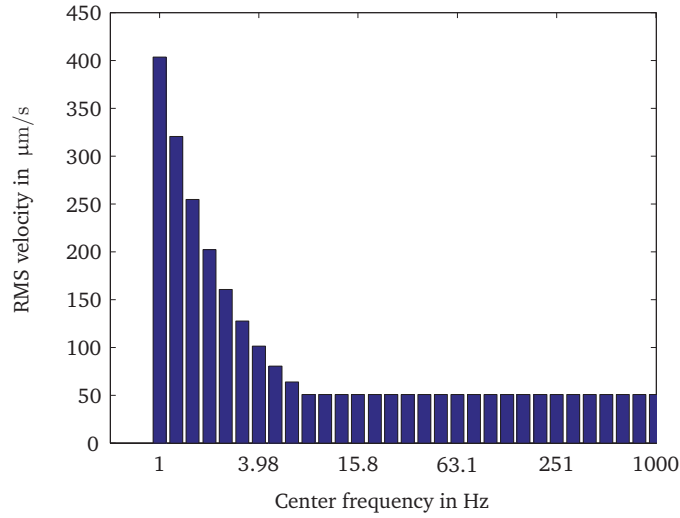


Figure 2.26: The rms velocity of the floor vibrations according to BBN criterion A.

For the analysis only translational vibrations, in x , y and z -direction, are taken into account. First, the positional noise of the probe due to the propagation of floor vibrations in z -direction is calculated using the model shown in figure 2.27. It is noted that these vibrations are measured by the probe and therefore do not contribute to its measurement uncertainty.

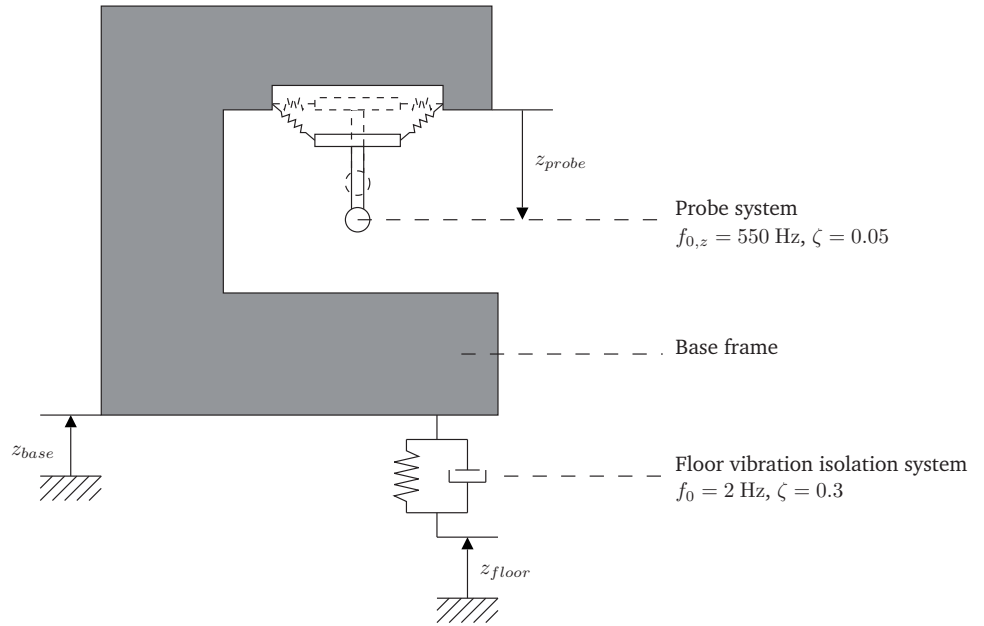


Figure 2.27: Simple dynamic system, used to model the propagation of floor vibrations to positional noise of the probe.

The base frame in most high accuracy coordinate measuring machines (CMMs) is supported by a vibration isolation system. The vibration isolation system functions as a filter, which is approximated with a Laplace transfer function of a single mass spring damper system [Dekkers 02]:

$$\frac{Z_{base}}{Z_{floor}} = \frac{2\zeta_{base}\omega_{0,base}s + \omega_{0,base}^2}{s^2 + 2\zeta_{base}\omega_{0,base}s + \omega_{0,base}^2} \quad (2.40)$$

Where $s = j\omega$ with ω the frequency, $\omega_{0,base}$ is the eigen frequency of the vibration isolation system

of base frame and ζ_{base} is the damping factor. The eigen frequency $\omega_{0,base}$ and damping factor ζ_{base} are assumed to be 2 Hz and 0.3 [Dekkers 02], respectively.

It is assumed that both the base frame and the connection between probe and base frame are rigid. Vibrations of the base frame are therefore directly applied to the probe. The transfer function of a free hanging probe is modeled using a mass-spring-damper system [Dekkers 02]:

$$\frac{Z_{probe}}{Z_{base}} = \frac{s^2}{s^2 + 2\zeta_{probe}\omega_{0,probe}s + \omega_{0,probe}^2} \quad (2.41)$$

The eigen frequency $\omega_{0,probe}$ and damping factor ζ_{probe} of the probe discussed in this thesis are 550 Hz and 0.05, respectively.

The positional noise $z_{rms,noise}$ of the probe due to floor vibrations is now given by:

$$z_{rms,noise} = \sqrt{\sum_{i=1}^N \left| z_{rms}(\omega_i) \frac{Z_{base}}{Z_{floor}} \frac{Z_{probe}}{Z_{base}} \right|^2} \quad (2.42)$$

Where $z_{rms}(\omega_i)$ are the rms floor displacements for the N center frequencies ω_i . Equation 2.42 results in a total rms positional noise of the probe of 1.2 nm, following BBN criterion A. The rms positional noise following BBN Criterion A is shown in figure 2.28.

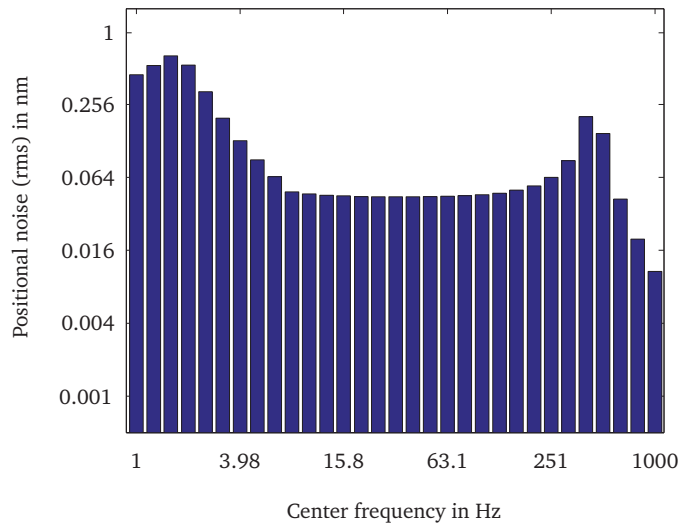


Figure 2.28: The rms positional noise due to floor vibrations following BBN criterion A.

The positional noise, as calculated in this section, is caused by a vibration of the center platform of the probe relative to its housing. As stated at the start of this section, this noise is measured by the piezo resistive strain gauges on the three slender rods and does not contribute to the measurement uncertainty. However, the positional noise does influence the trigger level and thereby the over travel distance and force, as discussed in section 2.1.4.

Deformations of other parts in the metrology loop, e.g. the stylus and center platform itself, due to floor vibrations can not be detected and compensated for with this probe. Their contribution to the measurement uncertainty due to the positional noise in z -direction is calculated to be 0.1 nm. Using a similar approach, the position noise in the x - and y -direction is calculated to be 0.3 nm, resulting in a calculated measurement deviation of 25 pm.

Of more interest is the measurement deviation when the probe tip is in contact with the work piece. A vibration of the work piece will result in a deformation of the stylus and center platform through the contact between probe tip and work piece. It is assumed that the influence of the work piece and the connection between base frame and work piece can be neglected.

	Sound pressure (rms) in μPa	Sound pressure level (SPL) in dB
Launching of the space shuttle	2000000000	160
Full symphony orchestra	2000000	100
Diesel freights train		
at high speed at 25 m	200000	80
Normal conversation	20000	60
Soft whispering at 2 m	2000	40
Unoccupied broadcast studio	200	20
Softest sound human can hear	20	0

Table 2.6: Sound pressure for several events [Blackstock 00].

The probe tip is connected to three silicon legs via a stylus, as discussed in section 3. The first eigen frequency of this sub-assembly is calculated using finite element simulation (FEM) to be 5 kHz in z -direction and 9 kHz in x - and y -direction, when the probe tip is in contact with the work piece. Using a damping factor ζ_{probe} of 0.01, the contribution of floor vibrations to the measurement uncertainty are calculated to be less than 0.1 nm in both the xy - and z -direction.

It is noted that for probes that have a low eigen frequency when in contact, e.g. 50 Hz or less, floor vibrations can result in a measurement deviation of 60 nm, or higher, depending on the dynamics of the probe system, the CMM and the isolation system used.

Acoustic excitations may also influence the positional noise and measurement uncertainty of the probe. Table 2.6 provides an overview of the sound pressure and sound pressure level (SPL) in several situations [Blackstock 00].

The sound pressure level (SPL) relates to the sound pressure according to [Norton 03]:

$$\text{SPL in dB} = 20 \log_{10} \frac{p}{p_0} \quad (2.43)$$

Where p is the sound pressure at the current SPL and p_0 is the reference sound pressure, i.e. the hearing threshold of 20 μPa .

The surface area of the probe, as discussed in this thesis, is approximately $5 \cdot 10^{-5} \text{ m}^2$ in z direction and $3 \cdot 10^{-6} \text{ m}^2$ in xy -direction. Also, the eigen frequency of the probe is higher in xy -direction, and therefore only the influence of acoustic excitations in z -direction will be discussed in this thesis. The amplitude of the force f_i due to acoustic excitation on the center platform in z -direction for a given frequency band i is given by $f_i = p_i A$.

For the analysis, the sound pressure level is assumed to have a power density spectrum which is equal in all bands of the frequency spectrum, i.e. pink noise. Further, it is assumed that the total sound pressure level does not exceed 60 dB, i.e. normal conversation. Following an approach similar to floor vibrations, as discussed at the start of this section, the positional noise due to acoustic excitation is calculated for the z -direction of the probe, as shown in figure 2.29.

The peak at 550 Hz in figure 2.29 corresponds to a vibration of the probing system in its first eigen frequency. The total positional noise of the probe over all frequency bands is 2 nm and the contribution to the measurement uncertainty of acoustic excitations is 0.1 nm. It should be clear from this calculation that acoustic excitation may have a significant influence depending on the environment and the probing system used.

Finally, the influence of vibrations due to the measurement instrument will be discussed briefly. Dynamic excitation due to machine vibrations may have a significant influence on the measurement behavior of the probe. Contributions include the control system of the machine and internal sources of vibrations, e.g. due to roller bearings. Once the sources of excitation are known, the calculation in this section can be used to obtain its influence on the measurement. In general it

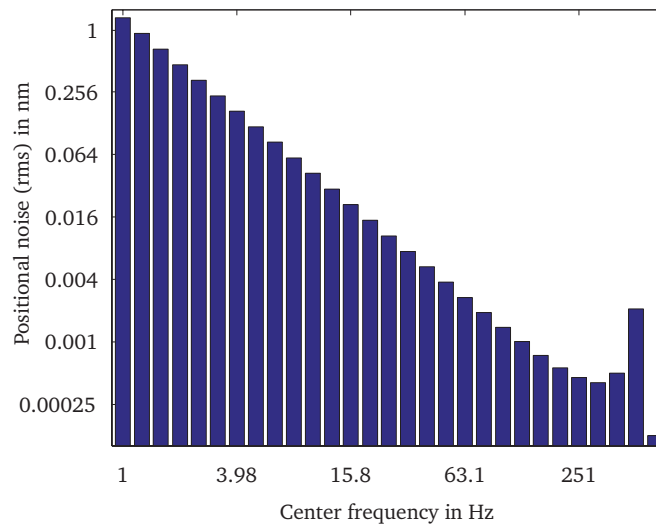


Figure 2.29: Positional noise due to acoustic excitation of the probe in z -direction.

can be stated that the first eigen frequency of the probe should be high, as to not interfere with the control system of the coordinate measuring machine [Brogan 91, Rao 03, Westphal 01].

Several measures can be taken in the machine to reduce the transfer of internal and external vibrations [Lam 97, Sciulli 97]. Also, the control system can be adjusted as not to excite the critical frequencies in the system and reduce machine vibrations [Franklin 91, Houpis 05, Inman 94, Westphal 01]. However, this is beyond the scope of this thesis and the reader is referred to the literature references mentioned in this paragraph.

Finally, as discussed in section 5.4, the positional deviation at the probe tip (rms) due to acoustic noise when freely suspended is measured to be approximately 0.9 nm when placed in open air at the university laboratory. When the probe is shielded the combined positional deviation due to floor vibrations and acoustic noise is measured to be less than 0.3 nm. Also, when the probe is brought into contact with a work piece in open air the positional deviation due to acoustic noise decreases to about 0.1 nm. As a result, the effect of acoustic noise and floor vibrations on the measurement uncertainty of the probing system as discussed in this thesis can be neglected.

2.1.10 Synchronization between probe and CMM

As mentioned in the previous section, when a vibration in the metrology loop is measured by both the probing system and CMM it can be compensated for. However, the deviation in the compensation depends on the phase difference between the measurement signal from the probing system and CMM. A phase difference may result from the mechanical behavior of the CMM and probing system. This results in a difference between the vibration as measured at the probe tip and as measured by the CMM.

A phase difference may also result from a time delay between the recording of the signal from the probing system and CMM, i.e. trigger delay. The third and final source under consideration is a difference in the phase change as a result of signal processing in the probing system and CMM. The influence of the mechanical behavior and trigger delay on the phase difference mainly depends on the CMM used. Therefore in this section, only the influence of the signal processing in the probing system on the phase difference between the signal from the probing system and CMM is considered. However, calculation of the contribution of other sources to the measurement deviation can be performed in a similar manner.

As an example the CMM developed by Ruijl [Ruijl 01] is discussed, as described in section 1.3.3. Here, the probing system is stationary and the work piece is mounted on a movable table. This is schematically shown in figure 2.30.

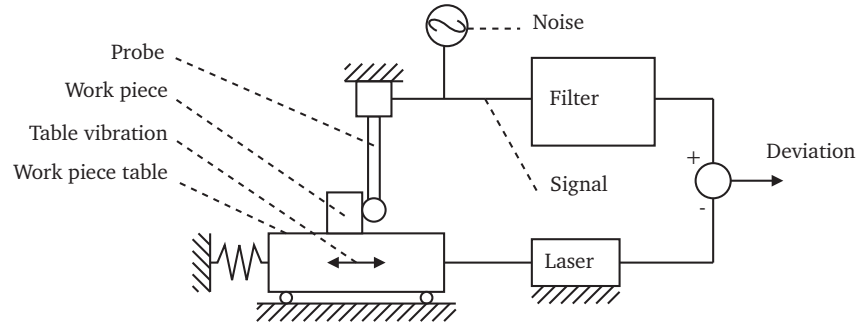


Figure 2.30: Schematic of the influence of a low-pass filter on the synchronization between probing system and CMM.

A mechanical vibration of the work piece table, e.g. due to the CMM controller, is measured by the probing system and laser interferometer of the CMM simultaneously. Vibrations of the work piece table in this design can be described by a sine-function with a frequency of 50 Hz and an amplitude of 30 nm [Ruijl 01]. To improve the mechanical behavior and reduce vibrations, the air flow to the air bearings used to guide the work piece table is controlled using an air buffer. As a result, the vibrational amplitude of the work piece table in the final design is reduced to 3 nm [Ruijl 01] during operation. As a practical upper limit a mechanical vibration with an amplitude of 50 nm and a frequency of 50 Hz is used in the remainder of this section.

As can be seen in figure 2.30 a low-pass filter is used to reduce the signal noise from the probing system:

$$H_{probe}(s) = \frac{1}{1 + \tau s} \quad (2.44)$$

Where $H_{probe}(s)$ is the transfer function from the probe signal, τ is the time constant of the filter and s is the Laplace transform variable.

However, this filter not only reduces the signal noise in the probing system, but also results in a phase change in the probe signal. Assuming the measurement system from the CMM, in the Ruijl CMM a laser interferometer, does not undergo any phase change, i.e. $H_{laser}(s) = 1$, the transfer function $H_{dev}(s)$ of the measurement deviation due to the phase difference between probe and laser is given by:

$$H_{dev}(s) = H_{probe}(s) - H_{laser}(s) = \frac{-\tau s}{1 + \tau s} \quad (2.45)$$

To minimize signal noise from the probing system, equation 2.44, the time constant τ of the filter should be as high as possible, i.e. the cutoff frequency f_c should be low. However, to improve the dynamic response, equation 2.45, the time constant τ of the filter should be low, i.e. the cutoff frequency f_c should be high. It is noted that:

$$f_c = \frac{1}{2\pi\tau} \quad (2.46)$$

Therefore, the optimum value is system specific. Figure 2.31 shows the noise from the probing system as a function of the cutoff frequency of the low-pass filter. The measurement deviation as a result of a mechanical vibration of the work piece table with a frequency of 50 Hz and different vibrational amplitudes is also shown as a function of the cutoff frequency.

As mentioned at the start of this section, the vibrations of the work piece table in this design are described by a sine-function with a frequency of 50 Hz and an amplitude of 50 nm. It can be seen in figure 2.31 that for a cutoff frequency of 1.3 kHz the noise from the probing system equals the measurement deviation as a result of work piece table vibrations. For this system, the minimum noise is therefore obtained at a cutoff frequency of 1.3 kHz.

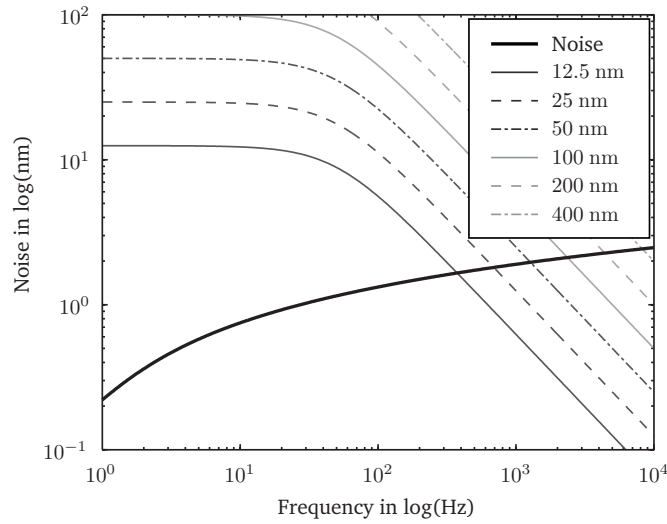


Figure 2.31: Influence of a low-pass filter in the probing system on probe system noise and the deviation due to synchronization between probing system and CMM as a function of the cutoff frequency of the filter and for different values of the vibrational amplitude of the work piece table.

2.2 Contact effects

2.2.1 Tip rotations during single point probing

Forces during a probing operation result in a deformation of the probe suspension and a deformation of its stylus and other elements in the structural loop of the probe tip, as discussed in section 2.3. These deformations often not only result in a translation of the probe tip, but also in a rotation. This is shown schematically in figure 2.32.

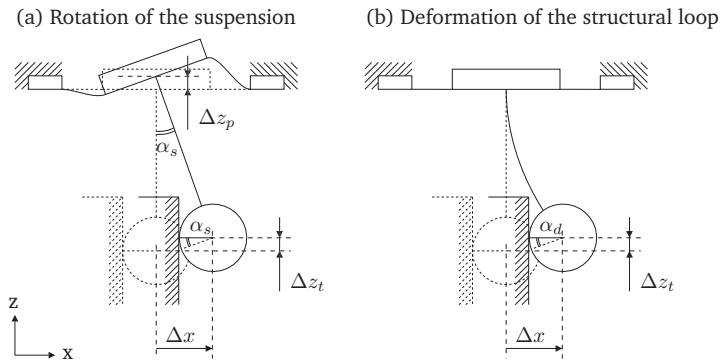


Figure 2.32: Rotation of the probe tip during probing results from (a) the suspension and (b) a deformation of structural elements, in this example the stylus.

The probe tip, of the probe discussed in this thesis, is connected to a center platform via a stylus, as discussed in appendix A. The suspension of the center platform consists of three slender rods, which allow the center platform to translate in z -direction and rotate around the x - and y -axis, relative to the probe holder. For this probe, the contribution of the deformation of the structural loop to the rotation of the probe tip is much smaller than the contribution of the suspension, i.e. $\alpha_d \ll \alpha_s$. The contribution of the deformations in the structural loop can therefore be neglected for the purpose of this section and only rotations due to the probe suspension are taken into account.

A rotation of the probe suspension α_s results in a displacement Δx at the probe tip, where $\Delta x \approx$

$l\alpha_s$. Here, l is the distance between the center point of the probe tip and the point of rotation. When the parts in the structural loop are rigid, the probe tip is rotated by the same angle α_s as the suspension. By using $\Delta z_t = \alpha_s r_t$, where r_t is the radius of the probe tip, the tip displacement in z -direction for a displacement Δx of the tip in x -direction can be calculated:

$$\Delta z_{tip,1} = \Delta x \frac{r_t}{l} \quad (2.47)$$

A rotation α_s of the stylus and other parts also results in a cosine error:

$$\Delta z_{tip,2} = l(1 - \cos \alpha_s) \approx l \left(1 - \cos \left(\frac{\Delta x}{l} \right) \right) \quad (2.48)$$

In the measurement range of $10 \mu\text{m}$ this results in a systematic deviation of approximately 1 nm , which can be neglected for the purpose of this section.

It is noted that a misalignment of the probe, e.g. as a result of manufacturing and assembly tolerances, may also contribute to the displacement of the probe tip in z -direction during probing. Based on measurements with the probe Widdershoven [Widdershoven 04] concluded that the contribution to the displacement of the tip results in a systematic deviation of less than 10 nm .

The rolling effect of the probe tip is illustrated in figure 2.33 for a measurement in direction **c**. The measurement directions are illustrated in figure A.1. The residuals in x -, y - and z -direction are shown between a displacement as measured by the probe and the same displacement as measured by the calibration setup. The residuals for the x and y direction are shifted by 40 and 20 nm , respectively, to improve readability. The distance between the probe tip and point of rotation l for both probes is approximately 8.5 mm .

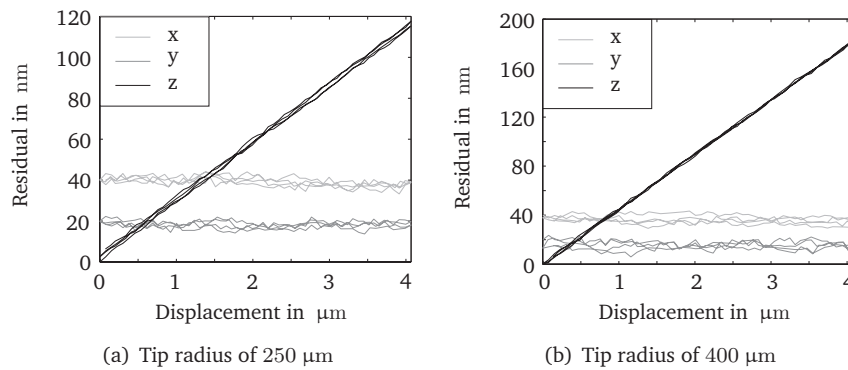


Figure 2.33: Residuals in x , y and z -direction between the probe and calibration setup over a $4 \mu\text{m}$ displacement: (a) residuals for probe 1 with a tip radius of $250 \mu\text{m}$, (b) residuals for probe 2 with a tip radius of $400 \mu\text{m}$.

The first point of interest is the z -residual, which shows a linear increase for displacements of the probe tip in the xy -plane. This is expected from the discussion on the rolling effect earlier in this section. The second observation is that the z residual increases to approximately 112 nm for probe 1, with a tip radius of $250 \mu\text{m}$, and 183 nm for probe 3, with a tip radius of $400 \mu\text{m}$. The measured z -residuals in figure 2.33 are thus in the same order of magnitude as is expected from equation 2.47. Finally, it is noted that the rolling effect may introduce stick-slip during single point probing, as discussed in section 2.3.6.

The rolling effect results in a repeatable shift in the point of contact between probe tip and work piece. Since this shift is measured by the probe, as shown in figure 2.33, it does not contribute to the uncertainty of the probe system. It does however influence the effective probing direction during calibration.

Following appendix A, the deviation \mathbf{D}_{dev} in the matrix containing the measurement directions \mathbf{D} is given by:

$$\mathbf{D}_{dev} = \mathbf{A}^{-1}\mathbf{M} - \mathbf{D} = \mathbf{A}^{-1} \begin{bmatrix} m_{1a} & m_{1b} & m_{1c} & m_{1d} \\ m_{2a} & m_{2b} & m_{2c} & m_{2d} \\ m_{3a} & m_{3b} & m_{3c} & m_{3d} \end{bmatrix} - \begin{bmatrix} 0 & 1 & -\frac{1}{2} & -\frac{1}{2} \\ 0 & 0 & \frac{1}{2}\sqrt{3} & -\frac{1}{2}\sqrt{3} \\ -1 & 0 & 0 & 0 \end{bmatrix} \quad (2.49)$$

Where \mathbf{A} is the measured sensitivity matrix and m_{1a} is the measured sensitivity of the strain gauges in rod 1 for a displacement in direction \mathbf{a} .

The deviation in measurement direction for probe 1, $\mathbf{D}_{dev,1}$, is measured to be:

$$\mathbf{D}_{dev,1} = \begin{bmatrix} 0 & 0.001 & 0.001 & 0.001 \\ 0 & 0.001 & 0.001 & 0.001 \\ 0 & -0.028 & -0.028 & -0.028 \end{bmatrix} \quad (2.50)$$

The deviations in x - and y -direction, 0.001, in matrix $\mathbf{D}_{dev,1}$ result from the least squares fit procedure used to calculate the measured sensitivity matrix \mathbf{A} , as discussed in appendix A.2. The deviation in z -direction, -0.028 , is caused by the rolling effect of the probe tip, as discussed earlier in this section. It is noted that for probe 1 $\Delta z_t = -0.028\Delta x$, which corresponds to the residual as shown in figure 2.33. The effective measurement direction \mathbf{D}_1^* for probe 1 during calibration is thus given by:

$$\mathbf{D}_1^* = \begin{bmatrix} 0 & 1 & -\frac{1}{2} & -\frac{1}{2} \\ 0 & 0 & \frac{1}{2}\sqrt{3} & -\frac{1}{2}\sqrt{3} \\ -1 & -0.028 & -0.028 & -0.028 \end{bmatrix} \quad (2.51)$$

The calibration procedure of the probe, as described in appendix A.2, uses three measurements in the xy -plane and a least squares fit procedure to calculate \mathbf{A} . As a result, the rolling effect is included in the calibration and the deviation in the measurement direction \mathbf{D}_{dev} on the calculation of the measured sensitivity matrix \mathbf{A} can be neglected [Widdershoven 04].

The residuals between the displacement as measured by probe and the calibration setup, as shown in figure 2.33, are calculated using the nominal measurement directions \mathbf{D} . By using the effective measurement direction \mathbf{D}_1^* the rolling effect for probe 1, as shown in figure 2.33, can be compensated for as shown in figure 2.34. It is noted that the residuals for the x - and y -direction are shifted by 40 and 20 nm, respectively, to improve readability.

Also, the point of contact between work piece and probe tip changes as a result of the rolling effect. Therefore the residuals in figure 2.34 include the effects of unroundness and roughness of the probe tip and the contact surface of the calibration setup over the length of the rolling effect, which is 115 nm for probe 1 for a 4 μm displacement.

Finally, it is noted that due to parasitic translations of the rods when they are translated out of the xy -plane, the probe tip will rotate around the z -axis when moved in vertical direction. Additionally, this rotation will result in a small displacement when the tip is not on the z -axis, e.g. due to manufacturing tolerances. This parasitic translation Δl of a rod with length l , width w and thickness t is schematically shown in figure 2.35.

Using standard elastic theory, moment $M(x)$ at position x is given by:

$$M(x) = F(x - l) + M_B \quad (2.52)$$

$$M_B = \frac{1}{2}lF$$

Using equation 2.52, the angle $\beta(x)$ at position x is calculated to be:

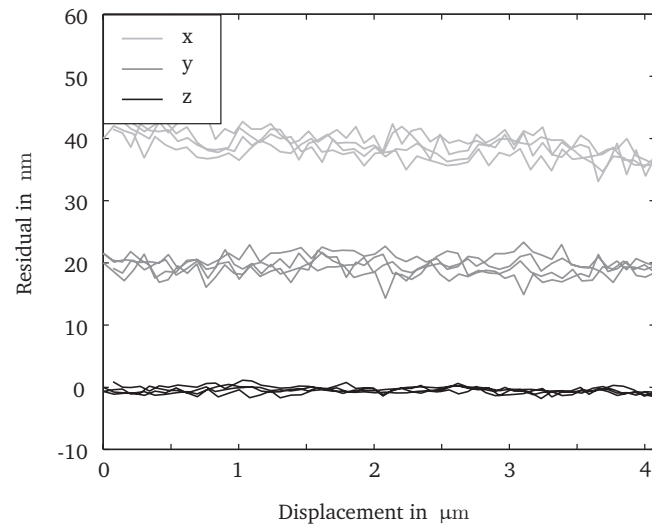


Figure 2.34: Residuals for probe 1 after compensation of the rolling effect.

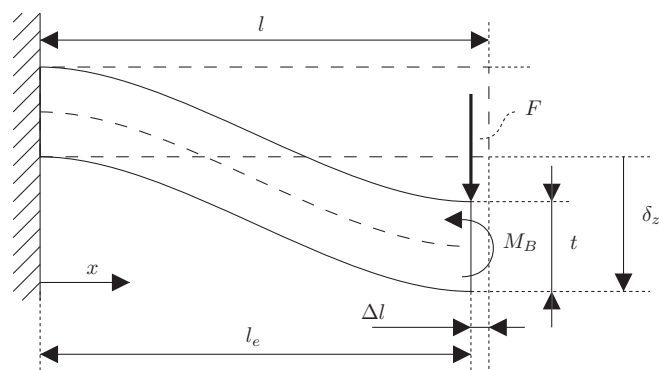


Figure 2.35: Simple model of a cantilever.

$$\beta(x) = \frac{F}{2EI} (x^2 - lx) \quad (2.53)$$

Where E and I are the Young's modulus and second moment of area of the cantilever, respectively. The infinitesimal length change dl due to the rotation $\beta(x)$ along the infinitesimal length dx is given by:

$$dl = dx (1 - \cos(\beta(x))) \quad (2.54)$$

The parasitic translation Δl is now given by:

$$\Delta l \approx \int_0^l 1 - \cos(\beta(x)) dx \approx \int_0^l 1 - \left(1 - \frac{1}{2}\beta^2(x)\right) dx = \int_0^l \frac{1}{2}\beta^2(x) dx \quad (2.55)$$

Combining equations 2.55 and 2.53 yields:

$$\Delta l \approx \frac{3}{5} \frac{\delta_z^2}{l} \quad (2.56)$$

Which for a displacement δ_z of 10 μm and a rod length l of 1.6 mm results in a parasitic displacement Δl of 37.5 nm. For a distance of 9 mm between the endpoint of the rod and the center of the probe tip, the resulting stylus rotation α is 4.17 μrad . For a probe tip with 250 μm radius, this corresponds to a displacement at the probe tip of 1 nm.

2.2.2 Micro-friction in normal contact

If two non-conforming bodies with different elastic properties are brought into normal contact, deformation of the bodies results in a tangential traction $q(r)$ at the interface, as well as a normal pressure $p(r)$ at radial position r [Johnson 85]. The normal pressure $p(r)$ results in a friction force which counteracts the tangential traction $q(r)$.

Assuming Hertz contact mechanics apply and the coefficient of friction is a constant, i.e. $\mu(r) = \mu$, this will result in a central region in the contact where the surfaces stick together and a region of slip towards the edge of the contact. At the transition between the regions, at radial position c , the tangential traction q is balanced by the friction force:

$$|q(c)| = \mu p(c) \quad (2.57)$$

It can be shown [Johnson 85] that the ratio between c and the edge of the contact, at radial position a , is constant for a given coefficient of friction and material combination. The value of c/a is shown in figure 2.36 and is given by:

$$\frac{a}{2c} \ln \left(\frac{a+c}{a-c} \right) = \frac{\beta}{\mu} \mathbf{E} \left(\sqrt{1 - \frac{c^2}{a^2}} \right) \quad (2.58)$$

Where $\mathbf{E} \left(\sqrt{1 - \frac{c^2}{a^2}} \right)$ is the complete elliptical integral of the second kind, defined by:

$$\mathbf{E}(k) = \int_0^1 \frac{\sqrt{1 - k^2 x^2}}{\sqrt{1 - x^2}} dx \quad (2.59)$$

and β is a measure of the difference in elastic constants of the two materials:

$$\beta \equiv \frac{1}{2} \left(\frac{\frac{1-2\nu_1}{G_1} - \frac{1-2\nu_2}{G_2}}{\frac{1-\nu_1}{G_1} + \frac{1-\nu_2}{G_2}} \right) \quad (2.60)$$

Here, ν_1 is the Poisson ratio of material 1 and G_1 its shear modulus. The shear modulus G relates to the Young's modulus via $G = E/2(1 + \nu_1)$.

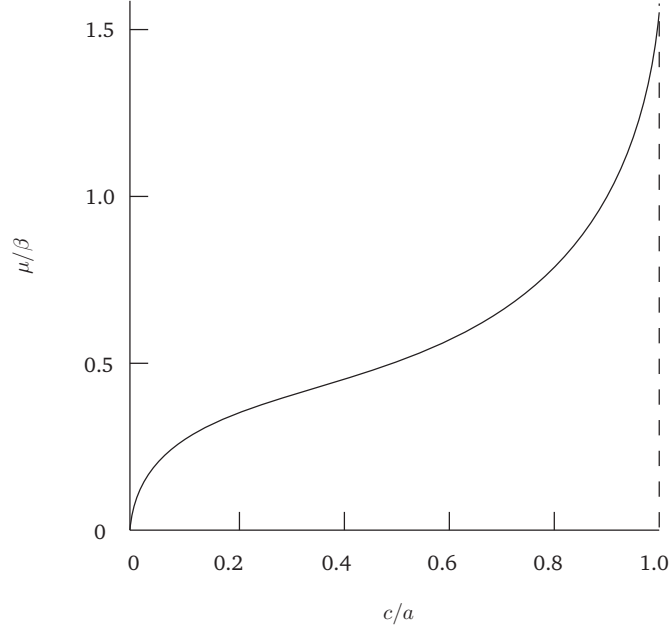


Figure 2.36: Radius c of the transition between the stick and slip region relative to the contact radius a in the normal contact of dissimilar solids.

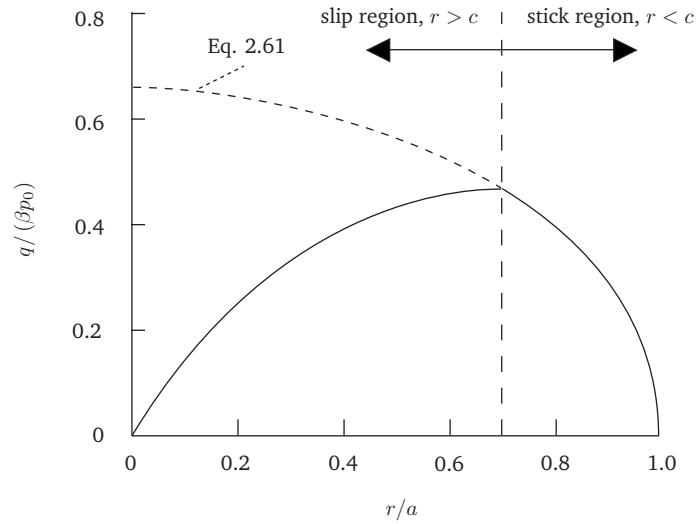


Figure 2.37: Tangential traction at the contact of dissimilar solids in the case of partial slip where $\mu/\beta = 0.66$ [Johnson 85].

As the load on the contact is increased, mating points on the two surfaces which initially lie in the slip region of the contact, $c < r < a$, undergo different tangential displacements. As the load increases these points may be enveloped by the central region, $r < c$, and further relative displacements are prevented by friction. The relative tangential displacement and strain in these points is maintained. The traction $q(r)$ at radial position r as a function of the a is given by [Johnson 85]:

$$q(r) = \frac{\beta p_0}{\pi} \left(-\frac{\sqrt{a^2 - r^2}}{r} + \frac{r}{a} \ln \left(\frac{a + \sqrt{a^2 - r^2}}{r} \right) + \frac{2}{ra} \int_r^a \frac{x^2}{\sqrt{x^2 - r^2}} \ln \left| \frac{x+r}{x-r} \right| dx \right) \quad (2.61)$$

Where p_0 is the maximum pressure in the contact.

The traction $q(r)$ over βp_0 is shown in figure 2.37 as a function of the dimensionless radial position r/a . In the slip region of the contact, where $r > c$, the tangential traction in the contact is given by equation 2.61. As mentioned before, once mating contact points are enveloped by the central stick region of the contact they experience no further relative displacements. Hence, the tangential traction equals the tangential traction when these contact points were first enveloped by the central region, as shown in the left part of figure 2.37.

Mossakovski [Mossakovski 63] and Spence [Spence 75] showed that, depending on the value of β , friction can increase the load required to produce a contact of a given size a by at most 5% compared to Hertz theory. Thus, for a given load it can be shown using equation G.1 that variations due to friction in the contact radius a are less than 1.6%. Using equation G.2 this would result in a maximum deviation in the indentation depth δ of 3.2%.

For a sapphire probe tip with a 50 μm tip radius, in normal contact with a planar aluminum work piece with a contact force of 2.94 mN equation G.2 yields a Hertz indentation of 31 nm. The contribution of micro friction to the measurement deviation of the probe in vertical probing is therefore approximately 1 nm.

2.2.3 Micro-friction in rolling contact

During probing in the xy -plane of the probe, discussed in this thesis, the tip of the probe rolls over the surface, as described in section 2.2.1. It is assumed that the probe tip can roll freely over the work piece, i.e. the resulting tangential force Q between the probe tip and work piece is zero. For a discussion on tractive rolling, where $Q \neq 0$, the reader is referred to Johnson [Johnson 85].

Tangential strains in the probe tip and work piece, as discussed in the previous section, results in a central area where both bodies stick together and an area of slip near the edge of the contact. When rolling, the difference in tangential strains in the stick region of the contact between the two bodies results in a small apparent slip, commonly referred to as creep. Thus, if the probe tip experiences a tensile tangential stress in the stick region of the contact with the work piece, the contact region at the surface of the tip is stretched. The effective circumference of the tip is thus increased. The original circumference of the probe tip O_o relates to the effective circumference of the tip in contact O_e via the creep ratio ξ , where $O_e = (1 + \xi) O_o$, and ξ is given by [Johnson 85]:

$$\xi = \frac{\beta a}{\pi r} \quad (2.62)$$

Where β is a measure of the difference in elastic constants of the two materials, given by equation 2.60, a is the radial position of the edge of the contact, equation G.1, and r is the reduced radius of the contact, equation G.5.

For the contact between a sapphire tip with radius $r_1 = 250 \mu\text{m}$ and a planar aluminum work piece $\beta = 0.168$. For a deflection of 7 μm and a stiffness c_t at the probe tip of 480 N/m the force between tip and work piece is 3.4 mN. Using equation G.1, the radius of the contact a is calculated to be 2.1 μm , which results in a creep ratio ξ of $4.4 \cdot 10^{-4}$.

For a rolling distance of 112 nm, as discussed in section 2.2.1, the contribution of micro slip during horizontal probing is $\ll 1$ nm.

2.2.4 Vibrating styli

As discussed in section 2.1.8 vibration of the probe tip can be used to reduce the sticking effect between probe tip and work piece due to surface forces. Several probes in which the stylus is vi-

brated have been developed [Bauza 05, Johnston 76, Kanda 00, Karrai 99, Lee 00B, Nishimura 01, Ohya 93, Saito 03, Vidic 98, Woody 03], some of which are discussed in section 1.4. These probes measure changes in the frequency content, vibration amplitude or phase of the measurement signal to detect the contact between probe tip and work piece [Bar 00, Rabe 02]. The principle of operation of a vibrating probe is schematically shown in figure 2.38. Since these vibrating probes are not the main focus of this thesis, only a brief description of some measurement effects associated with them will be discussed.

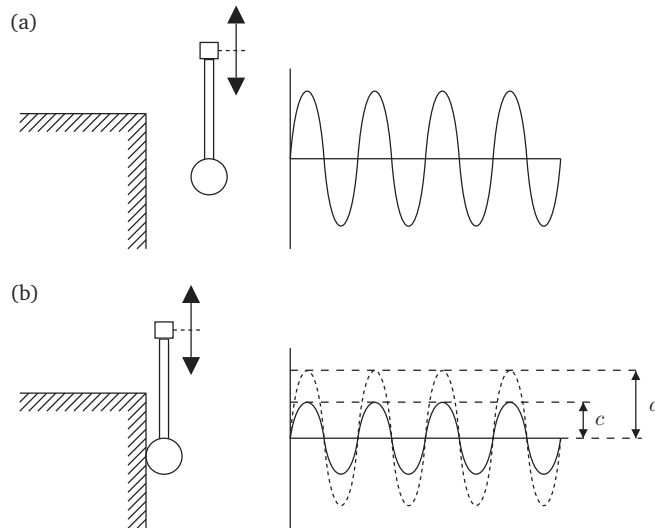


Figure 2.38: Operation principle of a vibration probe: (a) probe tip is approaching the work piece, (b) probe tip in contact with the work piece.

The direction of vibration for the vibrating probes is mostly 1D, as shown in figure 2.39. An example of an axial vibration direction is the UMAP probe by Mitutoyo, as discussed in section 1.4, and for the orthogonal direction the probe developed at the University of North Carolina at Charlotte (UNCC). A 3D vibration, consisting of a combination of axial and orthogonal motions, is also possible. However, this method is more complex due to differences in eigen frequency of the vibrations and cross effects. When the vibrations in each direction can be distinguished, e.g. by utilizing differences in eigen frequency, this effect can be used to calculate the 3D tip displacement.

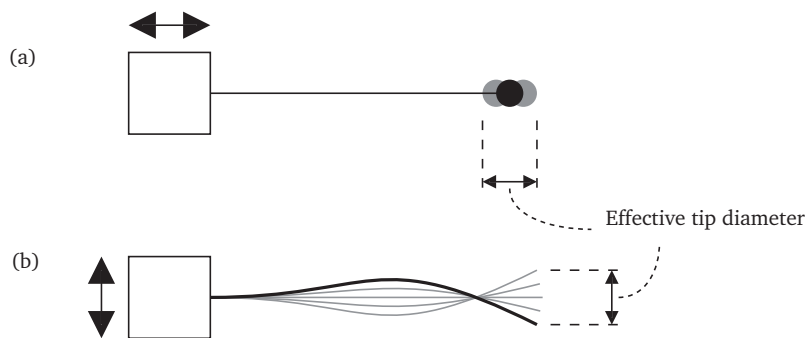


Figure 2.39: Direction of vibration: (a) axial, (b) orthogonal, or a combination of (a) and (b).

As shown in figure 2.39, the effective tip diameter is influenced by the vibration amplitude. The diameter of the stylus of the UNCC probe is approximately $7\text{ }\mu\text{m}$. However, the effective tip diameter of the UNCC probe is typically $30\text{ }\mu\text{m}$ or more as a result of the stylus vibration. The vibration of the stylus can be controlled by controlling the amplitude of the oscillator [Bauza 05].

Most vibrating probes produce a single measurement signal. In order to perform 3D measurements,

the direction of approach should therefore be known. In most vibrating probes, the changes in amplitude and phase of the vibration are caused by physical contact between probe tip and work piece. The influence of layers on the surface of the work piece, e.g. water or air layers, on the measurement with a vibrating stylus is beyond the scope of this thesis. However, it is likely that they do influence the measurement to some extent. Measurements by Freund et al. [Freund 99] of the thickness of the adsorbed water layer on gold, graphite or titanium using a STM show that the thickness can easily reach 30 nm or more for a relative humidity of 60% or more. The thickness of the adsorbed water layer also depends on material properties, in particular its hydrophilicity, as discussed in appendix C.4.

As mentioned before, the UMAP probe [Nishimura 01] is an example of a probe that is vibrated in axial direction. For these probes changes in amplitude and phase in axial direction are mainly caused by a collision between probe tip and work piece. For the orthogonal probing direction these changes are mainly caused by friction between the probe tip and work piece. The influence of the contact on the changes in amplitude and phase are thus dependent on the direction of the contact relative to the vibration direction, i.e. the probe sensitivity is influenced by the nature and direction of the contact.

A non-contact vibrating probe was developed by Takaya et al. [Takaya 99, Takaya 00]. Here, an 8 μm sphere is optically trapped using a laser beam. Using optical radiation pressure the sphere is forced to vibrate with an amplitude of approximately 100 nm. Changes in the amplitude and phase of the vibration are caused by an air damping effect [Takaya 04]. It is noted that changes in the thickness or properties of the air layer around the work piece, e.g. due to air humidity, influence the measurement. Another problem to be solved with this technique is the required numerical aperture (NA) of the laser beam, which limits the usability of the system when measuring holes or vertical planes.

Another factor of interest for vibrating probes is plastic deformation of the work piece. The UNCC probe consists of a carbon fiber which vibrates at $f = 32 \text{ kHz}$ with an amplitude of approximately 10 μm [Bauza 05]. The equivalent mass m_{eq} of the vibration is taken as 1/3 of the mass of the carbon fiber between the free end and the closest node, i.e. $m_{eq} = l/3\pi r_t^2 \rho$. Where the length l between the free end and the closest node is 160 μm , the radius of the stylus r_t is 3.5 μm and the specific mass ρ is 1750 kg/m^3 . Neglecting all damping, using an equivalent mass of $3.6 \cdot 10^{-12} \text{ kg}$ and a tip diameter r_t of 3.5 μm for the contact between a carbon fiber and an aluminum work piece, equation 2.4 yields an allowed relative speed between tip and work piece of 9.7 mm/s.

Neglecting damping and effects of layers on the surface and assuming a sinusoidal vibration, the tip position $x(t)$ and speed $v(t)$ are given by:

$$\begin{aligned} x(t) &= 10 \cdot 10^{-6} \cos(\omega t) \\ v(t) &= -10 \cdot 10^{-6} \omega \sin(\omega t) = -2 \sin(\omega t) \end{aligned} \quad (2.63)$$

Where $\omega = 2\pi f = 2 \cdot 10^5$.

Using an approach speed v_{CMM} of the coordinate measuring machine (CMM) of 1 mm/s and a vibrational frequency of 32 kHz, the time of the collision with the highest relative speed is given by:

$$x(t) = 10 \cdot 10^{-6} \cos(\omega t) = 10 \cdot 10^{-6} - 1 \cdot 10^{-3} t \quad (2.64)$$

It follows from equation 2.64 that the collision takes place at $\omega t = 6.21$ with a relative speed $v_{max} = v_{CMM} + 22 = 23 \text{ mm/s}$.

The admissible vibrational speed of the probe tip during the first collision is $9.7 - v_{CMM} = 8.7 \text{ mm/s}$. From equation 2.63 this can be seen to occur at $\omega t = 6.28$. It can thus be shown that the above calculation results in a plastic deformation of the work piece in 94% of the probing operations.

2.2.5 Wear of the probe tip and work piece

According to Weckenmann *et al.* [Weckenmann 04] and Renishaw [Renishaw 06A, Renishaw 06B] the wear of the probe tip and work piece is predominantly caused by adhesive wear and abrasive wear.

In the case of abrasive wear, small particles are removed from one or both surfaces and act as an abrasive at the contact area. The particles may also adhere to the surfaces where they act as an abrasive. Depending on the material combination a material buildup may occur on one of the two materials, adhesive wear, or both surfaces may suffer abrasive wear. An example of the latter is the contact between ruby and steel. The harder ruby particles attach to the steel and act as an abrasive. Since the atomic attraction between the materials is low, wear rather than material build up occurs.

Figure 2.40 shows the result of an abrasive wear experiment by Renishaw [Renishaw 06A] between a ruby probe tip with a nominal radius of 1.875 mm and a planar steel work piece. In these experiments a scanning measurement is performed over 5600 m with a single point contact. A contact force of 1.5 N was applied, resulting in a flat of approximately 150 μm in diameter. This corresponds to a 1.5 μm form error of the tip. It is noted that material is also removed from the planar steel work piece. However, since this wear is not concentrated in a single spot, its contribution to the measurement uncertainty is not significant. This effect could be much more significant on master work pieces or on standards which are used for the recalibration of the measuring instrument, as the wear is repeated very often [Weckenmann 04].

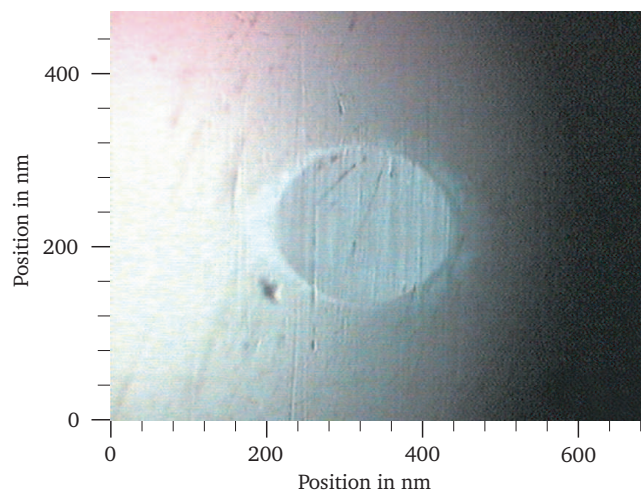


Figure 2.40: Abrasive wear on a ruby tip due to the contact with a planar stainless steel work piece [Renishaw 06B].

The experiments were performed to illustrate the effect of abrasive wear. The conditions under which these experiments were performed are extreme, even for conventional scanning applications [Renishaw 06A].

The contact forces during a scanning measurement with the probe discussed in this thesis are in the order of 0.5 mN for a 250 μm tip radius. Also, the length of a scanning measurement with a single contact point is limited due to the nature of the products to be measured. The influence of the wear of the tip on the measurement uncertainty is therefore neglected.

The second contribution to the wear of the probe tip and work piece is adhesive wear, caused by the transfer of material from one surface to another due to local welding effects [Renishaw 06A]. As a result, after the surface material starts to adhere, the materials in contact are now the same, which promotes the buildup of material. A high surface hardness, a large difference in the hardness of the surfaces or an affinity between the materials of probe tip and work piece increases the rate of adhesive wear. Also, the degree of adhesive wear is directly proportional to the contact force and the distance scanned [Renishaw 06B].

	Optimum	To be avoided	Other suitable materials
Stainless steel	Ruby	Silicon Nitride (abrasive wear)	
Cast iron	Zirconia	Silicon Nitride (abrasive wear)	Ruby, Tungsten carbide
Aluminum	Silicon Nitride		Ruby (may suffer adhesive wear)

Table 2.7: Selection of tip material [Renishaw 06A].

Adhesive wear occurs when scanning an aluminum work piece with a relatively hard ruby (aluminum oxide) tip. Figure 2.41 (a) shows the adhesive wear between a ruby probe tip with a nominal radius of 1.875 mm and a planar aluminum work piece during scanning with a single point contact and a contact force of 1.5 N. The scanning is performed over new work piece material over a continuous distance of 350 m. The amount of material transfer, often referred to as pick up, is minute and immeasurable on the form of the stylus ball, even with the highest precision measuring equipment [Renishaw 06A, Weckenmann 04].

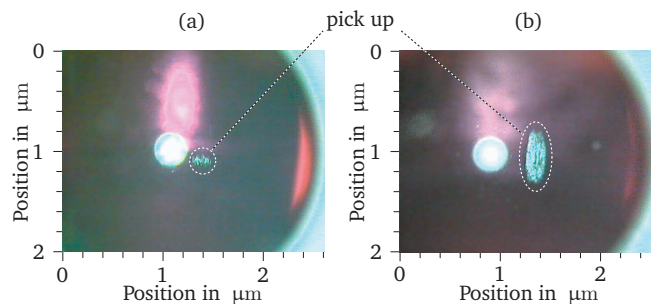


Figure 2.41: Adhesive wear on a ruby tip due to the contact with a planar aluminum work piece [Renishaw 06A].

Significant adhesive wear only occurs in extreme cases, where the probe tip repeatedly scans the same component, without leaving time for an oxide coating to form. This is shown in figure 2.41 (b) where, under the same conditions as for figure 2.41 a, the probe tip was repeatedly scanned over the same path several hundred times. The patch, under these unusual circumstances, is approximately 200 by 500 μm and has a height of approximately 2 μm [Renishaw 06A, Weckenmann 04].

Similar experimental results were obtained by Meli [Meli 07] who scanned a polished tungsten carbide flat. Using a probing force of 2.2 mN at a speed of 0.4 mm/s he found an average wear of 3 nm per meter scan length with a ruby sphere 125 μm in diameter.

Regular qualification of the tip can reduce the influence of the tip wear on the measurement uncertainty. However, repeated calibration of the probe against the same artifact may result in wear of the artifact. The optimum choice for the material of the probe tip for different work piece materials is shown in table 2.7.

2.2.6 Probe tip cleaning

Particles on the scanning path are collected by the probe tip as it passes over the surface. These particles include metal oxide particles of the work piece and air-borne particles like coolant mist or paper dust. Performing the measurement in clean room conditions will greatly reduce contamination of the probe tip.

At the moment of writing, the standard for mass still consists of platinum-iridium artifacts kept in National laboratories. From these platinum-iridium artifacts other mass standard are derived,

often made from stainless steel. These artifacts are naturally sensitive to contaminations and hence many publications with respect to the cleaning of surfaces originate from this field [Clarkson 01, Davidson 03, Girard 90, Ikeda 93, Pinot 95, Schwartz 94, Seah 94]. In this section three methods of cleaning a probe tip will be discussed: manual cleaning with solvent, cleaning with solvent in an ultrasonic bath and cleaning by immersion in pure boiling water.

First manual cleaning is discussed, where mechanical wiping with a solvent is used to remove marks. As a solvent ultrapure ethanol can be used, which is applied to the tip using lens tissue. To avoid redistribution of contaminants the tissue should always be dragged in the same direction and a fresh area of tissue should be used for each motion. An advantage of manual cleaning is that it can be used for localized cleaning. The result is however dependent on the operator skills and cleaning technique and requires a force between the tissue and probe tip. Unless the probe suspension is fixated during cleaning this method is therefore not suitable for fragile probing systems.

The second method is ultrasonic cleaning, where an ultrasonic bath is used in combination with a solvent, e.g. acetone and/or ethanol. In general, ultrasonic cleaning during approximately 10 minutes will be more effective than manual cleaning [Davidson 02]. Good results can be obtained with stainless steel and glass, but all plastics and reactive materials should be avoided.

Finally, cleaning by immersion of the probe tip in de-ionized boiling water is discussed. Experiments by Davidson *et al.* [Davidson 02] show that this is the most effective and repeatable cleaning procedure when used on stainless steel weights. As discussed by Shea *et al.* [Seah 94] steam can also be used with similar results. It is noted that all equipment, especially glassware and supports, should be thoroughly cleaned before using it.

2.3 Geometric effects for tactile probes

In many tactile probes, including the probe discussed in chapter 3, a suspension is deformed as a result of a displacement of the probe tip. The deformation of the suspension is measured, e.g. by strain gauges, and the tip position can be calculated.

A deformation of the suspension also results in a force between probe tip and object. This force will result in a deformation of sphere and object at the contact surface, as discussed in section 2.3.3. The force is also exerted on the structural loop through the CMM between the probe tip and object. The elements of this structural loop have a finite stiffness and will deform as a result of this force.

We distinguish three parts of the structural loop. The first part of the structural loop is the probe itself and its holder, used to connect the probe to the CMM. The second part is the CMM and the third part is the object to be measured. The effects of the structural loop through the probe, CMM and object are discussed in sections 2.3.1, 2.3.2 and 2.3.3, respectively. Then, in section 2.3.4, the effects of tip radius on the measurement is discussed. Finally, the effect of the probe tip sticking to the work piece as a result of surface forces is discussed in section 2.3.5.

2.3.1 Finite stiffness effects of the probe

For measuring micrometer sized features a thin and relatively long stylus is required, resulting in a low stylus stiffness. The effects of the finite stiffness of the part of the structural loop through the probe are measured during the calibration of the probe, as discussed in appendix A.2. As a result a reduced stiffness in this loop will result in a reduced deformation of the suspension for a given displacement of the probe tip. Therefore the measurement signal for a given tip displacement will decrease compared to the situation where the structural loop through the probe has infinite stiffness.

During calibration of the probe the sensitivity coefficients in the transformation matrix \mathbf{A} will therefore decrease to compensate for this effect. As a result a deformation of the probe and holder

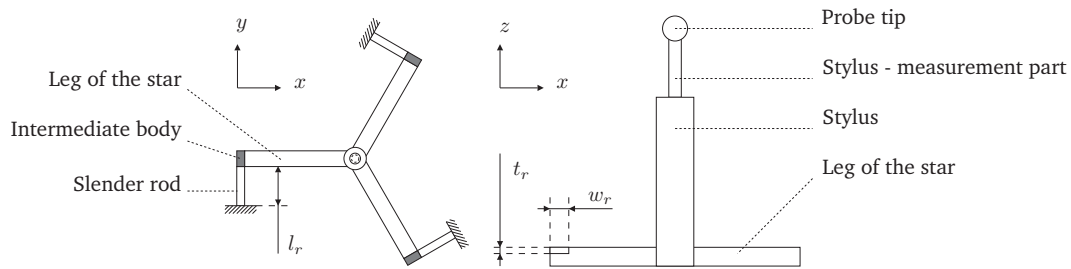


Figure 2.42: Top view (left) and front view (right) of the stiffness model used to calculate the effects of a finite stiffness in the probing system.

does not directly influence the measurement uncertainty. However, since the measurement signal for a given tip displacement decreases, the measurement resolution of the probe decreases.

This is discussed using a model of the probe by Pril (see section 1.5), as shown in figure 2.42. The results from this section are obtained with a stainless steel stylus with a measurement length of 0.5 mm and a total length of 8 mm.

The slender rods, the legs of the star and the stylus are modeled using beam elements, as discussed in appendix D.4. Using this model two situations are compared. In the first situation, all elements except the slender rods are given an infinite stiffness. As a result a displacement of the tip will be completely transmitted to the slender rods. In the second situation all elements are given a realistic stiffness and the radius of the measurement length of the stylus is varied.

Now, the ratio χ between the deformation of the slender rods in the first situation to the deformation of the slender rods in the second situation can be calculated. The ratio χ is a measure for the decrease in sensitivity as a result of the finite stiffness effects of the elements in the probe. This is shown in figure 2.43 where the ratio χ is given for different radii of the measurement part of the stylus.

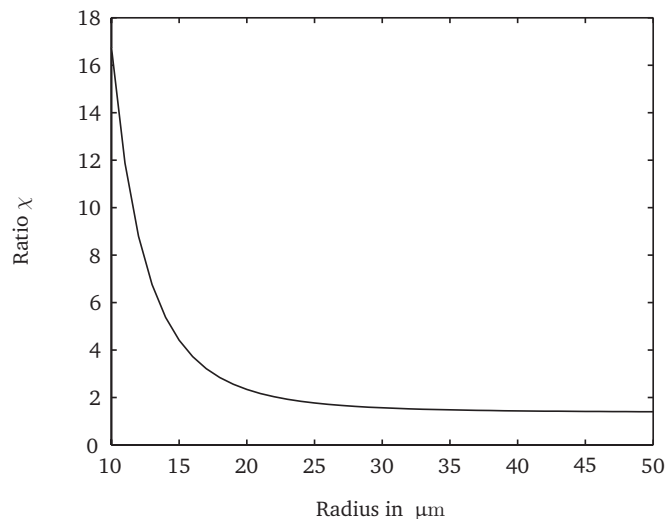


Figure 2.43: Ratio χ of the stiffness coefficient c_{xx} at the probe tip in x direction as a function of the radius of the measurement part of the stylus.

It is noted that even for an increasing stylus radius a ratio χ of 1 is not obtained. This is caused by a finite stiffness in the other parts of the metrology loop; e.g. the intermediate body. As a result some loss in sensitivity will remain even for large stylus radii.

It should be clear from figure 2.43 that the sensitivity decreases for a decreasing radius of the measurement part of the stylus, as expected. As discussed in appendix D.4, the ratio χ will decrease,

improving the sensitivity, when the stiffness of the rods is decreased.

The stiffness in z direction of a rod c_{zz} as a function of its length l_r , width w_r , thickness t_r and Young's modulus E_r , is given by [Young 02]:

$$c_{zz} = \frac{E_r t_r^3 w_r}{l_r^3} \propto \left(\frac{t_r}{l_r} \right)^3 \quad (2.65)$$

As is well known, decreasing the width w_r , thickness t_r or Young's modulus E_r of a rod or increasing its length l_r reduces its stiffness. For the probe under consideration, the width of the rods is limited by the width of the aluminum tracks and the required separation between them; see section 1.5. Since the rod material is set, the best option to influence the stiffness of the rod in this design is to change the length and thickness of the rods.

However, the bending of the rods is measured using piezo resistive strain gauges mounted on top of the rods. The maximum stress σ_{max} and the moment M due to a force F_r on the end of the rod are given by:

$$\sigma_{max} = \frac{M t_r}{2 I_r} \quad (2.66)$$

$$M = \frac{6 E_r I_r}{l_r^2} x_{lz} \quad (2.67)$$

Combining equation 2.66 with 2.67 yields:

$$\sigma_{max} = \frac{M t_r}{2 I_r} = \frac{3 E_r t_r}{l_r^2} x_{lz} \propto \frac{t_r}{l_r^2} \quad (2.68)$$

By decreasing both the rod thickness t_r and length l_r and keeping the ratio of $t_r l_r^{-2}$ the same, the maximum stress σ_{max} in the rod for a given displacement of its endpoint x_{lz} remains the same. However, as seen in equation 2.65 the stiffness of the rod will decrease.

Theoretically, any required stiffness can therefore be obtained without any loss in maximum stress for a given displacement of the endpoint of the rod. Practically however, decreasing the rod size is limited as a result of the uncertainties and processing conditions during manufacturing. An important parameter is the length and resistance of the piezo strain gauges, as discussed in section 3.1.2. Therefore in [Pril 02] an optimum rod length l_r of 1.6 mm is calculated.

During manufacturing of the probe suspension, changing the thickness of the rods is a matter of using a different wafer, for a silicon on insulator (SOI) wafer, or changing one process parameter, the etching time of the membrane. However, changing the rod length requires modifications in several process masks. Therefore an optimum rod height is calculated, given a rod length of 1.6 mm and a width of 160 μm , as a function of the radius of the measurement part of the stylus, as shown in figure 2.44. It can be seen that the optimum sensitivity with this probe is obtained at a rod thickness of 33 μm when the stylus radius $> 50 \mu\text{m}$.

In figure 2.43 a rod thickness $t_{r.orig}$ is used of 30 μm . As shown in equation 2.68 the sensitivity is decreased by decreasing the thickness of the rod. Therefore the ratio χ as a function of the radius of the measurement part of the stylus using the optimum rod thickness $t_{r.opt}$ is compensated for the influence of the rod height on the maximum stress.

$$\text{Ratio } \chi^* = \frac{t_{r.orig}}{t_{r.opt}} \text{Ratio } \chi \quad (2.69)$$

The ratio χ^* is shown in figure 2.45 as a function of the radius of the measurement part of the stylus. The graph from figure 2.43 is shown as a reference.

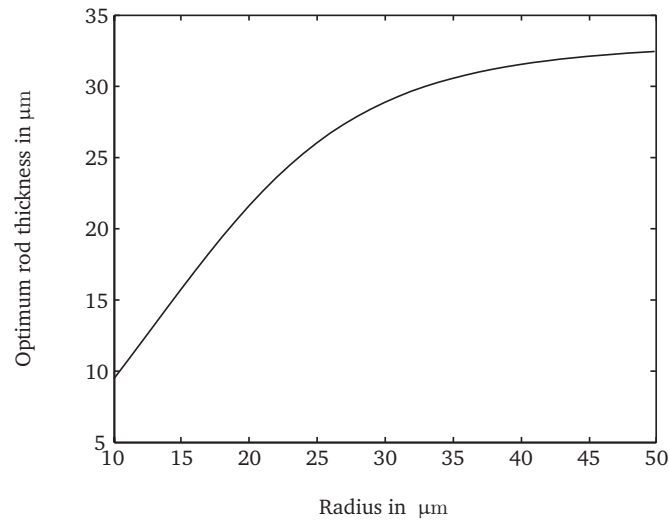


Figure 2.44: The rod height at which an optimal sensitivity is obtained as a function of the radius of the measurement part of the stylus.

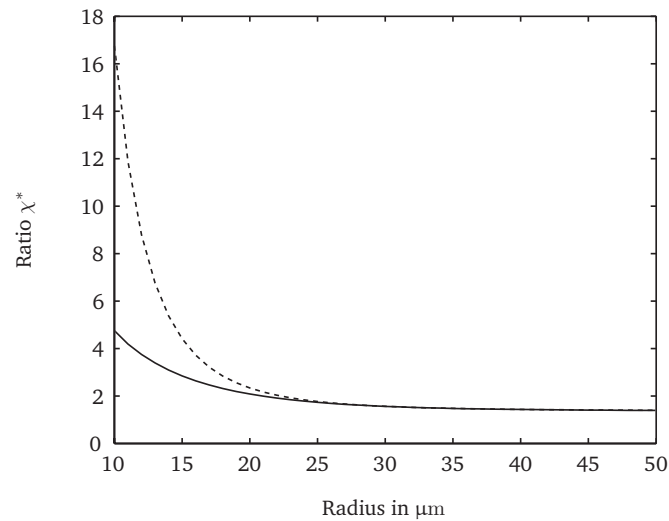


Figure 2.45: Ratio χ^* of the stiffness coefficient C_{xx} at the probe tip in x direction for the original and the optimized height of the slender rods as a function of the radii of the measurement part of the stylus.

As can be seen in figure 2.45, the minimum radius of the measurement part of the stylus is $21\text{ }\mu\text{m}$ for a measurement length of $500\text{ }\mu\text{m}$ and a maximum decrease in sensitivity of a factor of 2 compared to the situation where the radius of the stylus is $> 50\text{ }\mu\text{m}$. When a decrease in sensitivity of a factor of 4 is accepted, the minimum radius of the stylus decreases to $11\text{ }\mu\text{m}$.

The radius of the upper part of the stylus limits the radius of the probe tip, since during probing the probe tip should be able to scan a wall parallel to the stylus without the risk of contact between stylus and wall. Therefore, finite stiffness effects limit the minimum tip radius that has practical use. It should be clear that the minimum tip radius is also influenced by the length of the upper part of the stylus. Decreasing the length of the upper part of the stylus by a factor of two will also decrease the minimum tip radius by the same amount and vice versa. From the above discussion it can thus be shown that a ratio of 50 between the length and radius of the measurement part of the stylus can be obtained with the tactile 3D probing system.

Finally, it is noted that decreasing the suspension stiffness also decreases the eigen frequency of the probe and increases the stick-slip during scanning measurements, as discussed in section 2.1.8. Also, the effect of the probe tip sticking to the work piece as a result of surface forces is increased when the suspension stiffness is decreased, as discussed in section 2.3.5.

2.3.2 Finite stiffness effects of the CMM

The second part of the structural loop between measurement object and probe tip is the coordinate measurement machine (CMM). The influence of deformations of the CMM on the measurement uncertainty depends on the calibration of the probe.

The first method is to calibrate the probe on the CMM. Similar to the calibration of the finite stiffness effects of the probe, discussed in the previous section, the finite stiffness effects of the CMM are included in the calibration results. Therefore, deformations of the CMM due to static probing forces are compensated for. Another advantage of the method is the alignment of the probe to the coordinate system of the CMM.

In the second approach, the probe is calibrated on a separate setup. The setup used in this thesis to do a separate calibration of the probe is discussed in section 1.6.1. In most cases, using a separate setup improves the measurement uncertainty of the calibration. Finite stiffness effects of the CMM in the second approach, if not measured or compensated for, will therefore result in a measurement deviation.

Typically the stiffness of the structural loop through the CMM is an order of magnitude higher than the stiffness of the loop through the probe, especially for probes with a small tip radius. Also, by paying attention to design principles [Hale 99, Schellekens 98, Slocum 92], e.g. separate the metrology loop from the structural loop, the contribution to the measurement uncertainty of the CMM can be reduced [Ruijl 01, Seggelen 07, Vermeulen 99].

2.3.3 Finite stiffness effects of the object

The final part of the structural loop between measurement object and probe tip is the object to be measured. Aspects that influence the measurement, include finite stiffness of the object to be measured and the material deformation of the contact surface between the tip of the probe and the object.

Deformations due to finite stiffness of the object result in a measurement deviation. This effect is not included in the calibration measurement of the probe. Depending on the design of the probe, a stiffness at the probe tip of 20 N/m and an over travel distance of $10\text{ }\mu\text{m}$ will result in a force of 0.2 mN . This force will result in a measurement deviation of 10 nm when the stiffness of the structural loop through the object between the probe tip and the CMM is $20 \cdot 10^3\text{ N/m}$.

There are several options to reduce the influence of the finite stiffness of the measurement object. These include decreasing the stiffness of the probe, compensation of the effect and low force probing. Decreasing the stiffness of the probe is discussed in section 2.3.1 and the main disadvantage

of this is stick-slip of the probe during scanning, as discussed in section 2.1.8 and an increase in the release distance of the probe, as discussed in section 2.3.5.

To compensate for finite stiffness effects in the measurement object the stiffness of the structural loop through the object needs to be known. The stiffness at the point of probing can be determined before the measurement or when the stiffness at the probe tip is known the probe itself can be used for the measurement. A stiffness at the probe tip of 20 N/m, see appendix D, and a resolution of 1 nm would result in a resolution of the force measurement of 20 nN.

When the CMM performs a single point measurement, as discussed in section 2.1.2, the first measurement point will be performed at the over travel distance of the CMM, typically 7 μm . When the probe is retracted in for example 1 μm intervals a force-distance curve at the point of probing can be determined, from which the stiffness at the point of probing can be calculated. When the stiffness of the object and probe are known, the measurement data can be compensated for the finite stiffness of the object.

Low force probing, as discussed in section 2.1.2, is similar to the above method. With this method, the probe is gradually retracted after contact as well to a position where the tip of the probe is just in contact with the object. When a measurement is made, the tip displacement and the forces between object and probe tip, will therefore be substantially reduced. Using this method a tip displacement of for example 0.1 μm will result in a force of 2 μN when the suspension stiffness is 20 N/m.

The second aspect is the material deformation of the contact surface between the tip of the probe and the object, as discussed in appendix G. The indentation δ in m of the probe tip with radius r in m and a planar work piece is given by:

$$\delta = \left(\frac{9F_{Hz}^2}{16rE_{red}^2} \right)^{\frac{1}{3}} \quad (2.70)$$

Here, F_{Hz} is the force between probe tip and work piece in N and E_{red} is the reduced Young's modulus, as given by equation G.5. A rod thickness of 10 μm and 30 μm results in a stiffness at the probe tip of 20 N/m and 480 N/m, respectively, as discussed in appendix D.4. An over travel distance of 7 μm results in a contact force F_{Hz} of 0.14 mN and 3.4 mN, respectively. The indentation of a sapphire probe tip, $E = 345 \cdot 10^9 \text{ Pa}$, and a planar aluminum work piece, $E = 70 \cdot 10^9 \text{ Pa}$, as a result of this force is shown in figure 2.46 as a function of the radius of the probe tip.

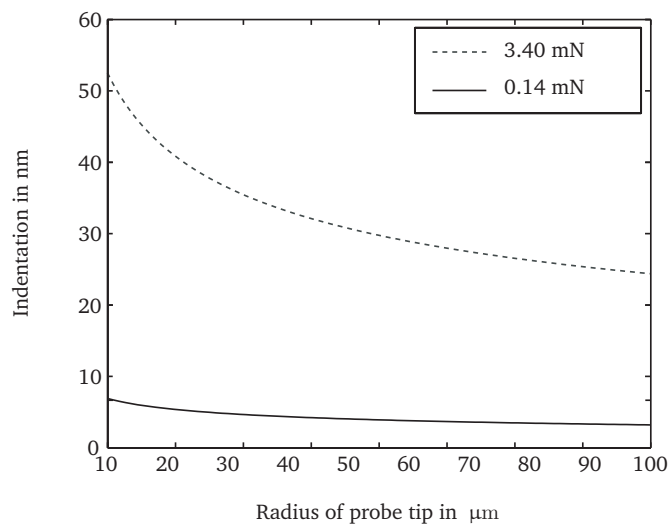


Figure 2.46: Indentation of probe tip and work piece as a function of the radius of the probe tip.

The indentation of the work piece may be compensated for when the Young's modulus of the work

piece is known. For an object consisting of different and/or unknown materials a reduced Young's modulus can be calculated using equation 2.70 [Laake 06]:

$$E_{corr} = \left(\frac{E_{r,max}^{-\frac{2}{3}} + E_{r,min}^{-\frac{2}{3}}}{2} \right)^{-\frac{3}{2}} \quad (2.71)$$

Here $E_{r,max}$ and $E_{r,min}$ are the maximum and minimum reduced Young's moduli that are expected to occur during the measurement, according to equation G.5. As a general case, a realistic upper bound $E_{r,max} = 257$ GPa is used for a sapphire tip against a synthetic diamond surface; $E = 1100$ GPa and $\nu = 0.1$. As a lower bound $E_{r,min} = 58$ GPa is used for a sapphire tip against an aluminum work piece; $E = 70$ GPa and $\nu = 0.33$.

Using equation 2.71 a reduced Young's modulus of $E_{corr} = 102$ GPa is obtained. The maximum deviation caused by the material deformation of the work piece surface is reduced from 31 nm to 12 nm, for a tip radius of 50 μm and a measurement force of 2.94 mN. Deviations as a result of the uncertainty in the stiffness at the probe tip and the measurement uncertainty of the probe are taken into account.

It is noted that the indentation and deformation of the calibration artifact, used to calibrate the probe, is taken into account by the calibration. The transformation matrix A includes the effects of the indentation and deformation of the calibration artifact.

Another aspect of the material deformation of the contact surface is that the probe tip and/or work piece may undergo elastic-plastic deformation. In appendix G the indentation at which the work piece will undergo elastic-plastic deformation δ_Y is calculated. Figure 2.47 shows the indentation of probe tip and work piece for a radius of the probe tip of 50 μm as a function of the force between probe tip and work piece.

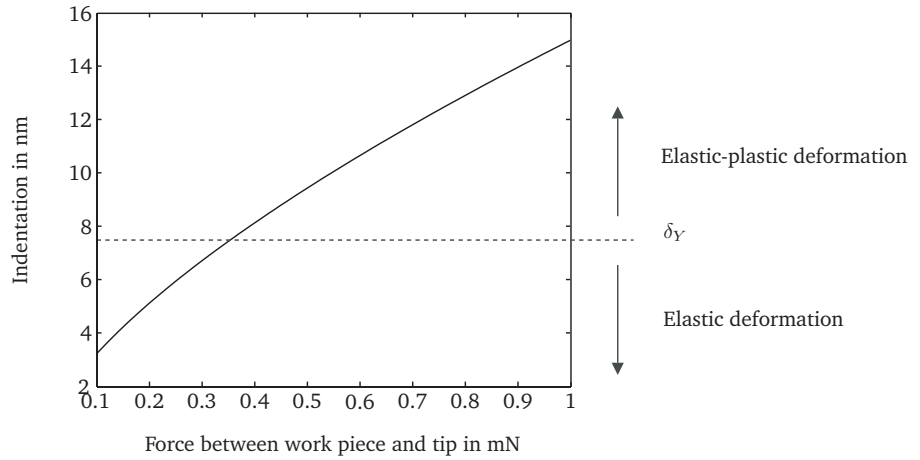


Figure 2.47: Indentation of probe tip and work piece as a function of the contact force for a 50 μm probe tip radius.

It can be seen that a planar aluminum work piece, contacted by a sapphire tip with a 50 μm radius, shows elastic-plastic deformation when the measurement force exceeds 0.36 mN. The stiffness at the probe tip for an over travel distance of 7 μm should therefore be 51 N/m or less. For a tip radius of 25 μm the suspension stiffness should be below 14 N/m.

Deformation of the contact surface due to dynamic forces during probing, e.g. as a result of the collision between probe tip and work piece, is discussed in section 2.1.3.

2.3.4 Radius of the probe tip

The influence of the radius of the probe tip during a scanning measurement of a profile is depicted in figure 2.48 for a probe with a perfect spherical tip. When, during a measurement, the probe tip

is in contact with the work piece at more than one point, the information obtained is mechanically filtered by the radius of the probe tip used. This filter has a low pass characteristic; the cut-off frequency increases with a decreasing radius of the probe tip, because a smaller probe tip can penetrate smaller roughness valleys than a bigger probe tip. As a result, the measurement of internal structures, like holes and trenches, differs from the measurement of protruding structures. Especially for internal structures and surface roughness, the radius of the probe tip limits the size of the structures that can be measured by the probe.

Therefore, by decreasing the radius of the probe tip, smaller structures can be measured. However, as discussed in the previous section, decreasing the radius of the probe tip increases the indentation of the contact surface for a given contact force and may lead to elastic-plastic deformation of the probe tip and/or the object to be measured.

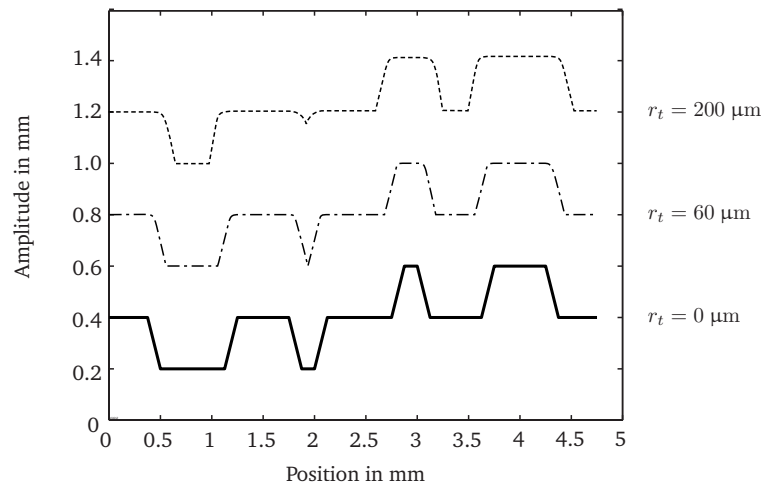


Figure 2.48: The measured profile for a different radius of the probe tip. Solid line: original profile, dash-dotted line: measured profile with radius 60 μm and dotted line: measured profile with radius 200 μm .

Due to the nonlinear effects of the locus traced by the tip while probing, the effect of the radius of the probe tip on the measurement results cannot easily be described by a simple multiplication of coordinates or filter characteristics. A method to reconstruct the original profile from the measurement data is discussed by Morel [Morel 2006]. The reconstructed profile, from the measurements shown in figure 2.48 is shown in figure 2.49, showing the nonlinear effect of the radius of the probe tip on the reconstructed surface.

Features on micro systems greatly vary in size. The radius of lenses for mobile applications are typically around 50 μm - 2 mm, the radius of a fuel injection nozzle is typically around 50 - 100 μm and holes in a micro sieve have a typical radius of 10 - 50 μm [Elwenspoek 01, Fukuda 98, Rijn 04]. This has led to an ongoing trend of probe tip miniaturization, as mentioned in section 1.4.

The minimum tip of the silicon 3D probe, discussed in this thesis, is limited by finite stiffness effects of the stylus. In section 2.3.1 a minimum radius of the stylus of 11 μm is calculated for a sensitivity loss of a factor of 4 and a measurement length of 500 μm . The minimum tip radius would therefore be around 12.5 μm , depending on the measurement task.

The radius of the stylus and the corresponding stiffness, also influences the release distance of the probe tip to the work piece, also referred to as a snap out effect, as discussed in the next section.

2.3.5 Release distance of the probe tip

As discussed in the previous section, the measurement data obtained for internal structures is filtered by the radius of the probe tip used. As a result the radius of the probe tip limits the size of internal structures and effects of surface roughness that can be measured by the probe.

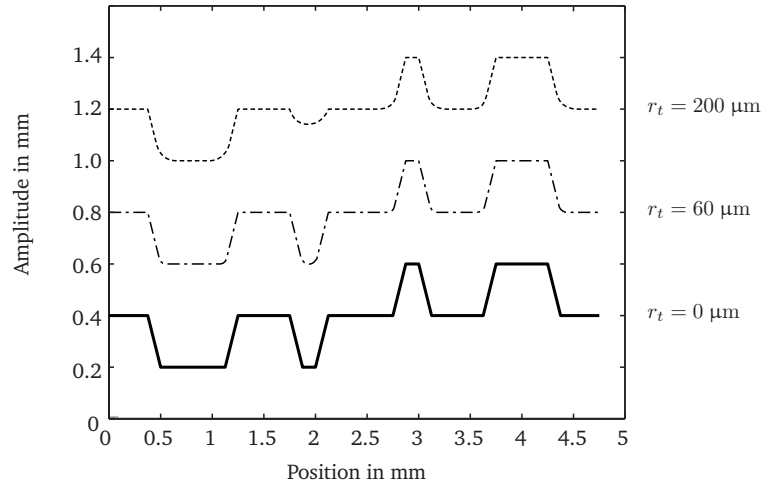


Figure 2.49: The reconstructed profile from the measured profile, shown in figure 2.48. Solid line: true profile, dash-dotted line: reconstructed from measurements with a probe tip radius of 60 μm and dotted line: reconstructed from measurements with a probe tip radius of 200 μm .

Another aspect to consider when probing small internal features is the minimum release distance x_{rel} , as depicted in figure 2.50. This is caused by surface forces between the probe tip and the work piece $F_{surface}$, as discussed in section 2.1.7 and figure 2.22. By decreasing the radius of the probe tip, the radius of the stylus also needs to be reduced. As the stiffness of the stylus in x-direction c_{xx} is proportional to the stylus radius to the power of three $c_{xx} \propto r_s^3$, and surface forces are proportional to the tip radius to the power of two $F_{surface} \propto r_t^2$, the release distance increases when the radius of the probe tip decreases.

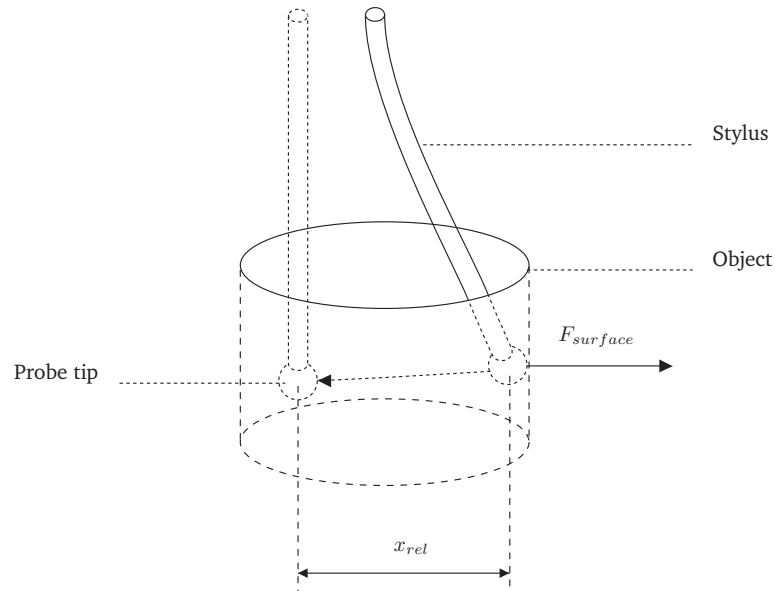


Figure 2.50: Schematic of the release distance x_{rel} during probing.

An approximation of this effect is discussed by the example of the fiber probe, discussed in section 1.4.2. The stiffness of the stylus at the tip of the probe is given by:

$$c_{xx} = \frac{3E\pi r_s^4}{4l_1^3 + 4l_2^3 + 12l_1l_2^2(1+\nu)} \quad (2.72)$$

Here, l_1 , l_2 and r_s are length 1, length 2 and radius of the stylus, as shown in figure 2.51. The Young's modulus E and Poisson ratio ν for a glass fiber are $72.5 \cdot 10^9$ Pa and 0.17, respectively.

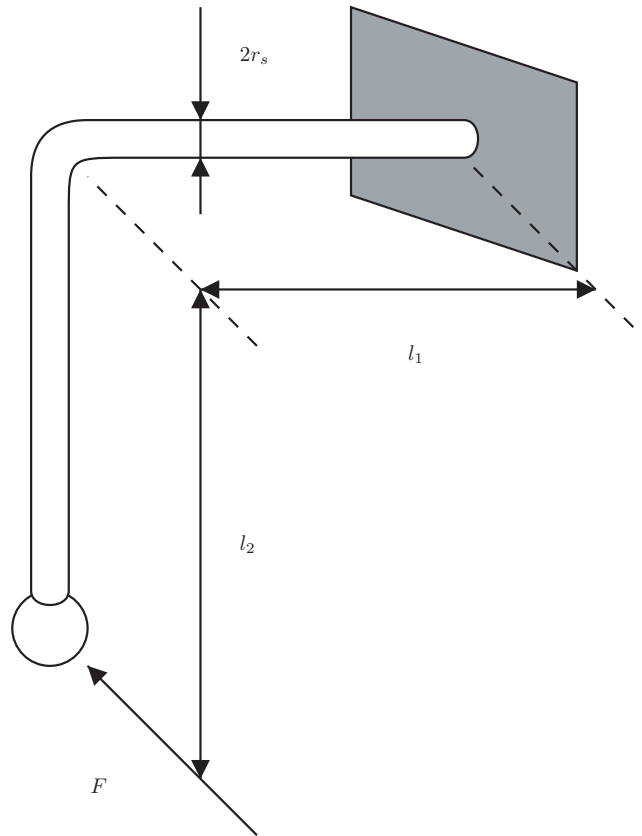


Figure 2.51: Stiffness model of the fiber probe.

For a stylus radius r_s of $10 \mu\text{m}$, a length l_1 of 4 mm and a length l_2 of 6 mm , equation 2.72 yields a stiffness at the probe tip of 2.17 mN/m . Assuming a surface force of $2 \mu\text{N}$, see section 2.1.7, this results in a release distance of 0.92 mm .

Even though the tip radius of this probe is only $15 \mu\text{m}$ and measurement forces are small, a release distance close to 1 mm makes scanning, see section 2.1.8, and probing of small holes highly impractical. By decreasing the adhesion of the probe tip to the work piece, as discussed in section 2.1.7, or by increasing the stiffness at the probe tip, the release distance can be reduced.

The stiffness of the redesigned probe, discussed in section 3 and appendix D, is approximately 20 N/m for a probe tip with a $25 \mu\text{m}$ radius and 480 N/m for a $250 \mu\text{m}$ radius tip. The release distance is calculated to be $0.25 \mu\text{m}$ for both probes, taking into account the additional surface forces for the larger tip. The measurement results of the effect of surface forces on the release distance, or snap out distance, of the 3D tactile probing system is discussed in section 5.3.

2.3.6 Anisotropic effects

When stiffness at the probe tip is not isotropic, the response of the probe will depend on the measurement direction. To describe this effect the directional response pattern of a probe, which is equivalent to the directional pretravel variations, is of interest [Aston 97, Bambach 80, Bartelt 02, Bartelt 03, Chan 97]. Other factors which may influence the directional response pattern include the suspension of the stylus, asymmetric moment of inertia of stylus, arrangement of probes in different directions, direction dependent sensitivity of probes, set-up of the axes, tip ball form deviation, and the direction dependent dynamic behavior of the probing system including styli combinations [Flack 01, Weckenmann 04].

As a result, the output signal for a measurement depends on the measurement direction. Unless compensated for, this effect would result in a measurement deviation that varies with the direction of the measurement. As an example, the directional response pattern for the Renishaw TP6 is shown in figure 2.52.

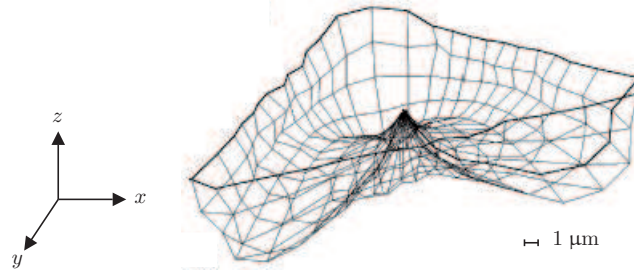


Figure 2.52: Pretravel variation of the Renishaw TP6 plotted in polar coordinates [Weckenmann 04, Wozniak 02A, Wozniak 02B].

An important contribution to a direction dependent stiffness at the probe tip for the probe discussed in this thesis is the anisotropic stiffness of the silicon base material from which the suspension is manufactured, as discussed in appendix D.3. However, since the effect is reproducible and the stiffness at the probe tip is known it can be compensated for when the probing direction is known [Kishinami 84, Moon 98, Shen 97, Weckenmann 79, Yang 96].

Even though the anisotropic stiffness of the suspension can be compensated for it does result in a measurement behavior which is direction dependent. This can be seen from the measurement results for the original probe by Pril [Pril 02], as shown in figure 2.53.

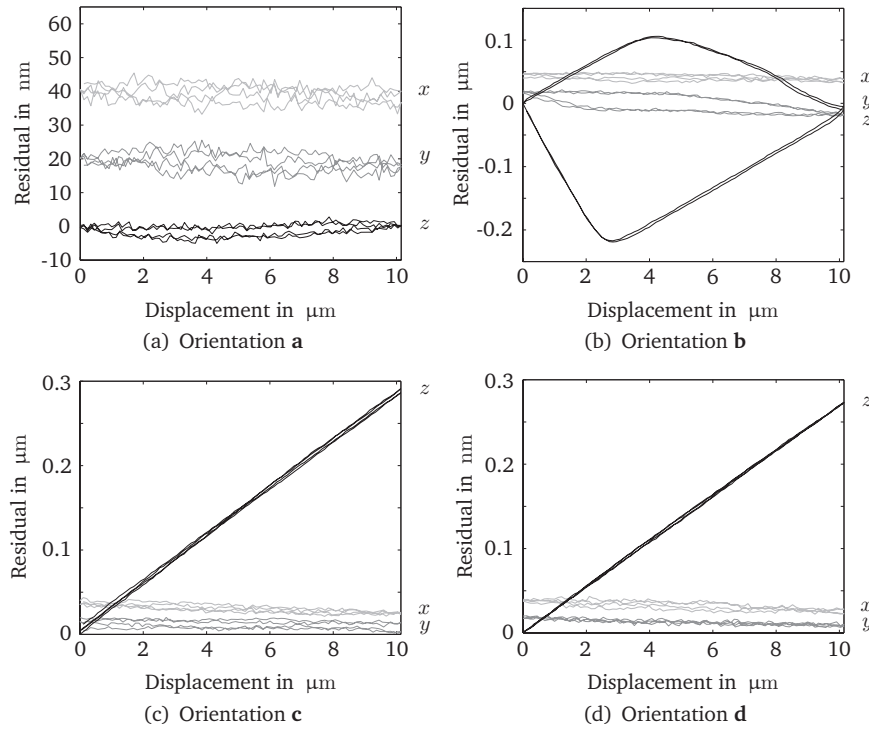


Figure 2.53: Residuals in x , y and z -direction between a displacement as measured by the probing system and the same displacement as measured by the calibration setup: (a) for orientation **a**, (b) for orientation **b**, (c) for orientation **c**, (d) for orientation **d**.

In these figures, direction **a** corresponds to the z -direction of the probe, i.e. the length direction

of the stylus. The directions **b** - **d** correspond to directions in the xy -plane as shown in figure A.1. It can be clearly seen from the results for directions **b** - **d** that the behavior of the probe is direction dependent. For measurements in directions **c** and **d** the z -residual shows a linear increasing deviation. This can be explained by the rolling of the probe tip over the work piece surface, as discussed in section 2.2.1.

This rolling effect is also observed for small displacements in direction **b**. However, for this direction the rolling effect is interrupted after approximately $4\text{ }\mu\text{m}$ and a hysteresis curve can be observed. The contact forces between probe tip and work piece for a measurement in x -direction are shown in figure 2.54.

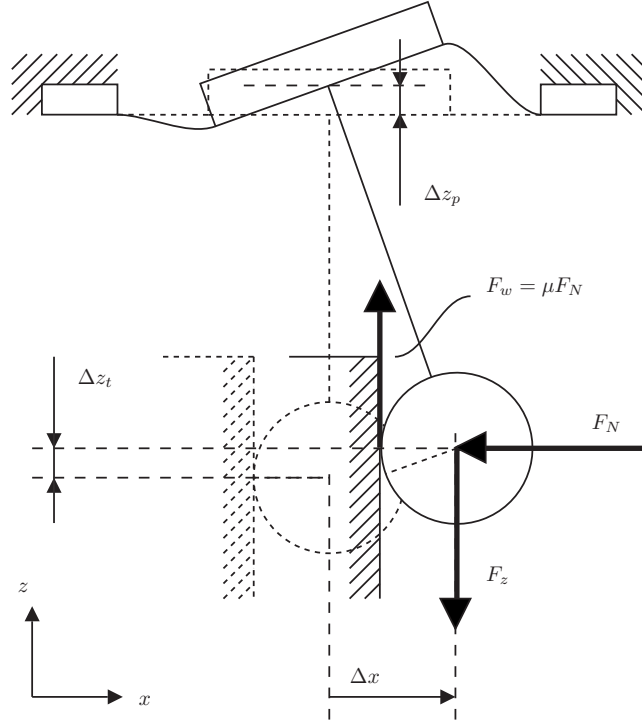


Figure 2.54: Forces between probe tip and work piece during horizontal probing.

It can be seen that slip is expected to occur when the force F_z in z -direction exceeds the friction force F_w .

The forces at the probe tip are given by:

$$\begin{bmatrix} F_x \\ F_y \\ F_z \end{bmatrix} = \mathbf{C}_{probe} \Delta \mathbf{X}_t + \mathbf{F}_s \quad (2.73)$$

Where \mathbf{F}_s is a vector containing the surface forces between probe tip and work piece, $\Delta \mathbf{X}_t$ are the displacements of the probe tip and \mathbf{C}_{probe} is the stiffness matrix for the probe tip.

The stiffness matrix \mathbf{C}_{probe} for the original probe by Pril [Pril 02], calculated using appendix D, is given by:

$$\mathbf{C}_{probe} = \begin{pmatrix} 190.2 & -1.5 & -43.1 \\ -1.5 & 167.0 & 2.7 \\ -43.1 & 2.7 & 1111.6 \end{pmatrix} [\text{Nm}^{-1}] \quad (2.74)$$

Taking into account the rolling effect, equation 2.47, the displacement vectors $\Delta \mathbf{X}_t$ at the probe tip for directions **b** - **d** are given by:

	Direction b	Direction c	Direction d
F_N	$191.5\Delta x + 1 \cdot 10^{-3}$	$173.4\Delta x + 1 \cdot 10^{-3}$	$171.1\Delta x + 1 \cdot 10^{-3}$
$F_w = \mu F_N$	$28.7\Delta x + 1.5 \cdot 10^{-4}$	$26.0\Delta x + 1.5 \cdot 10^{-4}$	$25.7\Delta x + 1.5 \cdot 10^{-4}$
F_z	$73.9\Delta x$	$6.9\Delta x$	$11.6\Delta x$

Table 2.8: Tip forces in N as a function of the tip deflection Δx in m for three probing directions.

$$\Delta X_{t,b} = \begin{pmatrix} 1 \\ 0 \\ -0.0277 \end{pmatrix} \Delta x \quad \Delta X_{t,c} = \begin{pmatrix} -\frac{1}{2} \\ \frac{1}{2}\sqrt{3} \\ -0.0277 \end{pmatrix} \Delta x \quad \Delta X_{t,d} = \begin{pmatrix} -\frac{1}{2} \\ -\frac{1}{2}\sqrt{3} \\ -0.0277 \end{pmatrix} \Delta x \quad (2.75)$$

The influence of surface forces on the contact between probe tip and work piece is discussed in section 2.1.7. A higher contact force F_N will result in a more intimate contact and an increase of the contact area between probe tip and work piece. In the measurements shown in figure 2.53 the surface force between the sapphire probe tip, with $r_t = 250 \mu\text{m}$, and aluminum work piece is therefore estimated to be 1 mN at the point of slip.

By combining equations 2.73, 2.74 and 2.75 and using a coefficient of friction μ of 0.15 [Blau 95, Rabinowicz 04], the forces at the probe tip can be calculated as a function of the applied tip deflection Δx . The result is shown in table 2.8, where Δx is the total length of the displacement vector in xy -direction.

From table 2.8 it can be seen that for directions **c** and **d**, the friction force F_w is larger than the force F_z in z -direction for all positive values of Δx . Hence, it is expected that rolling of the probe tip on the work piece surface is not interrupted by a slip effect, which corresponds to the results shown in figure 2.53 (c) and (d).

For direction **b** it can be seen in table 2.8 that $F_w < F_z$ when $\Delta x < 3.3 \mu\text{m}$ and $F_w > F_z$ when $\Delta x > 3.3 \mu\text{m}$. The point of slip, as obtained by the above calculation is in the same order of magnitude as the point of slip of the probe for a measurement in direction **b**, figure 2.53 (b).

It can thus be seen that the measurement behavior of the probe is influenced by micro scale effects³ and that the anisotropic stiffness of the silicon suspension results in a mechanical behavior of the probe which is direction dependent. By compensation of the anisotropic stiffness in silicon, as discussed in section 3.2.1, an isotropic stiffness can be obtained with the probe. As a result, slip of the probe tip over the measurement surface is prevented in all measurement directions.

2.4 Thermal effects in probe

Thermal distortions are, in general, the largest source of non repeatable positional deviations in machines [Bryan 90]. In appendix E.3 general design considerations are discussed for coordinate measuring machines and probes. In this section, the influence of thermal deviations on the measurement results with the probe are discussed.

As discussed in appendix E.3, the probe is only a part of the metrology loop between probe tip and work piece through the coordinate measuring machine (CMM). Also, it is useful to distinguish between parts that only require short term stability, e.g. drift of the local coordinate system, and parts that require long term stability, e.g. reference scales.

As mentioned in appendix E.3, it is important to characterize the heat flow into the system. Therefore, the two main internal sources of heat in and near the probe holder will be discussed first:

³Since the influence of gravity is neglectable on this scale and without taking into account surface forces, a force in a given direction would result in either stick or slip of the probe tip on the measurement surface in direction **b**, regardless of the displacement Δx .

- self heating of the piezo resistive strain gauges
- electronics

Self heating due to the piezo resistive strain gauges arises from the electrical power which is dissipated in the resistors. The electrical power P follows from the voltage V over the strain gauge and the resistance R in Ω of the strain gauge itself. For a voltage V of 2.5 V, corresponding to a bridge voltage of 5 V, and a resistance R of 50 k Ω , the power P for a single resistor is given by:

$$P = \frac{V^2}{R} = 125 \mu\text{W} \quad (2.76)$$

Pril [Pril 02] estimated the maximum rise in temperature due to self heating in his probe to be 47 mK. Using finite element simulation a maximum rise in temperature of 46 mK was obtained for the redesign of the probe⁴, as discussed in chapter 3.

The second heat source near the probe holder are the electronics used to amplify the signal from the slender rods. To minimize the heat production near the probe holder, the electronic components are split in pre-amplifiers, located near the probe holder, and main amplifiers. Most heat, approximately 8 mW, is produced by the main amplifiers, which are placed at approximately 50 mm away from the probe holder, as shown in figure 2.55. It is therefore assumed that the influence of the main amplifiers on the temperature variations in the probe holder can be neglected.

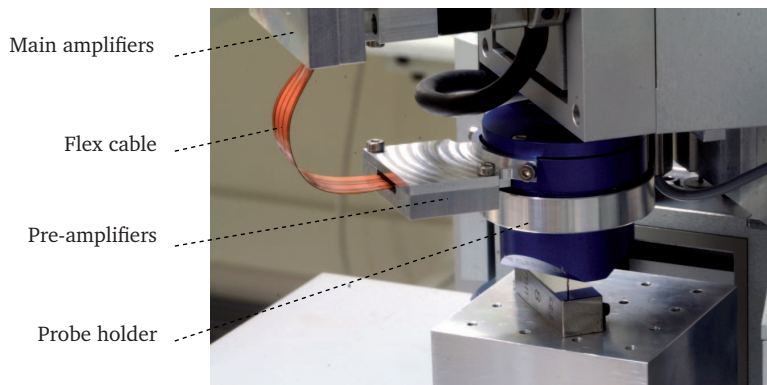


Figure 2.55: Photo of the redesigned probe, as discussed in chapter 3, with electronics.

To minimize signal noise, e.g. due to environmental electromagnetic radiation, the pre-amplifiers are positioned close to the probe holder, as shown in figure 2.55. The heat produced by the pre-amplifiers is approximately 4 mW. Only a fraction of this heat is transferred to the probe holder.

Once equilibrium is obtained, it is expected that the temperature variations in the chip are below 10 mK. Since self heating introduces a repeatable and constant offset its contribution to the measurement uncertainty for the probe, as discussed in this thesis, can be neglected.

In the original design by Pril [Pril 02] the materials used in the probe show large variations in the coefficient of thermal expansion α , e.g. for aluminum $\alpha = 23.2 \cdot 10^{-6} \text{ K}^{-1}$ and for silicon $\alpha = 4.2 \cdot 10^{-6} \text{ K}^{-1}$ at 293 K. To reduce thermal stresses in the design, the materials used in the redesign are thermally matched, as discussed in chapter 3.

To measure the drift of the probe, two separate setups are used, as shown schematically in figure 2.56. The setup is placed in a temperature controlled laboratory, where the maximum temperature variation is measured to be 1 K. To reduce the influence of thermal variations the setup is placed inside an isolation box. The maximum temperature variation inside the isolation box during a typical measurement is measured to be 30 mK. The maximum temperature variation in the probe

⁴With respect to the thermal design the system by Pril and the redesign show significant differences. Pril uses a supply voltage of 1 V and a resistance of about 10 k Ω in his model. Also, thermal barriers are greatly reduced in the redesign, allowing better heat dissipation. The close agreement between the results is therefore coincidental.

itself is less than 10 mK. A similar result was obtained by Ruijl [Ruijl 01], who obtained a reduction in temperature variations of a work piece relative to environmental temperature variations by a factor of 1000 with the use of thermal shielding and an enclosure.

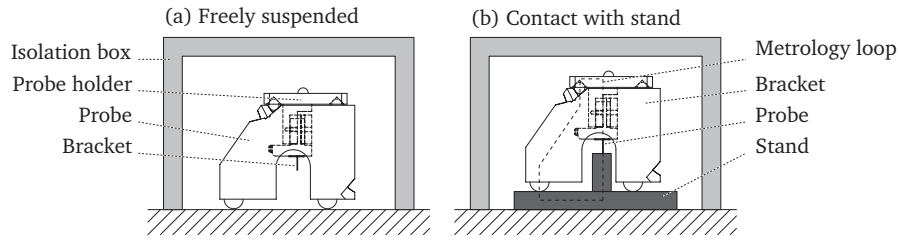


Figure 2.56: Schematic of the setup used to measure the probe drift, (a) probe is freely suspended, (b) probe is in contact with a stand.

In the left hand picture, the probe is not in contact with the work piece. In this setup the drift in the measurement signal due to electronics and the silicon chip can be analyzed. For the probe, discussed in this thesis, the result of a drift measurement with a freely suspended probe over a 50 hour period is shown in figure 2.57.

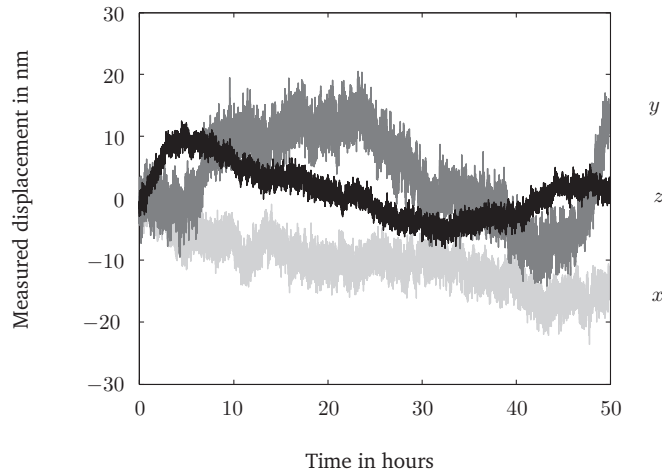


Figure 2.57: Drift in x , y and z -direction of a freely suspended probe over a period of 50 hours.

It can be seen that the mean drift is less than 2 nm per hour. Assuming a measurement time of 30 minutes, the maximum deviation due to thermal deformations, i.e. the worst case drift, is 10 nm.

Thermal drift in the second setup, shown in figure 2.56 (b), results from drift in electronics and drift in the thermal loop through the stand, bracket, probe holder and stylus, as indicated in this figure. The measurement result for this setup is shown in figure 2.58. It can be seen that the drift measurements shown in figures 2.57 and 2.58 are in the same order of magnitude. However, as discussed in appendix E.3, it is possible for thermal variations in different sections of the metrology loop to cancel each other out, figures E.4 and E.5. Looking at figure 2.56 (b) it can therefore be seen that the expansion of the stylus and probe holder is partly compensated by the expansion of the bracket and stand.

The influence of an expansion of stylus and probe holder is therefore estimated using equation E.1. For a steel stylus with $l_0 = 6.8$ mm and $\alpha = 10 \cdot 10^{-6} \text{ K}^{-1}$ and an Invar probe holder with $l_0 = 30$ mm and $\alpha = 4 \cdot 10^{-6} \text{ K}^{-1}$, a temperature variation of 10 mK will result in a total expansion of 2 nm.

The second point of interest is the long term stability of the probe. As mentioned in appendix E.3, the long term stability of the probe is influenced by changes in its sensitivity, e.g. due to

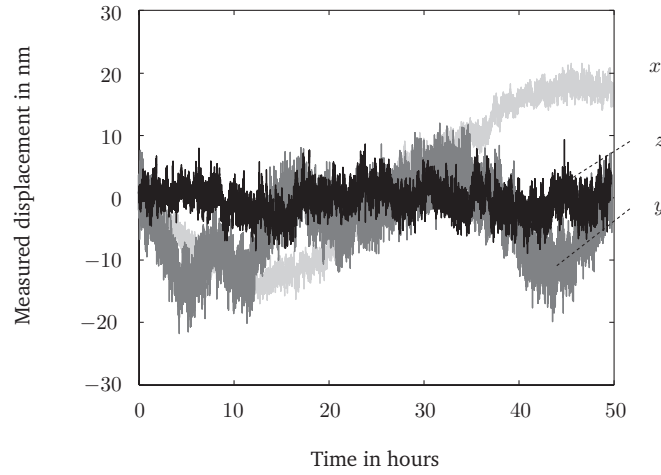


Figure 2.58: Drift of the probe in contact with the stand over a period of 50 hours.

thermal fluctuations. For the probe, discussed in this thesis, the displacement of the probe tip is measured using piezo resistive strain gauges. These are deposited on each of the three slender rods in the probe suspension, as discussed in appendix A. A transformation matrix \mathbf{A} is used to give the relation between the measurement signal from the strain gauges on the slender rods and the displacement of the probe tip, as shown in equation 1.3.

Changes in the transformation matrix \mathbf{A} of a particular probe influence its measurement behavior and hence its measurement uncertainty. It is therefore important that the transformation matrix \mathbf{A} remains constant in-between two successive calibrations, i.e. long term stability is required. Figure 2.59 shows the drift in the sensitivities of all three rods during a 16 hour measurement. The standard deviation in the sensitivity coefficients in this measurement is $8 \cdot 10^{-11}$ V/nm which corresponds to a deviation of 2 nm over a 10 μm measurement.

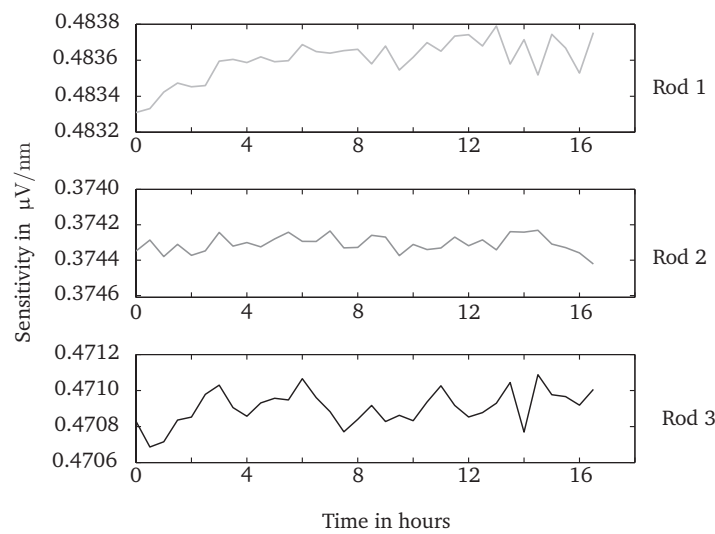


Figure 2.59: Measured sensitivities of the three strain gauges during a 16 hour measurement.

2.5 Assembly and hysteresis

All precision probes discussed in section 1.4 consist of multiple parts and hence require assembly. The main influence on the behavior of the probe results from deviations introduced by assembly and hysteresis as a result from the connection between components.

2.5.1 Deviations in assembly

First, the influence of assembly and manufacturing deviations on the measurement behavior is discussed. Most ultra precision coordinate measuring machines are constructed in such a way that they obey the Abbe principle [Ruijl 01, Vermeulen 99]. The Abbe principle was first published in 1890 and states [Abbe 90]:

The measuring instrument is always to be constructed that the distance being measured is a straight line extension of the graduations on the scale that serves as a reference...

As a restatement to cover those situations where it is not possible to design 'in line', Bryan defined a generalized Abbe principle as [Bryan 79A, Bryan 79B]:

A displacement measuring system should be in line with the functional point (i.e. center of stylus ball or tool tip) whose displacement is to be measured. If this is not possible either the slide ways that transfer the displacement must be free of angular motion, or angular motion data must be used to calculate the consequences of the Abbe offset.

This can be understood by looking at figure 2.60. When the probe housing moves in x -direction it experiences a rotation R_z around the z -axis due to deviations in the guide ways. As a result of this displacement, the distance as measured by the scales and the true displacement of the probe tip differs by a length of Δx , where:

$$\Delta x = h_x R_z \quad (2.77)$$

Where h_x is the Abbe offset.

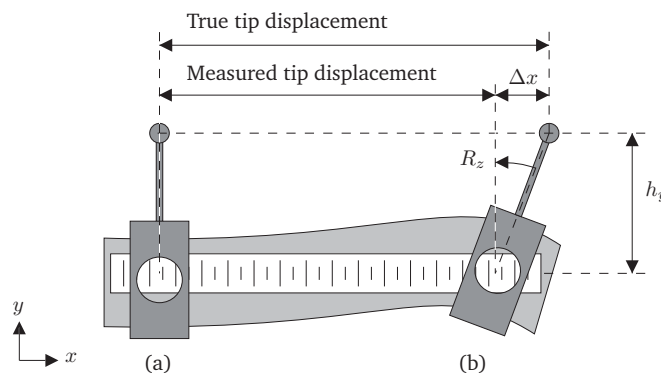


Figure 2.60: Schematic of the Abbe deviation Δx .

To provide an indication of this error, the angular deviation R_z in a guide way is estimated to be 0.1 mrad for precision roller bearings, and 0.25 μ rad for precision air bearings. The allowed Abbe offset $h_{x,max}$ for a deviation Δx of 5 nm or less is shown in table 2.9.

Therefore, the allowed deviation in the structural loop between the probe tip and the measurement system of a CMM using roller bearings should be less than 50 μ m. This includes manufacturing and assembly deviations of both the CMM and the probe. As the assembly and manufacturing of precision probes typically involves the handling of small and fragile components the contribution

	R_z	$h_{x,max}$
Roller bearing	0.1 mrad	50 μm
Air bearing	0.25 μrad	20 mm

Table 2.9: Estimation of the allowed Abbe offset for precision roller and air bearings.

of deviations as a result of assembly of the probe can be significant. One possibility is to use of an mechanism to align the probe tip with the measurement systems and thereby adjusting for these deviations. However, such a mechanism may influence the measurement uncertainty and behavior in the structural and/or metrology loop of the CMM.

Deviations in the position of the probe tip relative to the suspension also influence the stiffness, as discussed in appendix D. This will result in anisotropic effects during a measurement, as discussed in section 2.3.6. For the probe discussed in this thesis, the contribution of deviations in the tip position to the stiffness is less than 3% for all directions.

2.5.2 Hysteresis

In the previous sections the finite stiffness of the probe, CMM and work piece are discussed. The contact force between tip and work piece thus results in a deformation of all elements in the structural loop through the CMM between probe tip and work piece. As the contact force changes during a probing operation the elements experience different deformations. If these deformations are not purely elastic, i.e. energy is adsorbed as a result of the deformation, the measurement is influenced by hysteresis. Typically the method used to connect the different parts of the metrology loop during assembly greatly influences the hysteresis effect.

With respect to the probe discussed in this thesis, the two main contributions to hysteresis are the connection of the chip to the probe holder and the presence of glue layers in the probe. First the connection of the chip in its holder is discussed.

Several variants have been manufactured to test the influence on hysteresis of the chip connection [Heldens 05, Widdershoven 04]. In the first design, shown in figure 2.61 (a), the chip is glued into the holder using a high stiffness epoxy compound. The design is such that a small clamping force exists between the chip and holder in radial direction. As a result the glue layers to the side of the chip are very thin. Using a high stiffness glue and minimizing the layer thickness results in a design with neglect able hysteresis, as shown by the residuals in figure 2.61 (b) for a measurement in direction **b**. The measurement directions are shown in figure A.1. The residuals for x and y are shifted by 40 and 20 nm respectively to improve readability. The measurement deviations of the probe are measured using the setup described in section 1.6.1 and the measurement method is described in appendix A.3. The measurement results discussed in this section are all compensated for the rolling effect, as discussed in section 2.2.1.

The hysteresis in the measurements is quantified using the hysteresis percentage H , defined by:

$$H = \frac{V_h}{V(x_{max}) - V(0)} \cdot 100\% \quad (2.78)$$

Here, V_h is the distance between the curves for the forward and backward movement of the probe, $V(0)$ is the voltage measured at the start of the measurement for each slender rod and $V(x_{max})$ is the maximum voltage measured during the measurement. This is schematically shown in figure 2.62.

For probe 1, shown in figure 2.61, the hysteresis percentage H is 0.1% or less for all slender rods. For most strain gauge applications the method of mounting of the strain gauges, e.g. using glue, may greatly increase the hysteresis percentage. A strain gauge which is properly installed should have a hysteresis of less than 0.2% [Window 92]. Other possible contributions to the hysteresis

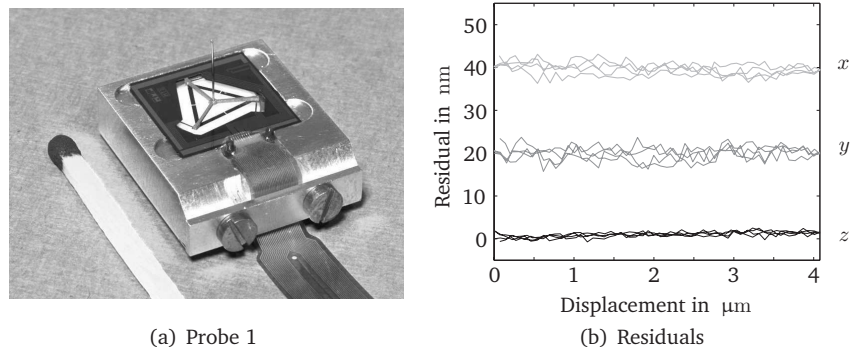


Figure 2.61: Original probing system as developed by Pril [Pril 02]: (a) Photo, (b) Residuals in x , y and z for a measurement in direction \mathbf{b} .

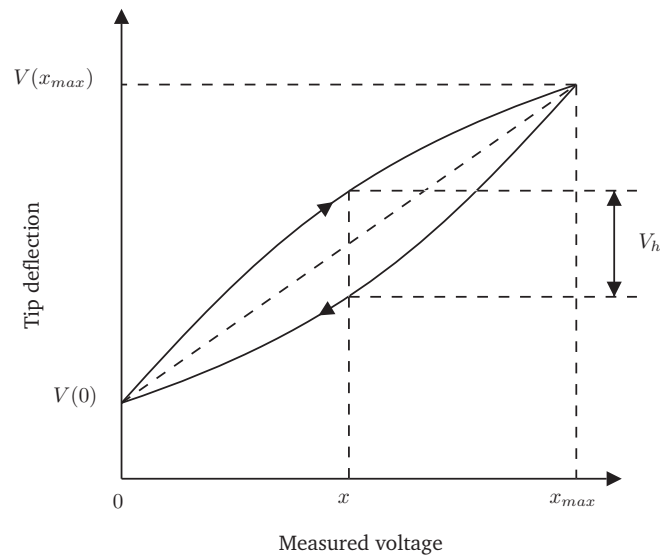


Figure 2.62: Hysteresis during probing measurement.

in this design include the influence of visco-elastic adhesives used during assembly of the probe [Ferry 80, Jones 06] and static charges in the probe chip [Wu 04]. Several alternative probes were manufactured to test the influence of the connection between chip and holder on the hysteresis in the design. These will be discussed in the remainder of this section.

For the second design, figure 2.63, the chip is glued between three orthogonal planes on the holder. As a result the thickness of the glue layer between chip and holder was increased. Also, the Young's modulus of the glue used was low compared to the glue used in figure 2.61 (a).

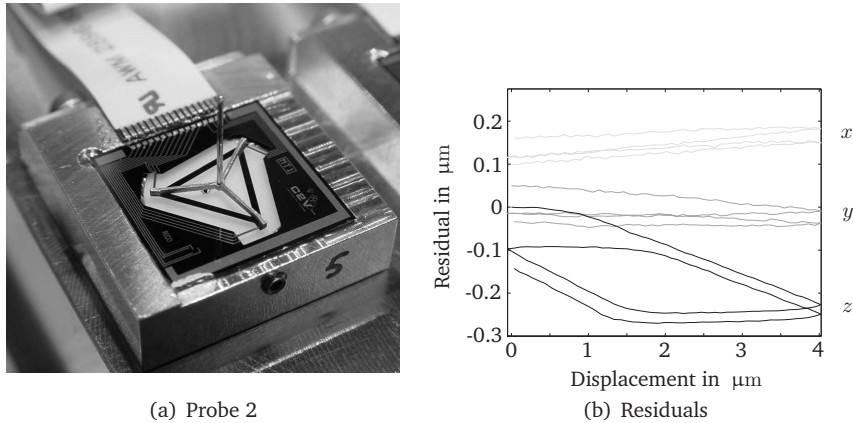


Figure 2.63: Probe 2 with chip glued between three orthogonal planes:
(a) Photo, (b) Residuals in x , y and z for a measurement in direction **b**.

Measurement direction **b**, used for the measurements, is in the xy -plane of the probe, away from the three orthogonal planes in the chip holder. Therefore the glue layer, used to fixate the chip, is loaded as a result of the contact force between the probe tip and work piece. The adsorbed energy as a result of deformations in the glue layer result in hysteresis, as shown in figure 2.63. The hysteresis percentage H for this direction is 0.5%.

From this graph it can also be seen that the measurement results are influenced by drift of the probe tip, caused by creep in the glue layer. The drift in the measurement signal for the three slender rods during a 3.5 hour measurement is shown in figure 2.64. As a result of the design of the probe holder, shown in figure 2.63, the deformation of the glue layer is lower in the measurement directions **a**, **c** and **d**. As a result the hysteresis percentage H in these directions is 0.25% or less and creep is reduced.

As a variation on the design of probe 2, the same holder and assembly method were used to manufacture another probe, hereafter referred to as probe 3. The only difference with probe 2 is a solder point in one corner of the chip. This solder point can be seen in the bottom corner of the chip shown in figure 2.63 (a). The residuals for a measurement in direction **b** with this probe are shown in figure 2.65. It can be seen that hysteresis and creep are reduced considerably.

To test the influence of micro friction in the contact when the chip is clamped into the holder, a new holder is manufactured as shown in figure 2.66. Hysteresis in this design is caused by micro friction in the contact between chip and holder. As expected, the contribution of micro friction in subsequent measurements decreases when the contact pressure increases.

Also, when micro friction plays a role in the contact between chip and work piece, an initial creep is observed caused by a progression of the point of slip in the contact. Once tangential forces decrease, the slip region is enveloped by the central stick region of the contact. As a result tangential stresses are present in the contact region. In practice, the tangential stress in the contact region is the result of the maximum tangential force in the contact up to that point in time. Creep due to micro slip is therefore not observed in subsequent measurements unless the point of slip exceeds the maximum point of slip experienced by the contact.

These effects were clearly observed in the measurements. Figure 2.66 (b) shows the residuals for

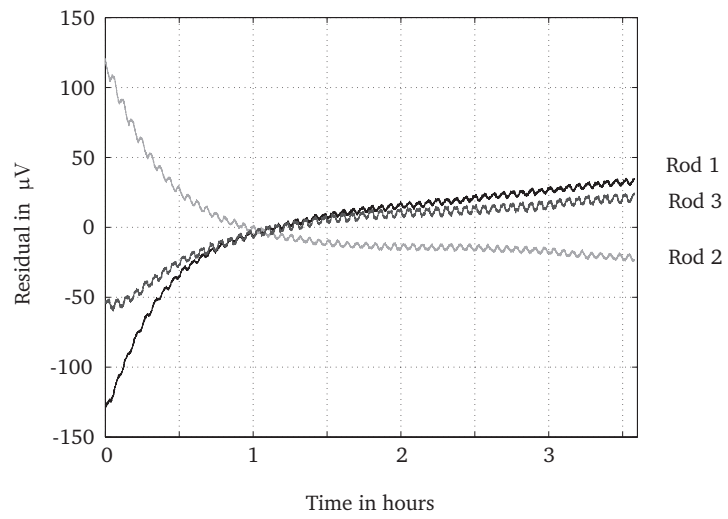


Figure 2.64: Drift in the measurement signal from the piezo resistive strain gauges on the three slender rods of probe 2.

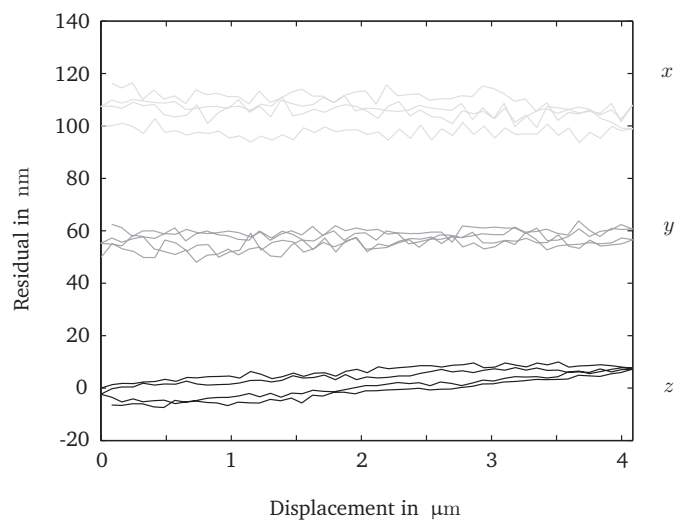


Figure 2.65: Residuals for probe 2, with solder point.

a measurement in which the probe tip was not displaced beyond the maximum displacement of the tip up to that point in time. Also, the contact pressure was sufficient to reduce the hysteresis percentage to less than 0.1%.

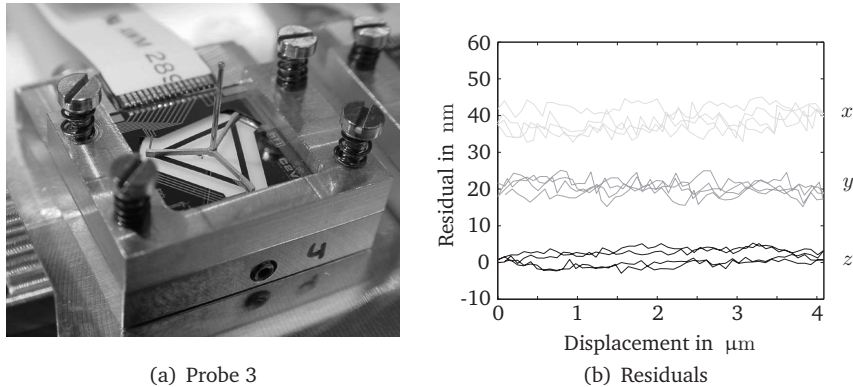


Figure 2.66: Probe 3 with chip clamped onto holder: (a) Photo, (b) Residuals in *x*, *y* and *z* for a measurement in direction **b**.

Finally, the influence of glue in the design is illustrated by the probe as shown in figure 2.67. The connection between the chip and holder is created in the same way as the probe shown in figure 2.61 (a), which showed a hysteresis percentage of 0.1% or less for all slender rods. The main difference between both designs is the use of a globtop, e.g. a droplet of glue to protect the wirebonds between the chip and flex cable. The polymer used as an adhesive for the globtop and probe assembly is expected to show visco-elastic behavior. Hence, hysteresis is expected to occur when the glue layers and visco-elastic material is subject to an increasing and decreasing load [Ferry 80, Jones 06].

The residuals for this probe for a measurement in direction **b** are shown in figure 2.67 (b). The hysteresis percentage for the rods vary between 0.4 and 2.2%, which is considerable. Also, creep is observed in the measurements. The effect is investigated using finite element simulation. It was calculated that the maximum displacement of the membrane, at the position of the globtop, was approximately 200 nm, which could cause the hysteresis. Measurements with an identical probe, but with the globtop removed, confirm the hypothesis that the globtop is responsible for the observed effects.

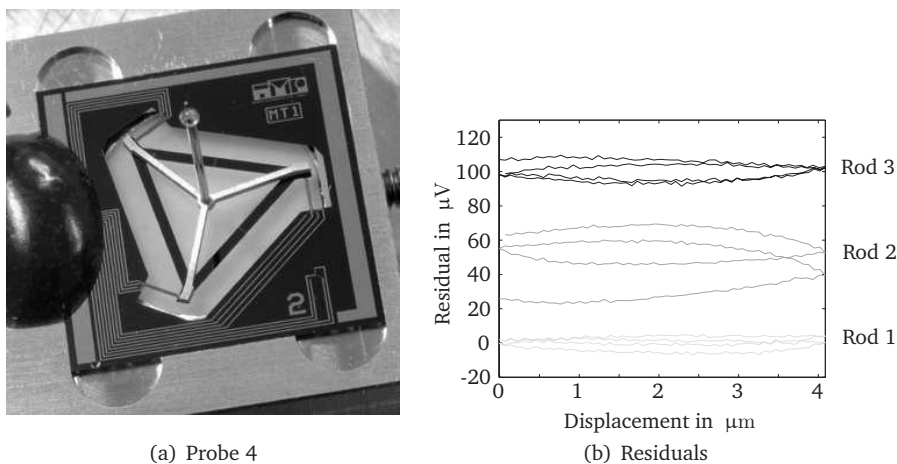


Figure 2.67: Probe 4 with globtop to protect wire bonds between flex cable and chip: (a) Photo, (b) Residuals in *x*, *y* and *z* for a measurement in direction **b**.

2.6 Conclusions

As mentioned at the start of this chapter, the problems associated with the interaction between the probe tip surface and a work piece become increasingly apparent as the scale of the measurement decreases. This includes plastic deformation in the tactile contact between a probe tip and a measurement surface. To avoid plastic deformation when probing a planar aluminum work piece with a sapphire probe tip with a radius of $150\text{ }\mu\text{m}$ at an approach speed of 1 mm/s , the equivalent mass and stiffness at the probe tip should be below 35 mg and 354 N/m , respectively.

As the contact region during probing approaches the grain size of the work piece material the effective Young's modulus typically increases, decreasing plastic deformation. Also, the mechanical properties at the surface of a material may be influenced by surface segregation and oxide layers.

However, the probing force is also influenced by collision dynamics. For low damped probes with an eigen frequency above 100 Hz the maximum contact force can be a factor of 3 higher than the contact force during the initial collision. The maximum contact force for these systems is a combination of over travel and impact forces. The effect of an increasing contact force in subsequent collisions can be avoided by using a probing system with a low eigen frequency. However, this also increases the settling time and hence the measurement time.

It is noted that plastic deformation on a micro scale can never be avoided completely due to the effects of surface roughness. The compliance between rough surfaces, i.e. with a root-mean-square (rms) surface roughness of 50 nm , can easily be an order of magnitude higher than the compliance between perfectly smooth surfaces.

A main aspect of the interaction between the probe tip and work piece is the effect of surface forces during probing. These forces arise primarily from van der Waals, electrostatic and hydrostatic forces. The balance between these forces depends on the environmental conditions, especially humidity, surface condition, material and relative motion. A typical value for the van der Waals force between a perfectly smooth planar aluminum work piece and a sapphire probe tip with a radius of $250\text{ }\mu\text{m}$ is $62\text{ }\mu\text{N}$. When a peak-to-peak roughness of 5 nm is assumed, the van der Waals force is reduced to about $1.2\text{ }\mu\text{N}$.

The electrostatic force greatly depends on the buildup of charge on the probe tip and work piece, e.g. as a result of friction during scanning. At atmospheric pressure and a gap in the order of centimeters the maximum charge density is limited to about $3 \cdot 10^{-5}\text{ C/m}^2$. This results in an electrostatic force of $80\text{ }\mu\text{N}$ for this contact. However, in most applications the charge density and the corresponding electrostatic adhesion will be considerably lower.

The final surface force under consideration is hydrostatic adhesion, caused by the adsorption of water molecules on the surface of the probe tip and work piece. Depending on material, temperature and relative humidity the thickness of the adsorbed layer is typically between a tenth and several tens of nanometers. In general, the hydrostatic attraction will show a monotonic increase with an increasing relative humidity and will decrease when the surface roughness increases. Using again the situation of a planar aluminum work piece against a sapphire probe tip with a $250\text{ }\mu\text{m}$ radius, a hydrostatic attraction of 0.23 mN is calculated.

The surface force between the probe tip and work piece also influences the measurement behavior of the probing system. Surface forces increase the stick slip during scanning and the release distance, or snap out distance, during single point probing. As surface forces are typically disturbing to the measurement measures can be taken to reduce their magnitude, e.g. selecting an optimum stiffness of the probe suspension for a given tip radius. It is calculated that the stick slip during scanning and the release distance of the tactile 3D probing system is about 0.15 and $0.25\text{ }\mu\text{m}$, respectively.

An important challenge when measuring miniaturized components is that the required measurement uncertainty is high, typically 100 nm or less. As a result many aspects that are neglected in conventional probing applications become of interest. This includes vibrations of the probe tip as a result of floor vibrations and acoustic excitation. For the tactile 3D probing system as discussed in this thesis the influence of these excitations on the measurement uncertainty is in the order of 0.1 nm and can be neglected.

Another aspect of the required measurement uncertainty is the influence of roundness and diameter of the probe tip on the measurement uncertainty. Measurements of the roundness and diameter of the tip are discussed in the previous chapter. However, as a result of wear and the collection of dust and debris on the tip surface the shape of the probe tip changes. For the probing system under consideration the wear of the probe tip, which is highest during scanning, is expected to be $\ll 1$ nm per 1 meter scan length.

It is noted that in the tactile 3D probing system, a deformation of the probe suspension is required to measure the tip displacement. Therefore the relative stiffness of the suspension and stylus influences the measurement behavior. To use small probe tip radii, the radius of the stylus and thereby the stiffness of the stylus needs to be reduced as well. As a result, when a decrease in sensitivity of a factor of 4 is acceptable, the minimum tip radius for a measurement length of 500 μm is 11 μm . It is noted, that a reduced resolution makes the probing system more susceptible to noise but does not directly influence its measurement uncertainty.

During measurements with the tactile 3D probing system in the xy -plane, the measurement signal shows a linear increasing displacement in z -direction. This displacement is repeatable and is caused by the rotation of the center platform in the probe suspension when probing in the xy -direction. This displacement is measured by the probing system and does not contribute to the measurement uncertainty.

However, this displacement in z -direction when probing in the xy -plane is influenced by the anisotropic stiffness of the probing system, e.g. due to the anisotropic Young's modulus in silicon. In the tactile 3D probing system, the chip design is therefore compensated for these effects and an isotropic stiffness is obtained at the probe tip when the stylus length is 6.8 mm, as will be discussed in the next chapter.

Finally, it is shown in this chapter that a mechanical clamping of the probe chip in a holder is feasible. However, the connection should be carefully designed to minimize the effects of creep and hysteresis during a measurement.

Chapter 3

Probe Development

3.1 General Design Considerations

The redesign of the probe will be discussed in this chapter. First specifications are discussed, then the design will be introduced using optimization models, experimental results and simulations.

3.1.1 Specifications

Specifications for the original design by Pril [Pril 02] are stated in appendix A. From chapter 2 some additions and modifications can be stated for the probe redesign:

1. Overall 3D repeatability during single point probing should be smaller than 20 nm, assuming a thermal stability of ± 0.1 K (update on requirement 1);
2. Probe tip should be visible to a camera at an angle of 60 degrees or less (update on requirement 4);
3. Time needed to take a measurement during single point probing should be less than 100 ms (update on requirement 6);
4. Measurement frequency during scanning should be 1 kHz or higher (addition to requirement 6);
5. When plastic deformation to the probe occurs, e.g. due to a control error, replacement costs should be reasonable compared to other cost factors, implying a maximum replacement cost of 3k Euro (addition to requirement 9);
6. Colliding mass should be less than 35 mg to avoid plastic deformation of an aluminum work piece during a collision with a 1 mm/s approach speed and a 150 μm tip radius (modification on implicit requirement 1);
7. The stiffness at the probe tip should be approximately 500 N/m when using a probe tip with a 250 μm radius and 350 N/m when using a probe tip with a 150 μm radius (modification on implicit requirement 2);
8. Over travel distance, at which plastic deformation to the probe suspension initiates, should be 200 μm or more (update on implicit requirement 4);

9. The eigen frequency of the probing system should be above 200 Hz to avoid resonance due to the control frequency of the coordinate measuring machine (additional requirement);
10. Stiffness at the probe tip should be the same in all directions (additional requirement).

3.1.2 Sensitivity of the probe

Tip deflection is measured using four piezo resistive strain gauges in a Wheatstone bridge configuration, as discussed in section 1.5. When the gauges are subjected to a strain ε , the relative resistance $\Delta R/R$ changes, according to [Middelhoek 89]:

$$\frac{\Delta R}{R} = G\varepsilon = G \frac{\Delta l}{l} \quad (3.1)$$

Where $\Delta l/l$ is the strain in the gauge and gauge factor G is given by [Elwenspoek 01]:

$$G = (1 + 2\nu + \pi_l E + \nu \pi_t E) \quad (3.2)$$

Where ν is the Poisson ratio, E the Young's modulus of the piezo resistive material and π_l and π_t are piezo electric coefficients in the longitudinal and transversal direction of the gauge, respectively. piezo electric coefficients are determined only by the type and physical characteristics of the semiconductor material [Window 92].

From equation 3.2 it can be seen that gauge factor G is influenced by two effects. First the change of geometry, indicated by $(1 + 2\nu)$, of the strain gauge. This effect is present in all materials and accounts for a gauge factor G between 1.6 and 2, depending on the Poisson ratio ν . The second effect is change in specific resistance of the material, indicated by $(\pi_l E + \nu \pi_t E)$. Change in specific resistance, often referred to as piezo resistive effect, results in a gauge factor between 100 and 175 for single-crystalline p-type silicon and -100 to -140 for n-type silicon. A typical value for polycrystalline and amorphous silicon is 30 [Middelhoek 89, Window 92].

Probe sensitivity for a tip displacement in z -direction, i.e. in the length direction of the stylus, is now discussed using the model of a simple cantilever with length l , width w and thickness t , as shown in figure 3.1. Using standard elastic theory, moment $M(x)$ at position x is given by:

$$M(x) = F(l - x) - M_B \quad (3.3)$$

$$M_B = \frac{1}{2}lF$$

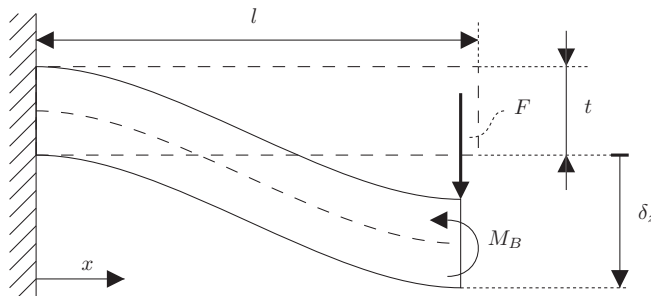


Figure 3.1: Simple model of a cantilever.

The force F required to displace the end of the cantilever by a distance δ_z is given by:

$$F = \frac{12EI}{l^3} \delta_z \quad (3.4)$$

Assuming a state of uniaxial normal stress in the cantilever, the longitudinal stress σ_{xx} at a height $t/2$ above the neutral surface, i.e. top surface, is given by:

$$\sigma_{xx} = \frac{M(x) \frac{t}{2}}{I} \quad (3.5)$$

Combining equations 3.3, 3.4 and 3.5 yields:

$$\sigma_{xx} = \frac{12E}{l^3} \left(\frac{1}{2}l - x \right) \frac{t}{2} \delta_z \quad (3.6)$$

Maximum longitudinal stress $\sigma_{xx,max}$ is obtained when $x = 0$ or $x = l$ and is given by:

$$\sigma_{xx,max} = \frac{3Et}{l^2} \delta_z \quad (3.7)$$

The relative resistance change $\Delta R/R$ as a function of tip displacement in z -direction for a single strain gauge is now given by:

$$\frac{\Delta R}{R} = G \frac{3t}{l^2} \delta_z \quad (3.8)$$

As discussed in section 1.5 and shown in figures 1.19 and 1.20, four piezo resistive strain gauges are deposited on each slender rod in a Wheatstone bridge configuration. The measured voltage V_m across the Wheatstone bridge is a function of resistance of the four piezo resistive strain gauges, R_1, R_2, R_3 and R_4 , and supply voltage V_0 , according to [Elwenspoeck 01]:

$$V_m = \frac{R_1 R_4 - R_2 R_3}{(R_1 + R_3)(R_2 + R_4)} V_0 \quad (3.9)$$

In most Wheatstone bridge configurations all resistor values, are chosen equal to each other, i.e. $R_1, \dots, R_4 = R_0$, resulting in a zero output voltage V_m . When resistance changes are small, i.e. $\Delta R \ll R$, the measured voltage changes approximately linear with $\Delta R_1, \dots, \Delta R_4$:

$$V_m \approx \frac{\Delta R_1 - \Delta R_2 - \Delta R_3 + \Delta R_4}{4R_0} V_0 \quad (3.10)$$

It can be seen that the measured voltage V_m is unaffected by disturbances that affect all resistors equal, e.g. homogeneous temperature deviations.

Assuming that all strain gauges exhibit an equal response to displacement δ_z , and combining equation 3.10 with equation 3.8 yields:

$$V_m \approx G \frac{3t}{l^2} V_0 \delta_z \quad (3.11)$$

It should be clear that sensitivity of the probe, equation 3.11, and maximum longitudinal stress $\sigma_{xx,max}$, equation 3.7, for a given displacement δ_y are both proportional to t/l^2 . Therefore, optimum sensitivity is always a balance between allowed over travel distance at which plastic deformation to the probe suspension initiates and required sensitivity.

Requirement 8, as stated in section 3.1.1, states a minimum over travel distance of 200 μm . Since silicon is a brittle material, its mechanical properties can vary significantly as a function of the processing conditions and structure dimensions [Jadaan 03]. The average fracture strength as stated in literature thus varies between 0.57 GPa, as tested on a specimen with a 2 μm thickness [Greek 97], and 4.9 GPa [Ballarini 98]. From literature, a value of 1 GPa is used as a relative safe value for the fracture strength of the slender rods [Bagdahn 02, Ding 01A, Ding 01B, Greek 99, Jadaan 03, Sharpe 01].

Using $\delta_z = 200 \text{ } \mu\text{m}$, $\sigma_{xx,max} = 1 \text{ GPa}$ and $E = 168.8 \text{ GPa}$, appendix D.3, equation 3.7 yields:

$$\frac{t}{l^2} \approx 10 \quad (3.12)$$

Combining this result with equation 3.4 yields for the stiffness of the slender rod c_r :

$$c_r = \frac{F}{\delta_z} \approx \frac{Ewt^3}{l^3} = \sqrt{1000}Ewt^{\frac{3}{2}} \quad (3.13)$$

Thus, given the requirement in equation 3.12, minimum probe stiffness is obtained when width w and thickness t are minimized. The main limitations to decreasing slender rod size are given by the manufacturing process. The minimum width w in the current manufacturing process is limited to approximately $160 \text{ } \mu\text{m}$. This results from the minimum width of the piezo resistive strain gauges, the aluminum connection tracks and space between tracks of the Wheatstone bridge circuit on the slender rods.

As discussed in sections 2.1.4 and 2.3.1, stiffness of the probe should be optimized for a specific measurement task and tip radius. Thickness t is used to control probe stiffness, since it is relatively simple to adjust it during processing, e.g. by choosing a SOI-wafer with a different device layer thickness. For practical reasons, the minimum thickness t for probe systems with a $250 \text{ } \mu\text{m}$ tip radius is therefore set to $30 \text{ } \mu\text{m}$. Using equation 3.12 this results in a rod length l of 1.7 mm . Rod dimensions in the probe are therefore given by $l = 1.7 \text{ mm}$, $w = 160 \text{ } \mu\text{m}$ and $t = 30 \text{ } \mu\text{m}$. Using equation 3.4 with $E = 168 \text{ GPa}$ results in a stiffness of a slender rod c_r of 140 N/m .

Finally, combining equation 3.12 with equation 3.11 and using $G = 30$ yields:

$$V_m \approx 900V_0\delta_z \quad (3.14)$$

From this equation it can be seen that by increasing supply voltage V_0 the signal, and thereby the signal to noise ratio, improves. However, by increasing the supply voltage, power dissipation in the slender rods also increases, as will be discussed in the next section.

3.1.3 Supply voltage and signal amplification

As discussed in the previous section, supply voltage V_0 to the Wheatstone bridge influences signal V_m , equation 3.14, and the power dissipated in the slender rods. As discussed in section 2.4 power dissipated in the slender rods causes a temperature rise of the probe system. Since the supply voltage is constant, equilibrium will be obtained and its influence on measurement uncertainty can be neglected.

For practical reasons an upper limit to the total power dissipation in the silicon chip is used of 2 mW , i.e. $170 \text{ } \mu\text{W}$ per strain gauge. Recalling equation 2.76, power dissipation P in a resistor with resistance R due to a supply voltage V_0 is given by¹:

$$P = \frac{V_0^2}{R} \quad (3.15)$$

For a maximum admissible power dissipation P of $170 \text{ } \mu\text{W}$ per strain gauge, supply voltage V_0 can be increased when the strain gauge resistance increases. As shown by equation 3.14 this increases measurement signal V_m for a given displacement δ_z .

However, Johnson noise [Johnson 28], also referred to as thermal noise, also increases when resistance R is increased:

¹By switching the power supply on and off during operation, the supply voltage V_0 can be increased for a given power consumption. However, the INA-118 amplifier used requires a settling time of 2 ms . Therefore switching power on and off is not practical with the INA-118, when operating at the required measurement frequency of 1 kHz . Implementation of a switching power supply is therefore not used in the current version of the probe system.

$$V_n = \sqrt{4KTRB} \quad (3.16)$$

Where V_n is noise voltage in V, T is temperature in K, R is resistance in Ω , B is bandwidth in Hz and K is the Boltzmann constant, i.e. $K = 1.38 \cdot 10^{-23}$ J/K.

Contributions of environmental noise, e.g. from a fluorescent tube, are less dependent on supply Voltage V_0 or resistance R . Therefore, with respect to these disturbances signal-to-noise ratio will improve when supply voltage V_0 and resistance R are increased.

By increasing resistance R of the piezo resistive strain gauges, supply voltage V_0 may thus be increased for a given power dissipation in the piezo resistive strain gauges. The signal-to-noise ratio of the INA-118 pre-amplifiers is measured as a function of total resistance of the Wheatstone bridge. It was found that an optimum signal-to-noise ratio with this amplifier is obtained when resistance R of the piezo resistive strain gauges is 50 k Ω . A maximum admissible power dissipation P of 170 μ W per strain gauge thus results in a maximum supply voltage V_0 of 5.8 V.

Using equation 3.14 with a supply voltage V_0 of 5 V results in a measurement signal of 4.5 μ V/nm. A displacement of 10 μ m, the measurement range, thus results in a signal of 45 mV. Ideally, probe electronics should produce a signal of 10 V when the probe tip is displaced by 10 μ m, i.e. measurement range of the probe. This requires the measurement signal across the Wheatstone bridge to be amplified 220 times, which is possible using an INA-118 amplifier operating at 1 kHz, the required measurement frequency. This results in an output signal of 1 mV/nm.

3.2 Layout of the chip

A top-view of the probe by Pril [Pril 02] is shown in figure 3.2. It can be seen that the chip outline is square. When slicing a wafer to release devices straight cutting lines are needed. Hence a square outline is used in many silicon MEMS components. However, due to the fragile nature of the probe, slicing is not possible and hence chips are broken out of the wafer. A square outline is therefore not a requirement anymore and other chip shapes can be considered.

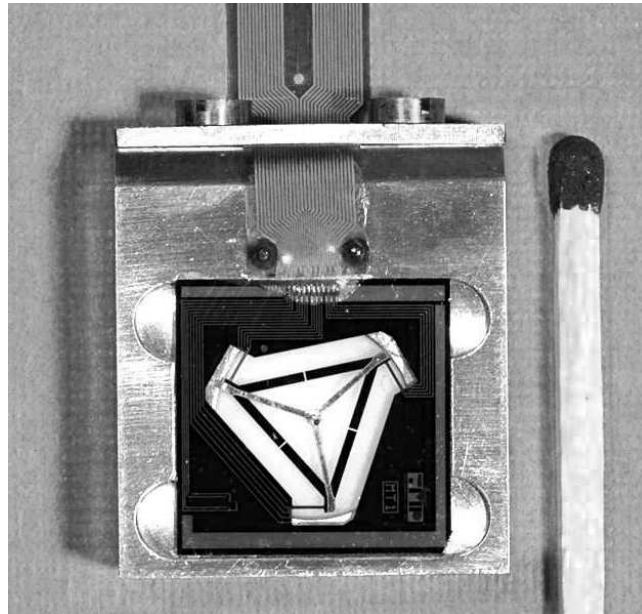


Figure 3.2: Top view of original probe by Pril [Pril 02].

From figure 3.2 it can be seen that the functional part of the chip shows a threefold symmetry. For optimum use of material a triangular outline or a six-corner polygonal outline is therefore preferred. A drawback of a polygonal shape with six edges is that it has three internal degrees of

freedom in the plane of the chip. As discussed in appendix E.2 these degrees of flexibility reduce the stiffness of the design during handling and therefore a triangular outline is preferred.

To obtain an isotropic stiffness at the probe tip, the slender rod position on the probe chip is optimized for a triangular area of the chip. This is shown schematically in figure 3.3.

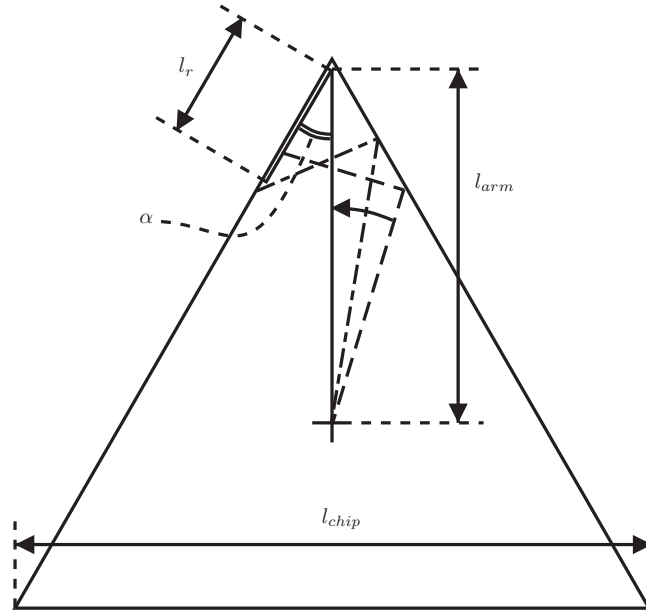


Figure 3.3: Schematic of the position of the slender rods within the chip.

In the optimization process the rod length is set to 1.7 mm, as discussed in section 3.1.2 and angle α between slender rod and arm of the central platform is varied. Arm length l_{arm} thus varies when the angle α changes. The effect of slender rod position on probe stiffness in xy - and z -direction is analyzed using finite element simulation. The resulting stiffness at the probe tip in x -direction, c_x , and in z -direction, c_z , is shown in figure 3.4 as a function of angle α .

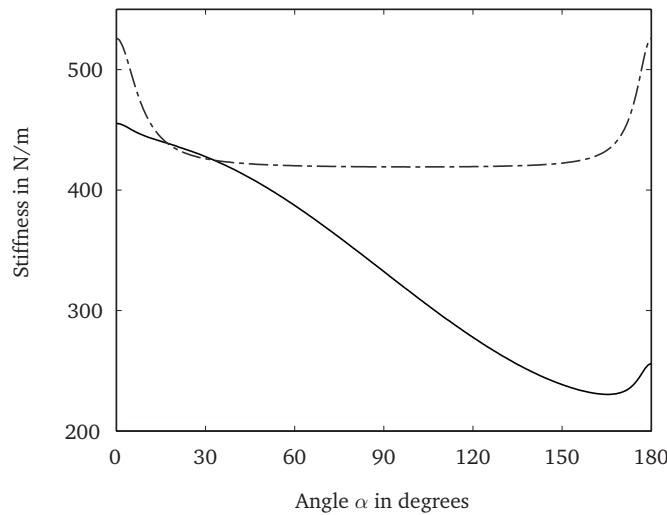


Figure 3.4: Stiffness c_x and c_z at the probe tip as a function of angle α between slender rod and arm in the center platform.

It is noted that when $\alpha = 0$ and $\alpha = 180^\circ$ the length direction of the slender rod and arm are aligned and the design is over constrained, as discussed in section E.2. This can also be seen in the analysis, where the stiffness c_x and c_z increases when the angle is below 30 or above 150 degrees, i.e. $\alpha < 30$ and $\alpha > 150$.

The ratio between stiffness c_z at the probe tip in z -direction and c_x in x -direction is shown in figure 3.5. It should be noted that the point of intersection between stiffness c_x and c_z in figure 3.4, where the ratio is 1, depends on stylus length and is therefore somewhat arbitrary. By choosing an appropriate stylus length, the stiffness at the probe tip can always be made isotropic. However, by optimizing the angle between rod and arm the stylus length at which the stiffness is isotropic can be maximized. By increasing stylus length at which an isotropic stiffness is obtained, the measurement behavior of the probe is improved. This corresponds to requirement 2 for the probe, as stated in section 3.1.1.

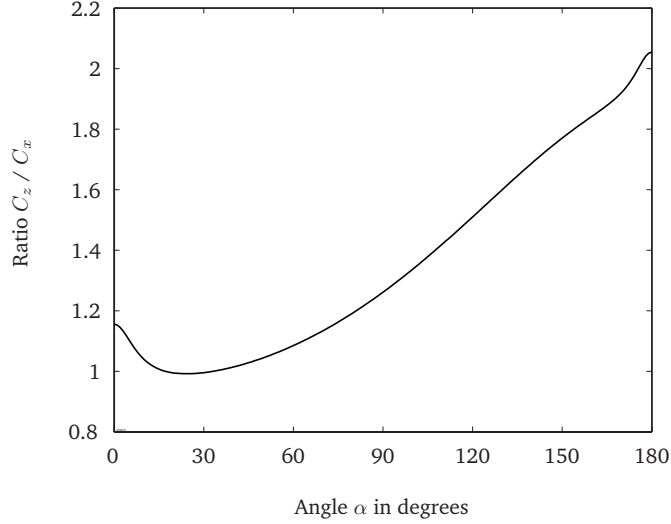


Figure 3.5: Ratio of c_z over c_x as a function of the angle α between the slender rod and arm in the center platform.

From figure 3.5 it can be seen that the optimum ratio of c_z over c_x is obtained when $\alpha = 24^\circ$. However, as discussed before, a value of $\alpha \geq 30^\circ$ is used to prevent the suspension from being over-constrained. From the viewpoint of stiffness, a value of $\alpha = 30^\circ$ is thus preferred for the probe.

The second point of interest with respect to chip layout is influence of slender rod position on probe sensitivity. Probe sensitivity can be calculated from transformation matrix \mathbf{A} . In Appendix D.7 the theoretical transformation matrix \mathbf{A}_{theory} is calculated, where:

$$\mathbf{A}_{theory} = \begin{pmatrix} A_{1x} & A_{1y} & A_{1z} \\ A_{2x} & A_{2y} & A_{2z} \\ A_{3x} & A_{3y} & A_{3z} \end{pmatrix} \quad (3.17)$$

Here, top-left element A_{1x} corresponds to the sensitivity of rod 1 for a displacement in x -direction. Probe tip position is assumed to be ideal, i.e. $p_{tx} = p_{ty} = 0$ and $p_{tz} = -l_{st}$, where stylus length l_{st} is set to 6.8 mm in the current design. Rod sensitivities for a displacement in x - and y -direction are shown in figure 3.6 as a function of angle α between rod and arm, as shown in figure 3.3.

It is noted that the rod sensitivities for a displacement in z -direction are equal, i.e. $A_{1z} = A_{2z} = A_{3z}$, and are not influenced by angle α between rod and arm. This is logical, since rod deformation for a displacement in z -direction is the same, regardless of the layout, when the probe tip position is ideal.

As discussed in Appendix D.7, probe sensitivity S_i in direction i is given by:

$$S_i \equiv \frac{|\mathbf{A}\mathbf{x}_{t_i}|}{|\mathbf{x}_{t_i}|} \quad (3.18)$$

Here, \mathbf{x}_{t_i} is a vector containing the direction i of the tip displacement, e.g. $\mathbf{x}_{t_i} = [100]'$ corresponds to a tip displacement in x -direction.

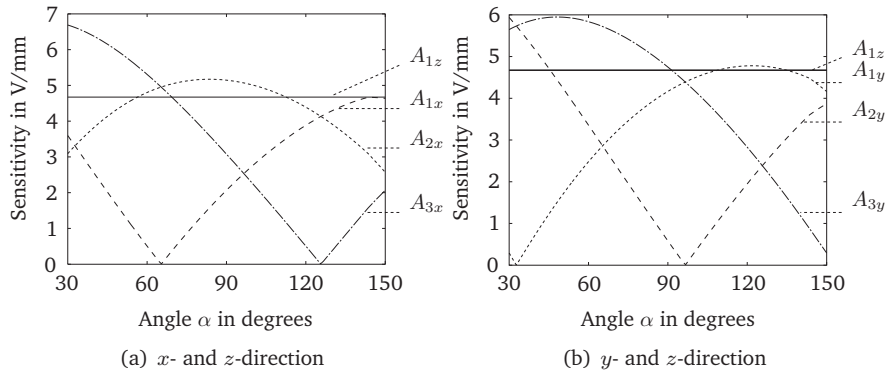


Figure 3.6: Sensitivities of the three rods, relative to sensitivity of rod 1 in z -direction A_{1z} : (a) sensitivities of rods 1, 2 and 3: A_{1x} , A_{2x} and A_{3x} , for a tip displacement in x -direction, (b) sensitivities of rods 1, 2 and 3: A_{1y} , A_{2y} and A_{3y} , for a tip displacement in y -direction.

Using this equation sensitivities S_x , S_y and S_z for a tip displacement in x -, y - and z -direction, respectively, can be calculated as a function of angle α between rod and arm, as shown in figure 3.7.

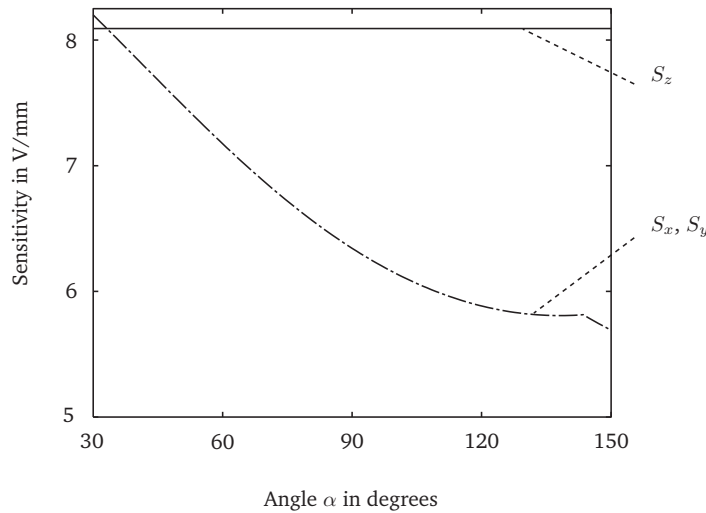


Figure 3.7: Sensitivities S_x , S_y and S_z of the probing system as a function of the angle α .

It is clear from figure 3.7 that sensitivities in the x - and y -direction are equal, regardless of chip layout. This is expected from the symmetric chip layout. Furthermore, when angle α between rod and arm is 30 degrees, sensitivities S_x , S_y and S_z are approximately the same.

As mentioned before, an optimum ratio between stiffness c_x in x -direction and stiffness c_z in z -direction is obtained when $\alpha = 30^\circ$. As shown in figure 3.7, sensitivity in x - and y -direction is also maximized with this layout, resulting in a design with a stiffness and sensitivity which is approximately equal in all directions.

Therefore a value for α of 30° is used in the probe, resulting in a design for the probe as shown in figure 3.8.

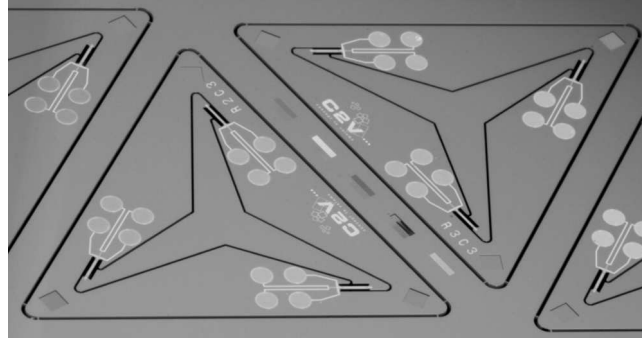


Figure 3.8: Top view of redesigned triangular chips in wafer.

3.2.1 Anisotropic effects

As discussed in appendix D.3 the Young's modulus and Shear modulus in single crystalline silicon depends on the orientation with respect to the crystal structure. The stiffness of a silicon structure is thus dependent on its orientation within the wafer. Therefore, the suspension stiffness in a micro electromechanical system, like the tactile 3D probe discussed in this thesis, may be direction dependent [Bos 07C].

As discussed later in this section, these variations in the elastic modulus are the main cause for an anisotropic stiffness in a single crystalline silicon suspension. In order to counteract the effects of the anisotropic elastic modulus an isotropic base material like polysilicon can be used [Ayazi 01, Howe 96, Tang 90]. There are also disadvantages to using a different base material however, like residual stresses and lower yield strength in the case of polysilicon [Chasiotis 05, Kahn 00, Kahn 01].

Another method is to align the structures along equivalent crystallographic orientations [Lee 03, Kim 01]. However, as discussed in section 3.2, the suspension of the tactile 3D probing system consists of three slender rods oriented in a triangular fashion. As mentioned at the start of this section, this results in an anisotropic mechanical stiffness. Unless this is compensated for, the measurement behavior of the probe is influenced by stick-slip and parasitic movements [Bos 07C], as discussed in section 2.3.6.

The effects of a different Young's modulus between the slender rods can be compensated by adjusting their dimensions [Bos 07C]. However, due to the production process, e.g. wet etching, adjusting the thickness of the cantilever is relatively complex and less accurate compared to adjusting its length or width. Even though adjusting the length of a structure is relatively simple it might influence its function, e.g. in a mechanism. It is therefore convenient to adjust the width.

It should be noted that variations in the structural dimensions may also result from deviations in the manufacturing process. Examples include thickness variations in the case of timed etching. From appendix D.3 it can be seen that variations in the Young's modulus can be as high as 37%. In this case the influence of the anisotropic Young's modulus in a silicon cantilever is the main cause for a non symmetric stiffness when thickness variations between the rods are less than 14%. Thus for suspensions similar to the tactile 3D probing system it can be concluded that variations in the elastic modulus are the main cause for an anisotropic stiffness.

The first step to compensate for the effects of the anisotropic Young's modulus in the sensor is to derive a model for the tactile 3D probe stiffness, as discussed in appendix D.5. When the ratio of the slender rod width w_r over its length l_r is small, the Young's modulus E of the rod's length direction can be used [Lekhnitskii 63]. The Young's modulus E and shear modulus G depend on the crystalline orientation of the slender rod. From appendix D it can be seen that rod 3 is oriented along the $\langle 011 \rangle$ crystallographic direction. Its Young's and shear modulus are therefore $1.688 \cdot 10^{11}$ Pa and $0.508 \cdot 10^{11}$ Pa respectively, as shown in figures D.3 and D.4. Rods 1 and 2 are rotated by 120° and 240° with respect to rod 3. Their Young's and shear modulus are $1.380 \cdot 10^{11}$ Pa and $0.696 \cdot 10^{11}$ Pa, respectively.

Using equation D.35 on the probing system by Pril [Pril 02] with rod length l_r of 1.625 mm, width w_r of 163 μm and thickness t_r of 30 μm , the stiffness matrix at the probe tip \mathbf{C}_{probe} is calculated to be:

$$\mathbf{C}_{probe} = \begin{pmatrix} 78.2 & -0.7 & -17.7 \\ -0.7 & 68.6 & 1.2 \\ -17.7 & 1.2 & 456.0 \end{pmatrix} \quad (3.19)$$

From equation 3.19 it is clear that $C_{11} \neq C_{22}$, resulting in an anisotropic stiffness in the xy -plane.

An isotropic stiffness in the xy -plane, i.e. $C_{11} = C_{22}$, can be obtained from equation D.35 by adjusting the dimensions of the slender rods. As discussed in this section, a convenient method is to adjust the width w_r of the rods. It can be shown that by increasing the width w_{r12} of rods 1 and 2 to 198 μm , an isotropic stiffness matrix in the xy -plane is obtained:

$$\mathbf{C}_{probe}^* = \begin{pmatrix} 83.2 & 0.0 & -0.7 \\ 0.0 & 83.2 & 0.0 \\ -0.7 & 0.0 & 516.8 \end{pmatrix} \quad (3.20)$$

It is noted that, in the probe by Pril, the stiffness in z -direction C_{33} is approximately 6 times higher than the stiffness in the xy -plane, C_{11} and C_{22} . As discussed in the previous section, the tactile 3D probing system as discussed in this thesis has a fully isotropic stiffness, i.e. $C_{11} = C_{22} = C_{33}$, when the stylus length l_s is 6.8 mm.

The results from equation 3.20 are verified using a Finite Element Model (FEM) with anisotropic material properties and show excellent agreement.

The stiffness of a compensated probe suspension is measured using the Mitutoyo Surftest SV-600 surface roughness measurement instrument. The tip of this instrument applies a constant force of 3.4 mN as it is moved over the slender rod under test, as shown in figure 3.9. By measuring the deflection of the tip, the stiffness can be calculated.



Figure 3.9: Setup used to measure the deflection of the slender rods.
A triangular aluminum plate is used to create a mechanical connection between the rods.

The measurement results for a non compensated sensor are given in the left-hand column of table 3.1. It can be seen that the deflections at rods 1 and 2 are similar, 46.5 and 46.7 μm respectively, but differ significantly from the deflection at rod 3, 43.8 μm . These results are in agreement with the results from finite element simulation, as shown by the right-hand column. It is noted that the deflection is influenced by the intermediate body and glue layer which are included in the model.

Finally, the measurement results on a compensated probe suspension are shown in table 3.2. The variations in the deflection of the suspension are significantly reduced with respect to the variations shown in table 3.1.

It is thus shown that an isotropic stiffness can be obtained with the tactile 3D probe as discussed in this thesis. This is discussed in appendix D.4 where the results of the anisotropic stiffness in single

	Deflection at the rod endpoint in μm	
	Measurement	Finite element simulation
Rod 1	46.5	49.1
Rod 2	46.7	49.1
Rod 3	43.8	46.5

Table 3.1: Deflection of the slender rods in a non compensated probe suspension due to an applied force of 3.4 mN.

	Deflection in μm
Rod 1	48.2
Rod 2	48.0
Rod 3	47.8

Table 3.2: Measured deflection at the endpoint of the slender rods in a compensated probe suspension due to an applied force of 3.4 mN.

crystalline silicon and stiffness effects of structural elements in the probe, e.g. the stylus, are used to obtain a probing system with isotropic suspension at its tip.

3.2.2 Center platform and stylus

As discussed in sections 2.3.1 and E.4, stiffness of the center platform and stylus should be as high as possible to assure that a probe tip displacement results in maximum slender rod deformation.

However, mass of stylus and center platform also contributes to the colliding mass of the probe. To prevent plastic deformation when probing an aluminum work piece by a probe with a 150 μm tip radius at an approach speed of 1 mm/s the colliding mass should be less than 35 mg, requirement 6 in section 3.1.1. Therefore, the design of the center platform and stylus requires a high specific stiffness, as discussed in the previous section.

For the chip redesign, a deep reactive ion etching (DRIE) procedure can be used to create high aspect ratio structures. Using this process, the aluminum three legged star, used in the original design to connect the stylus to the three slender rods, can be replaced by a silicon structure. From table E.1 it can be seen that specific stiffness of silicon when compared to aluminum is 63% higher. Also, thermal bending deformation of silicon, table E.3, is 169% lower with respect to aluminum.

For reasons of thermal stability and boundary conditions in processing of silicon wafers it was decided to use a solid cross section for the three legs in the center platform. The force on a leg in the center platform in the current chip design, as discussed in section 3.2, is schematically shown in figure 3.10.

It can be shown that stress $\sigma_{xx}(x)$ in the length direction of the arm at position x and shear stress $\tau_{xy}(x)$ are given by:

$$\begin{aligned}\sigma_{xx}(x) &= \frac{t}{2} \frac{F(l + a_1 - x)}{I(x)} = F \frac{6(l + a_1 - x)}{w(x)t^2} \\ \tau_{xy}(x) &= F \frac{3a_2}{t^2 w(x)}\end{aligned}\quad (3.21)$$

As discussed in the previous section, efficient use of material, and thereby a light and stiff construction, is obtained when the von Mises equivalent stress σ_e is uniform across the structure. Using

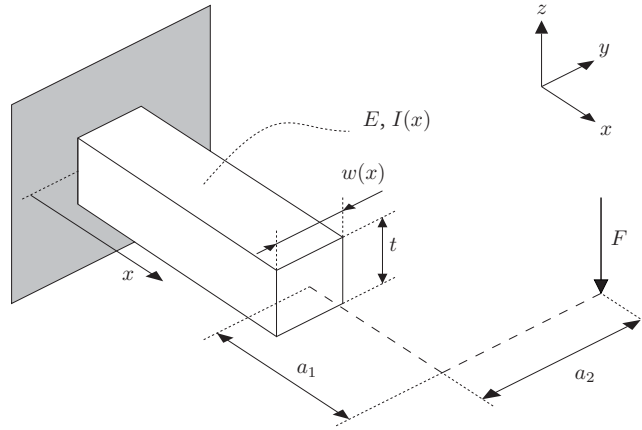


Figure 3.10: Schematic of force on the arm in center platform of chip.

the approach from appendix F with equation 3.21 yields for the equivalent von Mises stress $\sigma_e(x)$ at position x :

$$\sigma_e^2(x) = \frac{9F^2}{t^4 w^2(x)} \left(4(l + a_1 - x)^2 + a_2^2 \right) \quad (3.22)$$

For an isotropic equivalent von Mises stress, i.e. $\sigma_e(x) = \sigma_e$, width $w(x)$ at position x is given by:

$$w(x) = c^* \sqrt{4(l + a_1 - x)^2 + a_2^2} \quad (3.23)$$

Where:

$$c^* = \frac{3F}{t^2 \sigma_e} \quad (3.24)$$

Constant c^* is used to control the weight of the center platform and match the stiffness of the arm to that of the stylus.

The specific stiffness of the stylus is improved by using a hollow tube, as discussed in the previous section. Using standard beam theory, the stiffness of the stylus with a length of 6.8 mm, outer radius of 0.2 mm and inner radius of 0.1 mm is calculated to be 2.3 kN/m.

From the design, as discussed in section 3.2, it was calculated that $a_1 = -2$ mm, $a_2 = 1$ mm and $l_{arm} = 10$ mm. Using these values, cantilever stiffness k described by equation 3.23, can be calculated to be:

$$k = c^* 3500 E t^3 \quad (3.25)$$

For optimum stiffness per weight, the stiffness of the center platform and the stylus should be equal. The stiffness k of a single arm, as given by equation 3.25, should thus be approximately 1200 N/m.

Using this stiffness in equation 3.25, i.e. $k = 1200$ N/m, and using $E = 138$ GPa and $t = 0.25$ mm results in $c^* = 0.16$. The results are checked using finite element simulation (FEM), resulting in the center platform design as shown in figure 3.11.

The combined mass of probe tip, stylus, center platform and intermediate body, as shown in figure 3.11 is 34 mg, thus satisfying requirement 6 as stated in section 3.1.1.

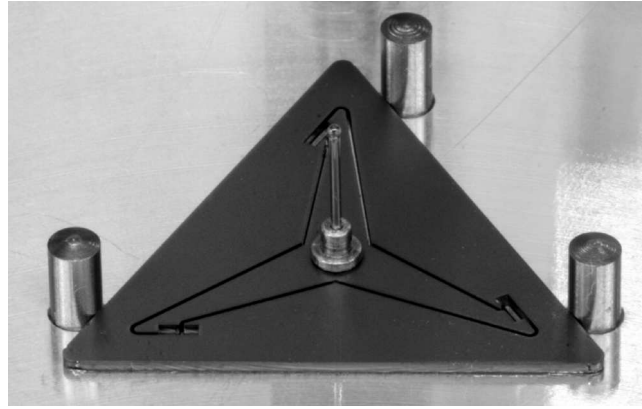


Figure 3.11: Photo of assembly of chip, stylus and probe tip.

3.2.3 Micro spherical tips

Currently, styli with ceramic tips are commercially available with a tip diameter of $125\ \mu\text{m}$. Smaller tips are currently not available. As discussed in section 2.3.4 the probe tip diameter limits the minimum size of structures that can be measured by the probe.

Therefore several micro spherical tips were manufactured with a diameter below $100\ \mu\text{m}$ using two different methods. The first method uses a glass fiber, which is given a set diameter using a wire drawing procedure. The fiber end is then locally heated to create a glass tip. This results in a thin fiber with tip, which can be glued into a larger hollow stylus in order to assemble it onto the probe chip.

It should be clear that assembling a thin fiber, e.g. $30\ \mu\text{m}$ diameter, into a small hole, e.g. $50\ \mu\text{m}$ diameter, is a challenging task. As an alternative a custom wire-drawing procedure can be used where a fiber is locally heated and stretched, as shown schematically in figure 3.12. This can be performed in several stages, thus creating a thin glass fiber on top of a thicker fiber, which can be handled more easily. The tip can again be manufactured by local heating.

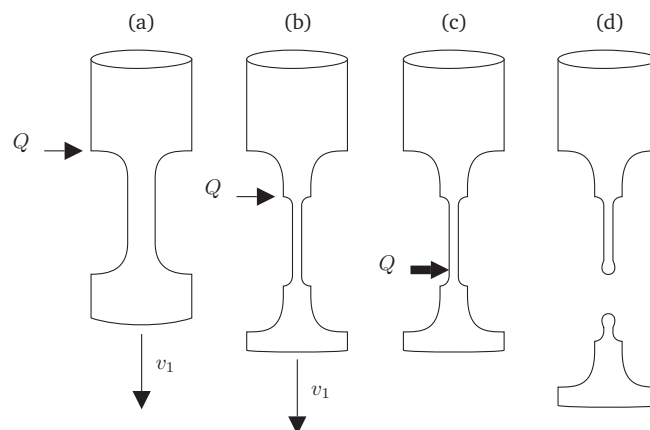


Figure 3.12: Schematic of manufacturing borosilicate micro tips: (a) wire drawing of fiber, (b) final wire drawing stage to create micro stylus, (c) local heating of stylus to create tip, (d) finished stylus with tip.

A borosilicate stylus manufactured using this procedure is shown in figure 3.13. The stylus is made out of borosilicate glass and stylus and tip have a diameter of approximately $40\ \mu\text{m}$ and $50\ \mu\text{m}$, respectively.

An important drawback of a borosilicate stylus is that it is an insulator. This may result in large



Figure 3.13: Photo of borosilicate stylus on 1 euro coin. The tip of the stylus is just above the island of Majorca.

electrostatic forces during scanning or probing, as discussed in appendix C.2. Also, stiffness of a borosilicate stylus is relatively low, i.e. its Young's modulus is 64 GPa. As a result, a borosilicate stylus is sensitive to effects of surface forces during measurements, as discussed in the previous chapter.

The second method uses a conductive, often metallic, material which is shaped using wire electrostatic discharge grinding (WEDG) [Alting 03, Masuzawa 00, Pham 04, Rajurkar 06]. By placing the work piece on a rotary axis axi-symmetrical products, e.g. a stylus, can be manufactured. Using this procedure a spherical tip can also be manufactured at the stylus end, which can be used as probe tip. However, as discussed by Sheu [Sheu 04, Sheu 05] this results in a relatively rough surface due to electro discharge craters.

Therefore, a one pulse electrostatic discharge (OPED) is used to create the tip. Stylus material in this research is tungsten carbide, which has a Young's modulus of 360 GPa. The manufacturing steps are shown schematically in figure 3.14.

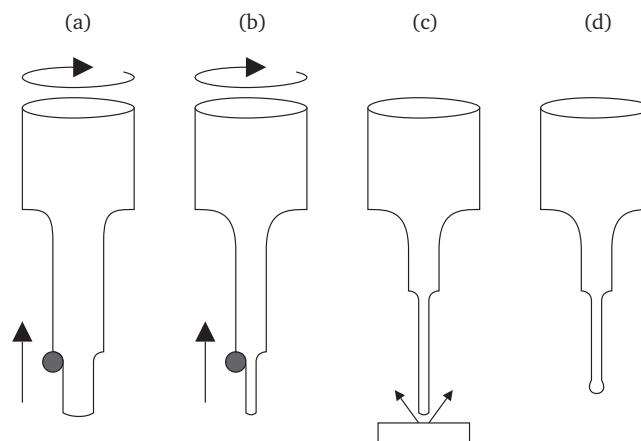


Figure 3.14: Schematic of EDM manufacturing of micro probe tips: (a) rough machining of stylus, (b) finish machining of stylus, (c) discharge manufacturing of tip, (d) finished stylus with tip.

Figure 3.15 shows the setup used to manufacture a tungsten carbide stylus. The stylus, as manufactured using this procedure is shown in figure 3.16. The tip diameter in this experiment is approximately 50 μm . It is noted that the tip surface, which is manufactured using a one pulse electrostatic discharge (OPED), is much smoother than the stylus surface, which is manufactured

using a wire electrostatic discharge grinding (WEDG) procedure.

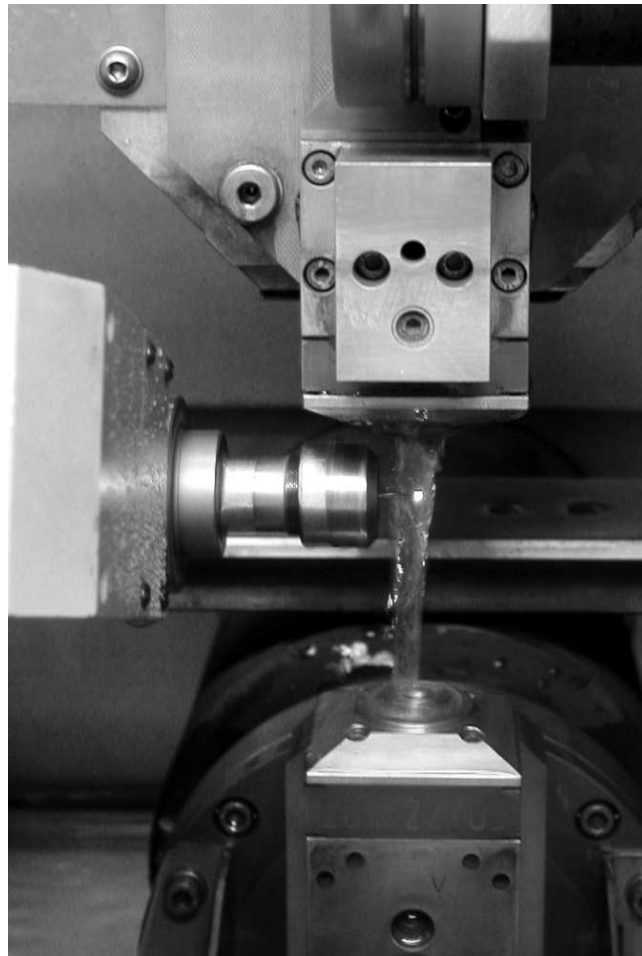


Figure 3.15: Setup used to manufacture a tungsten carbide stylus using wire electrostatic discharge grinding (WEDG). The stylus is mounted on a rotary axis.

It is obvious that the energy of a one pulse electrostatic discharge increases as the peak current and/or pulse duration increases. Increasing pulse energy results in a larger tip diameter. Also tip roundness deteriorates for a higher energy pulse due to unbalanced shrinking forces [Sheu 04, Sheu 05]. Finally, it should also be obvious that the energy needed to create a tip decreases with decreasing stylus diameter.

Using wire electrostatic discharge grinding, a tungsten carbide rod with a diameter of $1\text{ }\mu\text{m}$ is manufactured by Egashira et al. [Egashira 05, Rajurkar 06]. The approach, as described in this section, is used by Sheu [Sheu 05] to create a stylus with a diameter of $10\text{ }\mu\text{m}$ and a tip of $15\text{ }\mu\text{m}$.

3.3 Probe holder

The probe holder is an intermediate component that provides the mechanical and electrical interface between silicon probe chip and coordinate measuring machine (CMM). The interface to a coordinate measuring machine is somewhat system specific. Therefore the NanoCMM developed by Van Seggelen [Seggelen 07] is used as an example.

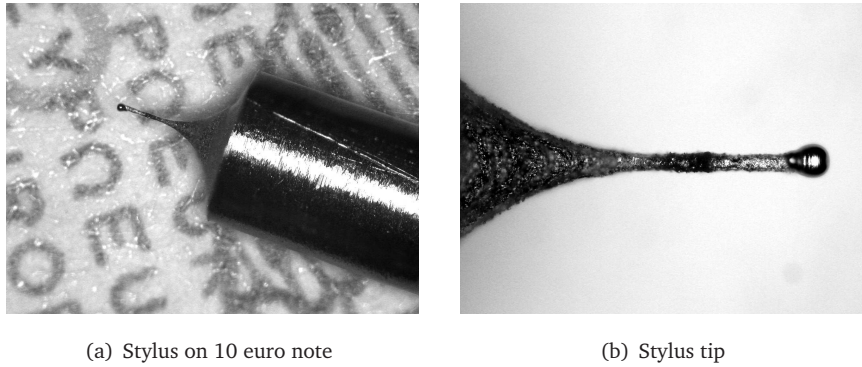


Figure 3.16: Tungsten carbide stylus with a tip diameter of $50\text{ }\mu\text{m}$, (a) stylus with a 10 euro note, letters shown are printed below the map of Europe, (b) photo zoomed in on stylus and tip.

3.3.1 Electronics

As discussed in section 1.5 a tip displacement results in a deformation of the probe suspension, which consists of three slender rods. On each slender rod four piezo resistive strain gauges are deposited in a Wheatstone bridge configuration. To amplify the Wheatstone bridge signal alternating current (AC) and discrete current (DC) electronics can be used. Typically, the influence of $1/f$ -noise in AC electronics is small in comparison to DC electronics [Horowitz 89]. However, DC electronics have the advantage that effects of capacitive coupling in probe chip and connections are reduced [Pril 02]. For this reason, DC electronics are used in the probe.

Custom build electronics allow the opportunity to optimize electronics to the application and can be integrated with probe housing. A schematic of the electronics used in the probe is shown in figure 3.17. It can be seen that the electronics are divided into three parts. The first part (a) is the probe chip where one Wheatstone bridge is deposited on each of the three slender rods in its suspension. In the second part (b) the Wheatstone bridge signal is amplified using an INA118 amplifier operating at a gain of 200. In the third part (c) the amplified signal is connected to two INA118 amplifiers operating at a gain of 1, thereby creating a differential output signal which is connected to CMM electronics using shielded twisted pair cables.

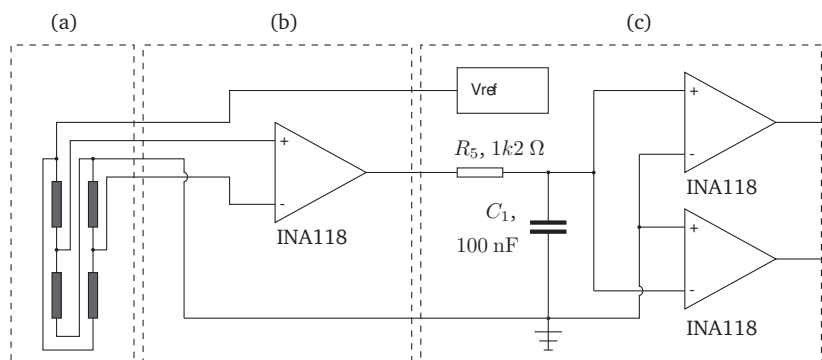


Figure 3.17: Schematic of probe electronics.

Resistor R_5 and capacitor C_1 function as a low-pass filter to reduce high frequency noise in the signal. The measurement frequency of the probe is 1 kHz , as stated by requirement 4 in section 3.1.1. The signal reduction to the measurement signal due to the low pass filter is set to a maximum of 1 dB , approximately 10% , resulting in a cutoff frequency of 1.3 kHz . This results in the RC value, as shown in figure 3.17.

The second point of interest is position of the electronics with respect to the probe and coordinate

measuring machine (CMM). As shown by equation 3.14 in section 3.1.2 a tip displacement of 1 nm corresponds to a measurement signal in the Wheatstone bridge of $4.5 \mu\text{V}$ for a 5 V supply voltage. The signal is therefore sensitive to environmental noise. To minimize effect of environmental noise on this signal the distance between chip and electronics should be minimized and shielded.

However, the heat dissipated by a single INA118 amplifier is approximately 4 mW during normal operation. To reduce heat dissipation to the probe holder the electronics are divided into two parts (b) and (c) as shown in figure 3.17. The amplifier, part (b), is placed next to the probe holder to reduce the influence of environmental noise on the measurement signal. The amplified signal is less sensitive and the second set of amplifiers, part (c), can therefore be placed at a certain distance from the probe holder, as schematically shown in figure 3.18.

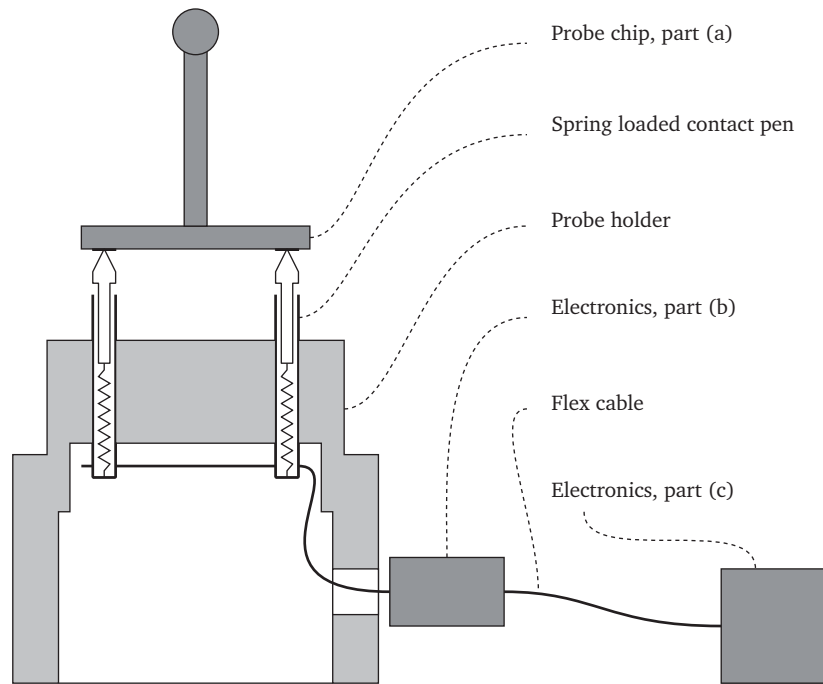


Figure 3.18: Schematic of the probe holder with position of electronic components.

From figure 3.18 it can be seen that the position of electronics in the holder is a trade off between heat dissipation and signal to noise ratio of the electronics. In this setup, a thermal barrier can be created between holder and electronics, while shielding all electronic connections between the probe chip and part (b) of the electronics. Figure 3.19 shows the assembled holder, where the spring loaded pens and part (b) of the electronics are mounted onto the holder.

The standard deviation in electronic noise when the probe is in contact with a work piece is measured to be 2 mV, which corresponds to 1.6 nm.

3.3.2 Clamping of the chip

The electrical connection between the probe chip and holder is discussed in the previous section. In this section the mechanical connection between the probe chip and holder will be discussed.

The mechanical connection is shown schematically in figure 3.20. The spring loaded pens, used to create the electrical connection, are used to supply the clamping force between the probe (1) and holder cap (2). The holder cap itself is clamped onto the holder using a fixation screw (3).

The assembly of probe chip, stylus and tip can now be replaced as a unit, which is electrically and mechanically coupled to the holder. In the original design by Pril [Pril 02] the probe chip is electrically connected to a flex-cable using wire bonds. However, this approach increases the replacement cost of the probe, requirement 5 in section 3.1.1, and makes assembly more difficult.

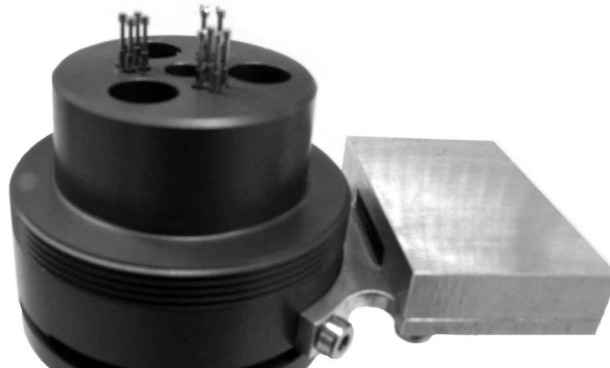


Figure 3.19: Photo of probe holder with spring loaded contact pens and holder for electronics, part (b).

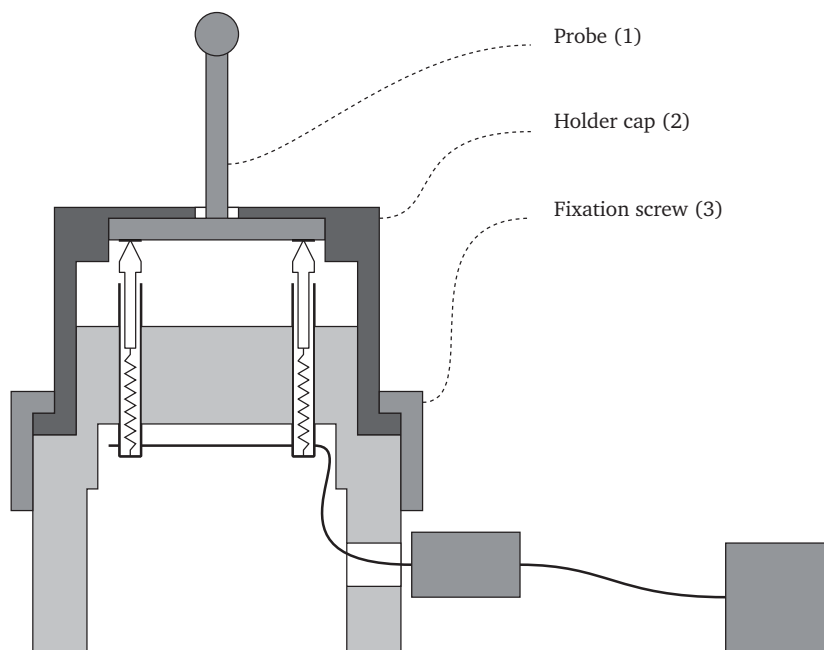


Figure 3.20: Schematic of clamping of the probe chip in the holder cap, using spring loaded pens to supply the clamping force.

An important challenge when a the probe chip is mechanically clamped onto the holder is micro friction in the contact region. This results from a different tangential strain distribution between two components, as schematically shown in figure 3.21. The resulting micro friction causes a hysteresis effect, as discussed in section 2.5.2.

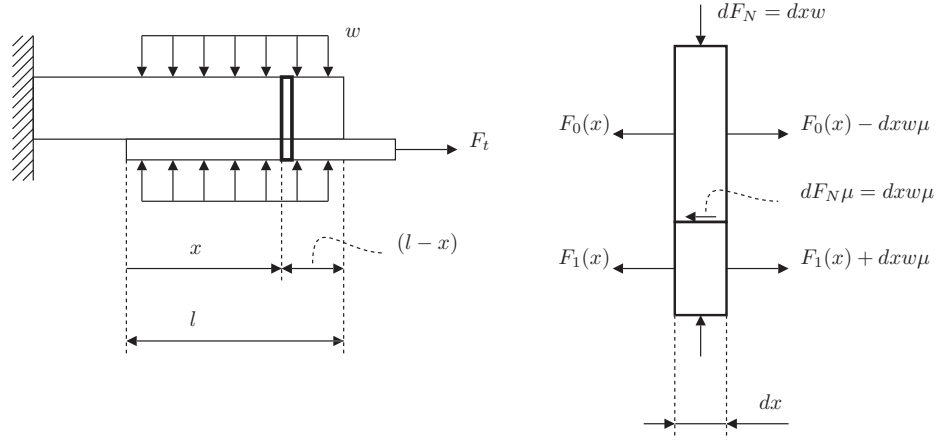


Figure 3.21: Schematic of micro friction in a mechanically clamped contact.

The force $F_0(x)$ at position x results in a stress $\sigma(x) = F_0(x)/A_0$. Where $A_0(x)$ and E_0 are the cross sectional area and Young's modulus of the top cantilever, respectively. The strain in the top and bottom cantilevers at position x is thus given by:

$$\begin{aligned}\varepsilon_0(x) &= \frac{F_0(x)}{A_0(x)E_0} = \frac{(l-x)w\mu}{A_0E_0} \\ \varepsilon_1(x) &= \frac{F_1(x)}{A_1(x)E_1} = \frac{F_t - (l-x)w\mu}{A_1E_1}\end{aligned}\quad (3.26)$$

To prevent micro slip in the contact the strains $\varepsilon_0(x)$ and $\varepsilon_1(x)$ should be equal along the contact region. It can easily be shown that this is satisfied when:

$$\frac{A_1(x)E_1}{A_0(x)E_0} = \frac{F_t}{(l-x)w\mu} - 1 \quad (3.27)$$

Equation 3.27 is satisfied when both cantilevers have a cross sectional area which varies with a linear relation to x , and $A_1(0) = 0$ and $A_0(l) = 0$.

However, the cross sectional area in the probe system can not be varied according to equation 3.27 and hence some micro slip will occur in the contact region. For the probe system the top cantilever, i.e. the holder cap (2), is assumed to have a much greater stiffness than the probe chip, i.e. $A_0(x)E_0 \gg A_1(x)E_1$. Position x where the top cantilever strain equals the bottom cantilever strain, is now given by:

$$\varepsilon_0(x) = \varepsilon_1(x) \Rightarrow F_1(x) = \frac{A_1(x)E_1}{A_0(x)E_0} F_0(x) = 0 \quad (3.28)$$

Using $F_1(x) = F_t - (l-x)w\mu$ yields $x = l - \frac{F_t}{w\mu}$.

The area affected by micro slip extends from the end of the cantilever, where $x = l$, to position $x = l - F_t/(w\mu)$. The length over which micro slip occurs in the contact region between both bodies thus equals $F_t/(w\mu)$. The micro slip region can be decreased by increasing the normal force per unit area w . The total elongation Δl_{tot} in the bottom cantilever due to micro slip in the contact is now given by:

$$\Delta l_{tot} = \int_l^{l-F_t/(w\mu)} \varepsilon_1(x) dx = \int_l^{l-F_t/(w\mu)} \frac{F_t - (l-x)w\mu}{A_1(x)E_1} dx \quad (3.29)$$

When the cross sectional area of the bottom cantilever is constant, i.e. $A_1(x) = A_1$, the total elongation Δl_{tot} in the bottom cantilever is given by:

$$\Delta l_{tot} = -\frac{1}{2} \frac{F_t^2}{w\mu A_1 E_1} \quad (3.30)$$

In the probe system, the chip is supported by three contact points each with a length and width of 2 mm. The pre-load force on each contact point is supplied by four spring loaded contact pens that give a total force F_N of 0.8 N. The cross sectional area A_1 is taken as the cross sectional area of the chip above the contact point, i.e. 2 mm by 0.5 mm. Using a suspension stiffness c_t of 480 N/m, the maximum force F_t at an over travel distance of 10 μm is 4.8 mN. Using a Young's modulus E_1 of 138 GPa and a coefficient of friction $\mu = 0.15$, thus results in a micro slip region of 160 nm. The total elongation Δl_{tot} due to micro slip in the contact between probe and holder cap is less than 0.1 nm.

3.3.3 Connection to measurement machine

As mentioned at the start of section 3.3, the interface to the coordinate measuring machine (CMM) is somewhat system specific and therefore the NanoCMM, developed by Van Seggelen [Seggelen 07], is used as an example. The design and measurement principle of the NanoCMM are discussed in section 1.3.

The NanoCMM metrology loop is manufactured from aluminum to reduce thermal gradients and effects of a homogeneous temperature deviation, as discussed in section E.3. Therefore the probe holder, as used in the NanoCMM, is also manufactured from aluminum. The density of aluminum is also relatively low, about 2700 kg/m³, thereby decreasing holder mass and power consumption in the z -actuator. The probe holder weight is further reduced by removing redundant material, as discussed in section 3.2.2, resulting in a total weight of 25 gr.

The NanoCMM z -axis is separated from the xy -stage. For the electrical connection between part (b) and (c), a flex-cable is thus used, as schematically shown in figure 1.8. Deformation of this flex cable due to a translation in z -direction is highly repeatable. The NanoCMM, with probe, is shown in figure 3.22. The probe close up photo in figure 3.23 shows the position of the electronics part (b) and (c) on the CMM.

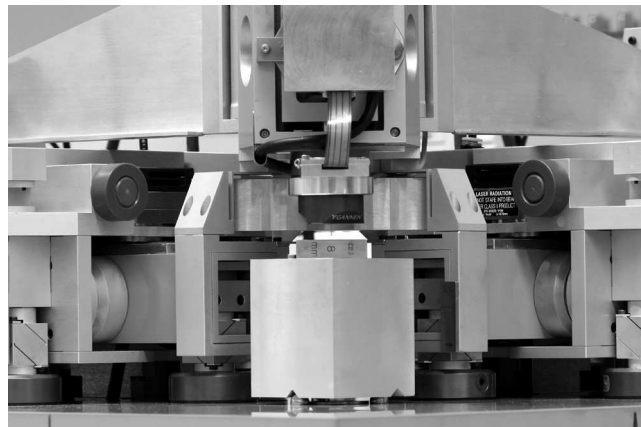


Figure 3.22: Photo of probe in NanoCMM by van Seggelen.

The mechanical connection between probe and CMM is done using three contact planes. Each contact plane is preloaded using a screw through its center. Finally, a photo of the probe with a

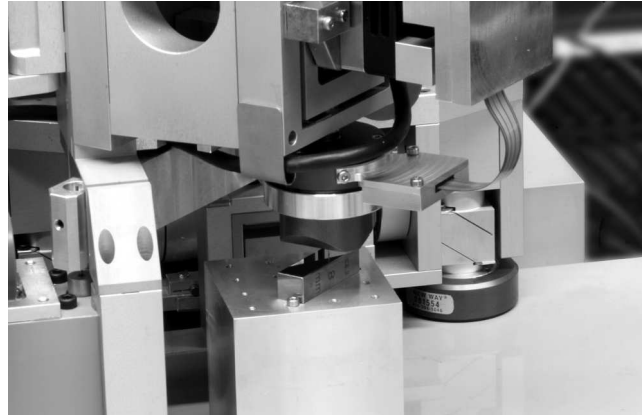


Figure 3.23: Close up of probe in NanoCMM by van Seggelen.

500 μm tip diameter as it approaches a free form surface using the NanoCMM is shown in figure 3.24.

3.4 Conclusion

The deflection of the probe tip is measured by piezo resistive strain gauges deposited on three slender rods that form the suspension of the probing system. Four piezo resistive strain gauges are deposited on each rod in a Wheatstone bridge configuration. Using a supply voltage V_0 of 5 V, a measurement signal of 4.5 μV per nanometer tip displacement is obtained. This signal is amplified using an INA-118 amplifier to produce a measurement signal of 1 mV per nanometer tip displacement, i.e. 10 V for a displacement of 10 μm .

By optimizing the layout of the probe chip an isotropic stiffness and sensitivity at the probe tip in each direction is obtained for a stylus length of 6.8 mm. The stiffness of the probe suspension is also optimized to obtain an aspect ratio of 50 between the length and radius of the stylus. This relatively high aspect ratio allows the use of small tips, e.g. with a 25 μm radius, on relatively large styli, e.g. 1 mm, making the probing system suitable for measuring MEMS and other miniaturized components.

To measure these small components several micro spherical probe tips are manufactured. The first method uses a borosilicate fiber which is given a set diameter using a wire drawing procedure. In the second method a tungsten carbide stylus is manufactured using electro discharge manufacturing (EDM). Both methods have been used to create a stylus with a 50 μm tip diameter.

To avoid plastic deformation of a work piece during probing, the design of the center platform and stylus are optimized to obtain a high stiffness per weight. As a result, a maximum colliding mass at the probe tip of 34 mg is obtained. This allows probing of an aluminum work piece by a sapphire probe tip with a radius of 150 μm at a velocity of 1 mm/s without plastic deformation of the work piece or probe tip.

Finally, the probe chip is clamped into the holder using spring loaded contact pens. These contact pens are also used to create the electrical connection between electronics and chip. As a result, the probe chip can easily be exchanged when damaged, reducing replacement costs.

The specifications, as stated at the start of this chapter have all been met.



Figure 3.24: Photo of probe approaching a free form surface.

Chapter 4

Suction gripper for micro assembly

Assembly is a crucial part in the realization of a product. Compared to assembly in the macro world, assembly in the micro world is influenced by scaling effects [Brussel 00, Tichem 04]. Therefore, during assembly of the probe as discussed in this thesis and other products containing micro components several additional aspects influence the assembly process when compared to conventional macro-scale assembly. These aspects include:

- The influence of surface forces on the assembly process: section 2.1.7;
- High requirements on the placement uncertainty: the required positional uncertainty and clearances between parts are in the range of 0.1 to 10 μm for micro components [Brussel 00, Tichem 02];
- Small and fragile components: typical product dimensions are 0.5 to 30 mm where dimensions of functional structural elements can be in the range of 10 to 100 μm [Brussel 00, Tichem 02];
- High contact stresses due to the colliding mass and stiffness of the assembler: section 4.3;
- Parts are often from different technological domains, e.g. semi-conductor and precision mechanical engineering: tolerances on parts may show a large variation and assembly often involves the joining of non conventional material combinations [Tichem 02].

First, the influence of these aspects on the manufacturing and assembly costs of products containing micro-parts is described. In section 4.2 several techniques, used in the assembly of these micro products, are briefly discussed. Then, in section 4.3, the influence of contact forces when handling micro-scale components in serial assembly is discussed. As discussed in section 4.5 a new suction gripper is developed, which is suitable for handling these micro-scale components in serial assembly. Experimental results with this gripper are given in section 4.6, and finally the assembly of the probe is briefly discussed in section 4.7.

4.1 Introduction

The costs that can be attributed to packaging and assembly are between 75-95% for most micro electromechanical systems (MEMS) [Maluf 04]. Figure 1 shows a model by Bos and Bullema [Bos 06, Bos 07A] which relates total product cost to component size. It can be seen that material costs decrease with component dimensions. However, further miniaturization eventually results in high requirements on the material used, especially its purity, increasing the material costs.

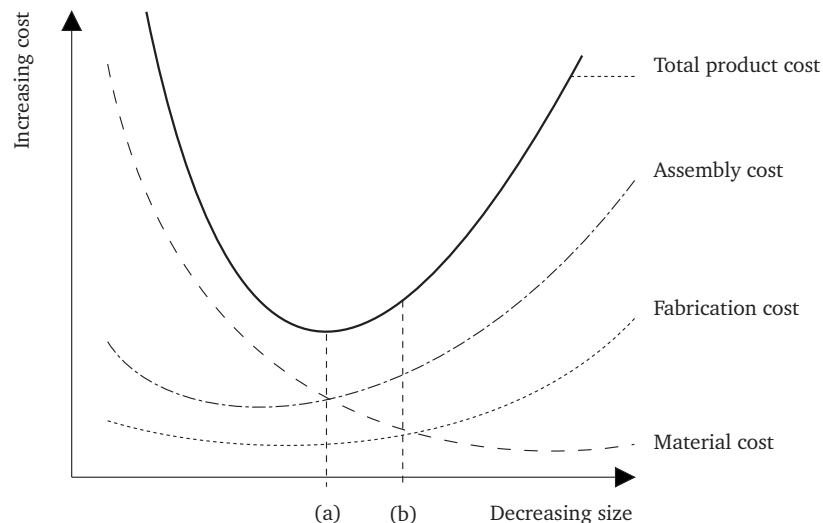


Figure 4.1: Model of the total product cost as a function of the size of the device [Bos 06, Bos 07A].

Fabrication costs, as described by Hayashi [Elwenspoek 01], increase for smaller components as it is more difficult to machine them. The cost of assembly also increases for smaller components as it is more difficult to handle them and the required placement uncertainty increases [Böhringer 99, Brussel 00].

The minimum total cost in figure 1 is obtained in point (a). Using this model, a further decrease in component dimensions, point (b), results in an increase in the total product cost. Decreasing the cost of fabrication of smaller components [Taniguchi 83] and improving the assembly speed and uncertainty results in a shift of the optimum product size, point (a), to smaller component dimensions and a reduction in total product cost.

4.2 Assembly techniques

From the previous paragraphs it should be clear that the assembly of micro products differs from assembling macro products at several key aspects. The use of macro scale assembly equipment to assemble micro components thus leads to many challenges, especially at the interface. However, several techniques have been demonstrated that work around or make use of these aspects [Böhringer 99, Brussel 00].

In general these techniques can be categorized as parallel or serial assembly [Cohn 97, Hsu 03]. As mentioned in the previous paragraph, since parts are small, fragile and often produced in batched, parallel assembly makes sense since the handling effort is distributed over a number of parts. Examples include flip-chip wafer-to-wafer transfer of parts [Cohn 96, Singh 97] and assembly using an array of micro grippers [Keller 97]. The parallel assembly of multiple parts where the relation between a part and its destination is known in advance is often referred to as deterministic parallel microassembly [Böhringer 99].

Another parallel assembly technique is stochastic microassembly; often referred to as self assembly. It is based on a system of particles evolving towards a state of minimal potential en-

ergy [Böhringer 99]. Several effects can be used as driving forces for the assembly process, including fluidic agitation and mating part shapes [Srinivasan 01, Syms 03, Yeh 94], vibratory agitation and electrostatic force fields [Böhringer 98], vibratory agitation and mating part shapes [Hosokawa 95] and mating patterns of self-assembling monolayers [Janssen 06, Ricco 92].

Parallel techniques offer high throughput and often good placement accuracy. However, they are only useful for a limited number of assembly operations and systems [Butler 98, Cohn 98, Langen 94]. Therefore serial assembly techniques, in which components are picked and placed individually, are still used for most micro assembly operations.

An important challenge in serial assembly is the contact between the macro-scale assembler and the component. The colliding mass and stiffness of the assembler is very high in relation to the mass and stiffness of most micro products. This results in high forces at the interface, as will be discussed in the next section.

4.3 Influence of contact forces

During a typical pick and place action the assembler first moves the attached gripper to the desired pick up location. There the assembler positions the gripper to make contact with the component.

The gripper then fixates the component to the gripper and the assembler moves the gripper and attached component to the placement location; e.g. a second component. When the component is positioned correctly it is released by the gripper and the assembler with gripper moves to the next pick up location. During these operations, collision and static forces are one of the main challenges for a successful assembly operation [Brussel 00].

The effect of the forces during collision and the static forces on the deformation of the component depends on the geometry of the contacting surfaces. In sections 2.1.3 to 2.1.5 the forces due to collision and over travel during a probing operation are discussed. For the sake of simplicity, a similar situation is assumed where a spherical component is placed on a planar surface. Using this approach, the influence of the colliding mass and the axial stiffness of the gripper on the admissible approach speed is calculated using Hertz contact theory [Johnson 85]. Compliance of the components, which results in a higher admissible speed, is not taken into account.

First the influence of the colliding mass on the admissible approach speed is calculated. The collision forces occur as a result of the relative difference in speed between gripper and component at the moment of contact. The maximum occurring Von Mises stress in the plane p_0 and the depth of indentation δ are given by [Johnson 85]:

$$p_0 = \left(\frac{6F_{Hz} E_{red}^2}{\pi^3 r^2} \right)^{\frac{1}{3}} \quad (4.1)$$

$$\delta = \left(\frac{9F_{Hz}^2}{16r E_{red}^2} \right)^{\frac{1}{3}} \quad (4.2)$$

Where F_{Hz} is the contact force and E_{red} is the reduced Young's modulus [Johnson 85]. During a collision the kinetic energy is absorbed by the elastic deformation of both bodies:

$$\frac{1}{2}mv^2 = \int_0^{\delta_Y} F_{Hz}(\delta) d\delta = \frac{\pi^5 r^3 (1.61\sigma_{0.2})^5}{60E_{red}^4} \quad (4.3)$$

Here $\sigma_{0.2}$ is the yield strength of the component and δ_Y is the depth of indentation at which plastic deformation begins, using the Tresca criterion [Tabor 51]. The mass m is the equivalent mass of the sphere, i.e. the mass that is 'felt' when trying to accelerate the sphere.

From equation 4.3 it can be seen that the admissible approach speed v decreases with a decreasing radius of the sphere. This can also be seen in figure 4.2 where we assume that the gripper is rigidly

connected to the component. The equivalent mass in this case is the mass of the component and gripper combined. The figure shows the admissible approach speed to prevent plastic deformation as a function of the mass of the gripper for several component radii.

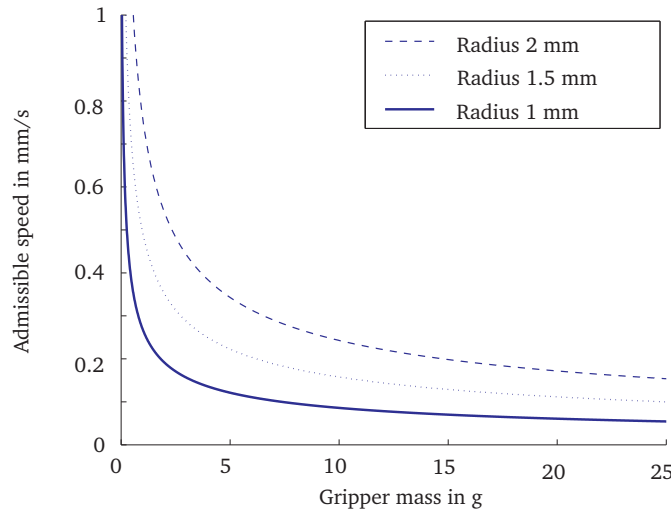


Figure 4.2: The effect of the gripper mass on the admissible approach speed when placing a sapphire sphere on a planar aluminum workpiece.

The moving mass of traditional grippers is often more than 100 grams, resulting in high collision forces. To prevent permanent damage, the collision speed therefore needs to be kept low, often well below 0.1 mm/s, also see figure 4.2. As a result assembly time and its contribution to the total product cost are high.

After the collision of the two components and when the contact is detected a signal is provided to the assembly robot to stop the movement of its head. The distance between the point of contact and the point at which the movement of the assembler ends is referred to as the over travel distance. The static force at the point of maximum over travel depends on the over travel of the assembler and the stiffness c between both components, i.e. the stiffness of the loop through the assembly robot between both components.

The over travel distance of the assembler depends on the approach speed of the assembler, its deceleration a and its reaction time t_r . The admissible speed regarding over travel v_{ovt} is given by [Vliet 96, Pril 02]:

$$v_{ovt} = -t_r a + \sqrt{t_r^2 a^2 + 170 \frac{r^2 \sigma_{0.2}^3}{c E_{red}^2} a} \quad (4.4)$$

From the viewpoint of dynamics a high stiffness of the assembler robot is advantageous. However, as seen in the above equation this also leads to a decreased admissible approach speed. This is also shown in figure 4.3, where the admissible approach speed is shown as a function of the stiffness between the components for $t_r = 2$ ms and $a = 10$ mm/s².

To decrease the over travel of the assembler an open loop placement can be used, where the gripper is moved to a predefined position. However, the position of the gripper is influenced by manufacturing and positional accuracies of both the components and the assembler. In the situation of a form closed loop [Schellekens 98], as can be found in many (semi)automated assemblers, this may result in high static forces during placement or release of the component when it is not in contact with the base component.

For both the open as well as closed loop systems it is therefore preferred to create a loop which is closed using a predefined force, often referred to as a force closed loop [Schellekens 98]. When

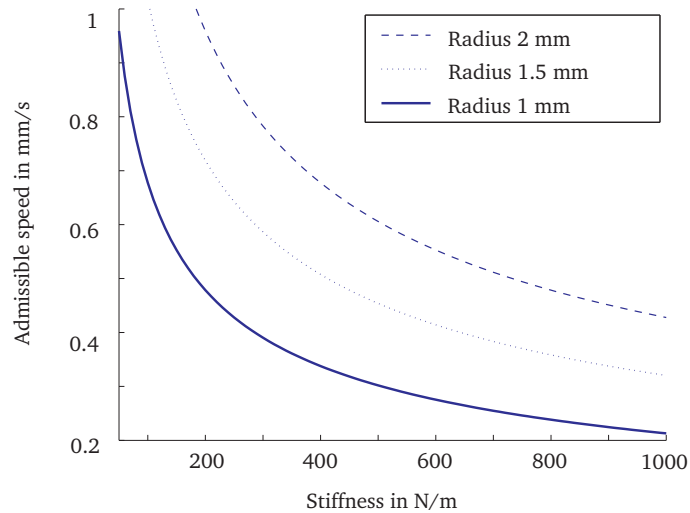


Figure 4.3: Effect of stiffness on the admissible approach speed when placing a sapphire sphere on a planar aluminum workpiece.

locally decreasing the loop stiffness, to reduce the static force, it is preferred to do this as close to the component as possible to minimize the negative effect on the dynamics of the system. One possibility is to realize this in the gripper, as will be discussed in section 4.

Another issue in micro assembly are surface forces as they are dominant over gravitational forces in the micro regime [Brussel 00]. There are possibilities to reduce the surface forces between a gripper and component, including the use of conductive materials, decreasing the contact area, use hard materials, use of a hydrophobic coating and working in a dry atmosphere or in ionized air [Brussel 00]. If the gravitational forces are not dominant over surface forces for a specific placement operation, an active release mechanism is needed.

4.4 Grippers for micro assembly

From the previous sections, several general requirements for a gripper can be stated:

- The gripper should be able to pick up a component at a specified position;
- The gripper should be able to release a component at a specified position;
- The contribution of the gripper to the positional uncertainty during assembly should be well, e.g. by a factor of 2-3, below the placement uncertainty of the assembly robot;
- The component should not be damaged during assembly, nor should physical properties of the component be changed by the interaction.

As discussed in section 4.3 and in chapter 2 these requirements are not as trivial as they may seem, especially when assembling micro components with macro scale equipment.

Several actuation principles can be used to pick up a component, including suction, electrostatic, magnetic, surface tension and friction forces. Tichem et al. [Tichem 04] provide an overview of grippers suitable for micro assembly, categorized by their actuation principle. Each actuation principle has its advantages and limitations when handling specific components. An example is the magnetic force which is influenced by the magnetic susceptibility of the component material. Also, the components may be damaged by the physical contact between gripper and component or by the actuation principle. An example of the latter is the damage that may be inflicted to sensitive electronic components by electrostatic gripping. The best actuation principle thus depends on the

part to be manipulated, the environment and the requirements to the assembly operation; e.g. cycle time and placement uncertainty.

As mentioned in section 4.3, the effects of surface forces are an important challenge during the handling of micro components. For a large number of components these surface forces are dominant over gravitational forces, making it more difficult to release them. Therefore care must be taken to minimize these forces during assembly and it is thus needed to use an active release mechanism.

An actuation principle that is widely used in both macro and micro assembly, is the suction gripper [Brussel 00, Tichem 04]. The design of this gripper usually consists of a thin tube or pipette connected to a vacuum pump and is thus cheap to manufacture and easy to replace. Also the cycle time can be well below 100 ms. Furthermore it has the option to release components using a puff of air, it is usable on a wide range of materials and it does not alter the properties of the gripped component.

The main limitation of a suction gripper is the physical contact between gripper and component. As discussed in section 4.3 this leads to high collision and static forces during the pick up and placement of components, possibly damaging them. Other limitations are the handling of certain kinds of porous materials and the possibility that small particles obstruct the tube. The presence of particles is a common problem during micro assembly, which is therefore usually performed in a clean room environment.

An advantage of a suction gripper is that the positional deviations between gripper and component after the pick up operation are small. However, several effects may change the relative position between component and gripper during the pick up operation. These include effects as a result of the suction forces, the feeding of the components and effects of the vibrations introduced by the collision between gripper and component. In many cases, the component is therefore re-oriented after the pick up operation; e.g. using a vision system.

To reduce the collision forces during assembly and thereby decreasing plastic deformation of the components Höhn et al. [Höhn 99] developed an aerostatic gripper. Here the component is suspended on an air cushion which prevents physical contact between gripper and component. The preload force is, similar to a vacuum preloaded air bearing, supplied by a suction nozzle. However, mechanical stops are needed to secure the lateral position and the rotation of the part around the gripper axis. Also, the stiffness of the gripper in axial direction is still high, which may result in high static forces during assembly, as discussed in section 4.3. A force closed loop would reduce the static forces caused by the over travel of the assembly robot.

4.5 Design of the gripper

Specifications for the gripper can be deducted from the general requirements discussed in the previous section. It is also mentioned that a suction gripper is useful to pick up and fixate a wide variety of materials, has a low cycle time, is widely used and it has the option to release components using a puff of air. The first two general requirements for a gripper, as mentioned in the previous section, can therefore be fulfilled using a suction gripper.

The third requirement: 'the contribution of the gripper to the positional uncertainty during assembly should be well below the placement uncertainty of the assembly robot' depends on the assembly robot used. A quick survey of assembly robots [Opstal 06] yields an achievable placement uncertainty of 5-100 micrometers. For the gripper to be useful in these assemblers the contribution to the placement uncertainty should therefore be well below 2 micrometers.

The fourth requirement: 'the components should not be damaged during assembly, nor should the properties of the component be changed by the interaction' depends on the actuation principle. A suction gripper does not change the properties of the components. However the physical contact may damage the components, as shown in section 4.3. Therefore the fourth requirement is made explicit by specifying that no plastic deformation should occur when a sapphire sphere with diameter of 1 mm is placed on a planar aluminum workpiece, $\sigma = 300 \cdot 10^{-6} \text{ N/m}^2$ and $E_{red} = 70 \cdot 10^9 \text{ Pa}$, with an approach speed of 1 mm/s. The assembly robot is assumed to decelerate with 10 mm/s^2

after a reaction time t_r of 2 ms. With these values a maximum equivalent mass of 1.4 gram and a maximum stiffness of the placement loop of 2500 N/m is obtained using equations 4.3 and 4.4.

The general requirements from the previous section thus lead to the following additional specifications for the new gripper design:

- The components are gripped and fixated using suction;
- The total positional uncertainty introduced by the gripper should be less than 2 micrometers;
- The equivalent mass which is rigidly connected to the component should be less than 1.4 gram;
- The stiffness of the gripper in axial direction should be less than 2500 N/mm.

The proposed design is shown in figure 4.4 [Bos 07A, Bos 07B]. In this design the needle of the suction gripper (10) is suspended using a radial porous air bearing (5). During a movement of the assembler, with attached gripper, the axial position of the needle is constrained using a mechanical stop (2). This mechanical stop is pre-loaded using a bellow (8), as shown in figure 4.4. The bellow is also used to prevent rotation of the needle around its axis. As a result the needle is constrained in 6 degrees of freedom (DOF) during movement of the assembler.

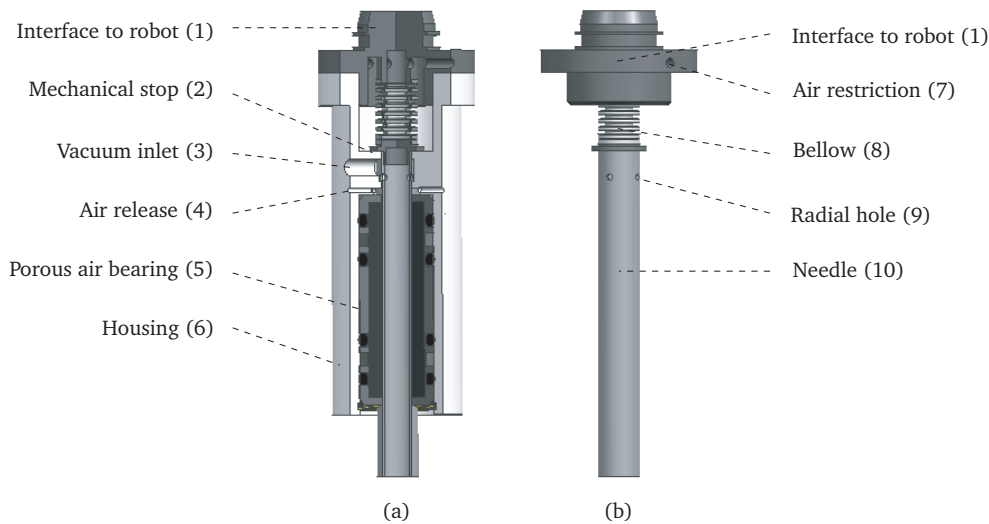


Figure 4.4: Schematic of the new gripper design, (a) front view of the gripper with a cutout section, (b) subassembly of the needle, bellow and interface to the robot.

During a pick up operation the assembler positions the gripper to make contact with the component to be picked up. When the gripper collides with the component the needle moves in axial direction into the gripper housing (6), guided by the porous air bearing (5). The equivalent mass during this collision is therefore limited to the mass of the needle and the equivalent mass of the bellow, which acts as a spring. For a given approach speed the collision force is thus reduced compared to a traditional gripper, as shown in the next section.

When, during a pick up or placement operation, the needle is moved from its axial zero position, the resistance of an electrical circuit between the mechanical stop and the needle is altered. A signal is given to the (robotic) assembler, which stops its movement. As discussed in section 4.3, the forces as a result of the over travel of the assembler are influenced by the stiffness of the loop between both components and thus by the bellow stiffness. Since the equivalent mass is low, as discussed in the previous paragraph, the forces due to accelerations of the needle are reduced. As a result the bellow stiffness can be decreased, which decreases the force as a result of the over travel of the assembler. The force as a result of the over travel of the assembler is thus reduced when the bellow stiffness is decreased.

To secure the component after contact between gripper and component a low pressure level, hereafter referred to as vacuum, is supplied to the vacuum inlet (3). The lateral position of the component is fixated via physical contact between the needle and component. The vacuum is supplied to the gripper needle using a vacuum inlet chamber in the gripper housing and radial holes in the needle (9), as shown in figure 4.4. By measuring pressure variations in the vacuum supply, contact with the component is detected.

A prototype version has been manufactured, as shown in figure 4.5. The gripper needle has a length of 45 mm and an outside diameter of 6.3 mm. For its high stiffness to weight ratio aluminum is selected for the needle, resulting in a mass of 1.3 grams. A second needle is manufactured from a high purity magnesium alloy (MgAl9Zn1). The magnesium needle weighs approximately 0.8 grams, well below the 1.4 grams specified. To allow the handling of miniature components a nozzle is mounted onto the gripper needle. The nozzle is exchangeable to allow handling different size components.

Magnesium has good material damping, but does not form a protective oxidation layer like aluminum. The corrosion rate of magnesium greatly depends on its purity, alloy components and the environment [Kainer 00]. For the high purity alloy used a corrosion rate of several micrometers per year is expected in a low-humidity clean room environment [Song 03]. These effects are not expected to influence the placement uncertainty introduced by the gripper. However, the properties of the air bearing will be influenced over time as a result of the increasing air gap, which limits the life span of a magnesium needle.

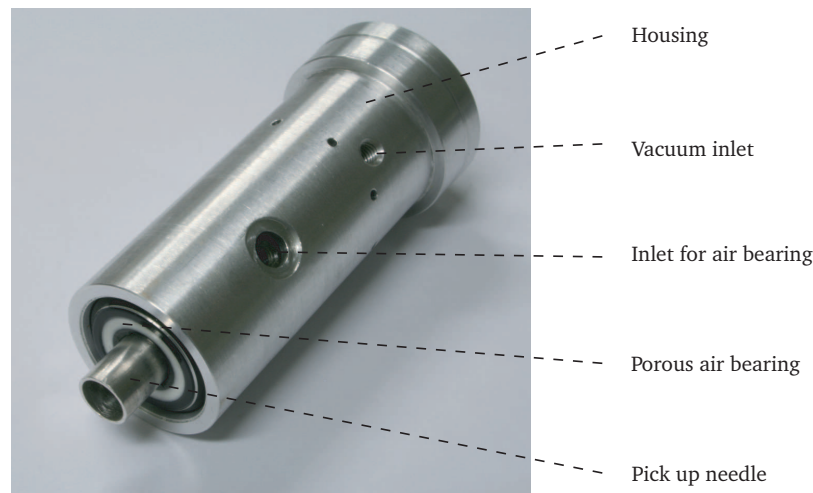


Figure 4.5: Picture of the assembled gripper.

A mechanical stop with an axial stiffness of approximately $2 \cdot 10^5$ N/m is used in the prototype gripper. The needle is preloaded using a bellow with an axial stiffness of 50 N/m. It can be calculated that a preload distance of 50 micrometers results in an axial eigen frequency of the needle of 180 Hz. Also, when the needle moves in the gripper housing, e.g. during a collision, air from within the bellow and the top chamber is forced out via several air restriction holes, indicated by (7) in figure 4.4. This functions as an air damper and further improves the dynamical behavior of the gripper.

In the proposed design the vacuum hose is connected to the gripper housing. The vacuum pressure is supplied to the gripper needle using a vacuum inlet chamber and radial holes in the needle, as discussed earlier. There is no direct physical contact between the vacuum hose and the needle. As a result the forces due to pressure variations in the hose and deformations of the hose during movement of the assembler operate on the gripper housing, decreasing their effect on positional deviations of the needle.

The needle itself is suspended using a radial air bearing. As a result, friction and hysteresis in the design are neglectable. The absence of friction also reduces the formation of particles. To prevent crosstalk between the air bearing and the vacuum inlet chamber an intermediate chamber

is manufactured. This chamber is connected to the environment using several holes, indicated by (4) in figure 4.4, in the gripper housing.

The center of mass of the needle is designed to be slightly above the center of the porous air bearing. As a result, the counter mass on the top of the needle partly balances the mass of the component when the gripper is accelerated in radial direction. Positional deviations of the needle with respect to the housing have been calculated to be less than 1 micrometer for components up to 1 gram and accelerations up to 10 G in any direction. When required, the dimensions of the gripper can be reduced using a custom air bearing or a magnetic bearing. This further reduces the equivalent mass and stiffness, making it even better suited for the assembly of small components.

4.6 Experimental results

As discussed in the previous section a vacuum chamber and radial holes in the needle are used to create a pressure in the needle. However, since the flow restriction between the vacuum chamber and the environment is limited, air will flow from the environment to this chamber or vice versa, depending on the pressure inside the chamber. A high flow loss is an indication of a poor flow resistance and may cause the gripper to blow away small components.

Figure 4.6 shows the flow loss in the gripper as a function of the pressure inside the needle. For this gripper a needle pressure of 20 kPa corresponds to a pick up or release force of approximately 0.5 N. With this fixation force the gripper with attached component can be accelerated up to 11 G without releasing the component; for a component mass below 1 gram and a coefficient of friction of 0.2. The flow loss at this pressure is approximately 0.02 l/s. Another issue is the flow loss in the porous air bearing. This is specified to be less than 0.02 l/s. A displacement of spheres with a diameter of 100 μm or larger on a planar surface has not been observed during assembly with this gripper as a result of this flow loss.

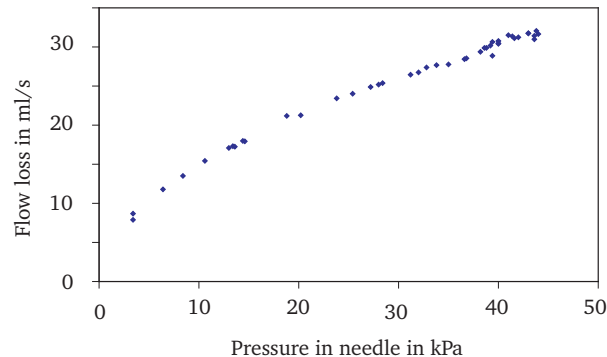


Figure 4.6: Flow loss in the gripper as a function of the pressure inside the needle.

The force during a collision is measured using the setup shown in figure 4.7. The gripper (2) is mounted on a column (1) using a clamp (4). The column is guided in vertical direction using roller bearings. A force sensor (5) is mounted under the gripper needle using a clamp (6). The column is risen so that the distance between the gripper needle and the force sensor is 1 mm. After release of the column gravity accelerates it with the attached gripper in the direction of the force sensor.

After a fall distance of 1 mm the gripper needle collides with the force sensor with a speed of approximately 130 mm/s. The gripper housing is connected to the column and the gripper needle is now in contact with the force sensor. Since the column continues its free fall after the collision, the needle is thus pushed inside the gripper housing. The forces between the gripper needle and the force sensor for the first 9 ms are shown in figure 4.8.

To protect the gripper a mechanical stop is implemented between the column (1) and sensor clamp (6). When the column collides with the mechanical stop its movement ends. The collision between

the column and the mechanical stop on the sensor clamp also results in vibrational forces between gripper and sensor. However, as this occurs at a later point in time, the forces as a result of this second collision are not shown in figure 4.8.

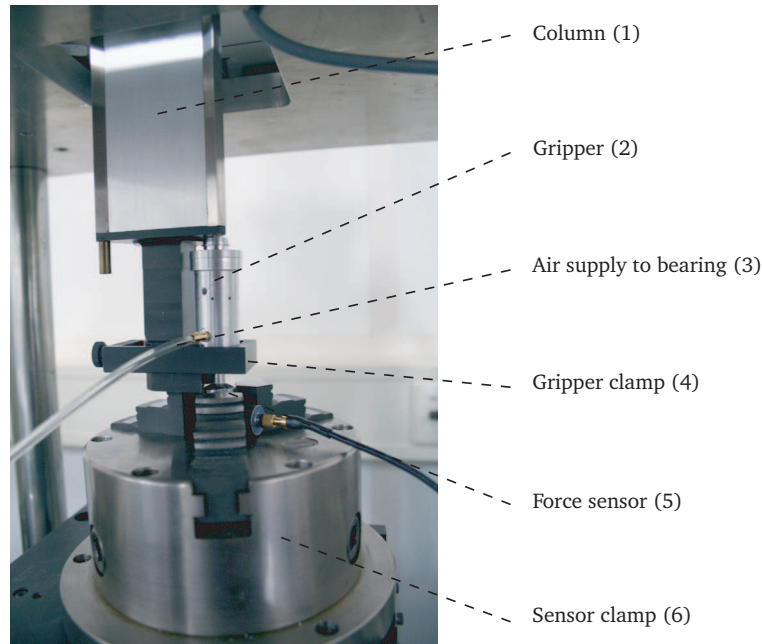


Figure 4.7: Setup used to measure the collision force.

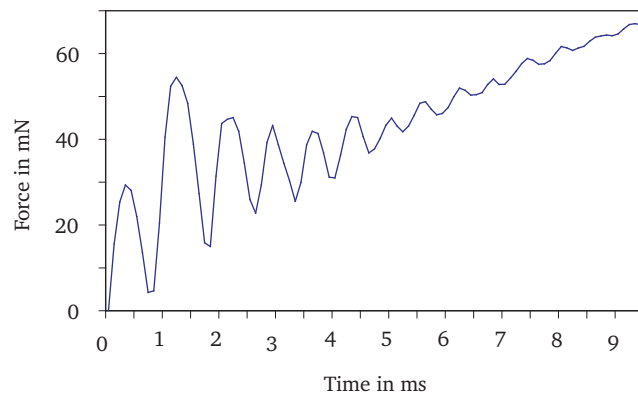


Figure 4.8: Forces as measured during a collision with the gripper at an approach speed of 130 mm/s.

It can be seen that even with an approach speed of 130 mm/s the forces during collision remain less than 60 mN. The initial build up of force is most likely caused by the preload of the bellow, as discussed in section 4.5. A preload force of 15 mN, indicates a preload distance of the bellows of approximately 300 micrometers. This is higher than required and as specified in the design. This may be caused by a poor length tolerance on the bellow. The preload force could be decreased by adjusting the internal dimension of the gripper housing after assembly.

Another point of interest are the peaks in the force curve. It can be seen that the maximum force is not achieved during the initial collision, but during the second collision. This is caused by the collision dynamics. The force sensor consists of a mass suspended on a spring. After the first collision, the gripper will bounce off the sensor. The sensor mass itself will also bounce off the gripper in the opposite direction. Since the column continues its movement, the relative speed during the second collision will be increased, resulting in a higher force. After the second collision

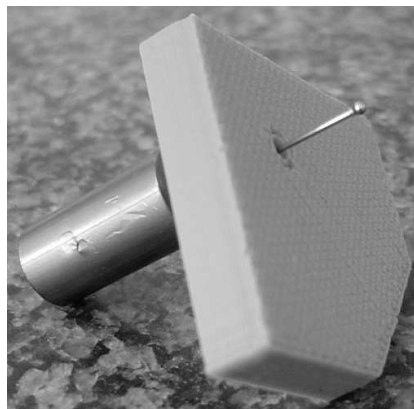
the vibration is damped within several milliseconds, showing the good dynamic behavior of the gripper as a result of the low moving mass and the air restriction holes. Finally it can be seen that the build up of force continues after the collision. This is expected since the column continues its free fall after the collision.

The gripper is successfully used to pick up and release several sapphire spheres with a diameter of 0.3 mm. Positional deviations of the needle with respect to the housing have been calculated to be less than 1 micrometer for accelerations up to 10 G and components up to 1 gram. The requirements as stated in section 4.5 have therefore been met.

4.7 Assembly of the probe

Initially, assembly of the probe by Pril [Pril 02] was performed manually by a skilled technician using tweezers and a microscope. This process is time consuming and the standard deviation in the 3D placement uncertainty at the probe tip is approximately 0.2 mm. Also, since the chip suspension is fragile, the yield during assembly was approximately 60 - 80%, which is insufficient.

Therefore, a redesign of the probe, as shown in figure 4.9, was developed to facilitate the assembly of the probe.



(a) Redesign of the probe



(b) Photo of chip on substrate

Figure 4.9: Photo's of the redesign of the probe where the chip is mounted on a ceramic substrate.

This redesign was assembled using an automated assembly line, developed by TNO Industry in Eindhoven, as shown in figure 4.10.

As mentioned at the start of this chapter, tolerances on parts may show a large variation for micro components. The styli used during assembly showed a standard deviation in length of approximately 0.1 mm due to manufacturing tolerances. The high stiffness of the assembler resulted in high contact forces, as discussed in section 4.3. The resulting plastic deformation of the stylus often rendered a part useless for further assembly. Also, the suspension of several test chips was damaged due to these forces.

To reduce the assembly forces the gripper, as discussed in this chapter, was developed and the design of the probe was modified, as shown in figure 4.11. An important improvement in the design is that the center platform of the suspension is integrated in the silicon chip using a deep reactive ion etching (DRIE). This eliminates deviations due to alignment of these parts. Also, no adhesive is required to assemble the components and the coefficient of thermal expansion of the center platform and chip are equal, which improves the measurement behavior. This eliminates the most critical step in the assembly.

A remaining critical step is the assembly of the stylus onto the probe chip. To reduce the influence of the stylus length on the assembly and improve handling of the stylus by a nozzle a support part



Figure 4.10: Automated assembler used to assemble the probe, photo courtesy of SenterNovem.

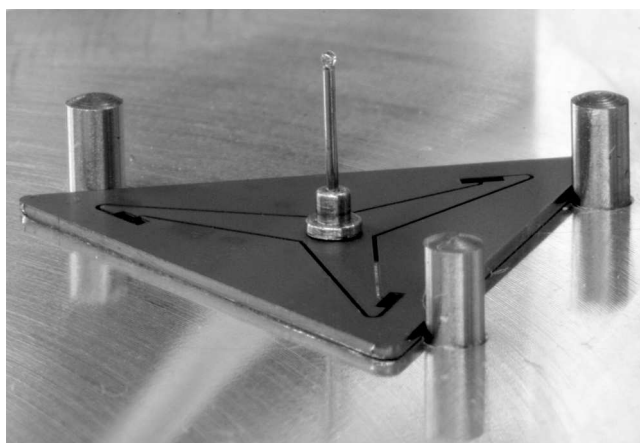


Figure 4.11: Photo of assembled probe.

is added to the stylus base. The support is in contact with the probe chip along its outer rim, thus increasing the contact area, which improves the alignment of the stylus with respect to the chip and the contact stiffness. The contact stiffness is of interest, since deformations of the glue layer between parts causes hysteresis during measurements, as discussed in section 2.5.2.

Assembly of the stylus onto the new probe chip is shown schematically in figure 4.12. It can be seen that the fragile parts do not deform during assembly, as the center platform is supported by the assembly plane. Also, alignment of the chip in the assembler is now done in a statically determinate way, in which all degrees of freedom in the plane are fixated once and a controlled force is used to position the chip in the assembler.

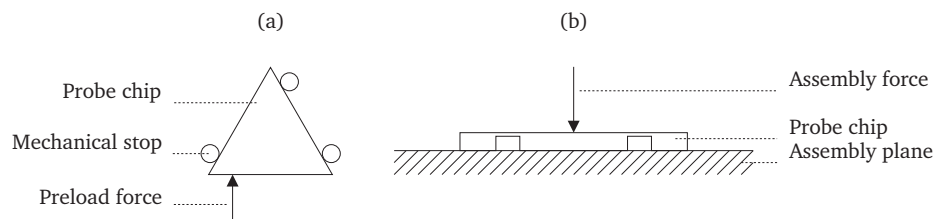


Figure 4.12: Schematic of the probe assembly, (a) top view and (b) side view.

Currently, assembly is performed manually using the tool shown in figure 4.13. The main virtues of the gripper, as discussed in this chapter, are used in the design of the tool. The probe chip (8) is aligned in the tool using three mechanical stops (4), as schematically shown in figure 4.12. A nozzle (3) is used to pick up a stylus and place it onto the probe chip (8). First, the nozzle (3) is positioned close to the chip (8) using the coarse adjustment handle (7) and guide way (1). Then, the stylus is placed onto the chip using a fine adjustment screw (5). The static force during placement is controlled by the over travel, as controlled by the fine adjustment screw (5) and the stiffness of the leaf springs (2).

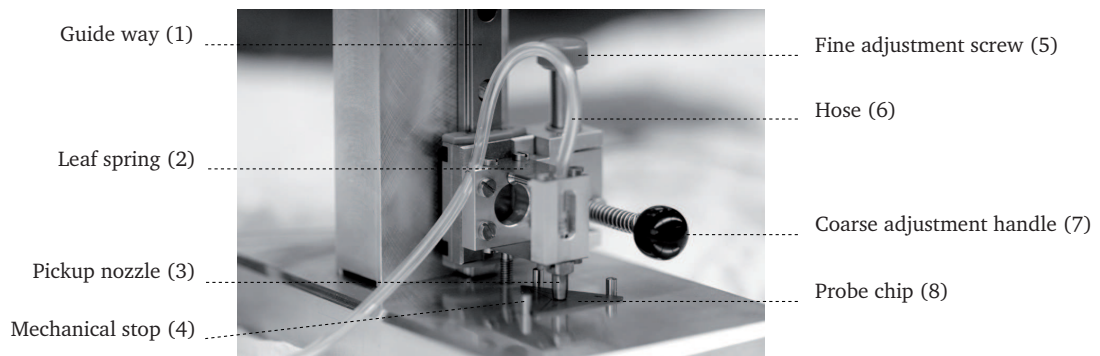


Figure 4.13: Closeup photo of assembly tool.

The development of the assembly tool and the redesign of the probe resulted in an improvement in placement uncertainty at the tip by a factor of 10 and an increase in yield during assembly from 60 - 80% initially, to over 95%.

Once the probe chip, stylus and tip are assembled they are placed into a holder cap, as shown in figure 3.20 and can be stored for future use. The yield during assembly and use of the probing system thus primarily effects the replacement costs of the probe chip. As a result the replacement costs of the probe with respect to the design by Pril [Pril 02] have been reduced by almost a factor of 10.

In future work the gripper, as discussed in this chapter, will be used in an automated assembler to assemble the probe. It is expected that yield and positional deviations during assembly will be improved further.

4.8 Conclusions

A new design for a suction gripper is proposed. In the design friction and hysteresis are neglectable. A prototype gripper is realized with a magnesium needle. It has a length of 45 mm, a diameter of 6.3 mm and a mass of 0.8 gram. A further reduction in gripper size is possible by using a custom air bearing or a magnetic bearing.

The needle in the prototype version is supported in axial direction using a bellows with a stiffness of 50 N/m. The axial needle position is prescribed by a mechanical stop, resulting in an eigen frequency of 180 Hz. Positional needle deviations with respect to the housing have been calculated to be less than 1 micrometer for accelerations up to 10 G and components up to 1 gram. The requirements as stated in section 4.5 have therefore been met.

The collision force with the gripper for an approach speed of 130 mm/s is measured to be 60 mN or less. The gripper is successfully used to pick up and release several sapphire spheres with a diameter of 0.3 mm.

Finally, the assembly method designed for the novel probing system is tested using a manual assembly tool. The development of the assembly tool and the redesign of the probe resulted in an improvement in placement uncertainty at the tip by a factor of 10 and an increase in yield during assembly from 60 - 80% initially, to over 95%. The resulting replacement costs of the probe with respect to the design by Pril [Pril 02] have been reduced by almost a factor of 10.

Chapter 5

Experimental results

Experimental results with the tactile 3D probing system are discussed in this chapter. Unless stated otherwise in text, the probing system used has a sapphire probe tip with a radius of 250 μm and a stylus length of 6.8 mm. The first step is the calibration of the probing system as discussed in the next section. After the calibration the probe is used in a series of measurements. One of the most important characteristics of 3D probes is their repeatability, which is discussed in section 5.2. As discussed in chapter 2 surface forces play an important role in the interaction between probe tip and work piece, especially when measuring miniaturized components. The influence of these forces on the measurement behavior of the probing system is discussed in section 5.3.

The dynamic excitation of the probing system and signal noise, e.g. due to acoustic noise and vibrations of the measurement mirror in the calibration setup, is discussed in section 5.4 using a frequency analysis of the probe signal. Then, in section 5.5 the drift of the probing system over a 60 hour period is discussed. Finally, the combined 3D measurement uncertainty of the tactile 3D probing system is calculated in section 5.6.

5.1 Probe calibration

Measurements are performed in a temperature controlled laboratory and the probe system is shielded using a grounded steel box with a polyethylene foam interior. The temperature inside the laboratory and inside the box as measured over a 50 hour period is shown in figure 5.1. From this graph it can be seen that the applied shielding greatly reduces short term temperature variations. The maximum temperature variation of the laboratory and inside the isolation box over a 50 hour period is approximately plus minus 0.2 and 0.1 K, respectively.

Before the tactile 3D probing system is used in measurements its behavior is calibrated, as discussed in appendix A.2. The calibration is performed in 4 directions, shown in figure A.1, which are given by the displacement matrix \mathbf{D} :

$$\mathbf{D} = \begin{bmatrix} 0 & 1 & -\frac{1}{2} & -\frac{1}{2} \\ 0 & 0 & \frac{1}{2}\sqrt{3} & -\frac{1}{2}\sqrt{3} \\ -1 & 0 & 0 & 0 \end{bmatrix} \quad (5.1)$$

As discussed in section A.2 a linear relation between the measured voltages and the displacement of the probe tip is determined. The measured sensitivity of each of the three rods for each of the

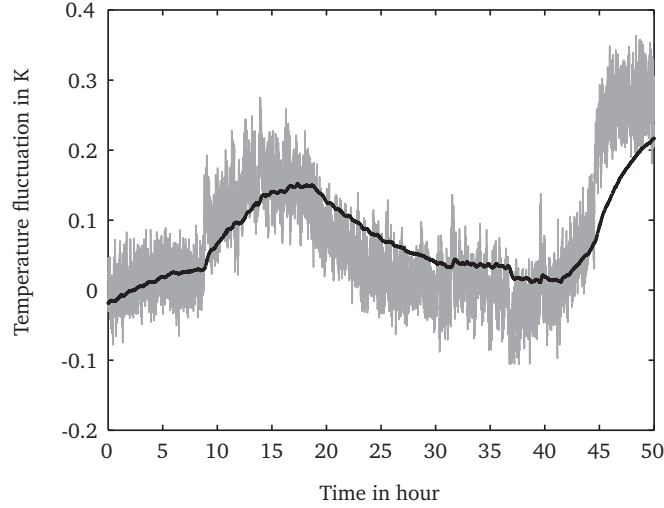


Figure 5.1: Measured temperature variation, grey line: temperature variation in the laboratory, black line: temperature variation inside the isolation box.

four measurement directions for the tactile 3D probing system is given by:

$$\mathbf{M} = 1 \cdot 10^6 \begin{bmatrix} 1.37 & -1.12 & -0.06 & 1.33 \\ 1.43 & -0.15 & 1.39 & -1.08 \\ 1.44 & 1.28 & -1.03 & -0.09 \end{bmatrix} \quad (5.2)$$

When the measured sensitivity matrix \mathbf{M} is known, the transformation matrix \mathbf{A} can be calculated:

$$\mathbf{A}^{-1} = \mathbf{M} \mathbf{D}^T (\mathbf{D} \mathbf{D}^T)^{-1} \quad (5.3)$$

For the tactile 3D probing system the transformation matrix \mathbf{A} is given by:

$$\mathbf{A} = 1 \cdot 10^{-7} \begin{bmatrix} -3.94 & -0.57 & 4.32 \\ -2.85 & 4.68 & -1.93 \\ -2.28 & -2.25 & -2.53 \end{bmatrix} \quad (5.4)$$

The probe tip displacements in x -, y -, and z -direction are indicated by Δt_x , Δt_y and Δt_z , respectively. Now that the transformation matrix \mathbf{A} is known, the displacement of the probe tip D_t in three dimensional space can be calculated as a function of the signals m_1 , m_2 and m_3 from the three slender rods:

$$D_t = \begin{bmatrix} \Delta t_x \\ \Delta t_y \\ \Delta t_z \end{bmatrix} = \mathbf{A} \begin{bmatrix} \Delta m_1 \\ \Delta m_2 \\ \Delta m_3 \end{bmatrix} \quad (5.5)$$

5.2 Probe repeatability

Once the transformation matrix \mathbf{A} is known, the measurement behavior of the probing system can be determined. The repeatability of the 3D tactile probing system is measured using a plane mirror differential laser interferometer setup, as discussed in section 1.6.1. Using this setup, the displacement of a mirror is measured by the probing system and laser interferometer simultaneously. The displacement as measured by the calibration setup d_c is one dimensional. Therefore it is multiplied by the direction in which the measurement is performed, see equation 5.1.

The residuals R in x -, y - and z -direction, r_x , r_y and r_z , respectively, between the displacement as measured by the laser interferometer and the same displacement as measured by the probing system in direction \mathbf{a} is thus given by:

$$R = \begin{bmatrix} r_x \\ r_y \\ r_z \end{bmatrix} = D_t - \begin{bmatrix} 0 \\ 0 \\ -1 \end{bmatrix} d_c \quad (5.6)$$

It is noted that in direction \mathbf{a} , a tip displacement in $-z$ -direction, it is assumed that the mirror of the calibration setup does not translate in x - or y -direction. Any displacement measured by the probing system in x - or y -direction, Δt_x and Δt_y , thus directly contributes to the residual between probe and laser in x - and y -direction, i.e. r_x and r_y .

The residuals in directions \mathbf{a} and \mathbf{b} for a repeatability test using 2050 measurement points are shown in figure 5.2. The residuals r_y and r_z have been given an offset of 20 and 40 nm, respectively, to improve readability of the graph. The maximum top-top deviation in figure 5.2 (a) is 11 nm. The standard deviation of the repeatability test is about 2 nm in all points.

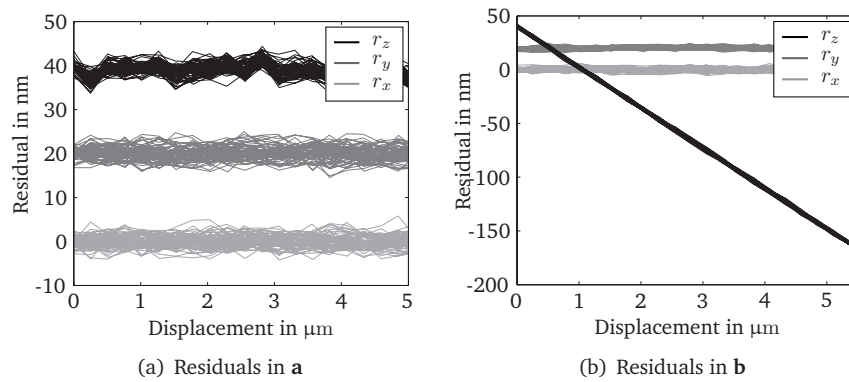


Figure 5.2: Residual between the displacement as measured by the tactile 3D probing system and the calibration setup.

In figure 5.2 (b) a linear increasing residual in z -direction, r_z , can be observed. This results from the rolling effect as discussed in section 2.2.1. Using equation 2.47 with a length l of 6.8 mm and a tip radius r_t of 250 μm , a displacement Δx of 5.5 μm of the probe tip in x -direction results in a displacement due to rolling of the probe tip on the work piece surface of 202 nm. Rolling of the probe tip on the work piece surface is thus accurately measured by the probing system and does not result in a measurement deviation.

The results from figure 5.2 are analyzed and the average value and standard deviation at each point is calculated. This is shown in figure 5.3, where a 95% confidence interval is indicated at each measurement point. The same graph for directions \mathbf{c} and \mathbf{d} is shown in figure 5.4. The standard deviation is about 2 nm in all points and for all directions of the repeatability test.

5.3 Effect of surface forces during measurements

The surface force measurements, as shown in figure 2.22 in section 2.1.7, were repeated with the new tactile 3D probing system. First the effects of the surface force when measuring in z -direction are discussed, as shown in figure 5.5. The probe tip is brought into contact with a steel gauge block at 25 nm positional increments. The probing system, used in this experiment, has an isotropic stiffness of 280 N/m.

From this graph it can be seen that the position of the probe tip is influenced by the work piece at a separation of approximately 125 nm. When the work piece is moved closer to the probe tip a snap in effect, as also shown in figure 2.22, is observed at a separation of approximately 50 nm.

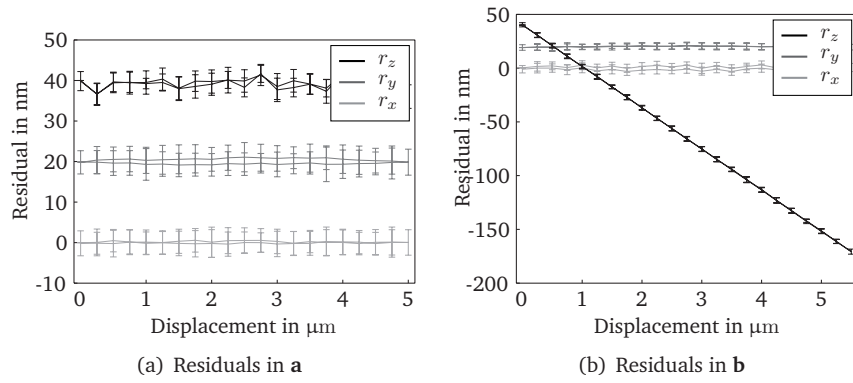


Figure 5.3: Residual between the displacement as measured by the tactile 3D probing system and the calibration setup. The vertical bars indicate a 95% confidence interval ($k = 2$).

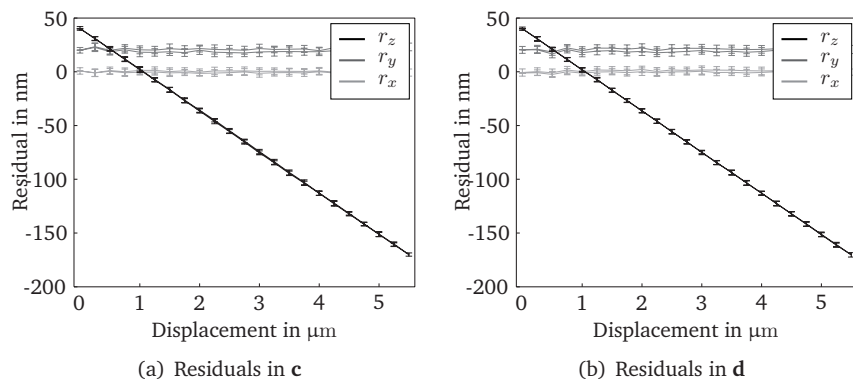


Figure 5.4: Residual between the displacement as measured by the tactile 3D probing system and the calibration setup. The vertical bars indicate a 95% confidence interval ($k = 2$).

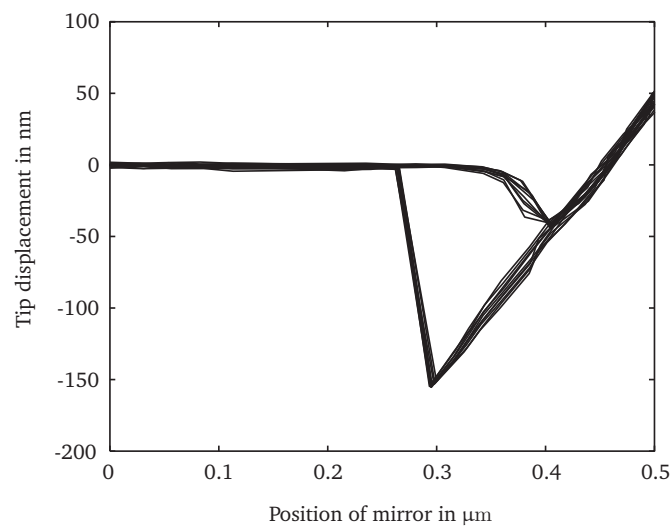


Figure 5.5: Measurement of the effect of surface forces when contacting a steel gauge block with a sapphire probe tip in z -direction.

The snap in force can be calculated to be approximately $14\ \mu\text{N}$. When the work piece is moved away from the probe tip after contact a snap out effect is observed at a separation of $150\ \text{nm}$, corresponding to a snap out force of $42\ \mu\text{N}$. From this graph it can also be seen that the snap in and snap out effects are repeatable.

This measurement is repeated in x -direction, orientation **b**, as shown in figure 5.6. From this graph it can be seen that the effect of the attraction between the work piece and probe tip is visible at a separation of $500 - 600\ \text{nm}$. Also, the snap in effect is much more pronounced when compared to figure 5.5. At a separation of $150\ \text{nm}$, corresponding to $42\ \mu\text{N}$, the probe tip snaps to the work piece. The increased snap in force in x -direction may be caused by the attraction between the stylus and work piece, as the stylus extended about $1\ \text{mm}$ over the steel gauge block in this experiment. Finally, after contact a snap out effect is observed at a separation of $210\ \text{nm}$, corresponding to a snap out force of $59\ \mu\text{N}$.

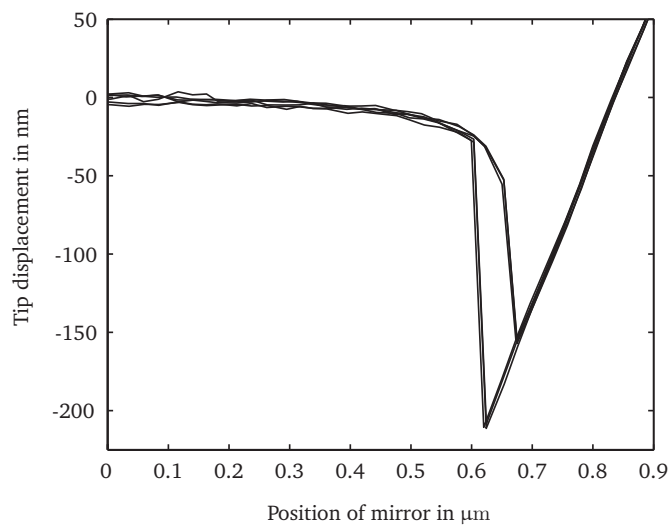


Figure 5.6: Measurement of the effect of surface forces when contacting a steel gauge block with a sapphire probe tip in xy -direction.

5.4 Frequency analysis

Figure 5.7 (a) shows the measurement signal in z -direction at a measurement frequency of $1\ \text{kHz}$ when the probe is freely suspended in open air. The standard deviation of this signal over a period of $1\ \text{second}$ is about $1\ \text{nm}$ with a top-top deviation of $5.4\ \text{nm}$. As mentioned in section 2.1.9 a freely suspended probe is susceptible to floor vibrations and acoustic excitations. This can be observed from the graph of the power spectral density of this signal, as shown in figure 5.7 (b). At the first eigen frequency of the probe, a vibration at $550\ \text{Hz}$ in z -direction, a clear peak can be observed in the power spectral density graph. The energy content of this peak corresponds to a root-mean-square (rms) noise of $0.9\ \text{nm}$.

The remaining peaks in figure 5.7 (b) are most likely the result of flicker noise in the electronic components. Flicker noise, often referred to as $1/f$ noise, results from fluctuations in the conductance and is proportional to $f^{-\gamma}$, where γ is in the range of $0.8 - 1.4$ [Hooze 94, Wong 03].

To decrease the positional noise of the probing system due to acoustic excitation a polyethylene foam shielding has been applied. The power spectral density of the probe signal when shielded is shown in figure 5.8 (a). The energy content of the peak at $550\ \text{Hz}$ is reduced to a root-mean-square (rms) noise of $0.3\ \text{nm}$. This shows that the applied shielding not only decreases thermal fluctuations of the probing system, but also decreases the influence of acoustic disturbances.

The positional noise due to acoustic noise and floor vibrations is also expected to decrease when the probing system is brought into contact with a surface. This is shown in figure 5.9 where the

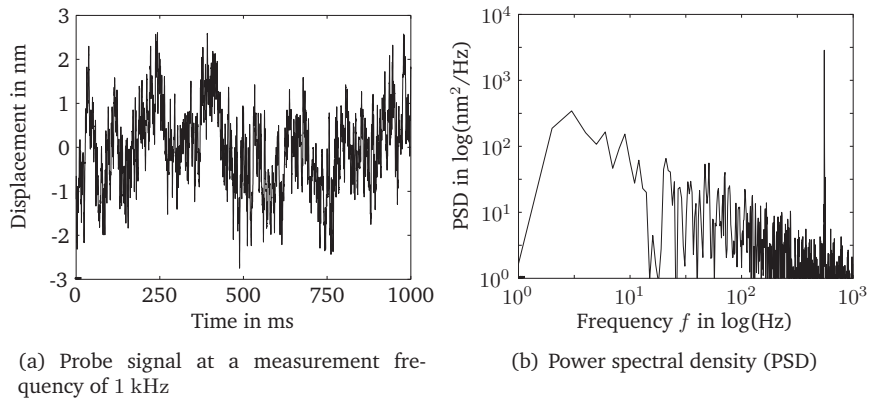


Figure 5.7: Measurement signal of the probe when freely suspended in open air: (a) time signal, (b) power spectral density (PSD) of the time signal.

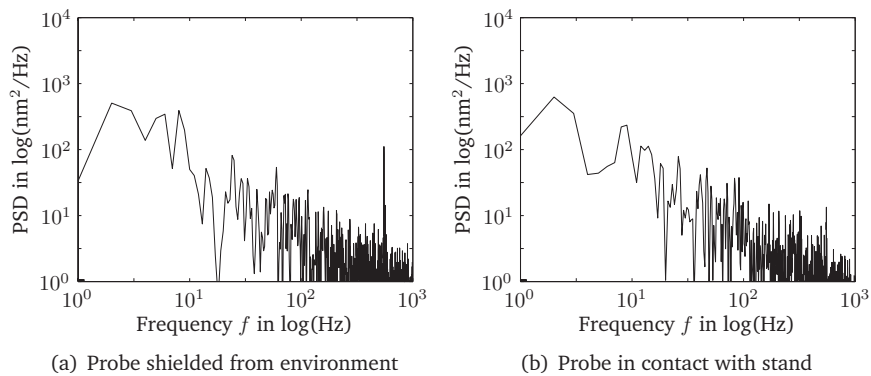


Figure 5.8: Power spectral density of probe signal: (a) freely suspended and shielded from environment, (b) probe in contact with a fixed aluminum stand at a nominal deflection of $2.6 \mu\text{m}$.

probe is placed in an aluminum bracket and positioned on top of a fixed aluminum stand. The nominal deflection of the probing system in this setup was measured to be $2.6 \mu\text{m}$.

Figure 5.8 (b) shows the power spectral density of the probe signal when in contact with the aluminum stand. The root-mean-square noise at 550 Hz, the eigen frequency of the probing system, is reduced to about 0.1 nm and is thus not expected to have a significant influence on the measurement uncertainty of the probing system.

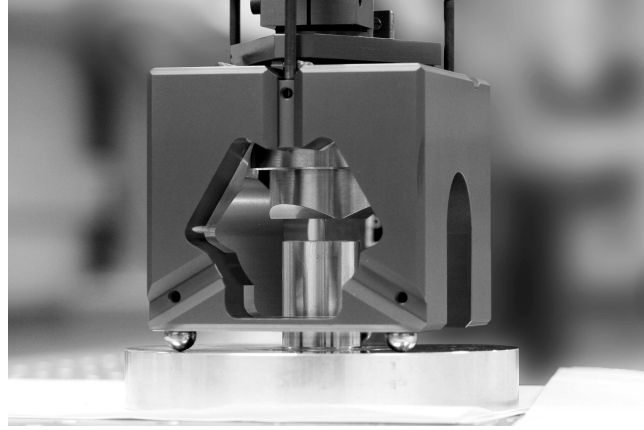


Figure 5.9: Photo of probe in contact with a fixed aluminum stand.

Finally, the influence of contact with the calibration setup, as described in section 1.6.1, is shown in figure 5.10. After contact with the calibration setup the frequencies 50, 150, 250, 350 Hz... contain a clear peak in the power spectral density graph. Typical sources of these odd order harmonic noise components include fluorescent lighting, power cables and ground loops. It should be clear by comparing figure 5.10 to figure 5.8 that these peaks are introduced by the calibration setup. It was found that the peaks result from the piezo actuator used to drive the measurement mirror.

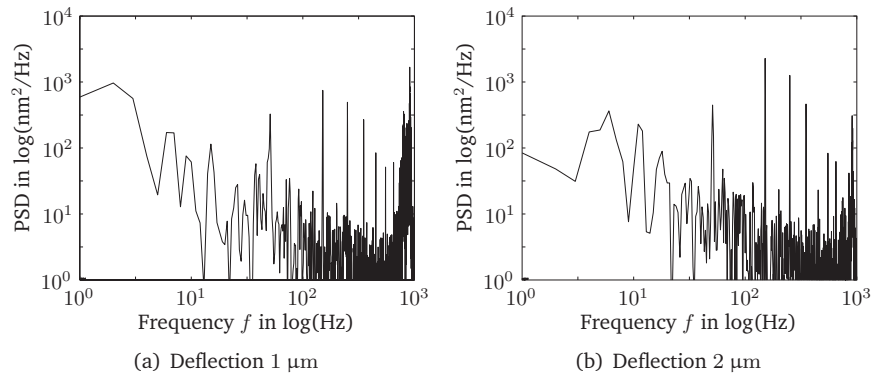


Figure 5.10: Power spectral density of probe signal when in contact with calibration setup: (a) at a deflection of $1 \mu\text{m}$, (b) at a deflection of $2 \mu\text{m}$.

A second observation from figure 5.10 is a peak around 900 Hz. This is caused by a vibration of the measurement mirror, with the added weight of the calibration artifact, in z -direction in its first eigen frequency. The experiment is repeated at displacements up to $8 \mu\text{m}$ at $1 \mu\text{m}$ intervals. The frequency and energy content of the peak around 900 Hz is approximately equal at each position. The standard deviation in the measurement signal of the probing system in contact with the calibration setup is less than 2 nm in x , y and z .

5.5 Drift of the probing system

The drift of the probing system is shown in figure 5.11. In the left hand graph the drift in the measurement signal of a freely suspended probe is shown, i.e. no contact between the probe tip and work piece. Measurements are taken at 10 second intervals and a running average is taken over 10 points to separate the effects of drift from signal noise.

From figure 5.11 (a) it can be seen that over a measurement period of 60 hours, the maximum top-top deviation due to drift in a 20 minute interval is 2 nm. A typical top-top deviation during this measurement over a 20 minute interval is 1 nm. The maximum and typical standard deviation over a 20 minute interval are 0.6 and 0.2 nm, respectively.

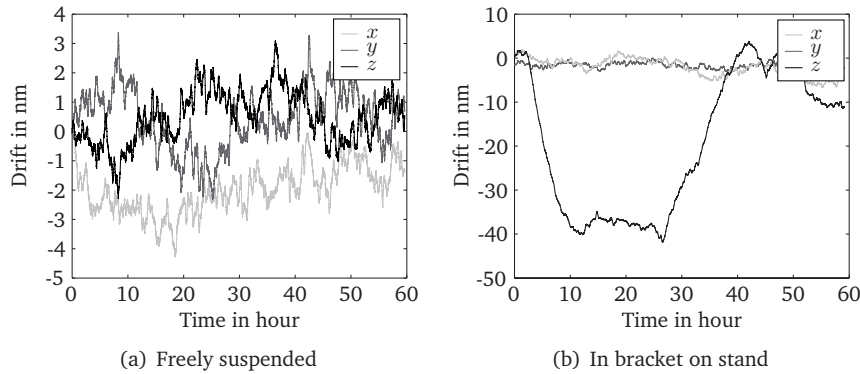


Figure 5.11: Drift of the probing system over a 60 hour period, (a) when freely suspended, (b) in bracket on stand.

Figure 5.11 (b) shows the drift in the measurement signal of the tactile 3D probing system when the tip is in contact with an aluminum stand, as shown in figure 5.9. It can be seen that during a 60 hour measurement the measurement signal in z -direction shows a top-top drift of approximately 45 nm.

This is caused by the difference in the coefficient of thermal expansion between the aluminum stand, $\alpha = 23.2 \cdot 10^{-6} \text{ K}^{-1}$, and the Invar probe holder, $\alpha = 3.6 \cdot 10^{-6} \text{ K}^{-1}$. The length of the Invar probe holder in z -direction is about 30 mm. The difference in the coefficient of thermal expansion, $19.6 \cdot 10^{-6} \text{ K}^{-1}$, over a length of 30 mm results in an difference in expansion of 588 nm/K. A drift of 45 nm thus results from a homogeneous temperature variation of 77 mK, also see figure 5.1. The thermal drift as measure on the aluminum stand is thus mainly caused by the stand itself.

From figure 5.11 (b) it can be seen that over a measurement period of 60 hours, the maximum top-top deviation due to drift in a 20 minute interval is 3 nm. A typical top-top deviation during this measurement over a 20 minute interval is 1 nm. The maximum and typical standard deviations over a 20 minute interval are 0.9 and 0.3 nm, respectively.

5.6 Uncertainty evaluation of the probing system

The 3D measurement uncertainty [Gum 93, Schellekens 02] of the tactile 3D probing system is shown in table 5.1. The total measurement uncertainty of the probing system ($k = 1$) within a $5.5 \mu\text{m}$ range, using the calibration setup discussed in section 1.6.1, is 8.7 nm. The uncertainty at 95% confidence interval ($k = 2$) is therefore 17.4 nm. The values from table 5.1 will be discussed in the remainder of this section.

The repeatability of the probing system is discussed in section 5.2. The results in this section are obtained using 2050 measurement points within a $5.5 \mu\text{m}$ range over a 60 hour period. Each measurement cycle lasted approximately 5 minutes and drift of the probing system during this

	Uncertainty in nm without compensation	Uncertainty in nm with compensation
<i>Probe uncertainty</i>		
3D repeatability	3.5	3.5
Hysteresis and micro slip	1.0	1.0
Drift in electronics	0.4	0.4
Uncertainty due to calibration	3.5	0.9
<i>Combined 3D uncertainty ($k = 1$)</i>	<i>5.1</i>	<i>3.8</i>
<i>Other effects</i>		
Tip roundness and diameter	5.8	5.8
Work piece deformation	4.0	< 1.0
<i>Combined 3D probe uncertainty ($k = 1$)</i>	<i>8.7</i>	<i>7.0</i>

Table 5.1: Uncertainty evaluation of the tactile 3D probing system.

	Uncertainty in nm without compensation	Uncertainty in nm with compensation
Dead path length	< 0.1	< 0.1
Refractive index of air	< 0.1	< 0.1
Wavelength instability	< 0.1	< 0.1
Periodic deviations	1.2	< 0.1
Drift in bracket and holder	0.9	0.9
Mechanical misalignment	3.2	< 0.1
<i>Combined setup uncertainty ($k = 1$)</i>	<i>3.5</i>	<i>0.9</i>

Table 5.2: Uncertainty evaluation of the calibration setup.

time is included in the repeatability of the probing system. The repeatability in all points and in all directions is about 2 nm, resulting in a combined 3D uncertainty ($k = 1$) in repeatability of 3.5 nm.

Hysteresis and micro slip result in a hysteresis curve, as discussed in section 2.5.2. Figures 5.3 and 5.4 in section 5.2 show that the distance d_h between the curves for the forward and backward movement is 2 nm or less for all directions, corresponding to a hysteresis percentage H of 0.04%. Using a square distribution a standard deviation due to hysteresis and micro slip of 0.6 nm is obtained, which results in a combined 3D uncertainty ($k = 1$) of 1 nm.

The drift in probe electronics is measured in section 5.5. For a freely suspended probe a typical standard deviation of 0.2 nm is obtained, resulting in a combined 3D uncertainty ($k = 1$) of 0.4 nm.

The uncertainty due to the calibration using the plane mirror differential laser interferometer, as discussed in section 1.6.1, is shown in table 5.2. The main contribution to the measurement uncertainty in the probe calibration is the mechanical alignment between the probe and measurement mirror in the various orientations. The mechanical alignment results in a systematic deviation, the influence of which can be decreased by improving the alignment or by compensating for its influence. Without this compensation the uncertainty due to calibration is 1.8 nm in each direction, resulting in a combined 3D uncertainty ($k = 1$) of 3.1 nm for the calibration of the probe. The contributions to the measurement uncertainty of the calibration are discussed in appendix H.

The contribution of the roundness and diameter of the probe tip is included after calibration,

as discussed in section 1.6.3. It is shown that the maximum contribution of tip roundness and diameter after calibration is 20 nm. Using a square distribution a standard deviation of 5.8 nm is obtained.

The final contribution is work piece deformation, as discussed in section 2.3.3. The contribution of work piece deformation can be compensated for or a low force probing strategy can be used, e.g. extrapolating measurement data to the point of zero contact force. It is noted that the effects of work piece deformation are included in the calibration procedure of the probing system. If no compensation or low force probing strategy is used, the maximum deviation due to work piece deformation will be plus minus 7 nm at a deflection of 5.5 μm . Using a square distribution a standard deviation of 4 nm is obtained.

5.7 Conclusions

Calibration of the tactile 3D probing system, as discussed in this thesis, is performed in a temperature controlled laboratory. The probing system is shielded using a steel box with a polyethylene interior, resulting in a maximum temperature variation of approximately 0.1 K. The resulting maximum top-top drift of a freely suspended probe is about 1 nm over a 20 minute measurement and 2 nm over a 60 hour measurement.

The repeatability of the probing system is measured over a 6 hour period using 2000 measurement points over a repeated 5.5 μm displacement at the probe tip. The single point repeatability at each position at a 95% confidence interval ($k = 2$) is measured to be 4 nm. The 3D repeatability at each position within the 5.5 μm tip displacement interval is measured to be 7 nm.

The effect of surface forces when probing an aluminum work piece using a sapphire probe tip with a 250 μm tip radius are measured. It is shown that the effect of surface forces when probing in z -direction, along the length direction of the stylus, in these experiments can be observed at a separation of 125 nm. At a separation of 50 nm, corresponding to approximately 14 μN , the probe tip snaps to the work piece. The snap out force in this experiment is measured to be approximately 42 μN .

When repeating the measurement in x -direction, the magnitude of the surface forces was measured to increase significantly. This may be the result of surface forces between the stylus and work piece, as the stylus extended about 1 mm over the work piece in these experiments.

Finally, the combined 3D uncertainty of the probing system with a 95% confidence interval ($k = 2$) is estimated to be 17.4 nm. Main contributions to the probing uncertainty include the systematic uncertainty due to probe calibration and the deformation of the work piece and probe tip. When these systematic deviations are compensated for or a low-force probing strategy is used, a combined 3D uncertainty ($k = 2$) of 14 nm can be obtained.

Chapter 6

Conclusions and recommendations

6.1 Conclusions

A new tactile probing system for 3D metrology on MEMS and other miniaturized components has been developed, manufactured and tested. The probing system has a 1D repeatability of 2 nm in any direction and has a combined 3D uncertainty ($k = 2$) of 17.4 nm. A ratio between the length and radius of the measurement part of the stylus of 50 can be obtained, making the probing system suitable for measuring deep and narrow structures.

Several micro spherical probe tips are manufactured. The first method uses a borosilicate fiber which is given a set diameter using a wire drawing procedure. In the second method a tungsten carbide stylus is manufactured using electro discharge manufacturing (EDM). Both methods have been used to create a stylus with a 50 μm tip diameter.

The design of the probing system is based on an analysis of the aspects that influence the measurement of miniaturized components using a tactile 3D probing system. The analysis presented serves as a reference work on the aspects that influence 3D tactile probing on miniaturized components and is based on simulation results, literature and experimental results, using the probe by Pril [Pril 02] and the novel tactile 3D probing system.

Assembly of the probing system is complicated by the effects of surface forces and fragility, size and manufacturing tolerances of parts. Assembly of the tactile 3D probing system is realized on an automated assembler robot for micro components developed by TNO Industry. Based on experimental results with the probing system and other micro products, the design of the tactile 3D probing system is optimized for assembly. To further facilitate assembly, a suction gripper has been developed for the assembly of miniaturized components.

The development of the assembly tool and the redesign of the probe resulted in an improvement in placement uncertainty at the tip by a factor of 10 and an increase in yield during assembly from 60 - 80% initially, to over 95%. Once the probe chip, stylus and tip are assembled they are placed into a holder cap and can be stored for future use. The yield during assembly and use of the probing system thus primarily effects the replacement costs of the probe chip. As a result the replacement costs of the probe with respect to the design by Pril [Pril 02] have been reduced by almost a factor of 10.

The requirements for the tactile 3D probing system are discussed in chapter 3. A main requirement is an overall 3D repeatability during single point probing of 20 nm or below, assuming a thermal stability of ± 0.1 K. The standard deviation in repeatability of the probing system is measured to be 2 nm for all measurement directions. The repeatability test is performed using 2000 measurement points taken in a 6 hour time frame over a repeated 5.5 μm displacement. The single point repeatability of the probing system at a 95% confidence interval ($k = 2$) is thus 4 nm and the 3D repeatability is 7 nm, satisfying the requirement.

The colliding mass and stiffness of the probing system should be below 35 mg and 350 N/m, respectively, to avoid plastic deformation during a collision with a 1 mm/s approach speed and a 150 μm tip radius. The colliding mass of the tactile 3D probing system is calculated to be 34 mg and the stiffness of the suspension can be as low as 20 N/m. Moreover, the stiffness of the probing system is isotropic for a stylus length of 6.8 mm.

The combined 3D uncertainty of the probing system with a 95% confidence interval ($k = 2$) is estimated to be 17.4 nm in a measurement range of 5.5 μm . Main contributions to the probing uncertainty include the systematic uncertainty due to probe calibration and the deformation of the work piece and probe tip. When these systematic deviations are compensated for or a low-force probing strategy is used, a combined 3D uncertainty ($k = 2$) of 14 nm can be obtained.

All requirements, as stated in section 3.1.1, are satisfied.

6.2 Recommendations

An important contribution to the measurement uncertainty of tactile 3D probes are deviations due to the roundness and diameter of the probe tip. Calibration of the probe tip is required to obtain the combined 3D uncertainty ($k = 2$) of 17.4 nm as stated in the previous section. This is especially challenging for probe tips with a diameter well below 1 mm and the contribution of the probe tip to the measurement uncertainty is thus a main effect when measuring miniaturized components. More work on calibration methods for these small probe tips is therefore required.

The aspect ratio of 50 between the length and radius of the measurement part of the stylus that can be obtained with the current probing system is sufficient for most measurement tasks on miniaturized components. However, further miniaturization will increase the need for smaller tips and higher aspect ratios. The manufacturing of smaller tips and improvements on the aspect ratio therefore remains a point of focus for future research.

The measurement range of the probing system is currently limited to 10 μm , which is sufficient for most precision coordinate measuring machines. By compensation of the anisotropic material properties of silicon, as discussed in this thesis, the stiffness at the probe tip can be made isotropic. As a result, the behavior of the probing system can be modeled over a larger range. It is expected that this will allow an increase in the measurement range of the probing system to 30 μm .

The measurement uncertainty and probing behavior is influenced by the aspects of micro probing, as discussed in chapter 2. This chapter and the experimental results discussed in chapter 5 will provide a solid foundation for future research and better modeling of probing systems. This will allow for a better error compensation and further improve the measurement uncertainty and probing behavior of the tactile 3D probing system discussed in this thesis.

Finally, an automated assembler can be used to assemble the probing system using the suction gripper discussed in chapter 4. It is expected that an automated assembler will further reduce assembly tolerances and improve yield.

Appendix A

Original probe by W. Pril

The probe was developed at the Precision Engineering section of the Eindhoven University of Technology by Pril in his Ph.D. work [Pril 02]. The operation of the probe is discussed in section 1.5. The original specifications, calibration and measurement results of this probe will be discussed in this appendix.

A.1 Specifications

The specifications for the probe, as described by Pril in his thesis [Pril 02], are:

1. The overall 3D uncertainty of the probe system should be smaller than 20 nm, assuming a thermal stability of ± 0.1 K;
2. It should be possible to use a 0.3 mm diameter sphere as a probe tip;
3. The stylus length should be larger than 4 mm;
4. The width of the probe house should be smaller than two times the stylus length;
5. It should be possible to measure with a probing speed of 1 mm s^{-1} , without damaging the workpiece;
6. The time needed to take a measurement should be less than three seconds;
7. The measurement range should be larger than the CMM over travel at a probing speed of 1 mm s^{-1} ;
8. The absolute maximum range of the probe system should be larger than the CMM over travel at maximum speed;
9. The cost of the probe system should be reasonable compared to the price of a high accuracy CMM, implying a maximum of 60,000 euro.

The implicit requirements in points 5, 7 and 8 lead to the following explicit specifications for the probe:

1. The equivalent mass of the probe, this is the mass that is 'felt' when accelerating the probe tip, should be less than 20 mg;
2. The stiffness of the suspension should be smaller than 200 N m^{-1} ;
3. The measurement range of the probe should be larger than $7 \mu \text{ m}$;
4. The maximum range of the probe should be larger than 0.5 mm.

Other requirements, as stated in the above mentioned thesis, are that it should be possible to deduce the (static) probing force from the tip position with a reproducibility of at most a few percent. Furthermore the natural frequency of the probe should be high, preferably a few hundred Hertz. This attenuates the free oscillation of the probe. Probe oscillation results in a higher collision force, hinders contact detection between probe and workpiece and increases the bouncing time after a collision.

A.2 Probe calibration

As mentioned in section 1.5 the displacement of the probe tip is measured using piezo resistive strain gauges deposited on each rod. A transformation matrix \mathbf{A} is used to give the relation between the measurement signal from the strain gauges on the slender rods and the displacement of the probe tip, as shown in equation 1.3. However, due to manufacturing and assembly tolerances the sensitivity coefficients in this matrix cannot be predicted with sufficient uncertainty in advance.

Therefore the transformation matrix \mathbf{A} is determined using the plane mirror differential laser interferometer setup, discussed in section 1.6.1. A displacement of the measurement mirror results in a displacement of the probe tip and deformation of the slender rods. The measurement signals from the strain gauges on the slender rods as a result of this displacement are recorded. Simultaneously, the displacement of the measurement mirror relative to the reference mirror is measured using a heterodyne laser interferometer.

By repeating this procedure at several positions, the relation between the displacement of the probe tip and the signals from the strain gauges can be determined. The sensitivity of each rod for this direction is calculated by fitting a line through the measurement results. The plane mirror differential laser interferometer setup used is explained in more detail in [Pril 02, Loon 97].

As mentioned in section 1.6.1 the probe can be oriented using three V-shaped grooves on the top and on a side of the bracket used to clamp the probe. Three spheres on the probe housing, that match the position of the V-shaped grooves, allow an operator to rotate the probe with respect to the bracket by 120 and 240 degrees respectively.

The measurement directions used to determine the behavior of the probe are shown in figure A.1. As shown in this figure the behavior of the probe is measured in the negative z -direction, figure A.1 a, and the x -direction, figure A.1 b. The third orientation is the result of a 120 degree rotation of the probe in the Kelvin clamp, shown in figure A.1 c. In theory this is sufficient to determine the transformation matrix \mathbf{A} .

However, direction c does not correspond to the y -direction and therefore the sensitivity coefficients $s_{1y} \cdots s_{3y}$ are influenced by the uncertainty in the calculation of $s_{1x} \cdots s_{3x}$. To improve the uncertainty of the method a fourth orientation is added, which corresponds to a 240 degree rotation of the probe in the Kelvin clamp, shown in figure A.1 d.

It is noted that the measurement directions from figure A.1 are normalized. The measurement signals Δm_1 , Δm_2 , Δm_3 in equation 1.3 are therefore equal to the sensitivity of each rod for a particular measurement direction. Using the results for four measurement directions in equation 1.3 yields:

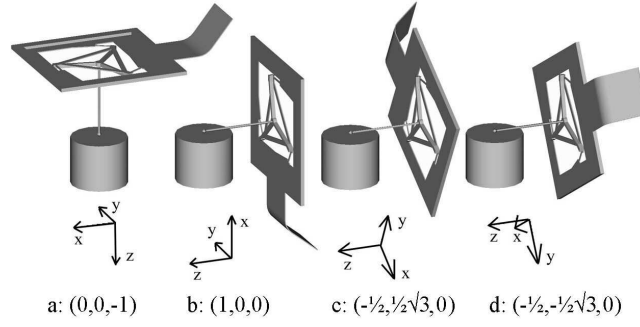


Figure A.1: Four directions for which the relation between the signal from the stain gauges on the slender rods and the probe tip displacement is measured.

$$\begin{bmatrix} 0 & 1 & -\frac{1}{2} & -\frac{1}{2} \\ 0 & 0 & \frac{1}{2}\sqrt{3} & -\frac{1}{2}\sqrt{3} \\ -1 & 0 & 0 & 0 \end{bmatrix} = \begin{bmatrix} s_{1x} & s_{2x} & s_{3x} \\ s_{1y} & s_{2y} & s_{3y} \\ s_{1z} & s_{2z} & s_{3z} \end{bmatrix} \begin{bmatrix} m_{1a} & m_{1b} & m_{1c} & m_{1d} \\ m_{2a} & m_{2b} & m_{2c} & m_{2d} \\ m_{3a} & m_{3b} & m_{3c} & m_{3d} \end{bmatrix}$$

$$\mathbf{D} = \mathbf{A}\mathbf{M} \quad (\text{A.1})$$

Here \mathbf{A} is the measured sensitivity matrix and m_{1a} is the measured sensitivity of the stain gauges in rod 1 for a displacement in direction \mathbf{a} . Since the probing directions and the measured sensitivities of the rods are known, the transformation matrix \mathbf{A} can be calculated. However, since four probing directions are used to determine the relation between three rods in three degrees of freedom (DOF) the system is overdetermined. Therefore a least-squares method is used to calculate \mathbf{A} :

$$\mathbf{A}^{-1} = \mathbf{M}\mathbf{D}^T (\mathbf{D}\mathbf{D}^T)^{-1} \quad (\text{A.2})$$

When the transformation matrix \mathbf{A} for a particular probe is known, it can be used in measurements.

A.3 Measurement results

In this section we will briefly show the calibration- and measurement results for a probe according to the original design by Pril, as discussed in this appendix. As discussed in the previous section, first the probe is calibrated to determine the relation between the voltage across the slender rod circuits and the displacement of the probe tip. This measurement is repeated in four directions, as shown in figure A.1. The output voltages for the probe of all three slender rod circuits for a displacement in x -direction are shown in figure A.2.

As discussed in section A.2, a linear relation between the measured voltages and the displacement of the probe tip is determined. This results in a measured sensitivity of each of the three rods for each of the four measurement directions \mathbf{a} , \mathbf{b} , \mathbf{c} and \mathbf{d} , as used in equation A.1:

$$\mathbf{M} = \begin{pmatrix} 0.4832 & -0.0923 & 0.2614 & -0.1284 \\ -0.3744 & 0.0983 & 0.0769 & -0.2057 \\ 0.4710 & 0.2625 & -0.1284 & -0.0959 \end{pmatrix} [\mu\text{V}\cdot\text{nm}^{-1}] \quad (\text{A.3})$$

When the measured sensitivity matrix \mathbf{M} is known, the transformation matrix \mathbf{A} for this probe can easily be found using equation A.2, thereby completing the calibration of the probe:

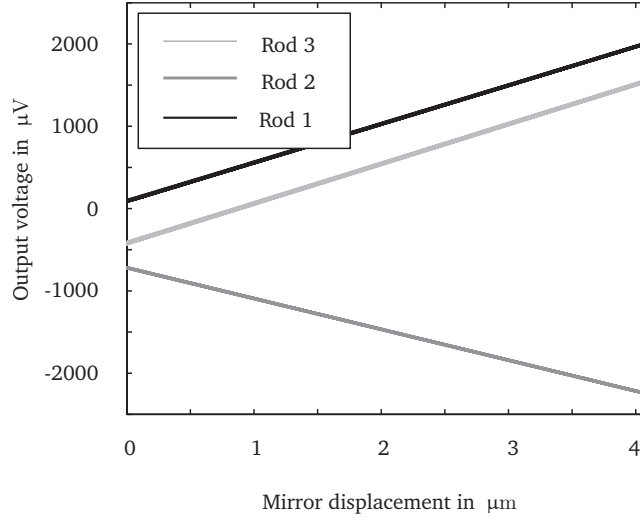


Figure A.2: Output voltages for original probe 1 of all three slender rod circuits for a displacement in x-direction.

$$\mathbf{A}^{-1} = \begin{pmatrix} -0.1059 & 0.2251 & -0.4832 \\ 0.1085 & 0.1632 & 0.3744 \\ 0.2495 & -0.0184 & -0.4710 \end{pmatrix} [\mu\text{V}\cdot\text{nm}^{-1}] \quad (\text{A.4})$$

It should be noted that the sensitivity coefficients in the transformation matrix \mathbf{A} are influenced by environmental variables. As a result they are not constant in time, as shown in figure A.3. The standard deviation in the sensitivity coefficients, as measured over a 16 hour interval, is $8 \cdot 10^{-11} \text{ V/nm}$ which corresponds to 2 nm over a 10 μm measurement.

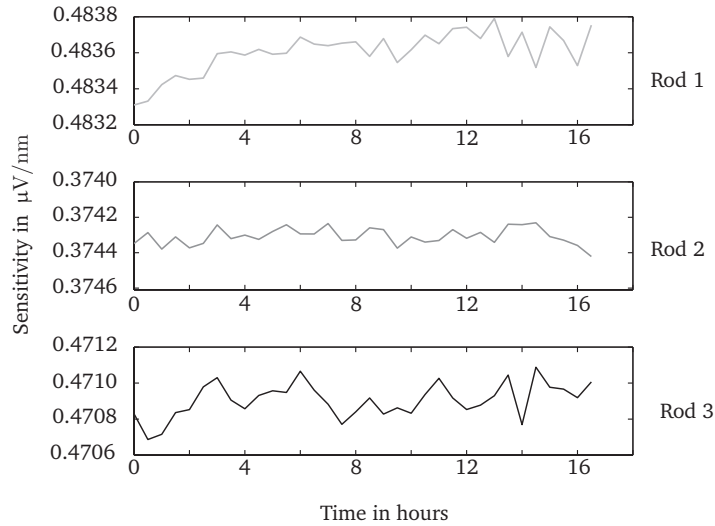


Figure A.3: Measured sensitivities of the three strain gauges during a 16 hour measurement.

When the probe is calibrated its behavior is analyzed using the setup used during the calibration procedure and described in section A.2. During a measurement the displacement of the probe tip as measured by the slender rod circuits is compared to the same displacement as measured by the calibration setup. Recalling equation 1.3:

$$\begin{bmatrix} \Delta x \\ \Delta y \\ \Delta z \end{bmatrix} = \mathbf{A} \begin{bmatrix} \Delta m_1 \\ \Delta m_2 \\ \Delta m_3 \end{bmatrix} = D_t \quad (\text{A.5})$$

Here D_t is the three dimensional displacement of the probe tip as measured by the signal from the slender rod circuits. The displacement as measured by the calibration setup d_c is one dimensional. Therefore it is multiplied by the direction in which the measurement is performed. The measurement direction for orientations **a** - **d** is given in equation A.1. The residual in all three directions r_x , r_y and r_z for a measurement in z -direction can thus be calculated using:

$$R_z = \begin{bmatrix} r_x \\ r_y \\ r_z \end{bmatrix} = D_t - \begin{bmatrix} 0 \\ 0 \\ -1 \end{bmatrix} d_c \quad (\text{A.6})$$

The residuals between the measurement of the probe and the calibration setup for the directions **a** - **d** are shown in figure A.4. It is noted that the residuals in x , r_x , and y , r_y , are shifted by 40 and 20 nanometers respectively. This is done throughout the paper to improve readability.

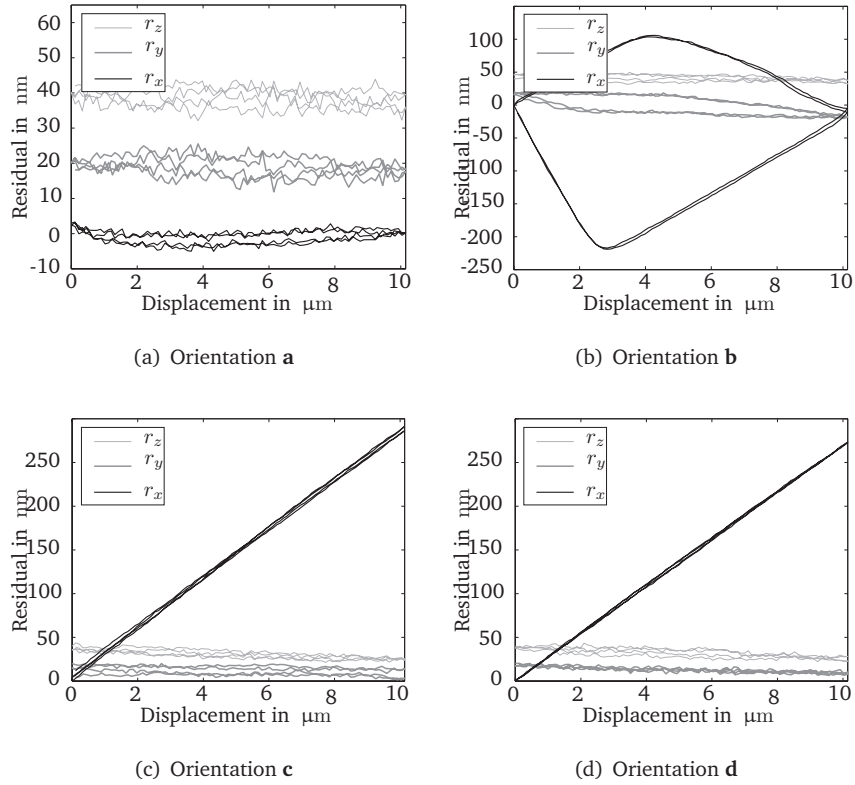


Figure A.4: Residuals in x , y and z -direction between a displacement as measured by original probe 1 and the same displacement as measured by the calibration setup: (a) for orientation **a**, (b) for orientation **b**, (c) for orientation **c**, (d) for orientation **d**.

From these figures several observations can be made. First for orientation **a** it can be seen that some hysteresis appears in the measurements. Also, the residuals, especially in r_z , appear to show some non linearities. It can also be seen that the maximum deviation is well within 10 nanometers. For orientations **c** and **d** a linear increasing z -residual, r_z , is observed. The same linear increasing z -residual is observed for orientation **b**. However, opposed to the other two orientations in the xy -plane of the probe, **c** and **d**, this linear increasing z -residual is interrupted after a displacement

of approximately $4\text{ }\mu\text{m}$ and a large hysteresis curve appears. Also the residuals in the x - and y -direction of the probe, r_x and r_y , show some hysteresis. Since the measurement directions **b**, **c** and **d** are in the xy -plane it can be concluded that the measurement results with the probe are influenced by the measurement direction.

These aspects of the measurement will be discussed in the remainder of this chapter. Also, several more general aspects of probing will be discussed. These are arranged according to several important influence factors, including contact effects, geometric effects, material effects, etc.

Appendix B

Contact of nominally flat rough surfaces

Often, the probe tip and work piece are assumed to be perfectly flat. Since both surfaces are perfectly smooth contact between them is continuous within the nominal contact area and absent outside it. However, practical objects have rough surfaces, resulting in a discontinuous contact area [Greenwood 67, Johnson 85]. Or in the words of Bowden [Bowden 54, Greenwood 99]:

Putting two solids together is rather like turning Switzerland upside down and standing it on Austria - the area of intimate contact will be small.

As a result of these rough surfaces high contact pressures may occur due to the small contact area of the roughness peaks [Weckenmann 04]. This results in smearing of the roughness peaks at the probed points [Uhlmann 03] or during scanning [Morel 2006, Zahwi 01].

Therefore, this section starts with a general theory of contact between nominally flat rough surfaces. The model presented will give an indication of the amount of plastic deformation present in the contact. It will be shown that, using this theory, plastic deformation of roughness peaks can never be avoided completely.

Theories about the influence of the surface roughness on the contact between two objects are used in describing friction [Bowden 54, Greenwood 99, Krim 96], electric contact resistance [Holm 58, Thomas 99] and thermal contact resistance [Cooper 69, Laraqi 03, Mikic 74A].

The Greenwood and Williams model [Greenwood 66] is widely accepted to describe the effects of the surface roughness on the contact between two objects [Bahrami 06, Johnson 85]. The main assumptions of this model are [Greenwood 66, Chang 87]:

1. The surfaces have homogeneous mechanical properties;
2. The asperity summits have a spherical shape all with constant radius κ_s . The mean summit curvature is of the same order as the root-mean-square curvature of the surface; $\bar{\kappa}_S \approx \sigma_\kappa$, as described by equation B.4;
3. The asperity heights z_s show a Gaussian distribution $\phi(z_s)$, where the distribution of surface heights is the same as the standard deviation of the surface heights;
4. The asperities deform elastically, i.e. Hertz theory can be applied for each individual summit;

5. Asperities are far apart and there is no interaction between them;
6. There is no bulk deformation; only the asperities deform during contact.

It should be noted that the assumption 'the surfaces have homogeneous mechanical properties', is not valid at a micro scale. Micro scale material effects like free surface energies, atomic vacancies, dislocations and grain boundaries can have a significant influence on the local mechanical properties of the material [Dingreville 04, Huang 00, Lima 99, Mizubayashi 99, Sanfeld 00]. As a result, local variations in the Young's modulus up to 10 % due to these effect are not uncommon [El-Deiry 02, Kalkman 01, Lee 00A, Ruud 94, Shull 96]. The Young's modulus at this scale can even be time dependent due to a relaxation effect [Kalkman 01]. These effects will result in a deviation in the calculated indentation of a few nanometers at maximum, as discussed in section 2.3.3. Moreover, local effects are averaged out over the roughness peaks in contact. Therefore the assumption 'the surfaces have homogeneous mechanical properties' is used for the analysis presented in this section.

Extensions of the Greenwood and Williamson model [Greenwood 66] include the use of non-uniform radii of curvature of the asperities [Whitehouse 70] and anisotropic surfaces [Bush 79]. McCool [McCool 86] compared the results from these models and concluded that the basic Greenwood and Williamson model, despite its simplistic form, gives very good results.

Originally Greenwood and Williams [Greenwood 66] defined a peak as all points higher than their immediate neighbors at the sample interval used. However, Greenwood and Wu [Greenwood 01] later concluded that this definition is wrong and gives a false idea of both the number and the radius of curvature of the peaks. Instead they propose to return to the Archard concept [Archard 57] that roughness consists of protuberances on protuberances on protuberances, as shown in figure B.1. This implies that contact may be plastic at light loads but becomes elastic at heavier loads.

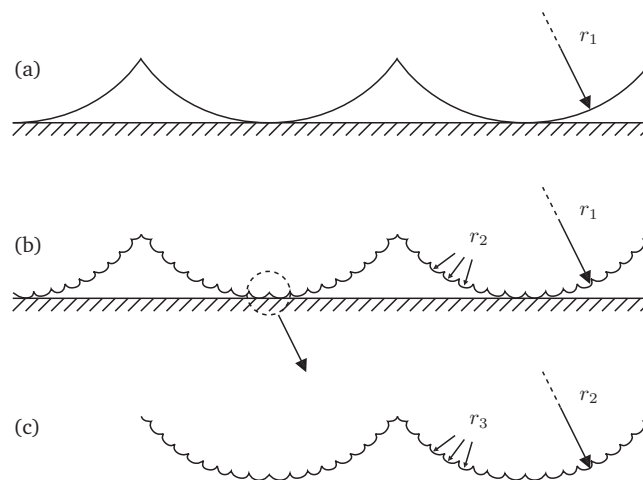


Figure B.1: Archard's model of protuberances on protuberances on protuberances, which he used to describe the effects of surface roughness [Archard 57].

In practice, the roughness of a surface is often measured using a profilometer. This apparatus draws a stylus over a sample length of the surface of the object and produces a trace of the surface profile, as shown in figure B.2. Note that the vertical magnification of a profilometer trace is typically 50 to 100 times larger than the horizontal magnification. The slopes of the roughness peaks on the real object are therefore not as steep as they appear in the picture. This effect is often referred to as the 'Talysurf delusion' [Greenwood 99], named after one of the more popular profilometers.

The center line through the trace is established by minimizing the mean square deviation of the points on the surface relative to this line. Using this center line, two definitions are now made. First, the separation d between two surfaces in contact is now defined as the distance between the datum planes of the surfaces through their center line. And secondly, the average roughness depth R_a , relative to the center line, is now defined as [Blunt 03, Johnson 85, Smith 02]:

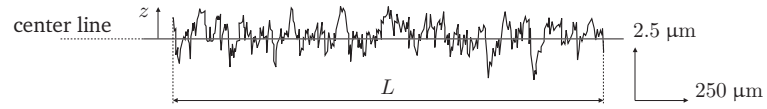


Figure B.2: Profilometer trace of a mild steel specimen after grinding [Greenwood 99].

$$R_a = \frac{1}{L} \int_0^L |z(x)| dx \quad (\text{B.1})$$

Where $z(x)$ is the distance of the surface at position x relative to the center line and L is the sampling length. Statistically the 'root mean square' or standard deviation σ_z of the distance $z(x)$ of the surface relative to the center line is also of interest:

$$\sigma_z = \sqrt{\frac{1}{L} \int_0^L z(x)^2 dx} \quad (\text{B.2})$$

The R_a value by itself does not provide information about the shape of the surface profile, i.e. about the distribution of the deviations from the mean [Johnson 85]. The cumulative height distribution of a sandblasted surface at different stages of wear is shown in figure B.3. The vertical axis has a normal probability distribution, which forms a straight line when the height distribution follows a Gaussian profile. The gradient of the line is a measure for the standard deviation σ_z .

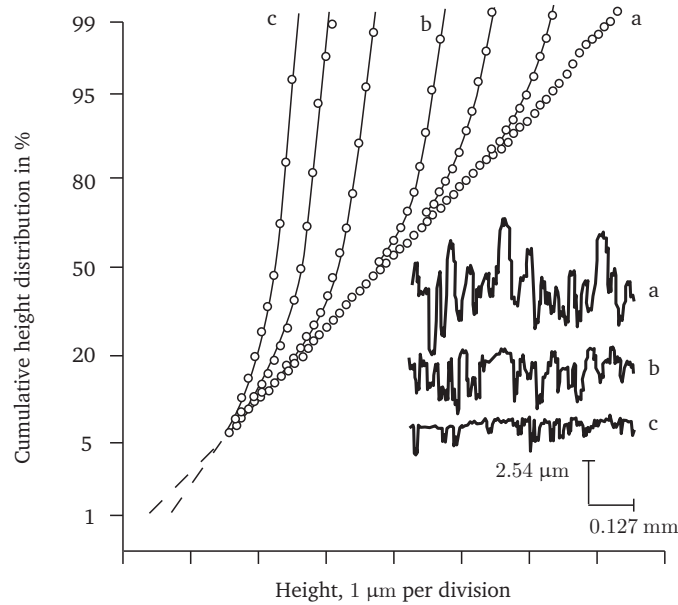


Figure B.3: Transitional topography due to wear of a sandblasted surface (a). As wear continues, the curve moves steadily to the left (b,c) [Greenwood 99, Williamson 69], original picture in inches.

It can be seen in this graph that even though the overall height distribution is not Gaussian, the higher parts of the surface, which are most interesting for the analysis, may be regarded as Gaussian [Greenwood 99]. It has been found that the upper part of most real surfaces can be regarded as Gaussian, even if the distribution as a whole is highly skewed [Bickel 63, Greenwood 66, Greenwood 99, Greenwood 01, Johnson 85, Stout 90, Whitehouse 94, Williamson 68, Williamson 69]. The assumption that the asperity heights z_s show a Gaussian distribution $\phi(z_s)$ can therefore be used for most practical surfaces.

As discussed at the start of this section, the shape of the roughness peaks is also of interest. When measuring the surface roughness using a profilometer, the surface height $z(x)$ is measured at discrete intervals of length Δx over the sample interval L . The curvature κ_i at position i can be calculated using [Greenwood 66, Johnson 85, Thomas 99]:

$$\kappa_i = \frac{z_{i+1} - 2z_i + z_{i-1}}{\Delta x^2} \quad (\text{B.3})$$

And the standard deviation is given by:

$$\sigma_\kappa = \sqrt{\frac{1}{n} \sum_{i=1}^{i=n} \kappa_i^2} \quad (\text{B.4})$$

Where $n = L/\Delta x$ is the total number of samples.

The curvature κ of a summit is equivalent to the radius r used to describe Hertz contact mechanics, e.g. in appendix G.

It should be clear from equations B.2, B.3 and B.4 that in practice the parameters σ_z and σ_κ , used to describe the surface, depend on the sampling length L and the sampling interval Δx used in the measurement. In terms of Archard's model, shown in figure B.1, the surface can be modeled as having a continuous spectrum of wavelengths. Neither wavelengths which are longer than the sample length L nor those who are shorter than the sampling interval Δx will be recorded faithfully by the profilometer. A practical limit for the sample length is the size of the specimen and a lower limit to the meaningful sampling interval is the radius of the profilometer stylus [Church 91, Johnson 85, Wu 99]. The effect of the stylus radius is comparable to the effect of mechanical filtering when scanning a work piece with the 3D tactile probe, as discussed in section 2.3.4.

Greenwood [Greenwood 01] proposed that the relation between load, approach and overall stress distribution for the asperity shown in figure B.4 will be close to that of a perfectly smooth asperity of the same general shape. Johnson [Greenwood 67, O'Connor 63, Vermeulen 64] measured the effect of a force distributed over a regular array of micro contacts and concluded that its effect is similar to a uniform force applied over the same area. As discussed by Greenwood [Johnson 85, Greenwood 01, McCool 86] the assumption that the asperity summits have a spherical shape all with constant radius κ_s can be used without a significant influence on the result. However, it should be noted that the smaller asperities will likely deform plastically, whereas the larger asperities may deform elastically.

As shown by Johnson [Johnson 85], the contact stresses in frictionless contact between two elastic solids depends only upon the relative profile of the two surfaces, i.e. upon the shape of the gap between them before loading. The system may therefore be replaced, without loss of generality, by a flat rigid surface in contact with a body having an effective Young's modulus E_{red} and a profile which results in the same gap between the surfaces before loading. The equivalent roughness σ and asperity slope κ between two nominally flat surfaces which have a root-mean-square roughness of σ_1 and σ_2 , respectively, is given by:

$$\sigma = \sqrt{\sigma_1^2 + \sigma_2^2} \quad (\text{B.5})$$

$$\kappa = \sqrt{\kappa_1^2 + \kappa_2^2} \quad (\text{B.6})$$

As mentioned at the start of this section, it is assumed that the asperity heights z_s show a Gaussian distribution $\phi(z_s)$. Here $\phi(z_s)$ expresses the probability of finding a summit height z_s or higher. If there are N summits in the nominal contact area A_0 , the number of summits in contact at separation d is given by [Greenwood 99, Johnson 85]:

$$n = N \int_d^\infty \phi(z_s) dz_s \quad (\text{B.7})$$

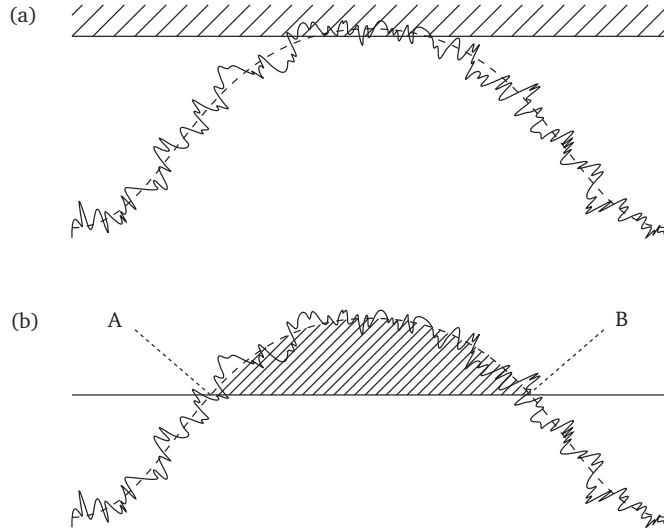


Figure B.4: Effect of roughness on the asperities. (a) Roughness on the asperity only influences the initial stages of contact (b) The region from A to B is taken as a single asperity, whose behavior depends on its overall size [Greenwood 01].

If summit i with height $z_{s,i}$ exceeds the separation d , the summit will be compressed by a distance $\delta_i = z_{s,i} - d$. Assuming, the summit will make contact in a circular area with radius a_i , the contact area A_i can be calculated using equation G.2:

$$A_i = \pi a_i^2 = \pi \delta_i \kappa_S \quad (\text{B.8})$$

The compression δ of summit i results in a force F_i , which is calculated using equation G.3:

$$F_i = \frac{4}{3} \sqrt{\kappa_S E_{red}} \delta_i^{\frac{3}{2}} \quad (\text{B.9})$$

Combining equations B.8 and B.9 with equation B.7 yields the total area of contact A and the total force F_c as a result of the compression of the summits in contact:

$$A = \pi \kappa_S N \int_d^\infty (z_s - d) \phi(z_s) dz_s \quad (\text{B.10})$$

$$F_c = \frac{4}{3} \sqrt{\kappa_S E_{red}} N \int_d^\infty (z_s - d)^{\frac{3}{2}} \phi(z_s) dz_s \quad (\text{B.11})$$

It is interesting to note that new contacts are continually forming. Initially these contacts have zero size and zero pressure. As a result the average size of the micro contacts (A / n) and the average contact pressure (F_c / A) are constant for an exponential distribution of summit heights z_s [Greenwood 99]. The results for a Gaussian distribution of summit heights z_s approximate to this.

For an aluminum surface with a Gaussian height distribution and a root-mean-square roughness σ of 40 nm loaded against a rigid plane, such that the mean planes are $0.1 \mu\text{m} = 2.5\sigma$ apart, the portion of asperities making contact is:

$$\int_{2.5\sigma}^\infty \phi(z_s) dz_s \quad i.e. \quad \phi(2.5) \equiv 0.0062 \quad (\text{B.12})$$

The reduced Young's modulus E_{red} and yield strength $\sigma_{0.2}$ for an aluminum work piece are 70 GPa and 280 MPa, respectively. Equation G.6 gives the indentation δ_Y at which elastic-plastic deformation begins. Assuming spherical summits with a constant curvature κ_S of 40 μm this yields $\delta_Y = 4.1 \text{ nm} \approx 0.1\sigma$.

Therefore all asperities higher than $2.5\sigma + \delta_Y \approx 2.6\sigma$ will have yielded, i.e. a fraction $\phi(2.6) = 0.0047$ or 0.47%. It should be noted that with this model for the contact between rough surfaces, as described in this section, it is not possible to avoid yield completely [Persson 00].

The following quote by Archard [Greenwood 99] illustrates the difference between Hertz contact mechanics, the first part, and the influence of surface roughness on this contact, the second part:

If the primary result of increasing the load is to cause the existing contact areas to grow, then area and load will not be proportional: but if the primary result is to form new areas of contact, then area and load will be proportional.

Appendix C

Surface forces

C.1 Van der Waals force

Van der Waals force, often referred to as London's or dispersion force, is caused by a momentary dipole moment between atoms resulting from interaction between electrons in the outermost band rotating around the nucleus [Feddema 01]. This moment exists even for atoms which do not contain a permanent polarization. While the average distribution of electrons is uniformly distributed around the nucleus, the outermost electrons of one atom are inducing a dipole on the other atoms with in turn induce a dipole on still more atoms [Israelachvili 74].

The resulting interaction energy E_i and force f_i between two atoms or molecules is given by [Feddema 01]:

$$\begin{aligned} E_i &= \frac{\lambda}{d_{cc}^6} \\ f_i &= \nabla E_i \end{aligned} \quad (C.1)$$

Where d_{cc} is the distance between the molecule centers and λ is the London constant. The London constant depends on temperature and material properties, such as the distortion polarization, permanent dipole moment and ionization energy.

Two notes should be made at this point. First, two atoms in close proximity will exert a repulsive force on each other, the Pauli repulsion. The repulsive force originates from the overlap the the electron clouds of the atoms. The Lennard-Jones potential describes this force F by an inverse relation to d_{cc}^{12} [Israelachvili 92, Ruan 94, Stifter 98], i.e.:

$$F \propto \frac{1}{d_{cc}^{12}} \quad (C.2)$$

Second, the relation between E_i and the distance between the molecule centers d_{cc} , changes from an inverse relation to the sixth power, equation C.1, to an inverse seventh power law at separations greater than 10 to 50 nm [Nayfeh 85]. This retardation is explained when accounting for the time of travel of the polarization field as it travels from one atom to the next [Feddema 01]. As the distance increases, the time of travel approaches the lifetime of the instantaneous dipole of the

original molecule. Instead of the induced fields being additive, they become subtractive, reducing the energy and force of the interaction [Kiefer 78, Langbein 71, Langbein 74].

The minimum distance between atomically smooth surfaces is commonly assumed to be 0.2 nm [Brussel 00]. In this work a distance of 0.4 nm [Arai 95] is used. It is assumed that both the Pauli repulsion and the retardation due to the time of travel of the polarization field can be neglected at this distance, and equation C.1 can be used.

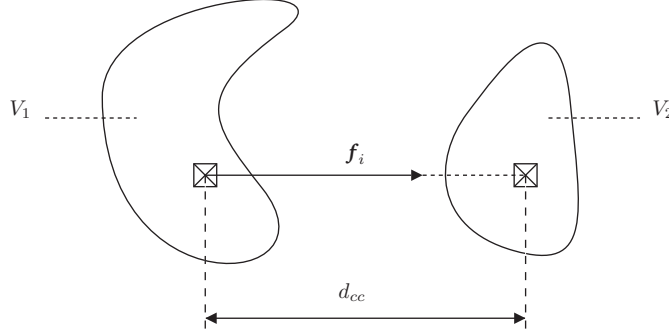


Figure C.1: Scheme for the integration of the interaction force f_i between two macroscopic bodies.

The interaction force between two macroscopic bodies $f_{i,m}$, shown in figure C.1, can now be calculated using [Hamaker 37]:

$$f_{i,m} = n_1 n_2 \int_{V_2} \int_{V_1} f_i(d_{cc}) dV_1 dV_2 \quad (C.3)$$

Where n_1 and n_2 are the number of atoms per unit volume in body 1 and 2, respectively.

The double volume integral from this equation was solved by Hamaker for two spheres [Hamaker 37]:

$$F_{vdw} = \frac{H d_{cc} r_1 r_2}{3} \left(\frac{8r_1^2 r_2^2 - (d_{cc}^2 - (r_1 - r_2)^2) (d_{cc}^2 - (r_1 + r_2)^2)}{(d_{cc}^2 - (r_1 - r_2)^2)^2 (d_{cc}^2 - (r_1 + r_2)^2)^2} \right) \quad (C.4)$$

Here, r_1 and r_2 are the sphere radii, d_{cc} is the distance between the centers and H is the Hamaker constant, where $H = \pi^2 n_1 n_2 \lambda$.

By letting r_2 go to infinity, Hamaker also determined the van der Waals force F_{vdw} between a sphere and an infinite half space:

$$F_{vdw} = \frac{2Hr_1^3}{3d_{ww}^2 (d_{ww} + 2r_1)^2} \quad (C.5)$$

Where d_{ww} is the distance between the wall and the edge of the sphere.

To obtain the geometry of more complex parts Derjaguin proposed the 'Derjaguin approximation' [Derjaguin 34]. Other papers on more complex shapes include [Argento 96, Hunter 01, Marvin 82, Tadmor 00].

An important influence factor for the van der Waals forces is the surface roughness of both parts. A rough estimate of this effect is described by Arai et al. [Arai 95], using the model shown in figure C.2. The effects of surface roughness are accounted for by increasing the distance between the wall and the edge of the sphere d_{ww} by half of the peak-to-peak surface roughness R_t :

$$\begin{aligned}
 d_{ww}^* &= d_{ww} + \frac{R_t}{2} \\
 F_{vdw}^* &= \left(\frac{d_{ww}}{d_{ww}^*} \right)^2 F_{vdw}
 \end{aligned} \tag{C.6}$$

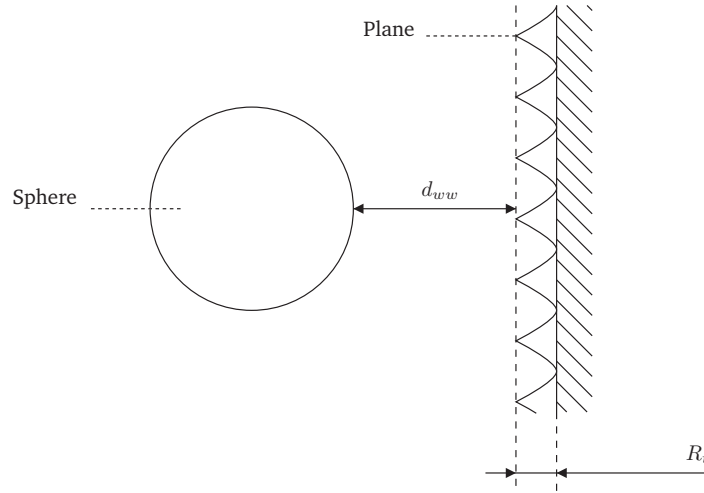


Figure C.2: Influence of the surface roughness on the van der Waals attraction.

The contact force between the objects will likely result in a local plastic deformation of the roughness peaks. This permanent deformation increases the effective contact area. The adhesion force between the surfaces thus increases for an increasing contact force [Jones 03].

As discussed in this section, the van der Waals energy E_i and force F_{vdw} depend on the Hamaker constant H . Using Berthelot's principle, the London constant λ_{12} between two particles of different materials equals the geometric mean of the interaction constants λ_{11} and λ_{22} of the individual materials [Berthelot 98, Lorentz 81]:

$$\lambda_{12} = \sqrt{\lambda_{11}\lambda_{22}} \tag{C.7}$$

And:

$$H_{12} = \sqrt{H_{11}H_{22}} \tag{C.8}$$

Where H_{12} is the Hamaker constant between two particles and the Hamaker constants of the individual materials are given by H_{11} and H_{22} .

Using Berthelot's principle and the Hamaker combining rule, the Hamaker constant H_{132} for two particles in a medium with a Hamaker constant H_{33} is given by [Hamaker 37, Hunter 01]:

$$H_{132} = H_{12} + H_{33} - H_{13} - H_{23} = \left(\sqrt{H_{11}} - \sqrt{H_{33}} \right) \left(\sqrt{H_{22}} - \sqrt{H_{33}} \right) \tag{C.9}$$

Note that the Hamaker constant H_{132} has a negative value, when:

$$H_{11} > H_{33} > H_{22} \quad \text{or} \quad H_{11} < H_{33} < H_{22} \tag{C.10}$$

When equation C.10 is satisfied, the dispersion interaction energy becomes repulsive [Neumann 79, Oss 79, Visser 72]. The Hamaker constant of several materials is shown in table C.1.

Material	Hamaker constant	Reference
Metals	16.2 - 45.5	[Visser 72]
Gold	44.0	[Klimchitskaya 00]
Silver	40.0	[Drauglis 69]
Copper	28.4	[Krupp 72]
Aluminum	36.0	[Klimchitskaya 00]
Iron	21.2	[Burke 67]
Quartz	5.5 - 41.3	[Visser 72]
Diamond	28.4	[Drauglis 69]
Carbon	21.7	[Feddema 01]
Water	4.38	[Krupp 72]
Sapphire	15.5	[Drauglis 69]
Silicon	25.6	[Drauglis 69]
SiO ₂	8.55 - 50	[Visser 72]
Germanium	30.0	[Büttner 70]

Table C.1: Hamaker constants for several materials. All values are given in 10^{-20} J.

As an example, the van der Waals force between an aluminum half space and a sapphire sphere with a radius of 250 μm is now calculated. First, the Hamaker constant is calculated using equation C.8. With the values from table C.1 a Hamaker constant of $23.6 \cdot 10^{-20}$ J is obtained. Using equation C.5 and assuming a distance between the edge of the sphere and wall d_{ww} of 0.4 nm [Arai 95] a van der Waals attraction force F_{vdw} of 61.5 μN is obtained.

The effect of surface roughness is taken into account using equation C.6. Assuming a peak-to-peak surface roughness R_t of 5 nm, a van der Waals force F_{vdw} of 1.17 μN , or 2% of 61.5 μN , is obtained.

C.2 Electrostatic attraction

Electrostatic attraction is the result of a buildup of charge in one or more objects. For a conductor, the electric field inside the object will be zero, and the electrostatic charge resides on the surface, as shown in figure C.3. Surface charge may result from a number of sources, including friction forces and differences in contact potential, often referred to as tribo-electrification or contact electrification [Fearing 95, Loeb 58, Verdonck 06].

It is assumed that the surface charge densities over surface 1 and 2, σ_1 and σ_2 , are constant [Becker 82, Feddema 01]. Using Gauss's law [Nayfeh 85] the interaction energy E_{i2} and force f_i between two infinitesimal small surface areas, as shown in figure C.3, is given by [Grant 90, Lorrain 88]:

$$\begin{aligned} E_{i2} &= \frac{\sigma_1 \sigma_2}{4\pi\epsilon_0 d} \\ f_i &= \nabla E_{i2} \end{aligned} \quad (\text{C.11})$$

Here, ϵ_0 is the permittivity in vacuum, $8.85 \cdot 10^{-12}$ C²/(Nm²), and d is the distance between the infinitesimal surface areas.

The force between the macroscopic bodies $f_{i,m}$, is obtained by integration of f_i over the surface areas S_1 and S_2 of body 1 and 2:

$$f_{i,m} = \int_{S_2} \int_{S_1} f_i(d) dS_1 dS_2 \quad (\text{C.12})$$

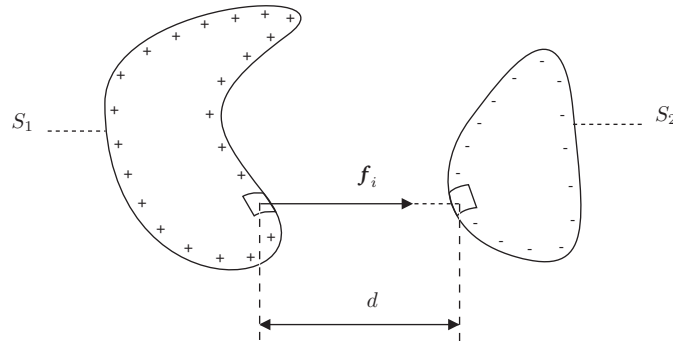


Figure C.3: Scheme for the integration of the interaction force f_i between two surfaces.

From this equation, the electrostatic force between two charged spheres F_{e2} can be calculated [Arai 95]:

$$F_{e2} = \frac{4\pi\sigma_1\sigma_2r_1^2r_2^2}{\epsilon_0d_{cc}^2} \quad (\text{C.13})$$

Where r_1 and r_2 are the radii of sphere 1 and 2, respectively, and d_{cc} is the distance between the sphere centers.

The electrostatic force between a charged sphere and a non charged conducting sphere F_{e1} is obtained in a similar way [Arai 95]:

$$F_{e1} = \frac{\epsilon - \epsilon_0}{\epsilon + \epsilon_0} \cdot \frac{\pi\sigma_1^2r_1^2r_2^2}{\epsilon_0d_{cc}^2} \quad (\text{C.14})$$

Where ϵ is the dielectric constant of the non charged conducting sphere.

The surface charge σ may be caused by contact electrification, as discussed at the start of this section. The surface charge due to contact electrification depends on the materials used, in particular on the contact potential difference between the materials, oxidation and impurities, the environment, for instance the relative humidity, and the conditions under which the transfer of charge took place, for example contamination of the surface and movements during contact. The relative importance of these effects is situation dependent. By movements during contact, e.g. by rubbing, a good insulator may accumulate charge whereas the total charge transferred between two metals is usually no greater than the charge acquired by a simple contact [Lowell 80].

First, the surface charge between two metal bodies that are brought into contact and are then separated is discussed. Harper [Harper 51, Harper 57] suggests that the bodies will exchange electrons by tunneling so that thermodynamic equilibrium is maintained. The difference in the surface potentials of the metals V_c will be:

$$V_c = \frac{\Phi_2 - \Phi_1}{e} \quad (\text{C.15})$$

Where Φ_1 and Φ_2 is the work function of material 1 and 2 and e is the electron charge, $0.1602177 \cdot 10^{-18}$ C.

The work function Φ for several materials is given in table C.2. The work function of a metal is sensitive to the presence of oxide, surface contamination and other factors [Lowell 80]. Therefore, a calculation of the contact potential based on 'handbook' values is a rough estimate at best.

Experiments shown that the charge transfer between metals is proportional to their contact potential difference V_c [Harper 51, Harper 67, Lowell 75]:

Material	Work function Φ in eV	Material	Work function Φ in eV
Aluminum	4.08	Copper	4.7
Gold	5.1	Iron	4.5
Platinum	6.35	Silver	4.30
Silicon	4.85	Titanium	3.7

Table C.2: Work function for several materials in electron volt, where $1 \text{ eV} = 1.60217646 \cdot 10^{-19} \text{ J}$ [Lide 98, Trigwell 01].

$$Q = C_0 V_c \quad (\text{C.16})$$

Where C_0 is the effective capacitance between the two adjacent bodies at the separation when tunneling becomes neglectable. As the two bodies are separated C_0 decreases until charge exchange by tunneling ceases. It is noted that C_0 has a weak dependency on the rate of separation. However, the effects of the separation rate can be neglected in most experiments [Harper 51, Harper 67, Lowell 75]. Harper [Harper 51, Harper 57] obtained a tunneling cut-off distance d_{cut} of 10 \AA , or 1 nm . Lowell [Lowell 75, Lowell 80] obtained an average value of 1000 \AA , or 100 nm , in his experiments. The latter value takes into account that due to surface roughness most of the two surfaces are separated by much larger distances when the closest point of separation is at 1 nm .

The effective capacitance C_0 for the contact between a sphere and a plane is given by [Castle 02, Harper 60, Lowell 75]:

$$C_0 = 4\pi\epsilon_0 r_1 \left(\gamma + \frac{1}{2} \ln \frac{2r_1}{d_{cut}} \right) \quad (\text{C.17})$$

Where r_1 is the radius of the sphere, d_{cut} is the separation between the wall and sphere at which tunneling ceases and γ is the Euler-Mascheroni constant, which is approximately 0.57721566 .

A rough estimate is given for the force between an aluminum sphere with a radius r_1 of 250 \mu m and a silicon wall. Using a tunneling cut-off distance d_{cut} of 50 \AA , or 5 nm , [Harper 60] a value of $1.6 \cdot 10^{-13}$ is obtained for C_0 . Using table C.2, a potential difference V_c of 0.77 V is obtained, which results in a charge Q on the aluminum sphere and silicon wall of approximately $1.2 \cdot 10^{-13} \text{ C}$. The resulting charge density on the sphere σ_1 is approximately $1.5 \cdot 10^{-7} \text{ C/m}^2$. Using equation C.13 and letting r_2 go to infinity, a force due to the contact potential difference between the sphere and wall of 8.3 pN is obtained.

When one or both objects are grounded, the static surface charge on the conductor and the associated forces are greatly reduced [Brussel 00]. However, the objects may be covered with insulator layers, such as native oxides. Experiments on silicon show a build up of 1 nm of native oxide after several days in air at room temperature [Morita 90]. This native oxide is a good insulator and can withstand a maximum field strength of up to $3 \cdot 10^9 \text{ V/m}$ [Sze 81].

The surface roughness of the object can prevent charge neutralization by intimate contact with a grounded conductor. The residual charges can be difficult to remove in a dielectric layer and can cause adhesion. Fearing [Fearing 95] describes the decay of the stored charge as a first order exponential, with time constant:

$$\tau = \rho \left(\epsilon + \epsilon_0 \frac{d_1}{d_2} \right) \quad (\text{C.18})$$

Where ρ and ϵ are the resistivity and relative permittivity of the dielectric, $\epsilon = 3.9\epsilon_0$ and $\rho = 10^{12} \text{ \Omega m}$ for SiO_2 . For a thickness d_1 of the dielectric layer of 10 nm and a thickness of the air layer d_2 of 20 nm a time constant of 39 seconds is obtained. Compared to the settling time of the probe, as discussed in section 2.1.5, the time needed to remove the stored charge is thus orders of

magnitude larger. Removing the stored charge by this mechanism is thus unfavorable with respect to the total measurement time.

The charge acquired by an insulator from a contact with a metal or other insulator depends on the nature of the insulator material, but also on the type and duration of the contact [Cottrell 78, Davies 67, Medley 53]. Significant amounts of charge may be generated by friction forces and differences in contact potential [Fearing 95]. The charge density observed on organic polymers after contact with metals is usually in the range of 10^{-5} to 10^{-3} C/m² [Lowell 80]. For good insulators, such as smooth silica and mica charge densities up to 10^{-2} C/m² have been observed at a gap of 1 μ m, less than the mean free path length of an electron in air [Horn 92]. This extreme charge density would result in a force of several Newtons for the contact between a sphere with a 250 μ m radius and a planar half space.

At atmospheric pressure and a gap in the order of centimeters the maximum charge density is limited to about $3 \cdot 10^{-5}$ C/m², due to the breakdown strength of air, which is about $3 \cdot 10^6$ V/m [Brussel 00, Koyano 96, Lowell 80]. Using the same approach as before with this value, a force due to the charge as a result of friction between a silicon sphere and an aluminum wall of 80 μ N is obtained.

C.3 Hydrostatic adhesion

As mentioned by Tsuchitani *et al.* [Brussel 00, Tsuchitani 94], the dominant force in micro structures is usually caused by the surface tension due to capillary condensation, when RH > 60%, or the hydrogen bonding force between water molecules adsorbed on the two surfaces. Hydrostatic attraction is increased by a high humidity, large radii of curvature, long contact times and hydrophilic surfaces.

Hydrostatic attraction arises from surface tension effects due to molecular attraction exerted on the outer molecules in a liquid. Due to this attraction the outer molecules experience a net attractive force toward the liquid interior, which causes the liquid surface to contract. At equilibrium there is a balance between the contracting forces and the repulsive collisional forces from the other molecules, which determines the surface area [Adamson 97, Israelachvili 92].

Figure C.4 shows a schematic of a sphere on a plane with a liquid film in between. The forces on the sphere due to surface tension in the liquid are often described in literature by capillary effects due to the pressure difference between the liquid and surrounding medium, and surface tension effects on the circumference of the circular edge between the liquid and sphere with radius r . The force F_{s1} in z -direction due to surface tension on the circumference is given by [Israelachvili 92]:

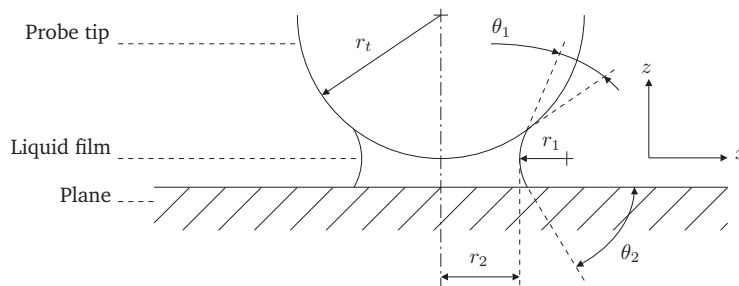


Figure C.4: Schematic of a sphere on a plane with a liquid film in between, forming a concave shaped meniscus. Note that the thickness of the water layer, which is typically a few nanometers, is highly exaggerated in this picture.

$$F_{s1} = 2\pi r \gamma \cos \theta \quad (\text{C.19})$$

Where θ is the angle at which the surface tension force is exerted and γ is the surface tension of

the liquid, for water at 20 °C $\gamma = 0.073$ N/m [Israelachvili 92]. By using $\theta = 0$ and $r = r_2$ equation C.20 is obtained [Arai 95, Fisher 26].

$$F_{s1} = 2\pi r_2 \gamma \quad (\text{C.20})$$

Capillary effects arise from the pressure difference Δp between the pressure inside the liquid and the environmental pressure. For the situation depicted in figure C.4, the pressure difference is given by the Young-Laplace equation [Bhushan 99, Chilamakuri 99]:

$$\Delta p = \gamma \left(\frac{1}{r_1} + \frac{1}{r_2} \right) \quad (\text{C.21})$$

And the force in z -direction due to capillary effects between the sphere and plane F_{s2} is given by:

$$F_{s2} = \pi r_2^2 \Delta p = \pi r_2^2 \gamma \left(\frac{1}{r_1} + \frac{1}{r_2} \right) \quad (\text{C.22})$$

The total force F_s is obtained by combining equations C.20 and C.22:

$$F_s = \pi r_2^2 \gamma \left(\frac{1}{r_1} + \frac{1}{r_2} \right) + 2\pi r_2 \gamma \quad (\text{C.23})$$

The radii of the meniscus r_1 and r_2 , the radius of the sphere r_t , the separation distance d and the contact angles θ_1 and θ_2 are connected via simple equations, see e.g. [Kralchevsky 01A, Kralchevsky 01B, Lazzar 99].

Common approximations when the tip radius r_t is much larger than r_1 , and hence $r_2 \gg r_1$ are [Pakarinen 05]:

$$\begin{aligned} \Delta p &= \gamma / r_1 \\ r_2^2 &\approx 2r_t r_1 (\cos \theta_1 + \cos \theta_2) \end{aligned} \quad (\text{C.24})$$

Using the above approximation with equation C.23 yields [Arai 95, Kralchevsky 01B, Orr 75]:

$$F_s \approx 2\pi r_t \gamma (\cos \theta_1 + \cos \theta_2) \quad (\text{C.25})$$

Where θ_1 and θ_2 are the contact angles at the surface of the probe tip and plane, respectively. Using $\theta_1 = 0$ and $\theta_2 = 0$, equation C.25 is reduced to [Bowling 88, Fearing 95, Tori 94]:

$$F_s \approx 4\pi r_t \gamma \quad (\text{C.26})$$

Other notable solutions for the forces between two objects include [Kolodezhnov 00, Lazzar 99, McFarlane 50, Willett 00].

Under the assumptions made with respect to equation C.26, the adhesion force due to the hydrostatic attraction is independent of the relative humidity. However, depending on the system, the relative humidity may have a strong influence on the adhesion force. This is discussed using the Gibbs free energy for an ideal gas [Adamson 97, Crassous 93, Stifter 00]. Using equation C.21, the change in the molar free energy ΔG at constant absolute temperature T and molar volume V due to a change in pressure is given by:

$$\begin{aligned} dG &= V dP = \frac{RT}{P} dP \\ \Delta G &= \int_{p_w}^{p_0} \frac{RT}{P} dP = RT \ln \frac{p_0}{p_w} \end{aligned} \quad (\text{C.27})$$

And:

$$\begin{aligned}\Delta G &= V\Delta P \\ RT \ln \frac{p_0}{p_w} &= V\gamma \left(\frac{1}{r_1} + \frac{1}{r_2} \right)\end{aligned}\quad (\text{C.28})$$

Where R is the universal gas constant, $R \approx 8314.5 \text{ J/kmol} \cdot \text{K}$, p_0 the partial pressure of water vapor in the air and p_w the vapor pressure of water. Equation C.28 is generally referred to as the Kelvin equation. Solving this equation for the Kelvin radius r_k yields:

$$\frac{1}{r_k} = \left(\frac{1}{r_1} + \frac{1}{r_2} \right) = \frac{RT}{\gamma V} \ln \frac{p_0}{p_w} \quad (\text{C.29})$$

The Kelvin radius r_k is a measure for the size of the meniscus that forms between the two surfaces for the given parameters. Also, it is used as a measure for the minimum distance that should be kept between the surfaces to prevent the formation of a stable layer of water between the objects [Brussel 00].

C.4 The influence of relative humidity on hydrostatic adhesion

An important point of interest with respect to the hydrostatic attraction is the influence of the relative humidity, which directly influences the adsorption of water on the surface of the objects [Bracken 97, Cleaver 04, Harriman 97]. The adsorption will naturally depend upon the partial pressure of water vapor, the temperature of the system and the affinity of the objects for water molecules. An important driving force for the adsorption is the relative humidity RH :

$$RH = \frac{p_0}{p_w} \quad (\text{C.30})$$

Where p_0 is the partial pressure of water vapor in the air and p_w is the vapor pressure of water. Variations in temperature are accounted for by the associated variation in the vapor pressure of water p_w .

The thickness of the adsorbed water layer also depends on the object, in particular its hydrophilicity. The thickness of the water layer is typically between a tenth and several tens of nanometers [Grigg 92, Heim 96, Hooton 04, Hu 95A, Hu 95B, Patel 97]. Also, especially for hydrophobic surfaces, water droplets may appear on the surface [Freund 99]. Figure C.5 shows the measurement results for the measurement of the thickness of the water layer on the head and disk of a magnetic recorder [Li 90, Tian 92].

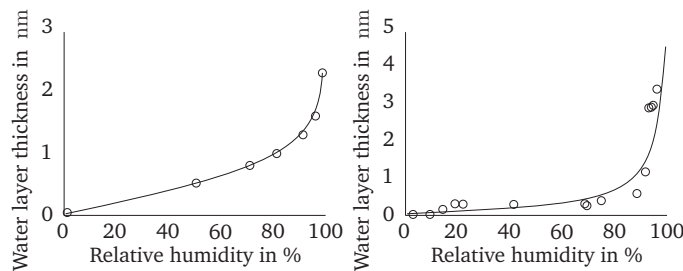


Figure C.5: Thickness of adsorbed water layer as a function of relative humidity. Left: Thickness of the water layer on the head of a magnetic recording drive [Tian 92]. Right: Thickness of the water layer on a Ni-Co-P coated disk [Li 90].

Most literature references, including [Christenson 88, Cleaver 04, Fisher 81, Harnby 96, Sugawara 93, Zimon 82], conclude that the hydrostatic adhesion increases monotonically with an increasing relative humidity RH . Another factor of influence is the surface roughness of the contact area. The effects of the surface roughness and relative humidity has been discussed by several authors, including [Harnby 96, McFarlane 50, Rabinovich 02]. The hydrostatic attraction is shown to decrease when the surface roughness increases.

This can be seen in figure C.6 a, where the surface roughness prevents the formation of a complete capillary meniscus at the point of contact. Therefore, capillary condensation only occurs around several discrete contact points. As a result, the radii r_1 and r_2 and the associated hydrostatic force F_s , as given by equation C.23, decreases.

When the thickness of the adsorbed moisture layer becomes larger than the mean asperity height, the attraction force shows a marked increase for many systems. At a critical relative humidity RH_c , sufficient water is adsorbed to engulf the asperities, as shown in figure C.6 b.

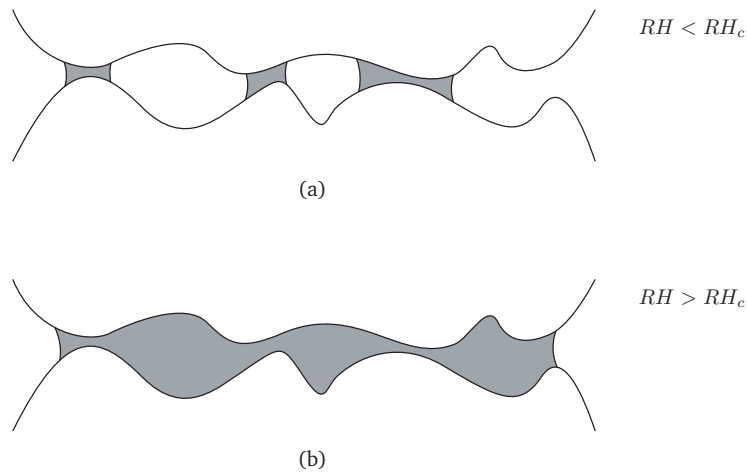


Figure C.6: Capillary condensation between rough surfaces.

Rabinovich *et al.* [Rabinovich 02] investigated the relation between the critical relative humidity RH_c and the surface roughness for glass spheres on a range of planar surfaces. The critical humidity in this experiment was observed to increase from 25%, for a RMS surface roughness of 0.2 nm, to 65%, for a RMS surface roughness of 3 nm.

When the relative humidity is further increased to the point of saturation, several authors [Chikazawa 84, Coelho 78A, Coelho 78B, Harnby 96, McFarlane 50, Rabinovich 02, Zimon 82] observed that in many systems the adhesive force was below the corresponding theoretical value, using equation C.23. The reduction in hydrostatic attraction is caused by the reduced Laplace pressure in the meniscus [Fisher 81, Christenson 88].

However, most experimental results found in literature on the effects of the relative humidity on the adhesive force are very system specific [Cleaver 04]. Influence factors include the surface roughness in the contact area, the rate of separation, chemical changes due to the presence of water, the contact time, the properties of the materials used, in particular their hydrophilicity, etc. Figure C.7 shows the adhesion force as a function of relative humidity for the contact between two glass objects, the solid line, and the contact of two gold-coated glass objects, the dashed line.

The contact between the uncoated glass objects shows a clear peak at 32.4% RH . A similar curve between potassium objects and glass objects was observed by Chikazawa [Chikazawa 84]. The adhesion between the potassium objects was observed to show a sudden increase at 65% RH , followed by a sharp drop at 70% RH . For glass samples a similar graph was obtained, with a peak adhesion between 70% and 80% RH . Christenson [Christenson 88] identified the maximum value of the hydrostatic adhesion between two smooth mica cylinders to occur at 70% RH . Similar results were obtained by Harnby *et al.* [Harnby 96] who observed an increase in adhesion with increasing RH . The critical value of RH at which the adhesion increased markedly was found to

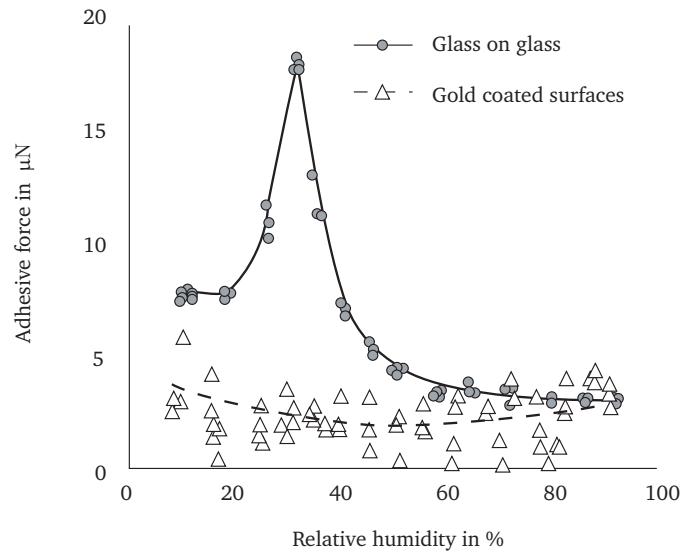


Figure C.7: Adhesion as a function of relative humidity between a sphere with a 37 μm diameter and a plane [Cleaver 04].

lie between 60% and 90% RH , which is in broad agreement with the results by Zimon [Zimon 82] and Tsuchitani [Tsuchitani 94].

As mentioned before, the relation between the relative humidity and the adhesion force is often complex. One example of this is the peak in the solid line for the two glass objects in figure C.7. It was only observed during measurements with a decreasing humidity and not during the same measurement and an increasing humidity level. Cleaver and Tyrrell [Cleaver 04] postulate that there may be an interaction between the silica surface and water vapor, as shown by [Biggs 95, Butt 99, Vigil 94], or a water-induced surface reaction at a high relative humidity [Clark 79, Trens 96]. Upon desorption the water layer would become supersaturated and the corrosion products precipitate out as needle-like structures on the surface. When the relative humidity is then increased, the increase in surface roughness as a result of these peaks prevents the occurrence of an adhesion peak.

Finally, Zimon [Zimon 82] performed several experiments in which he applied a hydrophobic coating on one or both of the surface areas. He defined an adhesion number as the relative number of particles that remained on the surface after applying a defined acceleration. Compared to the experiments with uncoated glass, where an adhesion number of over 90% was observed, the adhesion number dropped to 2% at 25% RH and 40% at 90% RH , when both surfaces were coated. When only one surface was coated the adhesion number was roughly in between the two above extremes.

As an example, the hydrostatic attraction between a sapphire sphere with a radius of 250 μm and an aluminum plane is calculated. For the calculation we assume a relative humidity RH of 60%, an absolute temperature T of 293.15 K and a molar volume of water V of $18 \cdot 10^{-6} \text{ m}^3/\text{mol}$. Using equation C.29 with $R = 8.3145 \text{ J/mol} \cdot \text{K}$ and $\gamma = 0.073 \text{ N/m}$ a Kelvin radius r_k of 1 nm is obtained. Since $r_t \gg r_k$, equation C.26 is used, which gives a total hydrostatic attraction F_s of 0.23 mN.

Appendix D

Stiffness and characteristics of the suspension

D.1 Introduction

In this appendix the stiffness of the sensor and important characteristics of a suspension with three slender rods, as drawn in figure D.1, are calculated. The calculations in this appendix partly expand on the theory presented in Appendix A of [Pril 02], Appendix C of [Widdershoven 04] and Appendix G in [Heldens 05].

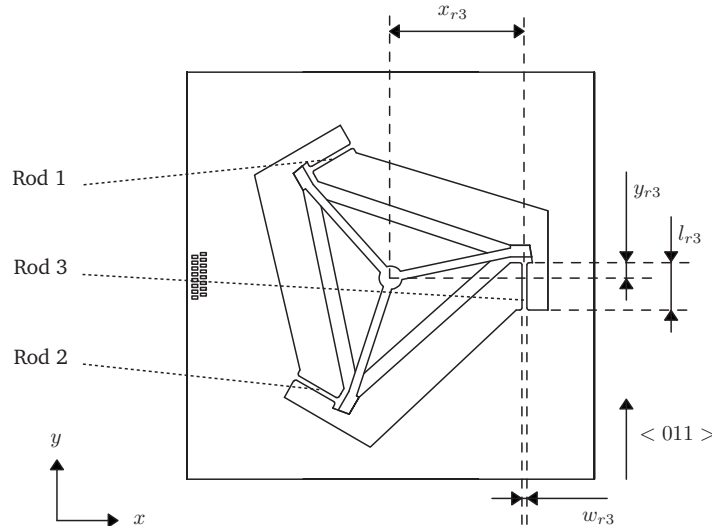


Figure D.1: Top view of the suspension used in the sensor with rod numbers and crystallographic direction, indicated by $\langle \dots \rangle$.

The three rods that make up the suspension of the sensor are indicated in figure D.1, along with their length l_r , width w_r and thickness t_r . The distance in m between the center point of the sensor and the end of the rod in x -direction and y -direction is given by x_r and y_r respectively.

First the stiffness matrix for a single rod in local coordinates is calculated in appendix D.2. This is

the basic element for the stiffness calculations. However, as discussed in appendix D.3, the Young's modulus and shear modulus of the silicon base material used in the suspension dependent on the crystallographic orientation within the wafer. As a result the stiffness of a rod depends on its orientation within the wafer.

Then in appendix D.4 a stiffness model of the sensor is calculated. The model is used to calculate the influence of the finite stiffness of the parts of the sensor; e.g. the stylus. The influence of the anisotropic Young's and shear modulus in silicon is discussed in appendix D.5.

The general assumptions made to calculate the stiffness of the sensor suspension are:

- The displacements and rotations of the slender rods are small, so that standard elastic theory can be applied;
- The effective length of a slender rod decreases when it is deformed outside the plane. These displacements are neglected;
- Translations of the probe tip are considered to be small with respect to the stylus length. Therefore, all second and higher order rotations of the intermediate body can be neglected.

D.2 Stiffness matrix for a slender rod

The local stiffness matrix for a slender rod is the stiffness matrix at the endpoint of the rod in local coordinates. The coordinate system shown in figure D.1 is the global coordinate system for the sensor. In the local coordinate system for a rod the z -axis is the symmetry axis of the suspension and the y -axis is parallel to its length direction, as shown in figure D.2.

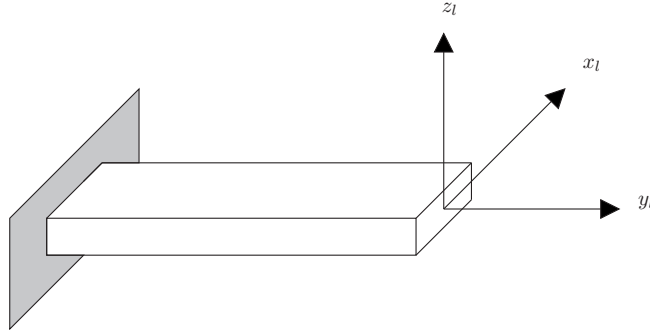


Figure D.2: Local coordinate system for a slender rod. .

The local forces and moments on the rod \mathbf{f}_l and the local displacements and rotations \mathbf{x}_l depend on the local stiffness matrix \mathbf{C}_l :

$$\mathbf{f}_l = \mathbf{C}_l \mathbf{x}_l \quad (\text{D.1})$$

Where:

$$\mathbf{f}_l = \begin{pmatrix} f_{lx} \\ f_{ly} \\ f_{lz} \\ m_{lx} \\ m_{ly} \\ m_{lz} \end{pmatrix}, \quad \mathbf{x}_l = \begin{pmatrix} x_{lx} \\ x_{ly} \\ x_{lz} \\ r_{lx} \\ r_{ly} \\ r_{lz} \end{pmatrix}$$

$$C_l \equiv \begin{pmatrix} c_{xx} & 0 & 0 & 0 & 0 & ck_{xz} \\ 0 & c_{yy} & 0 & 0 & 0 & 0 \\ 0 & 0 & c_{zz} & ck_{zx} & 0 & 0 \\ 0 & 0 & ck_{zx} & k_{xx} & 0 & 0 \\ 0 & 0 & 0 & 0 & k_{yy} & 0 \\ ck_{zx} & 0 & 0 & 0 & 0 & k_{zz} \end{pmatrix} \quad (D.2)$$

And [Young 02]:

$$\begin{aligned} c_{xx} &= \frac{E_r t_r w_r^3}{l_r^3}, \quad c_{yy} = \frac{E_r t_r w_r}{l_r}, \quad c_{zz} = \frac{E_r t_r^3 w_r}{l_r^3} \\ ck_{xz} &= \frac{1}{2} \frac{E_r w_r^3 t_r}{l_r^2}, \quad ck_{zx} = -\frac{1}{2} \frac{E_r w_r t_r^3}{l_r^2} \\ k_{xx} &= \frac{1}{3} \frac{E_r w_r^3 t_r}{l_r}, \quad k_{zz} = \frac{1}{3} \frac{E_r w_r^3 t_r}{l_r} \\ k_{yy} &\approx \frac{G_r w_r t_r^3}{l_r} \left(\frac{1}{3} - 0.21 \frac{t_r}{w_r} \left(1 - \frac{1}{12} \frac{t_r^4}{w_r^4} \right) \right) \end{aligned} \quad (D.3)$$

Here l_r , w_r and t_r are the length, width and thickness in m of the rod, as shown in figure D.1. The rods are manufactured from a silicon wafer. Therefore their Young's modulus E_r in Pa and shear modulus G_r in Pa depend on their orientation within the wafer, as discussed in appendix D.3.

Note that c_{yy} is at least two orders of magnitude larger than the other c -constants because the length of the rods l_r is at least one order of magnitude larger than the thickness t_r of the rods. As a result, the rotation of the intermediate body around the z-axis and its displacement in x - and y -direction can be neglected.

D.3 Mechanical behavior of single crystalline silicon

In the previous section the local stiffness matrix for a rod is shown. However, the Young's modulus E and shear modulus G in single crystalline silicon depend on the orientation with respect to the crystallographic structure [Ballarini 05, Bos 07C, Johansson 88, Wortman 65], as shown in figure D.3 and figure D.4. Therefore, the stiffness of a silicon rod depends on its orientation within the wafer.

The suspension of the 3D tactile sensor consists of three rods, as shown in figure D.1. When the ratio of the width w_r over the length l_r of a rod is small, the Young's modulus E_r in Pa and the shear modulus G_r in Pa in its length direction can be used [Lekhnitskii 63]. The length direction of rod 3 is oriented along the $\langle 011 \rangle$ crystallographic direction. The Young's modulus of rod 3 E_{r3} and its shear modulus G_{r3} are $168.8 \cdot 10^9$ and $50.8 \cdot 10^9$ Pa, respectively, as shown in figure D.3 and figure D.4.

Rods 1 and 2 are rotated by 120° and 240° with respect to rod 3. As a result their length directions are oriented along equivalent crystallographic directions. The Young's modulus of rods 1 and 2 E_{r12} and their shear modulus G_{r12} are $138.0 \cdot 10^9$ and $69.6 \cdot 10^9$ Pa, respectively.

D.4 Stiffness model of the sensor

In this appendix a stiffness model of the 3D tactile sensor is presented, based on the schematic model presented in figure D.1. The sensor is considered as a series of elastic elements, each with its own stiffness matrix. The local stiffness matrix of a slender rod in the suspension is presented in appendix D.2. The stiffness matrices for the other elements can be obtained in a similar way.

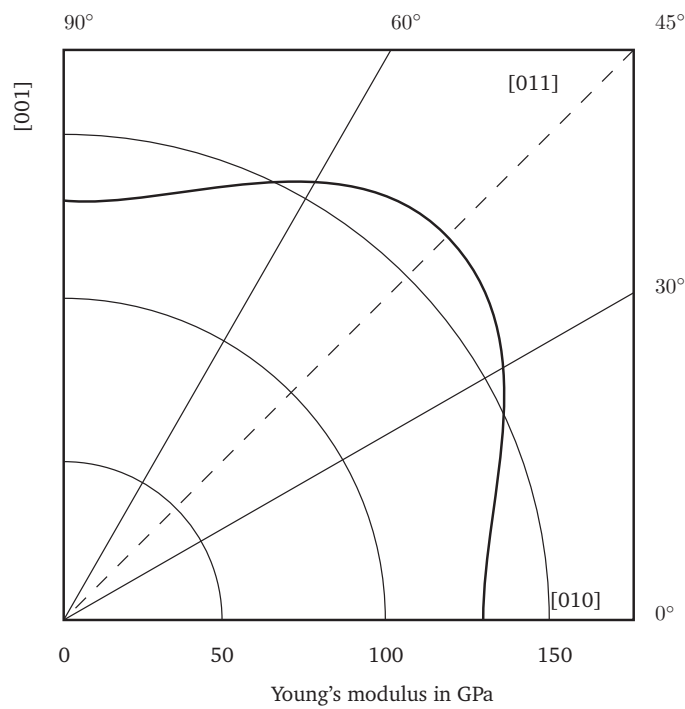


Figure D.3: Young's modulus as a function of the crystallographic direction in silicon in the (100) plane.

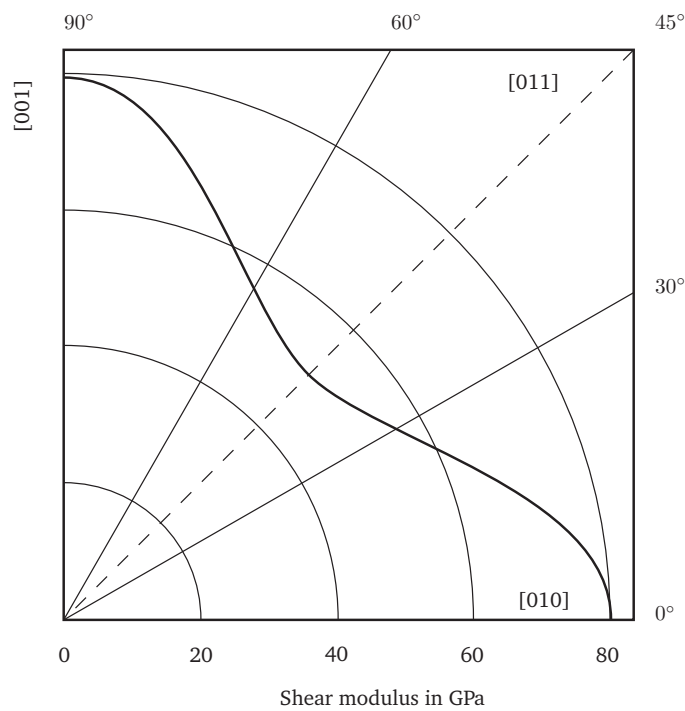


Figure D.4: Shear modulus as a function of the crystallographic direction in silicon in the (100) plane.

First the local stiffness matrices for each element are transformed into global coordinates. The following must hold for this transformation:

$$\mathbf{f}_l = \mathbf{C}_l \mathbf{x}_l \quad \equiv \quad \mathbf{f}_g = \mathbf{C}_g \mathbf{x}_g \quad (\text{D.4})$$

Here \mathbf{f} are the forces and moments on the element, \mathbf{C} is the stiffness matrix and \mathbf{x} are the displacements and rotations of the element. The subscript l indicates local variables and the subscript g global variables.

The local forces and moments \mathbf{f}_l can be transformed to global forces \mathbf{f}_g using [Paul 81]:

$$\mathbf{f}_g = \mathbf{T}_{lg}^F \mathbf{R}_{lg}^F \mathbf{f}_l = \mathbf{T}_{lg}^F \mathbf{R}_{lg}^F \mathbf{C}_l \mathbf{x}_l \quad (\text{D.5})$$

Transformation matrices \mathbf{T}_{lg} and \mathbf{R}_{lg} indicate translations and rotations of the element from local to global coordinates. Superscript F is used to indicate a transformation of forces and moments. It is noted that in equation D.5 rotations as a result of transformation matrix \mathbf{R}_{lg}^F are executed before translations as a result of \mathbf{T}_{lg}^F .

Transform global displacements and rotations \mathbf{x}_g to local displacements and rotations \mathbf{x}_l :

$$\mathbf{x}_l = \mathbf{T}_{gl}^P \mathbf{R}_{gl}^P \mathbf{x}_g \quad (\text{D.6})$$

The subscript gl of the transformation matrices \mathbf{T} and \mathbf{R} indicates a transformation from global to local coordinates. Superscript P is used to indicate a transformation of displacements and rotations.

Combining equations D.4, D.5 and D.6 gives:

$$\mathbf{T}_{lg}^F \mathbf{R}_{lg}^F \mathbf{C}_l \mathbf{T}_{gl}^P \mathbf{R}_{gl}^P \mathbf{x}_g = \mathbf{C}_g \mathbf{x}_g \quad (\text{D.7})$$

Freeing the global stiffness matrix leads to:

$$\mathbf{C}_g = \mathbf{T}_{lg}^F \mathbf{R}_{lg}^F \mathbf{C}_l \mathbf{T}_{gl}^P \mathbf{R}_{gl}^P \quad (\text{D.8})$$

It is noted that:

$$\mathbf{T}_{gl}^F \mathbf{R}_{gl}^F = (\mathbf{T}_{lg}^F \mathbf{R}_{lg}^F)^{-1} \quad (\text{D.9})$$

The transformation matrix \mathbf{T} takes into account translations in x , y and z direction, as shown in figure D.5. The transformation matrix from global to local forces and moments \mathbf{T}_{gl}^F is given by:

$$\mathbf{T}_{gl}^F = \begin{bmatrix} 1 & 0 & 0 & 0 & 0 & 0 \\ 0 & 1 & 0 & 0 & 0 & 0 \\ 0 & 0 & 1 & 0 & 0 & 0 \\ 0 & t_z & -t_y & 1 & 0 & 0 \\ -t_z & 0 & t_x & 0 & 1 & 0 \\ t_y & -t_x & 0 & 0 & 0 & 1 \end{bmatrix} \quad (\text{D.10})$$

The transformation matrix from global to local displacements and rotations of the element \mathbf{T}_{gl}^P is given by:

$$\mathbf{T}_{gl}^P = \begin{bmatrix} 1 & 0 & 0 & 0 & t_z & -t_y \\ 0 & 1 & 0 & -t_z & 0 & t_x \\ 0 & 0 & 1 & t_y & -t_x & 0 \\ 0 & 0 & 0 & 1 & 0 & 0 \\ 0 & 0 & 0 & 0 & 1 & 0 \\ 0 & 0 & 0 & 0 & 0 & 1 \end{bmatrix} \quad (\text{D.11})$$

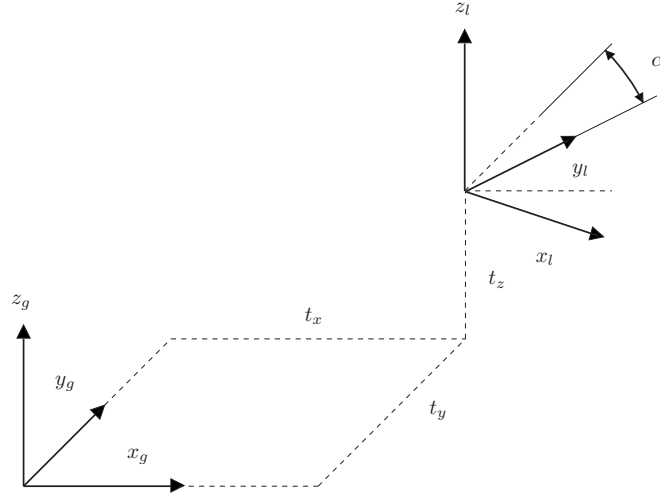


Figure D.5: Transformation from global to local coordinate system.

The transformation matrix \mathbf{R} only takes into account rotations around the z axis, as shown in figure D.5:

$$\mathbf{R}_{gl}^F = \mathbf{R}_{gl}^P = \begin{bmatrix} \cos(-\alpha) & -\sin(-\alpha) & 0 & 0 & 0 & 0 \\ \sin(-\alpha) & \cos(-\alpha) & 0 & 0 & 0 & 0 \\ 0 & 0 & 1 & 0 & 0 & 0 \\ 0 & 0 & 0 & \cos(-\alpha) & -\sin(-\alpha) & 0 \\ 0 & 0 & 0 & \sin(-\alpha) & \cos(-\alpha) & 0 \\ 0 & 0 & 0 & 0 & 0 & 1 \end{bmatrix} \quad (\text{D.12})$$

When the global stiffness matrices for each element are known they can be combined. First, the global stiffness matrix \mathbf{C}_{r1} of rod 1 is combined with the global stiffness matrix \mathbf{C}_{l1} of the leg of the star connected to rod 1. Since the rod and leg are serial elements the combined stiffness matrix \mathbf{C}_{rl1} can be calculated using:

$$\frac{1}{\mathbf{C}_{rl1}} = \frac{1}{\mathbf{C}_{r1}} + \frac{1}{\mathbf{C}_{l1}} \quad (\text{D.13})$$

The stiffness at the center point of the star \mathbf{C}_{rl} can be obtained by combining the matrices \mathbf{C}_{rl1} , \mathbf{C}_{rl2} and \mathbf{C}_{rl3} . Since the elements $rl1$, $rl2$ and $rl3$ are parallel \mathbf{C}_{rl} can be calculated using:

$$\mathbf{C}_{rl} = \mathbf{C}_{rl1} + \mathbf{C}_{rl2} + \mathbf{C}_{rl3} \quad (\text{D.14})$$

Note that in this approach the center of the intermediate body is taken as the point of rotation. Parasitic movements of the intermediate body during probing are thus not taken into account. The method will therefore result in a diagonal stiffness matrix for the intermediate body.

The stiffness matrix at the sensor tip \mathbf{C}_t can be found by taking into account the stiffness of the stylus \mathbf{C}_{st} and the position of the tip, relative to the intermediate body:

$$\mathbf{C}_t = \begin{bmatrix} C_{xx,t} & 0 & 0 \\ 0 & C_{yy,t} & 0 \\ 0 & 0 & C_{zz,t} \end{bmatrix} \quad (\text{D.15})$$

Where:

$$\begin{aligned}
C_{xx,t} &= \left(\frac{1}{C_{xx,rl}} + \frac{l_{st}^2}{C_{\beta\beta rl}} + \frac{1}{C_{xx,st}} \right)^{-1} \\
C_{yy,t} &= \left(\frac{1}{C_{yy,rl}} + \frac{l_{st}^2}{C_{\alpha\alpha rl}} + \frac{1}{C_{yy,st}} \right)^{-1} \\
C_{zz,t} &= \left(\frac{1}{C_{zz,rl}} + \frac{1}{C_{zz,st}} \right)^{-1}
\end{aligned}$$

Here l_{st} is the length of the stylus and $C_{xx,st}$ is its bending stiffness in x direction.

Note that the probe tip is assumed to be positioned exactly above the rotation point of the intermediate body. Displacements as a result of an off axis position of the sensor tip are therefore not taken into account, resulting in a diagonal stiffness matrix at the sensor tip. The stiffness model discussed in section D.5 does take these effects into account as well the parasitic movements of the intermediate body.

For the redesign, discussed in section 3, the stiffness matrix at the sensor tip C_t for a stylus length l_{st} of 7 mm and a length l_r , width w_r and thickness t_r of the rods of 1.6 mm, 160 μm and 30 μm , respectively, the stiffness matrix in N/m is given by:

$$C_t = \begin{bmatrix} 280.5 & 0 & 0 \\ 0 & 297.0 & 0 \\ 0 & 0 & 425.2 \end{bmatrix} \quad (D.16)$$

When all elements except the slender rods are taken as infinitely stiff, the same calculation yields:

$$C_t = \begin{bmatrix} 428.3 & 0 & 0 \\ 0 & 467.8 & 0 \\ 0 & 0 & 469.3 \end{bmatrix} \quad (D.17)$$

From equation D.16 and D.17 it can be seen that $C_{xx,t} \neq C_{yy,t}$, due to the anisotropic Young's and shear modulus of the silicon base material, as discussed in appendix D.3. Another point of interest is the ratio of the coefficients between both equations. Ideally, a tip displacement should result in a deformation of the slender rods only. However, since the intermediate parts have a finite stiffness, a tip displacement will also result in a deformation of the intermediate parts. A low stiffness of the intermediate parts will therefore result in a lower deformation of the slender rods for a given tip displacement.

By comparing equation D.16 to equation D.17 it can be seen that the ratio of $C_{zz,t}$ between both equations is 1.10. The ratios of $C_{xx,t}$ and $C_{yy,t}$ are 1.53 and 1.58, respectively, due to a relative low bending stiffness of the stylus compared to its axial stiffness.

Decreasing the thickness t_r of the slender rods to 10 μm yields:

$$C_t = \begin{bmatrix} 15.6 & 0 & 0 \\ 0 & 17.0 & 0 \\ 0 & 0 & 17.3 \end{bmatrix} \quad (D.18)$$

When all elements except the slender rods are taken as infinitely stiff, the same calculation yields:

$$C_t = \begin{bmatrix} 15.9 & 0 & 0 \\ 0 & 17.4 & 0 \\ 0 & 0 & 17.4 \end{bmatrix} \quad (D.19)$$

It can be seen that the ratio of $C_{xx,t}$, $C_{yy,t}$ and $C_{zz,t}$ between equation D.18 and D.19 is 1.02, 1.02 and 1.01, respectively.

Decreasing the ratio indicates a higher deformation of the slender rods for a given tip displacement and thus an increase in sensitivity. However, the bending of the rods is measured using piezo resistive strain gauges mounted on top of the rods. Decreasing the height of the rods also decreases the strain in the rod at the position of the strain gauges. Therefore, an optimum rod height can be calculated for a given sensor design, in which the ratio between the height of the rods and the sensitivity loss due to finite stiffness effects is maximized. This is discussed in more detail in section 2.3.1.

Finally, the anisotropic stiffness of the sensor suspension can be compensated by adjusting the width w_r of rod 1 and 2, as discussed in appendix D.5 and section 3.2.1. An isotropic stiffness is obtained for a stylus length l_{st} of 6.7 mm:

$$\mathbf{C}_t = \begin{bmatrix} 19.7 & 0 & 0 \\ 0 & 19.7 & 0 \\ 0 & 0 & 19.7 \end{bmatrix} \quad (\text{D.20})$$

D.5 Stiffness model of the suspension

In the previous section a stiffness model of the sensor is discussed. However, as already mentioned several assumptions were made that limit its use when analyzing the influence of the anisotropic stiffness in silicon and an off-axis position of the sensor tip. Therefore a model of the suspension is introduced in this section in which all elements other than the slender rods are assumed to have infinite stiffness.

First the stiffness matrix for each rod is calculated using equation D.2. Here c_{xx3} is the element c_{xx} of stiffness matrix \mathbf{C}_{r3} of rod 3. As mentioned in appendix D.3 rod 1 and rod 2 are oriented along equivalent crystallographic directions. Therefore $\mathbf{C}_{r1} = \mathbf{C}_{r2} = \mathbf{C}_{r12}$ with coefficients $c_{xx12} \dots k_{zz12}$.

As shown in figure D.1, the rods have a relative rotation to rod 3 within the suspension. The rotated stiffness matrices \mathbf{C}_{r1}^R and \mathbf{C}_{r2}^R for a rotation around the z axis of 120 and 240 degrees respectively are given by:

$$\begin{aligned} \mathbf{C}_{r1}^R &= \begin{pmatrix} \mathbf{R}_{120} & \emptyset \\ \emptyset & \mathbf{R}_{120} \end{pmatrix} \mathbf{C}_{r12} \begin{pmatrix} \mathbf{R}_{120} & \emptyset \\ \emptyset & \mathbf{R}_{120} \end{pmatrix}^{-1} \\ \mathbf{C}_{r2}^R &= \begin{pmatrix} \mathbf{R}_{120} & \emptyset \\ \emptyset & \mathbf{R}_{120} \end{pmatrix}^2 \mathbf{C}_{r12} \begin{pmatrix} \mathbf{R}_{120} & \emptyset \\ \emptyset & \mathbf{R}_{120} \end{pmatrix}^{-2}, \end{aligned} \quad (\text{D.21})$$

Where \mathbf{R}_{120} is a rotation matrix for a rotation of 120 degrees about the z -axis:

$$\mathbf{R}_{120} = \begin{pmatrix} \cos(120) & -\sin(120) & 0 \\ \sin(120) & \cos(120) & 0 \\ 0 & 0 & 1 \end{pmatrix} \quad (\text{D.22})$$

The position \mathbf{p}_{r3} at which the endpoint of rod 3 is connected to the intermediate body, as shown in figure D.1, is given by:

$$\mathbf{p}_{r3} \equiv \begin{pmatrix} x_r \\ y_r \\ 0 \end{pmatrix} \quad (\text{D.23})$$

\mathbf{p}_{r1} and \mathbf{p}_{r2} can be calculated by rotating \mathbf{p}_{r3} about the z -axis, over 120 and 240 degrees respectively; analogous to equation D.21.

During probing, a force \mathbf{f}_t is applied to the probe tip. The position of the tip \mathbf{p}_t and the force vector \mathbf{f}_t are given by:

$$\mathbf{p}_t = \begin{pmatrix} p_{tx} \\ p_{ty} \\ p_{tz} \end{pmatrix} \quad (\text{D.24})$$

$$\mathbf{f}_t = \begin{pmatrix} f_{tx} \\ f_{ty} \\ f_{tz} \end{pmatrix} \quad (\text{D.25})$$

Due to the force \mathbf{f}_t , the intermediate body will translate over \mathbf{x}_i and rotate over \mathbf{r}_i . The translations and rotations of the intermediate body are gathered together in \mathbf{d}_i :

$$\mathbf{d}_i = \begin{pmatrix} \mathbf{x}_i \\ \mathbf{r}_i \end{pmatrix} = \begin{pmatrix} x_{ix} \\ x_{iy} \\ x_{iz} \\ r_{ix} \\ r_{iy} \\ r_{iz} \end{pmatrix} \quad (\text{D.26})$$

Due to the translation and rotation of the intermediate body, the free ends of the rods will be displaced over \mathbf{d}_r :

$$\mathbf{d}_{rn} = \begin{pmatrix} \mathbf{x}_i + \mathbf{r}_i \times \mathbf{p}_{rn} \\ \mathbf{r}_i \end{pmatrix}, \quad n = 1, 2, 3 \quad (\text{D.27})$$

The forces \mathbf{f}_{rn} and moments \mathbf{m}_{rn} acting on the rods, gathered together in \mathbf{g}_{rn} , can be calculated by multiplying \mathbf{d}_{rn} with \mathbf{C}_{rn} :

$$\mathbf{g}_{rn} \equiv \begin{pmatrix} \mathbf{f}_{rn} \\ \mathbf{m}_{rn} \end{pmatrix} = \mathbf{C}_{rn} \mathbf{d}_{rn}, \quad n = 1, 2, 3 \quad (\text{D.28})$$

Assuming a static situation, the sum of forces and the sum of moments acting on the intermediate body should equal zero:

$$\begin{aligned} \mathbf{f}_t + \sum_{n=1}^3 -\mathbf{f}_{rn} &= 0 \\ \mathbf{p}_t \times \mathbf{f}_t + \sum_{n=1}^3 (-\mathbf{m}_{rn} + \mathbf{p}_{rn} \times -\mathbf{f}_{rn}) &= 0 \end{aligned} \quad (\text{D.29})$$

By solving these equations, the rotations and translations of the intermediate body can be written as function of the applied force on the probe tip:

$$\mathbf{d}_i = \begin{pmatrix} \frac{2}{3} f_{tx} (c_{r_{xx}} + c_{r_{yy}})^{-1} \\ \frac{2}{3} f_{ty} (c_{r_{xx}} + c_{r_{yy}})^{-1} \\ \frac{1}{3} f_{tz} (c_{r_{zz}})^{-1} \\ \frac{2}{3} (p_{ty} f_{tz} - p_{tz} f_{ty}) (k_{r_{xx}} + k_{r_{yy}} + c_{r_{zz}} x_r^2 + 2ck_{r_{zz}} y_r + c_{r_{zz}} y_r^2)^{-1} \\ \frac{2}{3} (p_{tz} f_{tx} - p_{tx} f_{tz}) (k_{r_{xx}} + k_{r_{yy}} + c_{r_{zz}} x_r^2 + 2ck_{r_{zz}} y_r + c_{r_{zz}} y_r^2)^{-1} \\ \frac{1}{3} (p_{tx} f_{ty} - p_{ty} f_{tx}) (k_{r_{zz}} + c_{r_{yy}} x_r^2 + c_{r_{xx}} y_r^2 - 2ck_{r_{xz}} y_r)^{-1} \end{pmatrix} \quad (\text{D.30})$$

Because l_r is at least one order of magnitude larger than t_r , $c_{r_{yy}}$ is at least two orders of magnitude larger than the other c_r -constants. As a result, displacements of the tip due to translations of the intermediate body in x - and y -direction or rotation about the z -axis are two orders of magnitude

smaller than displacements of the tip due to rotations of the intermediate body. Neglecting displacements of the intermediate body in x - and y - directions the applied force on the tip can be written as function of the displacement of the intermediate body:

$$\mathbf{f}_t = \begin{pmatrix} \frac{3}{2}(k_{r_{xx}} + k_{r_{yy}} + c_{r_{zz}}x_r^2 + 2ck_{r_{zx}}y_r + c_{r_{zz}}y_r^2)r_{iy}p_{tz}^{-1} + 3c_{zz}p_{tx}p_{tz}^{-1}x_{iz} \\ \frac{3}{2}(k_{r_{xx}} + k_{r_{yy}} + c_{r_{zz}}x_r^2 + 2ck_{r_{zx}}y_r + c_{r_{zz}}y_r^2)r_{ix}p_{tz}^{-1} + 3c_{zz}p_{ty}p_{tz}^{-1}x_{iz} \\ 3c_{r_{zz}}x_{iz} \end{pmatrix} \quad (\text{D.31})$$

Assuming that the intermediate body does not rotate around the z -axis, i.e. $r_{tz} = 0$, the displacement of the intermediate body is dependent on the tip displacement according to:

$$\mathbf{d}_i = \begin{pmatrix} \mathbf{x}_t + \mathbf{r}_t \times -\mathbf{p}_t \\ \mathbf{r}_t \end{pmatrix} = \begin{pmatrix} x_{tx} - r_{ty}p_{tz} \\ x_{ty} + r_{tx}p_{tz} \\ x_{tz} - r_{tx}p_{ty} + r_{ty}p_{tx} \\ r_{tx} \\ r_{ty} \\ r_{tz} \end{pmatrix} \equiv \begin{pmatrix} 0 \\ 0 \\ x_{iz} \\ r_{ix} \\ r_{iy} \\ 0 \end{pmatrix} \quad (\text{D.32})$$

It follows that:

$$\begin{aligned} x_{iz} &= x_{tz} + p_{ty}p_{tz}^{-1}x_{ty} + p_{tx}p_{tz}^{-1}x_{tx} \\ r_{ix} &= -x_{ty}p_{tz}^{-1} \\ r_{iy} &= x_{tx}p_{tz}^{-1} \end{aligned} \quad (\text{D.33})$$

By substituting the equations of D.33 into equation D.31, the applied force on the tip \mathbf{f}_t can be written as a function of the tip displacement \mathbf{x}_t :

$$\mathbf{f}_t = \mathbf{C}_{probe} \cdot \mathbf{x}_t \quad (\text{D.34})$$

Where \mathbf{C}_{probe} is the stiffness matrix at the probe tip:

$$\mathbf{C}_{probe} = \begin{pmatrix} C_{11} & C_{12} & C_{13} \\ C_{21} & C_{22} & C_{23} \\ C_{31} & C_{32} & C_{33} \end{pmatrix} \quad (\text{D.35})$$

And:

$$\begin{aligned}
\mathbf{C}_{11} &= \left(\left(\frac{1}{2}c_{zz12} + c_{zz3} \right) x_r^2 + 3c_{zx12}y_r + \frac{3}{2}c_{zz12}y_r^2 \right) p_{tz}^{-2} \\
&\quad + \left(\frac{1}{2}k_{yy12} + \frac{3}{2}k_{xx12} + k_{yy3} \right) p_{tz}^{-2} \\
&\quad + (c_{zz12} - c_{zz3}) 2x_r p_{tx} p_{tz}^{-2} + (2c_{zz12} + c_{zz3}) p_{tx}^2 p_{tz}^{-2} \\
\mathbf{C}_{22} &= \left(\left(\frac{1}{2}c_{zz12} + c_{zz3} \right) y_r^2 + (c_{zx12} + 2c_{zx3}) y_r + \frac{3}{2}c_{zz12}x_r^2 \right) p_{tz}^{-2} \\
&\quad + \left(k_{xx3} + \frac{1}{2}k_{xx12} + \frac{3}{2}k_{yy12} \right) p_{tz}^{-2} \\
&\quad + ((c_{zz12} - c_{zz3}) y_r + c_{zx12} - c_{zx3}) 2p_{ty} p_{tz}^{-2} + (c_{zz3} + 2c_{zz12}) p_{ty}^2 p_{tz}^{-2} \\
\mathbf{C}_{33} &= c_{zz3} + 2c_{zz12} \\
\mathbf{C}_{12} = \mathbf{C}_{21} &= ((c_{zx3} - c_{zx12}) x_r + (c_{zz3} - c_{zz12}) x_r y_r) p_{tz}^{-2} \\
&\quad + ((c_{zz12} - c_{zz3}) y_r + c_{zx12} - c_{zx3}) p_{tx} p_{tz}^{-2} \\
&\quad + (c_{zz12} - c_{zz3}) x_r p_{ty} p_{tz}^{-2} + (2c_{zz12} + c_{zz3}) p_{tx} p_{ty} p_{tz}^{-2} \\
\mathbf{C}_{23} = \mathbf{C}_{32} &= ((c_{zz12} - c_{zz3}) y_r + c_{zx12} - c_{zx3}) p_{tz}^{-1} + (c_{zz3} + 2c_{zz12}) p_{ty} p_{tz}^{-1} \\
\mathbf{C}_{13} = \mathbf{C}_{31} &= (c_{zz12} - c_{zz3}) x_r p_{tz}^{-1} + (c_{zz3} + 2c_{zz12}) p_{tx} p_{tz}^{-1}
\end{aligned}$$

For an isotropic suspension, $\mathbf{C}_{r1} = \mathbf{C}_{r2} = \mathbf{C}_{r3}$, equation D.35 reduces to [Widdershoven 04]:

$$\begin{aligned}
\mathbf{C}_{probe} &= \begin{pmatrix} \frac{3}{2}b \cdot p_{tz}^{-2} + 3c_{rzz} p_{tx}^2 p_{tz}^{-2} & 3c_{rzz} p_{tx} p_{ty} p_{tz}^{-2} & 3c_{rzz} p_{tx} p_{tz}^{-1} \\ 3c_{rzz} p_{tx} p_{ty} p_{tz}^{-2} & \frac{3}{2}b \cdot p_{tz}^{-2} + 3c_{rzz} p_{ty}^2 p_{tz}^{-2} & 3c_{rzz} p_{ty} p_{tz}^{-1} \\ 3c_{rzz} p_{tx} p_{tz}^{-1} & 3c_{rzz} p_{ty} p_{tz}^{-1} & 3c_{rzz} \end{pmatrix} \\
b &= k_{rxx} + k_{ryy} + c_{rzz} x_r^2 + 2ck_{rzz} y_r + c_{rzz} y_r^2
\end{aligned} \tag{D.36}$$

Note that for an ideal position of the probe tip, $p_{tx} = p_{ty} = 0$ and $p_{tz} = l_{st}$, this stiffness matrix reduces to a diagonal matrix where $\mathbf{C}(1,1) = \mathbf{C}(2,2)$, in accordance with the stiffness matrix calculated by Pril [Pril 02].

D.6 Stresses in the slender rods

It is assumed that the slender rods are infinitely stiff for loads in their length direction, compared to other stiffnesses, i.e. $c_{ryy} = \infty$. The forces and moments acting on the rods are transformed to their local frames, i.e. their length direction is aligned to the y-axis:

$$\begin{aligned}
\mathbf{g}'_{r3} &= \mathbf{g}_{r3} \\
\mathbf{g}'_{r1} &= \begin{pmatrix} \mathbf{R}_{120} & \emptyset \\ \emptyset & \mathbf{R}_{120} \end{pmatrix}^{-1} \mathbf{g}_{r1} \\
\mathbf{g}'_{r2} &= \begin{pmatrix} \mathbf{R}_{120} & \emptyset \\ \emptyset & \mathbf{R}_{120} \end{pmatrix}^{-2} \mathbf{g}_{r2}
\end{aligned} \tag{D.37}$$

$$\tag{D.38}$$

From these forces and moments, the stresses in the rods can be calculated. The shear and tensile stresses, gathered together in a vector σ_n , can be calculated by multiplying \mathbf{g}'_{rn} with a 6x6 matrix \mathbf{S} [Pril 02]:

$$\sigma_n \equiv \begin{pmatrix} \sigma_{n_{xx}} \\ \sigma_{n_{yy}} \\ \sigma_{n_{zz}} \\ \sigma_{n_{yz}} \\ \sigma_{n_{xz}} \\ \sigma_{n_{xy}} \end{pmatrix} = \mathbf{S} \mathbf{g}'_{rn} \quad (\text{D.39})$$

Where:

$$\mathbf{S} = \begin{pmatrix} 0 & 0 & 0 & 0 & 0 & 0 \\ -\frac{\beta(\alpha-\frac{1}{2})t_r l_r}{I_{rz}} & \frac{1}{A_r} & -\frac{(\alpha-\frac{1}{2})w_r l_r}{2I_{rx}} & -\frac{1}{I_{rx}} & 0 & \frac{x_r}{I_{rz}} \\ 0 & 0 & 0 & 0 & 0 & 0 \\ 0 & 0 & 0 & 0 & 0 & 0 \\ \frac{1}{A_r} & 0 & 0 & 0 & \frac{G_r t_r}{k_{ryy} l_r} & 0 \\ 0 & 0 & \frac{1}{A_r} & 0 & 0 & 0 \end{pmatrix} \quad (\text{D.40})$$

Here, I_{rx} and I_{rz} are the second moment of area around the x - and z -axis, respectively, and A_r is the cross-section of the rod. The dimensionless parameters α and β indicate the position on the rod in local coordinates in y - and z -direction, respectively, as shown in figure D.2. Naturally, the maximum stress will be at the ends of the slender rod, i.e. $\alpha = 0$ and $\alpha = 1$, at the top and top and bottom, i.e. $\beta = \frac{1}{2}$ or $\beta = -\frac{1}{2}$.

For slender rod 1, equation D.39 yields:

$$\sigma_1 = \mathbf{S} \mathbf{g}'_{r1} = \frac{t_r}{2l_r^3 l_{st}} \begin{pmatrix} 0 \\ E_r (-12\alpha x_r x_{tx} + (6\alpha l_r - 12\alpha y_r - l_r) x_{ty} - 12\alpha l_{st} x_{tz}) \\ 0 \\ 0 \\ -2G_r l_r^2 x_{tx} \\ -E_r t_r (-2x_r l_r x_{tx} + (l_r - 2y_r) x_{ty} - 2l_{st} x_{tz}) \end{pmatrix} \quad (\text{D.41})$$

Here, E_r is the Young's modulus and G_r is the shear modulus of the slender rod, and x_{tx} , x_{ty} and x_{tz} are the displacements of the probe tip in x -, y - and z -direction, respectively. The length l_r , width w_r and thickness t_r of the slender rod and their position in the chip, given by x_r and y_r , are indicated in figure D.1.

D.7 Conversion matrix

The resistance of the piezo resistive strain gauges, located on the surfaces of the slender rods, depends on the local strain. As discussed, the stress at the top surface is given by equation D.39, where $\beta = \frac{1}{2} t_r$. Using Hooke's law, i.e. $\sigma = E\varepsilon$, the strain ε at the top surface is given by:

$$\varepsilon_n \equiv \begin{pmatrix} \varepsilon_{n_{xx}} \\ \varepsilon_{n_{yy}} \\ \varepsilon_{n_{zz}} \\ \varepsilon_{n_{yz}} \\ \varepsilon_{n_{xz}} \\ \varepsilon_{n_{xy}} \end{pmatrix} = \frac{\sigma_n}{E_r} \quad (\text{D.42})$$

Polysilicon strain gauges are sensitive to longitudinal and transversal strain only. Therefore the relative change of their resistance $\Delta R/R$ can be described as:

$$\frac{\Delta R}{R} = G_l \varepsilon_{yy} + G_t \varepsilon_{xx} \quad (\text{D.43})$$

where the longitudinal and transversal gauge factors G_l and G_t are introduced. On each of the rods four strain gauges are located, i.e. $R_1 \dots R_4$. The resistance change is measured in a full Wheatstone bridge circuit, as discussed in section 3.1.2. The measured voltage V_m across the bridge in first order approximation can be calculated using:

$$V_m = \frac{V_0}{4} \left(\frac{\Delta R_1}{R_1} - \frac{\Delta R_2}{R_2} - \frac{\Delta R_3}{R_3} + \frac{\Delta R_4}{R_4} \right) \quad (\text{D.44})$$

where V_0 is the supply voltage of the bridge circuit. The relative change of resistance can be calculated using equations D.43 and D.42, with $\alpha = -\frac{1}{2}$ for R_1 and R_4 and with $\alpha = \frac{1}{2}$ for R_2 and R_3 . The strain can be expressed in the tip displacement \mathbf{x}_t . As the model is linear, the voltages V_{m_1} , V_{m_2} , and V_{m_3} show a linear relation to the tip displacements. Hence the dependence can be written in matrix form:

$$\begin{pmatrix} V_{m_1} \\ V_{m_2} \\ V_{m_3} \end{pmatrix} = \mathbf{A} \mathbf{x}_t \quad (\text{D.45})$$

The theoretical transformation matrix \mathbf{A}_{theory} , as given by equation D.45, can be worked out to be:

$$\mathbf{A}_{theory} = V_0 \frac{3t_r G_l}{4l_r^2 p_{tz}} \begin{pmatrix} 4p_{tx} + 2x_r + 2\sqrt{3}y_r - \sqrt{3}l_r & 4p_{ty} - 2\sqrt{3}x_r + 2y_r - l_r & 4p_{tz} \\ 4p_{tx} + 2x_r - 2\sqrt{3}y_r + \sqrt{3}l_r & 4p_{ty} + 2\sqrt{3}x_r + 2y_r - l_r & 4p_{tz} \\ 4p_{tx} - 4x_r & 4p_{ty} - 4y_r + 2l_r & 4p_{tz} \end{pmatrix} \quad (\text{D.46})$$

Note that for an ideal position of the probe tip, $p_{tx} = p_{ty} = 0$ and $p_{tz} = -l_{st}$, the theoretical transformation matrix \mathbf{A}_{theory} , as given by equation D.46, corresponds to the theoretical stiffness matrix as calculated by Pril [Pril 02].

The sensitivity S_i of the probe for a given direction i is now given by:

$$S_i \equiv \frac{|\mathbf{A} \mathbf{x}_{t_i}|}{|\mathbf{x}_{t_i}|} \quad (\text{D.47})$$

Appendix E

Design considerations

E.1 Fundamentals of determinism

The behavior of the probing system is deterministic, i.e. its behavior obeys cause and effect relationships. The following quote by Donaldson illustrates the deterministic behavior of machine tools [Donaldson 72A, Hale 99]:

A basic finding from our experience in dealing with machining accuracy is that machine tools are deterministic. By this we mean that machine tool errors obey cause-and-effect relationships, and do not vary randomly for no reason. Further, the causes are not esoteric and uncontrollable, but can be explained in terms of familiar engineering principles. These explanations are not simply educated (or uneducated) guesses, but are based on tests which are designed to isolate the sources of error. Once isolated, it is usually found that the source of error can be reduced to a satisfactory level by relatively simple and inexpensive means.

Determinism is both a principle, as illustrated by the quote above, and a philosophy, as illustrated by the following quote [Bryan 84]:

A determinist will never agree that a fixed value of non-repeatability can be assigned to a given machine. Such a value does not exist. Non-repeatability depends primarily on the time, money, and skill (culture) of the user.

A consequence of determinism is that once cause and effect relationships are known their influence on machine deviations can be compensated for. Therefore, an important aspect of a measuring instrument is its repeatability, i.e. ability of a measuring instrument to provide closely similar indications for repeated applications of the same measurand under the same conditions of measurement. Ideally, a measuring instrument should be insensitive to disturbances, e.g. environmental changes, and its behavior should be repeatable. This is the basis of the principles of precision machine design as described in literature [Brouwer 07, Corbett 00, Hale 99, Schellekens 98, Slocum 92]. An important design principle is that of exact-constraint design, as will be discussed in the next section.

E.2 Exact-constraint design

An unconstrained rigid body has six degrees of freedom, i.e. it can translate in x -, y - and z -direction and rotate around the x -, y - and z -axis. When not all degrees of freedom for a given body are constrained, the body is free to move in the unconstrained degrees of freedom. Fixation of this body in space therefore requires all six degrees of freedom to be fixated.

A non-rigid body may have one or more degrees of flexibility, relatively speaking, that act as additional degrees of freedom. For example, torsional stiffness of an open shoe-box is low in comparison to the stiffness of other deformations. Thus, an open shoe-box has one internal degree of freedom. Therefore seven degrees of freedom need to be constrained to fixate this body in space.

An ideal constraint would be rigid in one or more degrees of freedom and would allow absolutely free motion in all other degrees of freedom. In practice stiffness of a constraint, such as a slender rod or a small-area contact between two surfaces, is finite in the direction of fixation. Also, it has a stiffness in the other degrees of freedom. However, since stiffness of a slender rod in its length direction is several orders of magnitude higher than stiffness in other directions, it is assumed that it only fixates one degree of freedom.

An important benefit of exact-constrained design is that it isolates sensitive parts or systems, e.g. the metrology frame, from the influence of manufacturing tolerances or deviations in the support frame or structural loop, e.g. due to temperature variations or loading of the frame. When a design is over-constrained it often suffers from backlash and requires tight tolerances in order to function properly. Therefore a divergence from exact-constraint design increases the cost of manufacturing [Smith 92].

When a degree of freedom is fixated more than once, geometric deviations in the support frame result in internal component stresses. This is shown for an in-plane mounting of a rectangular component in figure E.1. Here, stress in the frame and component is shown due to a force on the left edge of the support frame.

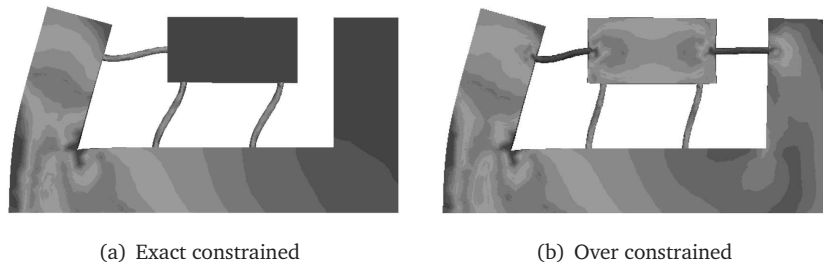


Figure E.1: Stress in a component (center block) due to a deformation in the frame: (a) component is connected to the frame in an exact constrained manner, (b) component is connected to frame in an over constrained manner, resulting in a higher material stress in the component.

As mentioned before, a slender rod can be used to fixate one degree of freedom, as shown in figure E.2 (a). Stiffness in the length direction of the slender rod is several orders of magnitude higher than stiffness in other degrees of freedom. Therefore, all rigid body points along the constraint line can move only at right angles to the constraint line, not along it [Blanding 92].

Two degrees of freedom can be fixated using two slender rods, as shown in figure E.2 (b). It should be noted that if two constraints were to lie on the same line, they fixate the same degree of freedom twice. Hence, two constraint lines on the same line result in one over-constrained degree of freedom, figure E.1 (b), rather than constraining two degrees of freedom.

When two constraint lines intersect each other, as shown in figure E.2 (b), a virtual point of rotation (PoR) is created. In figure E.2 (b), two rods fixate rigid body translation in x - and y -direction and allow rigid body rotation around the z -axis through the instantaneous point of rotation (PoR).

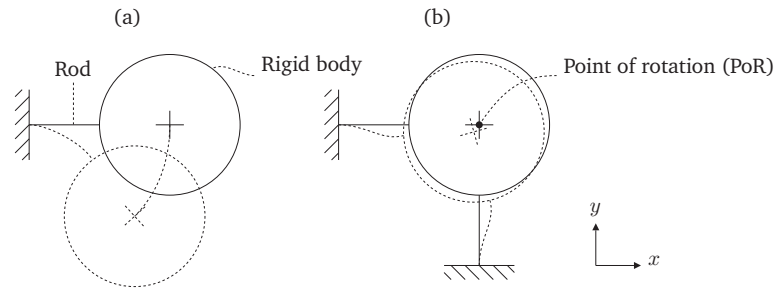


Figure E.2: Schematic fixation: (a) one degree of freedom is fixated: translation in x -direction and (b) two degrees of freedom are fixated: translations in x - and y -direction.

In order to constrain rotation around the z -axis as well, a third constraint is required which reacts with a moment around the axis of rotation. This is shown in figure E.3, where three slender rods fixate translations in x - and y -direction and rotation around the rigid body z -axis. Each slender rod prevents rotation about the instantaneous point of rotation (PoR) formed by the other pair of slender rods. As a result three degrees of freedom in the xy -plane are exactly constrained.

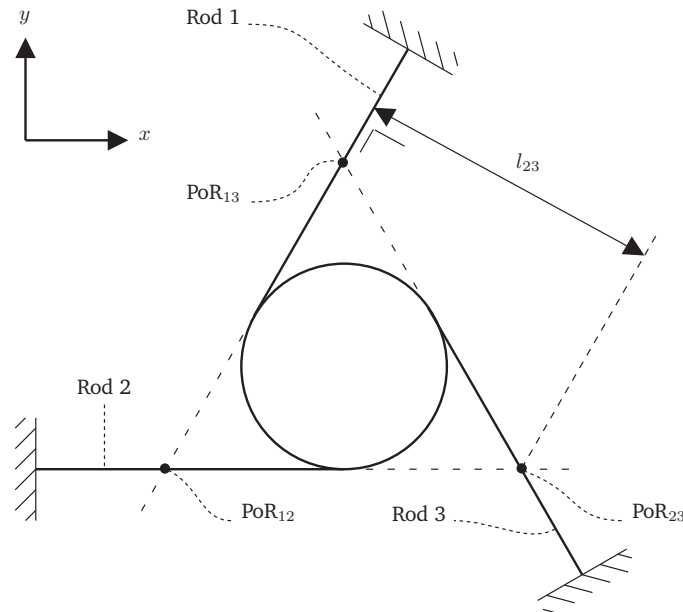


Figure E.3: Schematic fixation of three degrees of freedom: translations in x - and y -direction and rotation around z -axis.

The lever arm length l_{23} is a relative measure of the constraint effectiveness, formed by rod 1, for a rotation around PoR_{23} . Ideally, lever arms for all three rods should have the same length. In this arrangement, constraint lines form an equilateral triangle, as shown in figure E.3, where triangle size is a measure for rotational stiffness for given slender rod dimensions.

E.3 Thermal design considerations

When considering the influence of thermal effects on the measurement, it is important to distinguish between short term stability and long term stability of the metrology loop [Ruijl 01]. Short term stability refers to the situation where the metrology loop has to be geometrically stable for the duration of the measurement only. Parts that require long term stability need to be geometrically stable during the time in-between two successive calibrations.

For an absolute measurement, all parts of the metrology loop should have long term stability. Changes in the metrology loop during the time in-between two successive calibrations influence the measurement result. Changes should therefore be neglectable with respect to the required uncertainty, or the influence on the measurement result should be known and compensated for.

In the situation of a coordinate measuring machine, all measured dimensions are relative with respect to the work piece. Therefore, the measurement result is only affected by drift in the metrology loop when it takes place during the particular measurement period. The parts of the metrology loop that only contribute to drift of the machine coordinate system therefore require short term stability.

As stated by Bryan [Bryan 90] thermal distortions are in principle repeatable if examined close enough. However, lack of physical understanding and modeling makes describing these effects highly complex. Therefore, thermal distortions seem non-repeatable in most applications [Ruij] 01]. Also, disturbances due to handling or heat radiation of an operator can introduce large measurement deviations [Dutschke 96].

It is noted that thermal deviations should be considered for all parts of the metrology loop. For coordinate measuring machines, this includes the contribution of the machine, probe and work piece. For example, for an aluminum work piece with a nominal length of 10 mm a homogeneous temperature change will result in a deviation of 230 nm/K, equation E.1.

Measures to reduce the thermal positioning or measurement deviations are often categorized as [Bryan 90, Breyer 91]:

1. Minimizing and controlling the heat flow into the system;
2. Optimizing the machine design to obtain a small sensitivity to thermal disturbances;
3. Compensation of the deviations via software methods.

In its simplest form, the influence of a homogeneous temperature change ΔT on the change in length Δl of an object with nominal length l_0 and a coefficient of thermal expansion α , is given by [Florussen 02]:

$$\Delta l = \alpha l_0 \Delta T \quad (\text{E.1})$$

For a beam with a constant thermal gradient in y -direction, G_y , the deflection at the end of the beam Δy is given by:

$$\Delta y = \alpha G_y \frac{l_0^2}{2} \quad (\text{E.2})$$

Where G_y is defined by:

$$G_y = \frac{T(y_2) - T(y_1)}{y_2 - y_1} \quad (\text{E.3})$$

Here $T(y_1)$ and $T(y_2)$ are the temperature at the top and bottom of the beam at position y_1 and y_2 , respectively.

Many precision machine designs use solid parts consisting of materials with a high thermal conductivity, e.g. aluminum, to minimize the influence of thermal gradients, equation E.2. When a homogeneous temperature distribution over all parts of the metrology loop is assumed, calculation of thermal distortions is relatively straightforward, e.g. using equation E.1.

Using this approach it is possible to create a system in which homogeneous temperature variations do not influence the measurement result. An example is the system shown in figure E.4, where all parts of the metrology loop, including the displacement probe, are made from the same material, e.g. aluminum. In this system, a change in temperature will, in principle, result in an expansion of

all components which, when combined, cancel each other out. Therefore, the probe measurement will not be influenced by temperature changes in this system¹. However, as mentioned by Ruijl [Ruijl 01] the two main limitations for this approach are:

1. The heat flow resistance at the interface between the separate components of the metrology loop;
2. The transient and frequency response if the time constants of the components of the metrology loop are different.

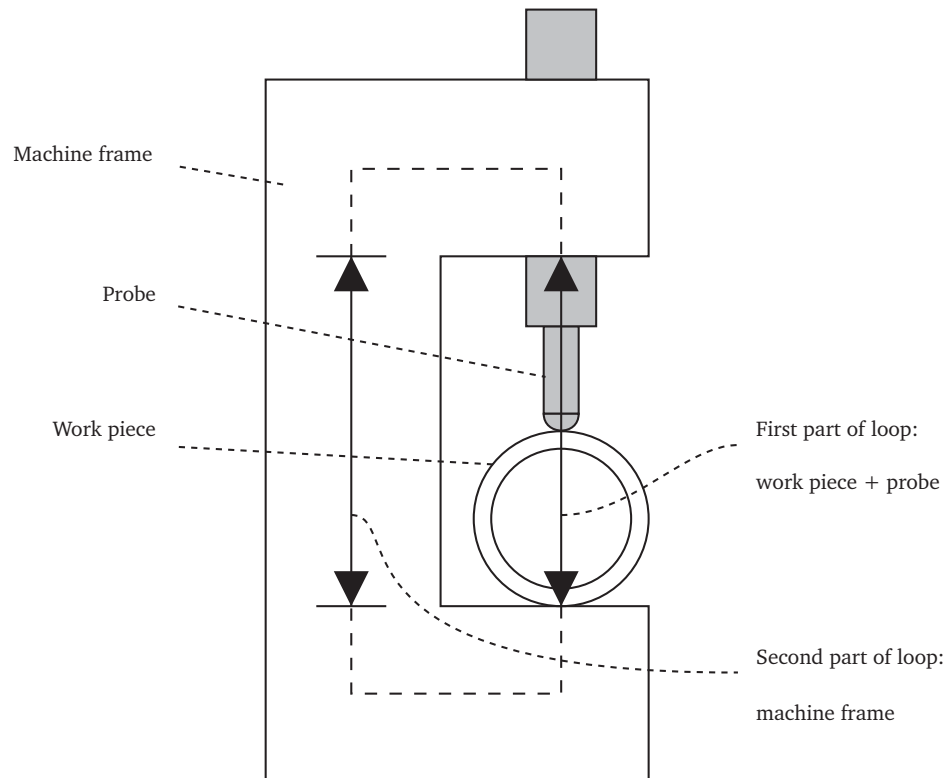


Figure E.4: Schematic of the thermal loop through a CMM frame, probe and work piece.

The method of assembly, e.g. glue, guide ways, gap of an air bearing and other local thermal resistances may greatly influence the thermal behavior of a system. For example, the heat flow resistance across the gap of an air bearing with a height of 10-15 μm equals the heat flow resistance of about 60-100 mm aluminum [Ruijl 01]. Forced heat convection, e.g. by internal water flow or external air flow, can be used to improve the heat conduction between the components.

Looking again at figure E.4 it can be seen that the time constants of the separate components in the metrology loop are not the same. It is assumed that all components in figure E.4 behave as a first order system, where the frame has a time constant of 1 hour and the work piece and probe both have a time constant of 10 minutes. Figure E.5 shows the relative thermal expansion of the first part of the metrology loop, consisting of work piece and probe, and the second part of the loop, consisting of the frame, as shown in figure E.4.

The difference between the expansion of the first and second part of the loop is measured by the probe as a displacement. The relative displacement as measured by the probe is shown by the solid line in figure E.5. It can be seen that, even though all parts of the loop are made out

¹It is noted that a change in temperature may influence the reference of the probe system, e.g. a graduated ruler, which will influence its sensitivity. However, when the probe tip is not displaced, as in figure E.4, the measurement result will remain unaffected.

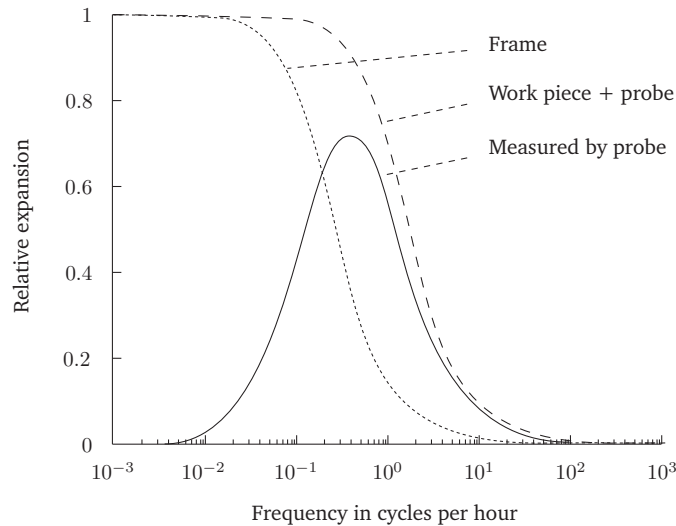


Figure E.5: Relative thermal expansion of both parts of the metrology loop and relative displacement as measured by the probe.

of the same material, the thermal loop is not thermally stable for temperature changes in the critical frequency range. By improving the heat conduction between the components and using an appropriate enclosure, the frequency spectrum can be controlled in a way in which it does not excite the critical frequency range.

E.4 Dynamic and thermal considerations

As discussed in section 2.3.1, a deformation in the structural loop of the probe between its tip and connection to the measurement instrument results in a decrease in measurement resolution. Stiffness of center platform and stylus should therefore be as high as possible to assure that a probe tip displacement results in a maximum slender rod deformation. However, the equivalent mass at the probe tip should be minimized to decrease plastic deformation during a probing operation as a result of impact forces, as discussed in section 2.1.3. These parts therefore require a light and stiff design.

This can be obtained by structure design, as will be discussed in the next paragraph, and by an appropriate choice of material. A light and stiff design is obtained for materials with a high Young's modulus E and low density ρ . Therefore, specific stiffness E/ρ is often used to compare materials, and should be as high as possible for a light and stiff design. Table E.1 lists specific stiffness for several common construction materials. Specific stiffness of ceramics, like silicon carbide (SiC) and boron carbide (B_4C), is often 10 times as high as for other construction materials. Therefore they are good materials when a light and stiff construction is needed.

A good indicator for an efficient use of material in the design of a structure is the von Mises equivalent stress, as discussed in appendix F. Efficient use of material, and thereby a light and stiff construction, is obtained when the von Mises equivalent stress σ_e is uniform across the structure. This is shown by the example of a simple cantilever, as shown in figure E.6.

It can be seen that stress in the cantilever is high at the point of fixation, i.e. fixed world, and decreases near its free end. This can be understood by looking at moment $M(x)$ at position x in the length direction of the cantilever. The moment is given by $M(x) = F(l - x)$, and is thus maximized near the fixed end, where $x = 0$, and minimized near the free end of the cantilever, where $x = l$. Since mechanical properties of the cantilever are uniform in its length direction, the stress distribution is not.

The second point of interest in figure E.6 is the stress distribution in the thickness direction of the cantilever. It can be seen that stress in the neutral plane of the cantilever is low, ideally zero,

Material	Young's modulus E in Pa	Density ρ in kg/m^3	Specific stiffness E/ρ	Normalized specific stiffness
	$\times 10^9$	$\times 10^3$	$\times 10^6$	
Cast iron	100	7.3	14	1.0
Invar	145	8.1	18	1.3
Aluminum	70	2.7	26	1.9
Steel	200	7.8	26	1.9
Granite	75	2.7	28	2.0
Zerodur	91	2.5	36	2.6
Tungsten Carbide	627	14.9	42	3.1
Silicon	100	2.3	43	3.1
Silicon carbide (SiC)	370	3.0	123	9.0
Boron carbide (B_4C)	450	2.5	179	13.0

Table E.1: Material properties of several construction materials [Vaccari 02].

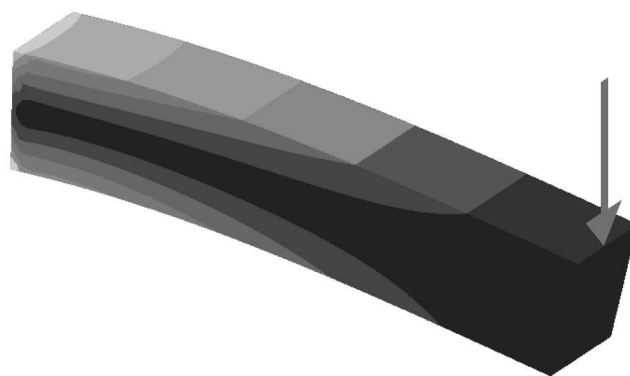


Figure E.6: Contour band plot of the von Mises stress in a simple cantilever with a force exerted on its free end.

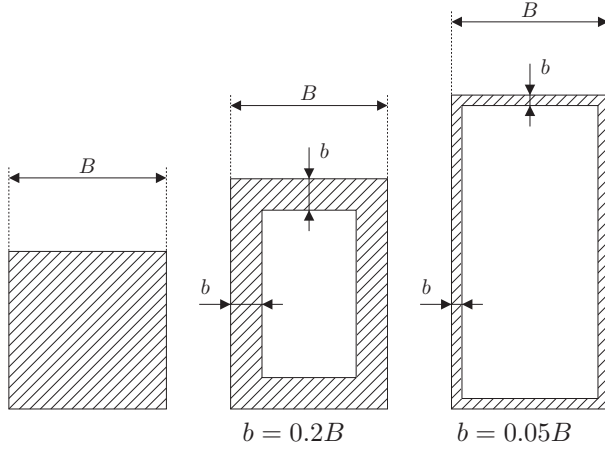
Cross-section			
			
<i>Mechanical properties of the structure</i>			
Stiffness	1	5.9	99
Frequency	1	2.4	10
<i>Thermal properties of the structure</i>			
Time constant	1	3.3	13.3
Bending deformation	1	2.5	10

Table E.2: Mechanical and thermal properties for three cantilevers with different cross sections and equal material volume. Values of the solid cantilever are scaled to unity and its height H is given by $H = 2B$.

whereas stress in the top and bottom plane of the cantilever are maximized. For pure bending, as shown in figure E.6, material near the neutral plane is not used effectively. To improve the structure's stiffness per weight, structural parts with a high stress, e.g. top and bottom plane, should be reinforced using material from structural parts with low stress, e.g. near the neutral plane. In the cantilever example of figure E.6 this would result in a hollow structure [Ruijl 01].

Eigen frequencies f_e of bending modes of such a cantilever can be described by the Euler-Bernoulli cantilever model [Karnovsky 04]. Following this model, natural frequencies f_e of cantilever bending modes are proportional to [Han 99]:

$$f_e \propto \sqrt{\frac{E}{\rho} \frac{I}{A}} \quad (\text{E.4})$$

Table E.2 shows the stiffness and eigen frequency of three cantilevers with different cross sections.

The second point of interest for these cantilevers are frame deformations due to thermal distortions. These distortions are especially important in the metrology frame, as discussed in section E.3, and are often a main source of measurement deviations [Bryan 90].

Cantilevers with a hollow cross section result in a higher stiffness per weight of the construction, as shown in table E.2. However, structures with a small wall thickness b also have a high area per volume and thus a low time constant with respect to homogeneous thermal variations of the environment. As a result these structures are more sensitive to environmental thermal disturbances.

However, thermal conductivity for a cantilever with hollow cross section also decreases when thickness b decreases. As a result, the structure is more susceptible to thermal deformations, e.g. bending, due to a thermal gradient. As discussed in [Breyer 91, Ruijl 01] bending deformation δ_f of a cantilever due to a constant heat flux is proportional to:

Material	Thermal conductivity λ in $\text{W/m} \cdot \text{K}$	Lin. thermal expansion α in K^{-1}	Thermal quotient λ/α	Normalized thermal quotient
		$\times 10^{-6}$	$\times 10^6$	
Granite	3.5	7	0.5	1.0
Steel	27	10	2.7	5.4
Boron carbide (B_4C)	29	6	4.8	9.7
Cast iron	60	11.5	5.2	10.4
Aluminum	237	23.2	10.2	20.4
Invar	16	1.5	10.7	21.3
Tungsten Carbide	100	7.3	13.7	27.4
Silicon Carbide (SiC)	120	4.6	26.1	52.2
Silicon	115	4.2	27.4	54.8
Zerodur	1.64	0.05	32.8	65.6

Table E.3: Material properties of several materials, sources [Vaccari 02].

$$\delta_f \propto \frac{\alpha}{\lambda} \frac{B}{2b} \quad (\text{E.5})$$

Where, α is the coefficient of linear thermal expansion and λ is the thermal conductivity of the structure material. Table E.3 lists the coefficient of linear thermal expansion α and thermal conductivity λ for several construction materials. It should be clear that bending deformation δ_f decreases when the ratio of λ/α increases.

The time constant and bending deformation δ_f are also shown in table E.2 for the three listed cantilevers. It should be clear that the thermal time constant of a hollow structure is higher than the thermal time constant of a solid structure. The response of a hollow structure to homogeneous environmental temperature variations is thus lower. In other words: it takes longer for the structure to reach its equilibrium temperature, but when in equilibrium it is less susceptible to homogeneous variations in environmental temperature. When the temperature of a structure is known, it is possible to compensate for the effects of a homogeneous temperature variation.

From table E.2 it can also be seen that a hollow structure is more sensitive to bending deformation due to a thermal gradient, i.e. due to a local heat source. Internal and external heat sources often result in a thermal gradient and thermal bending deformations are therefore a main influence on measurement deviations in the metrology loop [Bryan 90]. Compensation of this effect requires detailed knowledge on the temperature distribution throughout the metrology frame. For these reasons a solid cross section of structures in the metrology frame is preferred for most applications. However, it should be clear that this is somewhat system specific.

From tables E.3 and E.1 it can be seen that the optimum material choice in a structure depends on its function. The function of structural loop can best be performed by a frame with a high specific stiffness [Hale 99, Schellekens 98, Slocum 92]. From tables E.1 and E.2 it can be seen that when the cantilever is used as a structural element it is ideally hollow and manufactured from a material with a high specific stiffness. The stiffness per weight of a hollow ($b = 0.05B$) boron carbide cantilever is approximately 1300 times that of a solid cast iron cantilever.

The function of metrology loop can best be performed by a frame with a high (thermal) stability. Minimum bending deformation due to a constant heat flux is obtained when the cantilever has a solid cross section and materials used have a high thermal conductivity and low coefficient of thermal expansion. From tables E.3 and E.2 it can be seen that the bending deformation δ_f of a hollow ($b = 0.05B$) granite cantilever is approximately 650 times higher than the bending deformation of a solid zerodur cantilever.

In high precision coordinate measuring machines, the metrology loop is often isolated from the structural loop [Ruijl 01, Seggelen 07]. Forces on the structural frame are thus isolated from the

metrology frame, which minimizes their influence on the measurement result. By using a different frame for metrology and structural loop, the design of each frame can thus also be optimized with respect to its function, as discussed in this section.

Appendix F

Von Mises equivalent stress

The root mean square maximum shear stress for a complex three-dimensional state of stress is given by [Fenner 89]:

$$\tau_m = \sqrt{\frac{1}{3} \left(\left(\frac{\sigma_1 - \sigma_2}{2} \right)^2 + \left(\frac{\sigma_2 - \sigma_3}{2} \right)^2 + \left(\frac{\sigma_3 - \sigma_1}{2} \right)^2 \right)} \quad (\text{F.1})$$

For simple uniaxial tension, where $\sigma_1 = \sigma_e$, $\sigma_2 = 0$ and $\sigma_3 = 0$, this becomes:

$$\tau'_m = \frac{\sigma_e}{\sqrt{6}} \quad (\text{F.2})$$

By equating τ_m and τ'_m we obtain:

$$2\sigma_e^2 = (\sigma_1 - \sigma_2)^2 + (\sigma_2 - \sigma_3)^2 + (\sigma_3 - \sigma_1)^2 \quad (\text{F.3})$$

Under plane stress conditions, where $\sigma_3 = 0$, the von Mises equivalent stress σ_e is obtained [Fenner 89]:

$$\sigma_e = \sqrt{\sigma_1^2 + \sigma_2^2 - \sigma_1\sigma_2} \quad (\text{F.4})$$

Where σ_1 and σ_2 are given by:

$$\sigma_{1,2} = \frac{\sigma_{xx} + \sigma_{yy}}{2} \pm \frac{1}{2} \sqrt{(\sigma_{xx} - \sigma_{yy})^2 + 4\tau_{xy}^2} \quad (\text{F.5})$$

When $\sigma_{yy} = 0$:

$$\sigma_{1,2} = \frac{\sigma_{xx}}{2} \pm \frac{1}{2} \sqrt{\sigma_{xx}^2 + 4\tau_{xy}^2} \quad (\text{F.6})$$

Which leads to:

$$\sigma_1\sigma_2 = \left(\frac{\sigma_{xx}}{2} + \frac{1}{2}\sqrt{\sigma_{xx}^2 + 4\tau_{xy}^2}\right) \left(\frac{\sigma_{xx}}{2} - \frac{1}{2}\sqrt{\sigma_{xx}^2 + 4\tau_{xy}^2}\right) = \frac{\sigma_{xx}^2}{4} - \frac{1}{4}(\sigma_{xx}^2 + 4\tau_{xy}^2) = -\tau_{xy}^2 \quad (\text{F.7})$$

Hertz contact mechanics

G.1 Introduction

Contact between probe tip and work piece causes elastic deformation of both probe tip and work piece. When the contact force is high enough plastic deformation will occur. The highest contact forces are observed during collision, as modeled in sections 2.1.3 - 2.1.5. For the elastic-plastic theory [Johnson 85, Dekkers 02] used in this model the following assumptions are made:

- Hertz contact theory is applicable;
- The probe tip is a perfectly smooth sphere;
- The work piece is a perfectly smooth plane.

The first section discusses the elastic deformation of a sphere on a plane, the following section considers the elastic-plastic deformation and in the last section the effects on probe design are discussed.

G.2 Elastic deformation

Hertz contact stress is used to describe the deformation of a planar work piece due to a force exerted by the probe tip, as depicted in figure G.1. Here, a probe tip with radius r , E-module E_1 and Poisson ratio ν_1 exerts a force F_{Hz} on a planar work piece with E-module E_2 and Poisson ratio ν_2 . Due to elastic deformations a circular contact surface with radius a and an indentation δ of the probe tip in the work piece arises.

Following Hertz contact theory the following equation's hold [Johnson 85]:

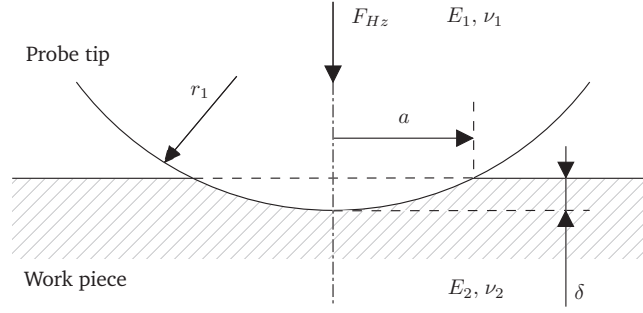


Figure G.1: Schematic view of contact between probe tip and work piece.

$$a = \left(\frac{3F_{Hz}r}{4E_{red}} \right)^{\frac{1}{3}} \quad (G.1)$$

$$\delta = \frac{a^2}{r} = \left(\frac{9F_{Hz}^2}{16rE_{red}^2} \right)^{\frac{1}{3}} = \frac{\pi^2 p_0^2 r}{4E_{red}^2} \quad (G.2)$$

$$F_{Hz} = \frac{4}{3} \sqrt{r} E_{red} \delta^{\frac{3}{2}} = \frac{\pi^3 p_0^3 r^2}{6E_{red}^2} \quad (G.3)$$

$$p_0 = \frac{3F_{Hz}}{2\pi a^2} = \left(\frac{6F_{Hz}E_{red}^2}{\pi^3 r^2} \right)^{\frac{1}{3}} \quad (G.4)$$

In these equations F_{Hz} is the Hertz contact force and p_0 is the maximum occurring Von Mises stress in the plane. The reduced radius r and the reduced E-module E_{red} are given by:

$$\begin{aligned} \frac{1}{r} &= \frac{1}{r_1} + \frac{1}{r_2} \\ \frac{1}{E_{red}} &= \frac{1 - \nu_1^2}{E_1} + \frac{1 - \nu_2^2}{E_2} \end{aligned} \quad (G.5)$$

For a planar work piece r_2 is infinite, thus $r = r_1$.

G.3 Elastic-plastic deformation

The elastic-plastic deformation takes place when the maximum occurring Von Mises¹ stress following equation G.4 exceeds 1.61 times the yield strength, $p_0 = 1.61\sigma_{0.2}$, the Tresca² criterion [Tabor 51, Johnson 85].

Using the Tresca criterion in equations G.2 and G.3 yields the indentation and pressing force at which elastic-plastic deformation begins:

$$\delta_Y = r \left(\frac{1.61\pi\sigma_{0.2}}{2E_{red}} \right)^2 \quad (G.6)$$

$$F_Y = \frac{\pi^3 r^2 (1.61\sigma_{0.2})^3}{6E_{red}^2} \quad (G.7)$$

¹Deformation work hypothesis: plastic deformation begins as soon as and there where the load per unit volume exceeds a critical value.

²Shear stress hypothesis: plastic deformation begins as soon as and there where the largest shear stress in the system exceeds a critical value.

For a sapphire probe tip with a radius of 0.25 mm in contact with a planar aluminum work piece, $E = 70$ GPa and $\sigma_{0.2} = 280$ MPa, the maximum contact force is 7 mN. For a measurement range of 30 μm the stiffness of the probe suspension should therefore be less than 230 N/m. A suspension with a higher stiffness or a measurement over a larger range will result in elastic plastic deformation of the work piece. This will be discussed on the basis of figure G.2.

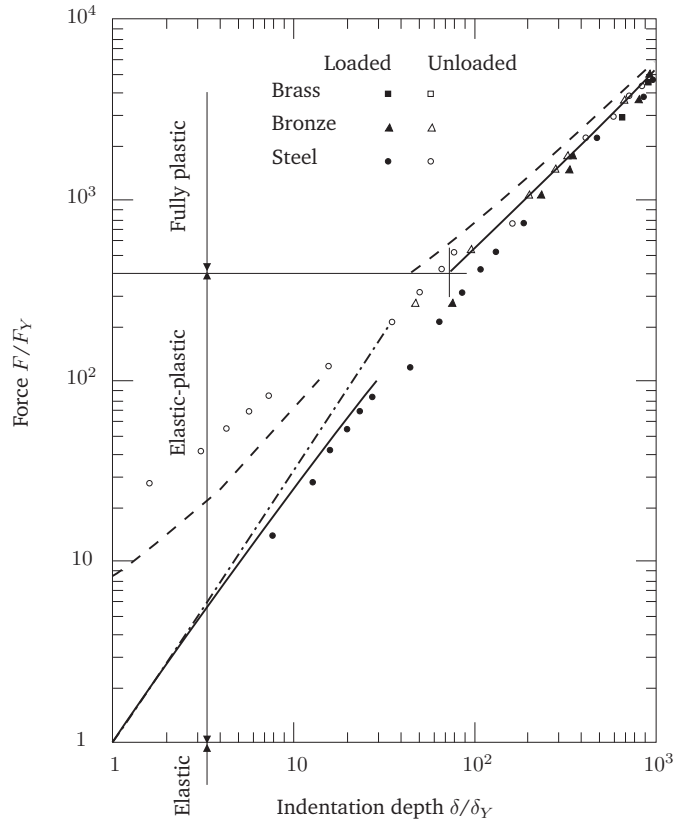


Figure G.2: Penetration into an elastic-plastic work piece by a spherical indenter. Solid line: penetration under load. Broken line: depth of unloaded crater [Johnson 85, Foss 22].

The dimensionless indentation $\frac{\delta}{\delta_Y}$ and the dimensionless pressing force $\frac{F_{Hz}}{F_Y}$ in this graph are given by:

$$\frac{\delta}{\delta_Y} \equiv 0.148 \left(\frac{\delta E_{red}^2}{r \sigma_{0.2}^2} \right) \quad (\text{G.8})$$

$$\frac{F_{Hz}}{F_Y} \equiv 0.043 \left(\frac{F E_{red}^2}{r^2 \sigma_{0.2}^3} \right) \quad (\text{G.9})$$

The solid line in figure G.2 represents the elastic-plastic indentation with load and can be approximated by [Dekkers2002, Foss1922]:

$$\frac{F}{F_Y} = \left(\frac{\delta}{\delta_Y} \right)^{A_F} 10^{B_F} \quad (\text{G.10})$$

The dashed line in this figure represents the remaining deformation δ_{pl} after removing the load and is approximated by:

$$\frac{\delta_{pl}}{\delta_Y} = \frac{\delta - \delta_Y}{\delta_Y} = \left(\frac{F_{Hz}}{F_Y} \right)^{A_\delta} 10^{B_\delta} - 1 \quad (\text{G.11})$$

Finally, the dashed-dotted line represents the pure elastic deformation, as discussed in the previous section. The coefficients in equations G.10 and G.11 are determined with figure G.2:

$$\begin{aligned} A_F &= 1.09 & A_\delta &= 0.78 \\ B_F &= 0.75 & B_\delta &= -1.04 \end{aligned}$$

G.4 Energy

In the previous section the indentation and the force at which elastic-plastic deformation begins has been derived (equation's G.6 and G.7). The maximum energy U which can be elastically stored follows from:

$$U_Y = \int_0^{\delta_Y} F_{Hz}(\delta) d\delta = \frac{\pi^5 r^3 (1.61 \sigma_{0.2})^5}{60 E_{red}^4} \quad (G.12)$$

It can be seen from this equation that the elastic energy a material can absorb until plastic deformation begins is relative to $\frac{\sigma_{0.2}^5}{E_{red}^4}$. By means of this ratio several materials can be compared. Table G.1 gives an overview of several engineering materials³.

Material	E in GPa	$\sigma_{0.2}$ in MPa	δ_Y in nm	F_Y in mN	U_Y in pJ
Copper	124	330	16.31	4.54	29.61
Bronze	100	310	19.94	5.21	41.55
Aluminum	70	280	29.26	6.91	80.82
Invar	145	483	29.04	11.82	137.32
Steel	200	885	63.08	47.06	1187.33

Table G.1: Mechanical properties of several engineering materials [Brady 02].

During a collision between probe tip and work piece the kinetic energy will be transformed into deformation energy. The kinetic energy during first contact is given by:

$$U_{kinetic} = \frac{1}{2} m_t v^2 \quad (G.13)$$

Here v is the relative velocity between probe tip and work piece in m/s and m_t is the dynamic mass of the probe in kg.

This equation is used in figure G.3 to calculate the kinetic energy for a probe with a tip radius of 0.25 mm and a dynamic mass of 40 mg in collision with a work piece at a relative speed v in mm/s.

When the kinetic energy during collision exceeds the values given in table G.1, the work piece will deform plastically. As can be seen in the graph above, copper and bronze exhibit elastic-plastic behavior at measurement speeds of 1.5 mm/s or higher. The first part of the indentation will be elastic deformation, as calculated in G.12. The second part is elastic plastic deformation and can be calculated using equation G.10:

$$\frac{1}{2} m_t v^2 = \int_0^{\delta_Y} F_{Hz}(\delta) d\delta + \int_{\delta_Y}^{\delta_{total}} F_{Hz}(\delta) d\delta \quad (G.14)$$

The plastic deformation to a work piece can now be calculated. This is done for several materials and for different probing speeds in table G.2.

³Material properties depend on heat treatment.

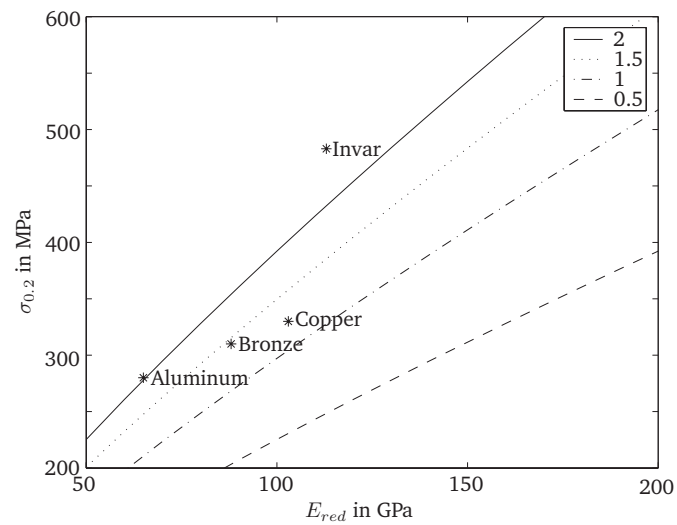


Figure G.3: Comparison between kinetic energy during collision and maximum energy for several materials from table G.1. As a reference the kinetic energy is shown for an approach speed of 2, 1.5, 1 and 0.5 mm/s.

Material	U_Y in pJ	Plastic deformation in nm		
		$v = 3$ mm/s	$v = 2$ mm/s	$v = 1.5$ mm/s
Copper	29.61	14.21	8.41	4.76
Bronze	41.55	14.19	7.68	2.41
Aluminum	80.81	12.90	0	0
Invar	137.31	6.63	0	0
Steel	1187.32	0	0	0

Table G.2: Plastic deformation of a planar work piece in collision with a probe tip with a radius of 0.25 mm and a dynamic mass of 40 mg.

In this appendix it has been assumed that the maximum relative velocity between probe tip and work piece occurs during first contact. However, the relative velocity is affected by probe dynamics, as shown in section 2.1.3.

Appendix H

Uncertainty evaluation of the setup

As stated in section H.1 the sensor calibrations in this thesis are performed using the plane mirror differential setup discussed in section 1.6.1. As a result the uncertainty of the calibration setup contributes to the calibration uncertainty of the probe, as discussed in section 5.6. Table 5.2 in section 5.6 states the uncertainty in the calibration of the probing system. The effects on measurement uncertainty, as mentioned in this table, are discussed in more detail in this appendix.

From the Guide to the expression of Uncertainty in Measurement [Gum 93]:

Although this Guide provides a framework for assessing uncertainty, it cannot substitute for critical thinking, intellectual honesty, and professional skill. The evaluation of uncertainty is neither a routine task nor a purely mathematical one; it depends on detailed knowledge of the nature of the measurand and of the measurement. The quality and utility of the uncertainty quoted for the result of a measurement therefore ultimately depend on the understanding, critical analysis, and integrity of those who contribute to the assignment of its value.

H.1 Traceability in length measurement

For each calibration, the traceability of the measurement is important to determine the uncertainty of the method. Traceability is defined as:

The property of the result of a measurement or the value of a standard whereby it can be related to stated references, usually national or international standards, through an unbroken chain of comparisons all having stated uncertainties.

Historically the first system of length measurement was probably used in Mesopotamia around 6000 B.C. for use in agriculture. The first known length standard is the Egyptian and Mesopotamian cubit. The cubit can be traced back to 3000 B.C. and corresponded to the length of the lower arm of the reigning Pharaoh.

Over 200 years ago, on the 22nd of June in 1799, the meter was introduced as the standard of length. The meter was defined as the ten-millionth part of the earth quadrant, the distance from

the pole to the equator on sea level. The first standard based on this definition was a platinum rod with a rectangular cross section. The distance between the end planes was based on a series of measurements between Duinkerken and Barcelona between 1792 and 1795. An interesting historical fact is that this first prototype meter bar was based on provisional results. Although it was later determined to be short by a fifth of a millimeter due to miscalculation of the flattening of the Earth, this length became the standard.

Since the requirements on the uncertainty of measurements have increased in time the definition of the meter has been adjusted several times. Our current definition of the meter was introduced in 1983 and is defined as the length of the path traveled by light in absolute vacuum during a time interval of $1/299792458$ of a second.

Comité Consultatif des Longueurs (CCL), formally the Comité Consultatif pour la Définition du Mètre, has recommended three principal means for the realization of the meter according to this definition. Of these three, the method most often used is based on stabilization of a number of recommended radiations [CCDM 92]. The method used by all national standard laboratories is the radiations method using an iodine-stabilised He-Ne laser at 473 THz or 633 nm, which has a typical relative standard deviation of $5 \cdot 10^{-11}$.

There are two ways of obtaining a measurement result that is traceable [Wetzels 98]. The first method is based on the system equation of a measurement system. This equation describes the relation between the measurement result and all the parameters that affect it. If the uncertainty of all parameters involved is known in relation to their respective standard, then their effect on the measurement can be calculated.

In the second approach, the measuring instrument is treated as a black box. The instrument is calibrated against another instrument that is part of a calibration chain, leading to the standard of length. The latter approach has the advantage that all parameters that affect the measurement are included in the calibration. A disadvantage lies in the fact that effects of the calibration itself are also included. These effects should be much smaller than the uncertainty of the probe under calibration. Therefore the number of steps in the chain of comparisons, necessary to connect a probe to a primary standard, should be minimized.

The calibration of the probes, discussed in this thesis, is performed using the second approach. The probes are calibrated using the plane mirror differential interferometer discussed in section 1.6.1. The measuring instrument in this setup, a laser interferometer, is calibrated using an iodine-stabilized He-Ne laser, which connects the setup to the primary standard. In the remainder of this appendix an overview is provided of the effects which influence the calibration and their contribution to the uncertainty of the method.

H.2 Refractive index of air

In laser interferometry the number N indicates the number of wavelengths that fit in a distance d . The wavelength λ is influenced by the medium, typically air, and environmental variations. The refractive index n is a measure for the difference between the wavelength of the light source in vacuum λ_{vac} and the wavelength in the medium λ under given environmental conditions:

$$d = N\lambda = \frac{N\lambda_{vac}}{n} \quad (\text{H.1})$$

In practical applications, the refractive index n is used to compensate for the effects of the medium and environmental conditions in which the measurement is performed. Several authors [Birch 88, Birch 94, Bönsch 98, Ciddor 96, Edlén 66, Owens 67] published relationships for the refractive index n in air for varying environmental conditions.

Under standard laboratory conditions, see table H.1, the refractive index of air can be calculated to be 1.00027. In other words, the wavelength in air is decreased by 0.027% with respect to the wavelength in vacuum. The maximum deviation, as stated in table H.1, is the maximum variation

	Nominal value	Maximum deviation
Temperature	21 °C	±0.2 °C
Air pressure	101 kPa	±0.6 kPa
Relative humidity	50%	±10 %
CO ₂ concentration	400 ppm	±50 ppm

Table H.1: Standard laboratory conditions and maximum variation at the calibration setup.

	Uncertainty	Sensitivity	Uncertainty in n
Temperature	0.12 °C	$9.5 \cdot 10^{-7}$	$1.1 \cdot 10^{-7}$
Air pressure	0.35 kPa	$2.7 \cdot 10^{-6}$	$9.4 \cdot 10^{-7}$
Relative humidity	5.8 %	$8.5 \cdot 10^{-9}$	$4.9 \cdot 10^{-8}$
<i>Combined uncertainty in n</i>			$9.4 \cdot 10^{-7}$

Table H.2: Uncertainty evaluation of the refractive index of air at the start of a measurement.

encountered within the polyethylene foam box used as shielding for the calibration setup when a measurement is initiated.

As stated at the start of this section the refractive index is influenced by environmental variables. For the purpose of this thesis a first order approximation can be used to calculate the influence of temperature ΔT , pressure ΔP and relative humidity ΔR variations on the variation Δn of the refractive index of air [Bos 00, Bos 02, Decker 97]:

$$\Delta n = -9.5 \cdot 10^{-7} \Delta T + 2.7 \cdot 10^{-6} \Delta P - 8.5 \cdot 10^{-9} \Delta R \quad (\text{H.2})$$

Using a square distribution of the maximum variation in the environmental variables, the uncertainty in the refractive index n at the start of the measurement is given by table H.2.

The uncertainty in the refractive index of air results in a deviation δd of the distance d as measured by the laser interferometer, equation H.1:

$$\frac{\delta d}{\delta n} = -\frac{N \lambda_{vac}}{n^2} = -\frac{d}{n} \quad (\text{H.3})$$

For a measurement range of 5.5 μm the uncertainty in the displacement measurement of the laser interferometer is thus 5 pm and can be neglected.

A change in the refractive index of air during the measurement influences the measurement when the optical path length of the measurement and reference beams is not equal when the measurement is initiated. This is referred to as dead path length and will be discussed in the next section.

H.3 Dead path length

As mentioned in the previous section, the dead path length l_d in an interferometric setup is defined as the difference in optical path length between the measurement and reference beams when the measurement is initiated [Leach 99, Zanoni 88]. Dead path deviations occur when there is a non-zero dead path and environmental conditions change during the measurement. The dead path length can be incorporated in equation H.1 to obtain the measured displacement d_c of the laser interferometer:

	Uncertainty	Sensitivity	Uncertainty in n
Temperature	0.02 °C	$9.5 \cdot 10^{-7}$	$1.9 \cdot 10^{-8}$
Air pressure	0.02 kPa	$2.7 \cdot 10^{-6}$	$5.4 \cdot 10^{-8}$
Relative humidity	1.2 %	$8.5 \cdot 10^{-9}$	$1.0 \cdot 10^{-8}$
<i>Combined uncertainty in n</i>			$5.8 \cdot 10^{-8}$

Table H.3: Uncertainty evaluation of the refractive index of air during a measurement period of 20 minutes.

$$d_c = \frac{N_c \lambda_{vac}}{4n_2} - \frac{l_d \Delta n}{n_2} \quad (\text{H.4})$$

here N_c is the number of fringes counted by the laser interferometer during the displacement, n_2 is the refractive index at the end of the measurement, Δn is the change in refractive index over the measurement time, i.e. $n_2 = n_1 + \Delta n$, and n_1 is the refractive index at the start of the measurement. It is noted that the number 4 in the denominator of equation H.4 depends on the setup used. For the calibration setup, as discussed in section 1.6.1, a value of 4 is used since the measurement and reference beams reflect two times at the measurement and reference mirror, respectively.

Ideally, at the start of the measurement the measurement mirror should therefore be aligned with the reference mirror. In the calibration setup as discussed in section 1.6.1 this would result in an equal optical path length between the measurement and reference beams, and hence a zero dead path length l_d .

However, a mechanism is used to position the work piece to make contact with the probe tip. The maximum resulting dead path length during probe calibration is 1 mm. Thermal expansion of components may result in a variation of the dead path length during the measurement. However, the calibration setup used is constructed such that homogeneous temperature variations do not effect the dead path length. The calibration is performed in a temperature controlled laboratory and the optical components are shielded. As a result the influence of variations in the dead path length during a measurement on measurement uncertainty are in the order of 10 pm and can be neglected.

The influence of a dead path length at the start of the measurement is an offset in the distance as measured by the laser interferometer. Since the displacement and not the absolute value of the measurement mirror is of interest, an offset at the start of the measurement does not influence the calibration of the probing system. However, variations in the refractive index of air during the measurement will influence the result when the dead path length l_d is non zero, as indicated by equation H.4.

Table H.3 shows the uncertainty in the value of the environmental variables during a 20 minute measurement and the resulting contribution to the uncertainty in the refractive index of air during a measurement.

Using equation H.4 with a dead path length l_d of 1 mm the uncertainty in the distance as measured by the laser due to the dead path length is 58 pm and can be neglected.

It is noted that by measuring the environmental variables, a correction to the wavelength during the measurement can be applied. The uncertainty in this compensation results from the uncertainty in the equations used, e.g. the uncertainty of the Edlén equations is approximately $1 \cdot 10^{-8}$, and the uncertainty with which the environmental variables are measured [Bos 00, Bos 02, Decker 97]. Another possibility is a direct measurement of the refractive index using a refractometer [Bos 02, Eickhoff 97, Flüge 03].

H.4 Wavelength instability

The nominal wavelength λ_{HeNe} of the stabilized Helium-Neon laser is approximately 633 nm and is specified to have a relative stability of $2 \cdot 10^{-9}$. For a dead path length of 1 mm and a measurement range of 5.5 μm a deviation of 2 pm is obtained, which can be neglected.

H.5 Periodic deviations

When the displacement as measured by a laser interferometer is plotted against the actual displacement of a mirror, an oscillation around the ideal straight line may be observed [Badami 00, Bobroff 87, Flügge 96, Sutton 87]. This effect results from polarization leakage in the interferometer and is known as periodic or non-linear deviations of the laser interferometer [Freitas 95]. Figure H.1 shows the periodic deviation of the calibration setup, discussed in section 1.6.1, as measured using the method by Cosijns [Cosijns 04].

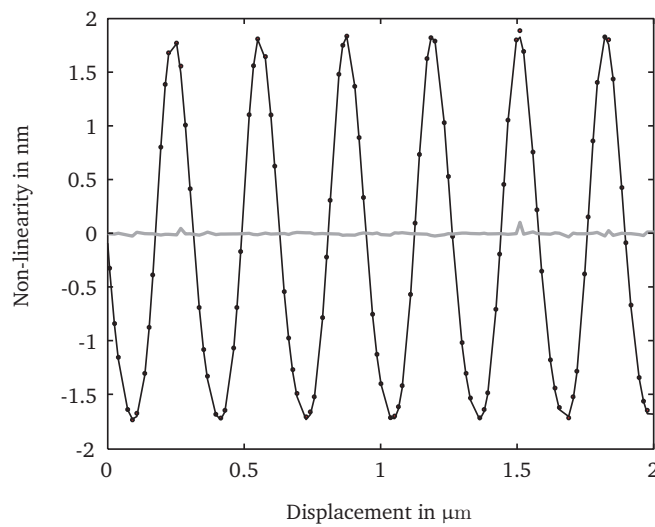


Figure H.1: Measured periodic deviation in the calibration setup as discussed in section 1.6.1, black line: periodic deviations without compensation, grey line: periodic deviations after compensation.

The deviations due to polarization leakage are typically defined as first or second order periodic deviations. First order periodic deviations have a frequency of one cycle per one wavelength optical path change, and second order periodic deviations have a frequency of two cycles per one wavelength optical path change [Cosijns 04]. The periodic deviations as shown in figure H.1 shown a peak-to-peak deviation of approximately 3.5 nm. It is noted that the deviations are first order periodic deviations since the calibration setup used is a double pass interferometer. Since the periodic deviation can be described by a sine-wave, the contribution of periodic deviations to the measurement uncertainty when no compensation is applied is 1.2 nm.

Several authors have published methods to compensate for periodic deviations in a laser interferometric setup [Cosijns 04, Eom 02, Heydemann 81, Hou 92, Hou 94, Picotto 91]. Typically, the distortions are described by a set of variables, which are estimated from the interferometric signal. This compensation can be performed in real-time by using two additional beam splitters to analyze the signal from the laser and to the detector [Bos 02, Cosijns 04, Hou 92, Hou 94]. Using the method by Cosijns [Cosijns 04] the periodic deviation of the calibration setup, the black line in figure H.1, can be compensated for. The remaining deviation due to periodic deviations in the calibration setup is indicated by the grey line in figure H.1 and has a top-to-top deviation of 0.1 nm.

The compensation of periodic deviations, as shown in figure H.1, is performed after the measurement. However, it was found that the parameters show a variation in time, possibly due to drift

in the setup. As a result, a compensation based on a constant set of variables is not sufficient to accurately predict the periodic deviations in the setup. Therefore a real-time measurement of the parameter set, used to describe the effect of distortions due to periodic effects, is needed to compensate for these effects in the calibration setup [Bos 03]. Currently, no real-time compensation for the distortions due to periodic deviations of the interferometer is implemented.

H.6 Mechanical misalignments

The calibration procedure of the tactile 3D probing system is discussed in appendix A.2. During the calibration of the probe its behavior is measured in 4 directions, as shown in figure A.1, indicated by the displacement matrix \mathbf{D} :

$$\mathbf{D} = \begin{bmatrix} 0 & 1 & -\frac{1}{2} & -\frac{1}{2} \\ 0 & 0 & \frac{1}{2}\sqrt{3} & -\frac{1}{2}\sqrt{3} \\ -1 & 0 & 0 & 0 \end{bmatrix} \quad (\text{H.5})$$

During the calibration it is assumed that the alignment between the probing system and the calibration setup is described by the displacement matrix \mathbf{D} . A variation in the direction in which the calibration is performed, e.g. due to misalignments in the calibration setup, will therefore influence the calibration result and hence the calculated transformation matrix \mathbf{A} . The result is a systematic deviation in the calculation of the probe tip displacement from the measurement signals of the slender rods, equation 5.5.

The effects of a mechanical misalignment on the measurement uncertainty of the calibration procedure are discussed in [Pril 02, Widdershoven 04]. The misalignment as a result of manufacturing tolerances in the bracket used to position the probing system on the setup, as shown in figures 1.21 and 1.22, is measured on a coordinate measuring machine to be in the order of 1.8 mrad. This results in a maximum deviation of approximately 0.1%, which corresponds to a deviation of 5.5 nm for a displacement of 5.5 μm .

From equation A.1 in appendix A.2 it is clear that the displacement matrix \mathbf{D} and the measured sensitivity matrix \mathbf{M} are coupled via transformation matrix \mathbf{A} , i.e. $\mathbf{D} = \mathbf{A}\mathbf{M}$. For the tactile 3D probing system as discussed in this thesis, the measured sensitivity matrix \mathbf{M} for the directions as indicated in \mathbf{D} is given by:

$$\mathbf{M} = 1 \cdot 10^6 \begin{bmatrix} 1.37 & -1.12 & -0.06 & 1.33 \\ 1.43 & -0.15 & 1.39 & -1.08 \\ 1.44 & 1.28 & -1.03 & -0.09 \end{bmatrix} \quad (\text{H.6})$$

The resulting transformation matrix of the tactile 3D probing system is shown in equation 5.4. The deviation between the displacement matrix \mathbf{D} and the calculated displacement $\mathbf{A}\mathbf{M}$ is now given by:

$$\mathbf{A}\mathbf{M} - \mathbf{D} = \begin{bmatrix} 0.000 & 0.001 & 0.001 & 0.001 \\ 0.000 & 0.001 & 0.001 & 0.001 \\ 0.000 & -0.038 & -0.038 & -0.038 \end{bmatrix} \quad (\text{H.7})$$

It is noted that the term -0.038 results from the rolling effect, as discussed in section 2.2.1. The rolling effect is not included in the displacement matrix \mathbf{D} and thus results in a deviation between the displacement matrix \mathbf{D} and the calculated displacement $\mathbf{A}\mathbf{M}$. However, this is an actual displacement of the probe tip and does therefore not contribute to the measurement deviation of the probing system.

The term 0.001 results from the mechanical misalignment of the probing system with respect to the calibration setup, as discussed at the start of this section. It is noted that a deviation of 0.1% corresponds to the value as calculated from the misalignment of the probing system and bracket with respect to the calibration setup.

The measurement deviation due to the mechanical misalignment of the probing system with respect to the setup during the calibration of the probing system is thus 5.5 nm for a 5.5 μm displacement. This contribution is systematic and hence a square distribution is used, resulting in a standard deviation of 3.2 nm. It is noted that the contribution to the measurement uncertainty is systematic and can thus be compensated for. The contribution to the measurement uncertainty after compensation is below 0.1 nm.

Bibliography

- [Abbe 90] E. Abbe, Messapparate für Physiker, Zeits, Für Instrumenten-Kunde, 10, p.446-448 (1890).
- [Abe 95] T. Abe, WC Messner, and M. Reed, Effective methods to prevent stiction during post-release-etch processing, Journal of Microelectromechanical Systems, 4, p.185192 (1995).
- [Adamson 97] A.W. Adamson, Physical Chemistry of Surfaces, ISBN 0471148733, John Wiley & Sons Inc (1997).
- [Alting 03] L. Alting, F. Kimura, H.N. Hansen, G. Bissacco, Micro Engineering, Annals of the CIRP, 52/2, pp. 635-658 (2003).
- [Amick 91] H. Amick, S. Hardash, P. Gillett, R.J. Reaveley, Design of Stiff, Low-Vibration Floor Structures, Proceedings of International Society for Optical Engineering (SPIE), 1619, p.180-191 (1991).
- [Aston 97] R.A.E. Aston, J. Davis, K.J. Stout, A probing question: A customer's investigation into the directional variability of a coordinate measuring machine touch-trigger probe, International Journal of Machine Tools and Manufacture, 37/10, p.1375-1382 (1997).
- [Arai 95] F. Arai, D. Ando, T. Fukuda, Y. Nonoda, T. Oota, Micro manipulation based on micro physics-strategy based on attractive force reduction and stress measurement, Proceedings of the International Conference on Human Robot Interaction and Cooperative Robots, 2, p.236-241 (1995).
- [Archard 57] J.F. Archard, Elastic deformation and the laws of friction, Proceedings of the Royal Society, A243, p.190-205 (1957).
- [Argento 96] C. Argento, R.H. French, Parametric tip model and force-distance relation for Hamaker constant determination from atomic force microscopy, Journal of Applied Physics, 80/11, p.6081-6090 (1996).
- [Ayazi 01] F. Ayazi, K. Najafi, A HARPSS Polysilicon Vibrating Ring Gyroscope, IEEE/ASME Journal of Microelectromechanical Systems, pp. 169-179 (2001).
- [Badami 00] V.G. Badami, S.R. Patterson, A frequency domain method for the measurement of nonlinearity in heterodyne interferometry, Precision Engineering, 24, pp. 41-49 (2000).
- [Bagdahn 02] J. Bagdahn, W.N. Sharpe, Fracture Strength of Polysilicon at Stress Concentration, Materials Science of Microelectromechanical System (MEMS) Devices IV, 687, p. 285-290 (2002).
- [Bahrami 04] M. Bahrami, Modeling of Thermal Joint Resistance for Rough Sphere-Flat Contacts in a Vacuum, Ph.D. thesis, Department of Mechanical Engineering, University of Waterloo, Waterloo, Canada (2004).

- [Bahrami 05] M. Bahrami, M.M. Yovanovich, J.R. Culham, A Compact Model for Spherical Rough Contacts, *Journal of Tribology*, 127/4, p.884-889 (2005).
- [Bahrami 06] M. Bahrami, J.R. Culham, M.M. Yovanovich, G.E. Schneider, Review of thermal joint resistance models for non-conforming rough surfaces, *ASME Journal of Applied Mechanics Review*, 59, p. 1-12 (2006).
- [Ballarini 98] R. Ballarini, *Contributive Research & Development Volume 130: The Role of Mechanics in Microelectromechanical Systems (MEMS) Technology*, AFRL-ML-WP-TR-1998-4209, Air Force Research Laboratory (1998).
- [Ballarini 05] R. Ballarini, S. Allameh, W.O. Sobovejo, *Mechanical Properties of Mems Structures*, Kluwer Academic (2005).
- [Bambach 80] M. Bambach, A. Fuerst, Bestimmung der Antastunsicherheit elektronischer 3-D-Tastsysteme, *VDI-Berichte 378*, p.15-20 (1980).
- [Bar 00] G. Bar, R. Brandsch, M. Bruch, L. Delineau, M.H. Whangbo, Examination of the relationship between phase shift and energy dissipation in tapping mode atomic force microscopy by frequency-sweep and force-probe measurements, *Surface Science*, 444/1-3, p. L11-L16 (2000).
- [Bartelt 02] R. Bartelt, *The Essentials of Industrial Metrology, Part 2: Form profiles with interruptions*, Exactly, Mahr, 2, www.mahr.com as it is on 08-2006 (2002).
- [Bartelt 03] R. Bartelt, *The Essentials of Industrial Metrology, The uncertainty of form measurement-Aspects to be observed*, Exactly, Mahr, 1, www.mahr.com as it is on 08-2006 (2003).
- [Bauza 05] M.B. Bauza, R.J. Hocken, S.T. Smith, S.C. Woody, Development of a virtual probe tip with an application to high aspect ratio microscale features, *Review of Scientific Instruments*, 76, p. 095112.1-095112.8 (2005).
- [Becker 82] R. Becker, *Electromagnetic Fields and Interactions*, ISBN 0486642909, Dover Publications (1982).
- [Bengisu 97] M.T. Bengisu, A. Akay, Relation of dry-friction to surface roughness, *ASME Journal of Tribology*, 119, p. 18-25 (1997).
- [Berthelot 98] D. Berthelot, *Compte Rendu Hebdomadaires des Seances de l'Academie des Sciences*, 126, 1703 (1898).
- [Bessason 99] B. Bessason, C. Madshus, H.A. Frøystein, H. Kolbjørnsen, Vibration criteria for metrology laboratories, *Measurement Science Technology*, 10, p.1009-1014 (1999).
- [Bhushan 99] B. Bhushan, *Principles and Applications of Tribology*, ISBN 0471594075, Wiley-Interscience (1999).
- [Bickel 63] E. Bickel, Some Fundamental Problems in the Measurement of Surface Roughness, *Proceedings of the International Production Engineering Research Conference*, p.667-674 (1963).
- [Biggs 95] S. Biggs, Steric and bridging forces between surfaces bearing adsorbed polymer: an atomic force microscopy study, *Langmuir*, 11, p.156-162 (1995).
- [Binggeli 94] M. Binggeli, C.M. Mate, Influence of capillary condensation of water on nanotribology studied by force microscopy, *Applied Physics Letters*, 65/4, p.415-417 (1994).
- [Birch 88] K.P. Birch, M.J. Downs, The results of a comparison between calculated and measured values of the refractive index of air, *Journal of Physics E: Scientific Instruments*, 21, pp. 694-695 (1988).

- [Birch 94] K.P. Birch, M.J. Downs, Correction to the updated Edlén equation for the refractive index of air, *Metrologia*, 31, pp. 315-316 (1994).
- [Blackstock 00] D.T. Blackstock, *Fundamentals of Physical Acoustics*, ISBN 0471319791, Wiley-Interscience (2000).
- [Blanding 92] D.L. Blanding, *Principles of Exact Constraint Mechanical Design*, Eastman Kodak Company, Rochester, New York (1992).
- [Blau 95] P.J. Blau, *Friction Science and Technology*, ISBN 0824795768, CRC (1995).
- [Blunt 03] L. Blunt, X. Jiang, *Advanced Techniques for Assessment Surface Topography: Development of a Basis for 3D Surface Texture Standards 'SURFSTAND'*, ISBN 1903996112, Butterworth-Heinemann Ltd (2003).
- [Bobroff 87] N. Bobroff, Residual errors in laser interferometry from air turbulence and non-linearity, *Applied Optics*, 26/13, pp. 2676-2682 (1987).
- [Böhringer 98] K.F. Böhringer, M. Cohn, K. Goldberg, R. Howe, and A. Pisano, Parallel microassembly with electrostatic force fields, *International Conference on Robotics and Automation* (1998).
- [Böhringer 99] K.F. Böhringer, R. Fearing, K. Goldberg, Microassembly, in *Handbook of Industrial Robotics*, S.Y. Nof, editor, John Wiley & Sons, p. 1045-1066 (1999).
- [Bönsch 98] G. Bönsch, E. Potulski, Measurement of the Refractive Index of Air and Comparison with Modified Edlén's Formulae, *Metrologia*, 35, pp. 133-139 (1998).
- [Bos 00] E.J.C. Bos, Improving measurement accuracy of a fringe counting interferometer using Labview, Internal report, PE2001-052, Eindhoven University of Technology (2000).
- [Bos 02] E.J.C. Bos, Ontwerp van een kalibratieopstelling voor lineaire meetsystemen tot 300 mm, Internal report, PE2002-100, Eindhoven University of Technology, in Dutch (2002).
- [Bos 03] E.J.C. Bos , H. Haitjema, P.H.J. Schellekens, I. Widdershoven, A calibration setup for a new type of nano probe, *Proceedings of Micro Systems Technologies* (2003).
- [Bos 04A] E.J.C. Bos, F.L.M. Delbressine, H. Haitjema, High-accuracy CMM metrology for micro systems, *VDI Berichte*, 1860, ISBN 3180918608, VDI Verlag GmbH, pp. 511-522 (2004).
- [Bos 04B] E.J.C. Bos , I. Widdershoven, H. Haitjema, Calibration and redesign of a Nano Probe Based on MST Technology, *Proceedings of Euspen* (2004).
- [Bos 05] E.J.C. Bos , F.L.M. Delbressine, A.H. Dietzel, 3D Tactile Sensor for Nanometrology, *Proceedings of Micro- and Nano-Engineering (MNE)* (2005).
- [Bos 06] E.J.C. Bos , J.E. Bullema, Packaging and Assembly of MEMS, *11th International Conference on the Commercialization of Micro and Nano Systems (COMS)* (2006).
- [Bos 07A] E.J.C. Bos, J.E. Bullema, F.L.M. Delbressine, P.H.J. Schellekens, A. Dietzel, A lightweight suction gripper for micro assembly, *Proceedings of the 7th Euspen International Conference, Bremen* (2007).
- [Bos 07B] E.J.C. Bos, J.E. Bullema, F.L.M. Delbressine, P.H.J. Schellekens, A. Dietzel, A lightweight suction gripper for micro assembly, *Precision Engineering* (2007).
- [Bos 07C] E.J.C. Bos, R.W.P. Heldens, F.L.M. Delbressine, P.H.J. Schellekens, A. Dietzel, Compensation of the anisotropic behavior of single crystalline silicon in a 3D tactile sensor, *Sensors and Actuators A: Physical*, 134/2, pp. 374-381 (2007).

- [Bowden 54] F.P. Bowden, D. Tabor, Friction and Lubrication of Solids, Oxford University Press, (1954).
- [Bowling 88] R.A. Bowling, A Theoretical Review of Particle Adhesion, in K.L. Mittal, ed., Particles on Surfaces I: Detection, Adhesion, and Removal, ISBN 0306430304, Plenum Press, p.129-142 (1988).
- [Bracken 97] E. Bracken, Combating humidity - the hidden enemy in manufacturing, Sensor Review, 17/4, p.283-290 (1997).
- [Brady 02] G.S. Brady, H.R. Clauser, J.A. Vaccari, Materials Handbook, ISBN 007136076X, McGraw-Hill, New York (2002).
- [Brand 02] U. Brand, S. Buettgenbach, Taktile dimensionelle Messtechnik für Komponenten der Mikrosystemtechnik, Technisches Messen, 12, pp. 542-549 (2002).
- [Bray 97] M. Bray, Stitching interferometer for large plano optics using a standard interferometer, Proceedings of SPIE, 3134, pp. 39-50 (1997).
- [Bressi 02] G. Bressi, G. Carugno, R. Onofrio, G. Rusos, Measurement of the Casimir force between Parallel Metallic Surfaces, Physical Review Letters, 88 (2002).
- [Breyer 91] K.H. Breyer, H.G. Pressel, Paving the Way to Thermally Stable Coordinate Measuring Machines, Progress in Precision Engineering, Springer-Verlag (1991).
- [Brogan 91] W.L. Brogan, Modern Control Theory, ISBN 0135897637, Prentice Hall (1991).
- [Brouwer 07] D.M. Brouwer, Design principles for six degree-of-freedom mems-based precision manipulators, ISBN 9789036525107, Ph.D. thesis, TUD, Delft, The Netherlands.
- [Brussel 00] H. van Brussel, et al., Assembly of Microsystems, Annals of the CIRP, 49/2, p.451-472 (2000).
- [Bryan 84] J.B. Bryan, The power of deterministic thinking in machine tool accuracy, First International Machine Tool Engineers Conference (1984).
- [Bryan 90] J.B. Bryan, International Status of Thermal Error Research, Annals of the CIRP, 39/2, p. 645-656 (1990).
- [Buks 01] E. Buks, M.L. Roukes, Metastability and the Casimir effect in micromechanical systems, Europhysics Letters, 54, pp. 220-226 (2001).
- [Burke 67] J.J. Burke, N.L. Reed, V. Weiss, editors, Surfaces and Interfaces; Volume I: Chemical and Physical Characteristics, ISBN 1512044105, Syracuse University Press (1967).
- [Bush 79] A.W. Bush, R.D. Gibson, G.P. Keogh, Strongly Anisotropic Rough Surfaces, Journal of Lubrication Technology, 101, p.1520 (1979).
- [Butler 98] J.T. Butler, W.D. Cowan, D.M. Burns, V.M. Bright, J.R. Reid, Automated assembly of micro-electro-mechanical systems, International Journal of Advanced Manufacturing Systems, 1/2, p. 135-148 (1998).
- [Butt 99] H.J. Butt, M. Kappl, H. Mueller, R. Raiteri, Steric forces measured with the atomic force microscope at various temperatures, Langmuir, 15, p.2559-2565 (1999).
- [Büttner 70] H. Büttner, E. Gerlach, Chemical Physics Letters, 5, p.91-92 (1970).
- [Bryan 79A] J.B. Bryan, Design and Construction of an Ultra-Precision 84 inch Diamond Turning Machine, Precision Engineering, 1/1, p. 13-18 (1979).
- [Bryan 79B] J.B. Bryan, The Abbe Principle revisited: an updated interpretation, Precision Engineering, 1/3, p. 129-132 (1979).

- [Cao 02] S. Cao, U. Brand, T. Kleine-Besten, W. Hoffmann, H. Schwenke, S. Buütefisch, S. Buüttgenbach, Recent developments in dimensional metrology for microsystem components, *Microsystem Technologies*, 8, pp. 3-6 (2002).
- [Casimir 48A] H.B.G. Casimir, D. Polder, The Influence of Retardation of the London-van der Waals Forces, *Physical Review*, 73/4, pp. 360-372 (1948).
- [Casimir 48B] H.B.G. Casimir, On the attraction between two perfectly conducting plates, *Proceedings of the Koninklijke Nederlandse Akademie van Wetenschappen, Serie B*, 51, pp. 793-796 (1948).
- [Castle 02] G.S.P. Castle, I.I. Inculet, G.S. Sines, L.B. Schein, Contact Charging Between Metals Revisited, *Industry Applications Conference, 37th IAS Annual Meeting*, p.606-609 (2002)
- [Cauchick-Mighel 98] P.A. Cauchick-Mighel, T.G. King, Factors which influence CMM touch-trigger probe performance, *International Journal of Machine Tools and Manufacture*, 38/4, p.363-374 (1998).
- [CCDM 92] Report of the 8th meeting of the Comité consultatif pour la définition du mètre, BIPM, France (1992).
- [Chan 97] F.M.M. Chan, E.J. Davis, T.G. King, K.J. Stout, Some performance characteristics of a multi-axis touch-trigger probe, *Measurement science and technology*, 8/8, p.837-848 (1997).
- [Chan 01] H.B. Chan, V.A. Aksyuk, R.N. Kleiman, D.J. Bishop, F. Capasso, Quantum Mechanical Actuation of Microelectromechanical Systems by the Casimir Force, *Science*, 291, pp. 1941-1944 (2001).
- [Chang 87] W.R. Chang, I. Etsion, D.B. Bogy, An Elastic-Plastic Model for the Contact of Rough Surfaces, *Journal of Tribology*, 109, p.257-263 (1987).
- [Chasiotis 05] I. Chasiotis, et al., Direct Measurements of Fracture Toughness and Crack Growth in Polysilicon MEMS, *Proceedings of the Materials Research Society* 854E, pp.U.10.6.1- U.10.6.6 (2005).
- [Chen 07] L.C. Chen, Automatic 3D surface reconstruction and sphericity measurement of micro spherical balls of miniaturized coordinate measuring probes, *Measurement Science and Technology*, 18, pp. 1748-1755 (2007).
- [Chetwynd 76] D.G. Chetwynd, G.J. Siddall, Improving the accuracy of roundness measurement, *Journal of Physics E: Scientific Instruments*, 9, pp. 537-544 (1976).
- [Chetwynd 87] D.G. Chetwynd, High-precision measurement of small balls, *Journal of Physics E: Scientific Instruments*, 20, pp. 1179-1187 (1987).
- [Chikazawa 84] M. Chikazawa, T. Kanazawa, T. Yamaguchi, The role of adsorbed water on adhesion force of powder particles, *Kona*, 2, p.54-61 (1984).
- [Chilamakuri 99] S.K. Chilamakuri, B. Bhushan, A Comprehensive Kinetic Meniscus Model for Prediction of Long-Term Static Friction, *Journal of Applied Physics*, 86, p.4649-4656 (1999).
- [Church 91] E.L. Church, P.Z. Takacs, Effects of the Non-Vanishing Tip Size in Mechanical Profile Measurements, *Proceedings of SPIE*, 1332, *Optical Testing and Metrology III: Recent Advances in Industrial Optical Inspection*, C.P. Grover, Ed., p.504-514 (1991).
- [Christenson 88] H.K. Christenson, Adhesion between surfaces in undersaturated vapours; a re-examination of the influence of meniscus curvature and surface forces. *Journal of Colloid and Interface Science*, 121/1, p.170-178 (1988).

- [Ciddor 96] P.E. Ciddor, Refractive index of air: new equations for the visible and near infrared, *Applied Optics*, 9, pp. 1566-1573 (1996).
- [Clark 79] D.E. Clark, C.G. Pantano, L.L. Hench, *Corrosion of glass; books for industry and the glass industry*, ISBN 0911993185, Ashlee Publications, New York (1979).
- [Clarkson 01] M. T. Clarkson, B. J. May, An investigation of methods for cleaning stainless steel weights, *Metrologia*, 38, pp. 161-171 (2001).
- [Cleaver 04] J.A.S. Cleaver, J.W.G. Tyrrell, The Influence of Relative Humidity on Particle Adhesion - a Review of Previous Work and the Anomalous Behaviour of Soda-lime Glass, *KONA powder and particle*, 22, p.9-22 (2004)
- [Coelho 78A] M.C. Coelho, N. Harnby, The effect of humidity on the form of water retention in a powder, *Powder Technology*, 20, p.197-200 (1978).
- [Coelho 78B] M.C. Coelho, N. Harnby, Moisture bonding in powders, *Powder Technology*, 20, p.201-205 (1978).
- [Cohn 96] M.B. Cohn, Y.-C. Liang, R.T. Howe, A.P. Pisano, Wafer-to-wafer transfer of microstructures for vacuum packaging, *Solid-State Sensor and Actuator Workshop* (1996).
- [Cohn 97] M.B. Cohn, *Assembly Techniques for Microelectromechanical Systems*, Ph.D. thesis, University of California (1997).
- [Cohn 98] M.B. Cohn, K.F. Böhringer, J.M. Noworolski, A. Singh, C.G. Keller, K.Y. Goldberg, R.T. Howe, Microassembly Technologies for MEMS, *Proceedings of SPIE*, 3513, *Microelectronic Structures and MEMS for Optical Processing IV*, p. 2-16 (1998).
- [Cooper 69] M.G. Cooper, B.B. Mikic, M.M. Yovanovich, Thermal Contact Conductance, *International Journal of Heat and Mass Transfer*, 12, p.279-300 (1969).
- [Corbett 00] J. Corbett, P.A. McKeown, G.N. Peggs, R. Whatmore, Nanotechnology: International developments and emerging products, *Annals of the CIRP*, 49/2, pp. 523-546 (2000).
- [Cosijns 02] S.J.A.G. Cosijns, H. Haitjema, P.H.J. Schellekens, Modeling and verifying nonlinearities in heterodyne displacement interferometry, *Precision Engineering*, 26, pp. 448-455 (2002).
- [Cosijns 04] S.J.A.G. Cosijns, *Displacement laser interferometry with sub-nanometer uncertainty*, Ph.D. thesis, ISBN 90-386-2656-8, Eindhoven University of Technology (2004).
- [Cottrell 78] G.A. Cottrell, The measurement of true contact charge density using soft rubber, *Journal of Physics D: Applied Physics*, 1, p.681-688 (1978)
- [Crassous 93] J. Crassous, E. Charlaix, H. Gayvallet, J.L. Loubet, Experimental Study of a Nanometric Liquid Bridge with a Surface Force Apparatus, *Langmuir*, 9, p.1995-1998 (1993).
- [Danzebrink 06] H.-U. Danzebrink, L. Koenders, G. Wilkening, A. Yacoot, H. Kunzmann, Advances in Scanning Force Microscopy for Dimensional Metrology, *Annals of the CIRP*, 55/2, pp. 841-878 (2006).
- [Davidson 02] S. Davidson, I. Severn, D. Bayliss, Mass standards: a high-precision study of commonly used methods for cleaning stainless steel weights, *Measurement Science and Technology*, 13, pp. 1178-1182 (2002).
- [Davidson 03] S. Davidson, A review of surface contamination and the stability of standard masses, *Metrologia*, 40/6, pp. 324-338 (2003).
- [Davies 67] D.K. Davies, Static electrification, *Institute of Physics Conference Series*, 4, p.29-36 (1967).

- [Decker 97] J.E. Decker, J.R. Pekelsky, Uncertainty evaluation of the measurement of gauge blocks by optical interferometry, Internal report, NRC Doc. 41374, National Research Council Canada (1997).
- [Derjaguin 34] B.V. Derjaguin, Untersuchungen über die Reibung und Adhäsion, *Kolloid Zeitschrift*, 69, p.155164, in German (1934).
- [Dekkers 02] J. Dekkers, Design of a 3D measuring probe, For nanometer applications, M.S. report, PE 2002-080, Eindhoven University of Technology (2002).
- [Destefani 01] J.D. Destefani, CMM's Make Contact, *Manufacturing engineering*, <http://www.sme.org/manufacturingengineering> as it is in 10/2006, September, 127:3 (2001).
- [Dey 00] F.K. Dey, J.A.S. Cleaver, P.A. Zhdan, Atomic force microscopy study of adsorbed water on lactose particles, *Advanced Powder Technology* 11/4, p.401-413 (2000).
- [Ding 01A] J. Ding, Y. Meng, S. Wen, Specimen size effect on mechanical properties of polysilicon microcantilever beams measured by deflection using a nanoindenter, *Materials Science and Engineering*, B83, p. 42-47 (2001).
- [Ding 01B] J. Ding, Y. Meng, S. Wen, Size effect on the mechanical properties of microfabricated polysilicon thin films, *Journal of Materials Research*, 16/8, p. 2223-2228 (2001).
- [Dingreville 04] R. Dingreville, J. Qu, M. Cherkaoui M., Effective Modulus of Nano-particles, 9th International Symposium on Advanced Packaging Materials, p.187-192 (2004).
- [Donaldson 72A] R.R. Donaldson, The deterministic approach to machining accuracy, Society of Manufacturing Engineers, Fabrication Technology Symposium (1972).
- [Donaldson 72B] R.R. Donaldson, A simple method for separating spindle error from test ball roundness error, *Annals of the CIRP*, 21, pp. 125-126 (1972).
- [Dorda 60] G. Dorda, Influence of relative humidity on surface conductivity of germanium, *Czechoslovak Journal of Physics*, 10/11, p.820-829 (1960).
- [Drauglis 69] E. Drauglis, R.D. Gretz, R.I. Jaffee, *Molecular Processes at Solid Surfaces*, ISBN 0070178275, McGraw-Hill (1969).
- [Dutschke 96] W. Dutschke, *Fertigungs Messtechnik*, B.G. Teubner Stuttgart, in German (1996).
- [Edlén 66] B. Edlén, The refractive index of air, *Metrologia*, 2/2, pp. 71-80 (1966).
- [Egashira 05] K. Egashira, K. Mizutani, EDM at low open-circuit voltage, *International Journal of Electrical Machining*, 10, pp. 21-26 (2005).
- [Eickhoff 97] M.L. Eickhoff, J.L. Hall, Real-time precision refractometry: new approaches, *Applied Optics*, 36, pp. 1223-1234 (1997).
- [El-Deiry 02] P.A. El-Deiry, R.P. Vinci, Strain Rate Dependent Behavior Of Pure Aluminum And Copper Micro-Wires, *Materials Research Society, Symposium Proceedings*, 695 (2002).
- [Elsdon 76] R. Elsdon, F.R.G. Mitchell, Contact electrification of polymers, *Journal of Physics D: Applied Physics*, 9, p.1445-1460 (1976).
- [Elwenspoek 01] M. Elwenspoek, R. Wiegerink, *Mechanical Microsensors*, ISBN 3540675825, Springer-Verlag (2001).
- [Eom 02] T. Eom, T. Choi, K. Lee, H. Choi, S. Lee, A simple method for the compensation of the nonlinearity in the heterodyne interferometer, *Measurement Science and Technology*, 13, pp. 222-225 (2002).

- [Evans 96] C.J. Evans, R.J. Hocken, W.T. Estler, Self-Calibration; Reversal, Redundancy, Error Separation and Absolute Testing, *Annals of the CIRP*, 45/2, pp. 617-634 (1996).
- [Fabish 79] T.J. Fabish, H.M. Saltsburg, M.L. Hair, Charge Transfer in Metal/Atactic Polystyrene Contacts, *Journal of Applied Physics*, 47/3, p.930-939 (1979).
- [Flack 01] D. Flack, CMM probing, Measurement Good Practice Guide No. 43, NPL (2001).
- [Fearing 95] R.S. Fearing, Survey of Sticking Effects for Micro Parts Handling, *Int. Conf. Robotics and Intelligent Systems*, Pittsburgh (1995).
- [Feddema 01] J.T. Feddema, P. Xavier, R. Brown, Micro-assembly planning with van der Waals force, *Journal of Micromechatronics*, 1/2, p.139-153 (2001).
- [Fenner 89] R.T. Fenner, *Mechanics of Solids*, ISBN 0632020180, Blackwell Scientific Publications, Great Britain (1989).
- [Ferry 80] J.D. Ferry, *Viscoelastic Properties of Polymers*, ISBN 0471048941, Wiley (1980).
- [Fisher 26] R.A. Fisher, On the Capillary Forces in an Ideal Soil; Correction of Formulae given by WB Haines, *Journal Agricultural Science*, 16, p.492-505 (1926).
- [Fisher 81] L.R. Fisher, J.N. Israelachvili, Direct measurement of the effect of meniscus forces on adhesion; a study of the applicability of macroscopic thermodynamics to microscopic liquid interfaces, *Colloids and Surfaces*, 3, p.303-319 (1981).
- [Florussen 02] G.H.J. Florussen, Accuracy Analysis of Multi-axis Machines by 3D Length Measurements, ISBN 90-386-2943-5, Ph.D. Thesis, Eindhoven University of Technology (2002).
- [Flügge 96] J. Flügge, Vergleichende Untersuchungen zur meßtechnischen Leistungsfähigkeit von Laserinterferometern und inkrementellen Maßstabmeßsystemen, PTB Bericht F-23, ISBN 3894296836 (1996).
- [Flügge 03] J. Flügge, R. Köning, H. Bosse, Recent activities at PTB nanometer comparator, *Proceedings of SPIE*, 5190, pp. 391-399 (2003).
- [Foss 22] F.E. Foss, R.C. Brumfield, Some measurements of the shape of Brinell ball indentation, *American Society for Testing and Materials (ASTM)*, 22/312, p.179-182 (1922).
- [Fracheboud 02] M. Fracheboud, F. Meli, S. Bottinelli, J-M. Breguet, R. Clavel, Palpeur à 3 degrés de liberté pour machine à mesurer par coordonnées avec une résolution de 5 nm, *Journées de Microtechnique*, in French (2002).
- [Franklin 91] G.F. Franklin, J.D. Powell, A. Emami-Naeini, *Feedback Control of Dynamic Systems*, ISBN 0131499300, Addison Wesley (1991).
- [Franks 91] A. Franks, Nanometric surface metrology at the National Physics Laboratory, *Nanotechnology*, 2, p. 11-18 (1991).
- [Freitas 95] J.M. De Freitas, M.A. Player, Polarization effects in heterodyne interferometry, *Journal of Modern Optics*, 42/9, pp. 1875-1900 (1995).
- [Freund 99] J. Freund, J. Halbritter, J.K.H. Hörber, How Dry Are Dried Samples? Water Adsorption Measured by STM, *Microscopy Research and Technique*, 44, p.327-338 (1999).
- [Fukuda 98] T. Fukuda, Wolfgang Menz (editors), *Micro Mechanical Systems: Handbook of Sensors and Actuators*, ISBN 0444823638, Elsevier Science (1998).
- [Furse 81] J.E. Furse, Kinematic design of fine mechanisms in instruments, *Journal of Physics E: Scientific Instruments*, 14 (1981).

- [Gao 96] W. Gao, S. Kiyono, T. Nomura, A new multiprobe method of roundness measurements, *Precision Engineering*, 19/1, pp. 37-45 (1996).
- [de Gennes 85] P.G. de Gennes, Wetting: statics and dynamics, *Reviews of Modern Physics*, 57/3, pp. 827-863 (1985).
- [Giacometti 99] J.A. Giacometti, S. Fedosov¹, M.M. Costa, Corona Charging of Polymers; Recent Advances on Constant Current Charging, *Brazilian Journal of Physics*, 29/2, p.269-279 (1999).
- [Girard 90] G. Girard, The washing and cleaning of kilogram prototypes at the BIPM, BIPM internal report (1990).
- [Gordon 99] C. G. Gordon, Generic Vibration Criteria for Vibration-Sensitive Equipment, International Society for Optical Engineering (SPIE), Conference on Current Developments in Vibration Control for Optomechanical Systems, July, p.22-39 (1999).
- [Grant 90] I.S. Grant, W.R. Philips, *Electromagnetism*, ISBN 0471927120, John Wiley and Sons Ltd (1990).
- [Greek 97] S. Greek, F. Ericson, S. Johansson, J.A. Schweitz, In situ tensile strength measurement and Weibull analysis of thick film and thin film micromachined polysilicon structures, *Thin Solid Films*, 292, p. 247254 (1997).
- [Greek 99] S. Greek, F. Ericson, S. Johansson, M. Furtsch, A. Rump, Mechanical characterization of thick polysilicon films: Youngs modulus and fracture strength evaluated with microstructures. *Journal of Micromechanics and Microengineering*, 9, p. 245251 (1999).
- [Greenwood 66] J.A. Greenwood, J.B.P. Williamson, The Contact of Nominally Flat Surfaces, *Proceedings of the Royal Society of London, Series A: Mathematical and Physical Sciences*, 295, p.300-319 (1966).
- [Greenwood 67] J.A. Greenwood, J.H. Tripp, The Elastic Contact of Rough Spheres, *Journal of Applied Mechanics*, 89, p.153-159 (1967).
- [Greenwood 84] J.A. Greenwood, K.L. Johnson, E. Matsubara, A Surface Roughness Parameter in Hertz Contact, *Wear*, 100, p.47-57 (1984).
- [Greenwood 99] J.A. Greenwood, Contact of Rough Surfaces, in I.L. Singer, H.M. Pollock, eds., *Fundamentals of Friction: Macroscopic and Microscopic Processes*, Series E: Applied Sciences, 220, ISBN 0792319125, Kluwer Academic Publishers (1999).
- [Greenwood 01] J.A. Greenwood, J.J. Wu, Surface Roughness and Contact: An Apology, *Meccanica*, 36, p.617-630 (2001).
- [Griesmann 04] U. Griesmann, J. Soons, Q. Wang, Measuring Form and Radius of Spheres with Interferometry, *Annals of the CIRP*, 53/1, pp. 451-454 (2004).
- [Grigg 92] D.A. Grigg, P.E. Russel, Tip-sample forces in scanning probe microscopy in air and vacuum, *Journal of Vacuum Science Technology A*, 10, p.680683 (1992).
- [Guijun 98] J. Guijun, H. Schwenke, E. Trapet, Optomechanical microprobe system for measuring very small parts on CMMs, *Proceedings of the SPIE*, 3454, pp. 348-353 (1998).
- [Gum 93] Guide to the Expression of Uncertainty in Measurement (GUM), 1st Edition, International Organization for Standardization (ISO), Switzerland, paragraph 3.4.8 (1993).
- [Haitjema 96] H. Haitjema, H. Bosse, R. Thalmann, A. Sacconi, International comparison of roundness profiles with nanometric accuracy, *Metrologia* 33, 67, (1996).
- [Hale 99] L.C. Hale, Principles and Techniques for Designing Precision Machines, UCRL-LR-133066, University of California, Ph.D. Thesis (1999).

- [Hale 01] L.C. Hale, A.H. Slocum, Optimal design techniques for kinematic couplings, *Precision Engineering*, 25/2, pp. 114-127 (2001).
- [Hamaker 37] H.C. Hamaker, The London-Van der Waals attraction between spherical particles, *Physica* 4, 1058 (1937).
- [Han 99] S.M. Han, H. Benaroya, T. Wei, Dynamics of Transversely Vibrating Beams using Four Engineering Theories, *Journal of Sound and Vibration*, 225/5, p.935-988 (1999).
- [Hansen 06] H.N. Hansen, K. Carneiro, H. Haitjema, L. De Chiffre, Dimensional Micro and Nano Metrology, *Annals of the CIRP*, 55/2, pp. 721-743 (2006).
- [Harnby 96] N. Harnby, A.E. Hawkins, I. Opalinski, Measurement of the adhesional force between individual particles with moisture present; Part 2: A novel measurement technique, *Chemical Engineering Research and Design*, 74A, p.616-626 (1996).
- [Harper 51] W.R. Harper, The Volta effect as a cause of static electrification, *Proceedings of the Royal Society A*, 205, p.83-103 (1951).
- [Harper 57] W.R. Harper, The Generation of Static Charge, *Advances in Physics*, 6/24, p.365-416 (1957).
- [Harper 60] W.R. Harper, Contact electrification of semiconductors, *British Journal of Applied Physics*, 11, p.324-331 (1960).
- [Harper 67] W.R. Harper, , *Contact and Frictional Electrification*, ISBN 188554006X, Oxford University Press (1967).
- [Harriman 97] L. Harriman, D. Simkins, Don't Sweat it, dehumidify, *Chemical Engineering*, August, p.80-87 (1997).
- [Hausotte 02] T. Hausotte, Nanopositionier- und Nanomessmaschine, ISBN 3932633717, PhD thesis, Technical University Ilmenau, Germany, 2002.
- [Heim 96] M. Heim, R. Eschrich, A. Hillebrand, H.F. Knapp, R. Guckenberger, Scanning tunneling microscopy based on the conductivity of surface adsorbed water; Charge transfer between tip and sample via electrochemistry in a water meniscus or via tunneling?, *Journal of Vacuum Science Technology B*, 14, p.14981502 (1996).
- [Heinz 99] W.F. Heinz, J.H. Hoh, Spatially resolved force spectroscopy of biological surfaces using the atomic force microscope, *Trends in Biotechnology*, 17/4, p.143-150 (1999).
- [Heldens 05] R.W.P. Heldens, Analyse en Optimalisatie van een Precisie Meettaster voor Coördinaten MeetMachines, M.S. report, MNSE 2005-003, Eindhoven University of Technology, in Dutch (2005).
- [Heydeman 81] P.L.M. Heydeman, Determination and correction of quadrature fringe measurements in interferometers, *Applied Optics*, 20, pp. 3382-3384 (1981).
- [Hidaka 06] K. Hidaka, P.H.J. Schellekens, Study of a Small-sized Ultrasonic Probe, *Annals of the CIRP*, 55/1, pp. 567570 (2006).
- [Hocken 05] R.J. Hocken, N. Chakraborty, C. Brown, Optical Metrology of Surfaces, *Annals of the CIRP*, 54/2, pp. 705719 (2005).
- [Holm 58] R. Holm, *Electric contacts handbook*, Springer-Verlag (1958).
- [Hooge 94] F.N. Hooge, 1/f Noise Sources, *IEEE Transactions on electron devices*, 41/11, pp. 1926-1935 (1994)
- [Hooton 04] J.C. Hooton *et al.*, An Atomic Force Microscopy Study of the Effect of Nanoscale Contact Geometry and Surface Chemistry on the Adhesion of Pharmaceutical Particles, *Pharmaceutical Research*, 21/6, p.953-961 (2004).

- [Hosokawa 95] K. Hosokawa, I. Shimoyama, H. Miura, Dynamics of self-assembling systems: analogy with chemical kinetics, *Artificial Life*, 1/4, p. 413-427 (1995).
- [Hou 92] W. Hou, G. Wilkening, Investigation and Compensation of the Nonlinearity of Heterodyne Interferometers, *Precision Engineering*, 14, pp. 91-98 (1992).
- [Hou 94] W. Hou, G. Wilkening, Heterodyne interferometer arrangement, U.S. Patent 5.331.400 (1994).
- [Houpis 05] C.H. Houpis, S.J. Rasmussen, M. Garcia-Sanz, Quantitative feedback theory: fundamentals and applications, ISBN 0849333709, CRC (2005)
- [Howard 02] R.M. Howard, Principles of Random Signal Analysis and Low Noise Design: The Power Spectral Density and its Applications, ISBN 0471226173, Wiley-IEEE Press (2002).
- [Howe 96] R.T. Howe, et al., Polysilicon integrated microsystems: technologies and applications, *Sensors and Actuators A*, 56, pp. 167-177 (1996).
- [Hsu 03] T.R. Hsu, MEMS Packaging, ISBN 0863413358, Institution of Electrical Engineers (2003).
- [Hu 95A] J. Hu, X.D. Xiao, D.F. Ogletree, M. Salmeron, Imaging the condensation and evaporation of molecularly thin films of water with nanometer resolution, *Science*, 268, p.267269 (1995).
- [Hu 95B] J. Hu, X.D. Xiao, M. Salmeron, Scanning polarization force microscopy: a technique for imaging liquids and weakly adsorbed layers, *Applied Physics Letters*, 67, p.476478 (1995).
- [Huang 00] H. Huang and F. Spaepen, Tensile testing of free-standing Cu, Ag and Al thin films and Ag/Cu multilayers, *Acta Materialia*, 48, p.3261-3269 (2000).
- [Hunter 01] R.J. Hunter, Foundations of Colloid Science, ISBN 0198505027, Oxford Science Publications (2001).
- [Höhn 99] M. Höhn, et al., Montagetechnik für Mikrosysteme, *iwb-newsletter* 7, 1/2, p.2-3 (1999).
- [Horn 92] R.G. Horn, D.T. Smith, Contact electrification and adhesion between dissimilar materials, *Science*, 256/5055, p. 362-364 (1992).
- [Horowitz 89] P. Horowitz, W. Hill, The art of electronics, ISBN 0521370957, Cambridge University Press (1989).
- [Ikeda 93] S. Ikeda, K. Uchikawa, Y. Hashiguchi, M. Nagoshi, H. Kasamura, K. Shiozawa, D. Fujita, K. Yoshihara, Surface Analytical Study of Cleaning Effects and the Progress of Contamination on Prototypes of the Kilogram, *Metrologia*, 30/3, pp. 133-144 (1993).
- [Inman 94] D.J. Inman, Engineering Vibration, ISBN 0132281732, Prentice Hall (1994).
- [Israelachvili 74] J.N. Israelachvili, The Nature of van der Waals Forces, *Contemporary Physics*, 15/2, p.159-177 (1974).
- [Israelachvili 92] J.N. Israelachvili, Intermolecular and Surface Forces, ISBN 0123751810, Academic Press (1992).
- [Jadaan 03] O.M. Jadaan, N.N. Nemeth, J. Bagdahn, W.N. Sharpe, Probabilistic Weibull behavior and mechanical properties of MEMS brittle materials, *Journal of Materials Science*, 38, p. 4087-4113 (2003).
- [Jansen 06] M. Jansen, Development of a Wafer Geometry Measuring System: A Double Sided Stitching Interferometer, ISBN 9038627580, Ph.D. Thesis, Eindhoven University of Technology, The Netherlands (2006).

- [Janssen 06] D. Janssen, Self-assembling monolayers for organic thin-film transistors, Ph.D. thesis, K.U. Leuven (2006).
- [Johansson 88] S. Johansson, Micromechanical properties of silicon, PhD Thesis, Uppasala University, Sweden, 1988.
- [Johnson 28] J. B. Johnson, Thermal Agitation of Electricity in Conductors, *Physical Review*, 32, pp. 97-109 (1928).
- [Johnson 85] K.L. Johnson, *Contact Mechanics*, ISBN 0-521-34796-3, Cambridge University Press (1985).
- [Johnston 76] J.S. Johnston, T.H. Neve, US Patent No. 3,986,385 (19 October 1976).
- [Jones 03] R. Jones, H.M. Pollock, D. Geldart, A. Verlinden, Inter-particle forces in cohesive powders studied by AFM: effects on relative humidity, particle size and wall roughness, *Particle Technology*, 132, p.196-210 (2003).
- [Jones 06] R.A.L. Jones, R.W. Richards, *Polymers at Surfaces and Interfaces*, ISBN 0521479657, Cambridge University Press (2006).
- [Kagami 83] J. Kagami, K. Yamada, T. Hatazawa, Contact between a Sphere and Rough Plates, *Wear*, 87, p.93-105 (1983).
- [Kahn 00] H. Kahn, et al., Fracture toughness of polysilicon MEMS devices, *Sensors and Actuators A*, 82, pp. 274-280 (2000).
- [Kahn 01] H. Kahn, A.H. Heuer, Polysilicon: mechanical properties, *Encyclopedia of Materials: Science and Technology*, Pergamon Press (2001).
- [Kainer 00] K.U. Kainer, *Magnesium: Eigenschaften, Anwendungen, Potentiale*, ISBN 3527299793, Wiley-VCH Verlag GmbH, Germany (2000).
- [Kalkman 01] A. J. Kalkman, A. H. Verbruggen, and G. C. A. M. Janssen, Young's modulus measurements and grain boundary sliding in free-standing thin metal films, *Applied Physics Letters*, 78/18, p.2673-2675 (2001).
- [Kanda 00] T. Kanda, T. Morita, M.K. Kurosawa, T. Higuchi, A flat type touch probe sensor using PZT thin film vibrator, *Sensors and Actuators A*, 83, p. 67-75 (2000).
- [Karnovsky 04] I. Karnovsky, O. Lebed, *Free Vibrations of Beams and Frames: Eigenvalues and Eigenfunctions*, ISBN 0071431896, McGraw-Hill (2004).
- [Karrai 99] K. Karrai, S. Manus, US Patent No. 6,006,594, (28 December 1999).
- [Keller 97] C.G. Keller, R.T. Howe, Hexsil tweezers for teleoperated micro-assembly, proceedings IEEE Workshop on Micro Electro Mechanical Systems (MEMS), Nagoya, Japan, p. 72-77 (1997).
- [Kiefer 78] J.E. Kiefer, V.A. Parsegian, G.H. Weiss, Some Convenient Bounds and Approximations for the Many Body Van der Waals Attraction between two Spheres, *Journal of Colloid and Interface Science*, 67/1, p.140-153 (1978).
- [Kim 96] B.J. Kim, Y. Sawamoto, T. Masuzawa, M. Fujino, Advanced vibroscanning method for micro-hole measurement: High speed and stability improvement of measurement technique, *International Journal of Electrical Machining*, 1, pp. 41-44 (1996).
- [Kim 99] B.J. Kim, T. Masuzawa and T. Bourouina, Vibroscanning Method for the Measurement of Micro- Hole Profiles, *Measurement Science and Technology* 10 (1999) (8), pp. 697705.
- [Kim 01] J. Kim, et al., Why is (111) silicon a better mechanical material for MEMS?, *Transducers*, pp. 662-665 (2001).

- [Kishinami 84] T. Kishinami, H. Nakamura, K. Saito, A. Kamei, Three Dimensional Curved Surfaces measurement using Newly Developed Three Dimensional Tactile Sensing Probe, Proceedings of the International Symposium on Metrology for Quality Control in Production, Tokyo, p.288-293 (1984).
- [Klimchitskaya 00] G.L. Klimchitskaya, U. Mohideen, V. M. Mostepanenko, Casimir and van der Waals forces between two plates or a sphere (lens) above a plate made of real metals, *Physical Review A*, 61 (2000).
- [Koenders 03] L. Koenders, C.H. Harms, E. Waltereit, G. Wilkening, An ultra-precision interference comparator for dimensional measurement using two tunneling microscopes as probes, *Measurement Science and Technology*, 14, pp. 943-952 (2003).
- [Kolodezhnov 00] V.N. Kolodezhnov, G.O. Magomedov, G.P. Maltsev, Refined determination of shape for the free surface of the liquid region in analysis of capillary interaction of powder particles, *Colloid Journal*, 62/4, p.443-450 (2000).
- [Koyano 96] K. Koyano, T. Sato, Micro Object handling System with Concentrated Visual Fields and New Handling Skills, Proceedings of ICRA, p.2541-2548 (1996).
- [Kralchevsky 01A] P.A. Kralchevsky, N.D. Denkov, Capillary forces and structuring in layers of colloid particles, *Current Opinion in Colloid & Interface Science*, 6, p. 383-401 (2001).
- [Kralchevsky 01B] P.A. Kralchevsky, K. Nagayama, Particles at fluid interfaces and membranes: attachment of colloid particles and proteins to interfaces and formation of two-dimensional arrays, ISBN 0444502343, Elsevier, Amsterdam (2001).
- [Krim 96] J. Krim, Atomic-Scale Origins of Friction, *Langmuir*, 12/19, p.4564-4566 (1996).
- [Krupp 72] H. Krupp, W. Schnabel, G. Walter, *Journal of Colloid and Interface Science*, 39 (1972).
- [Kumar 92] A. Kumar, M.M. Perlman, Sliding-Friction Electrification of Polymers and Charge Decay, *Journal of Polymer Science, Part B: Polymer Physics*, 30, p.859-863 (1992).
- [Küng 05] A. Küng, F. Meli, Self calibration method for 3D roundness of spheres using an ultra-precision coordinate measuring machine, Proceedings of Euspen, pp. 193-196 (2005).
- [Küng 07] A. Küng, F. Meli, Ultraprecision micro-CMM using a low force 3D touch probe, *Measurement Science and Technology*, 18, pp. 319-327 (2007).
- [Laake 06] L. van Laake, Design of a Planar 3D Probe with Nanometer Uncertainty, Internal Student report, Eindhoven University of Technology (2006).
- [Lam 97] M.J. Lam, Hybrid Active/Passive Models with Frequency Dependent Damping, Ph.D. thesis, Virginia Polytechnic Institute and State University (1997).
- [Lamoreaux 97] S.K. Lamoreaux, Demonstration of the Casimir Force in the 0.6 to 6 μm range, *Physical Review Letters*, 78, pp. 5-8 (1997).
- [Lamoreaux 05] S.K. Lamoreaux, The Casimir force: background, experiments, and applications, *Reports on Progress in Physics*, 68, pp. 201-236 (2005).
- [Langbein 71] D. Langbein, Non-Retarded Dispersion Energy Between Macroscopic Spheres, *Journal of Physics and Chemistry of Solids*, 32, p.1657-1667 (1971).
- [Langbein 74] D. Langbein, Theory of van der Waals Attraction, ISBN 0387067426, Springer-Verlag (1974).
- [Langen 94] H.H. Langen, A study on micromachining/assembly, Ph.D. thesis, University of Tokyo (1994).

- [Laraqi 03] N. Laraqi, Thermal Resistance for Random Contacts on the Surface of a Semi-Infinite Heat Flux Tube, *Journal of Heat Transfer*, 125/3, p.532-535 (2003).
- [Lazzer 99] A. de Lazzer, M. Dreyer, H.J. Rath, Particle Surface Capillary Forces, *Langmuir* 1999, 15, p.4551-4559 (1999).
- [Leach 99] R.K. Leach, Calibration, traceability and uncertainty issues in surface texture metrology: Version 2, NPL Report CLM 7 (1999).
- [Leach 01] R. Leach, J. Haycocks, K. Jackson, A. Lewis, S. Oldfield, A. Yacoot, Advances in traceable nanometrology at the National Physics Laboratory, *Nanotechnology*, 12, p. R1-R5 (2001).
- [Leach 04A] R.K. Leach, J. Murphy, A. Wilson, Design of a co-ordinate probe for characterising three-dimensional micro-structures, NPL Report CBTLM 30, pp. 148 (2004).
- [Leach 04B] R.K. Leach, J. Murphy, The Design of a Co-ordinate Measuring Probe for Characterising Truly Three-Dimensional Micro-Structures, *Proceedings of Euspen*, pp. 230232 (2004).
- [Lebrasseur 00] E. Lebrasseur, T. Bourouina, J-B. Pourcie, M. Ozaki, T. Masuzawa, H. Fujita, Resonant-Type Micro-Probe for Vertical Profiler, *Technical Proceedings of the 2000 International Conference on Modeling and Simulation of Microsystems, MSM 2000*, pp. 285-288 (2000).
- [Lee 00A] H.-J. Lee, G. Cornella, J.C. Bravman, Stress relaxation of free-standing aluminum beams for microelectromechanical systems applications, *Applied Physics Letters*, 76/23, p. 3415-3417 (2000).
- [Lee 00B] D.W. Lee, T. Ono, M. Esashi, Cantilever with Integrated Resonator for Application of Scanning Probe Microscope, *Sensors and Actuators A*, 82, p. 11-16 (2000).
- [Lee 03] D. Lee, J. Woolman, et al., Microvalves for SMA-based Actuator in Compact Kinetic Energy Missile, *SPIE 10th Annual International Symposium, The international Society for Optical Engineering*, Vol. 5055, pp. 300-306 (2003).
- [Lekhnitskii 63] S.G. Lekhnitskii, *Theory of elasticity of an anisotropic elastic body*, Holden-Day Inc., San Francisco, 1963.
- [Li 90] Y. Li, D. Trauner, F.E. Talke, Effect of humidity on stiction and friction of the head/disk interface, *IEEE Transactions on Magnetics*, 26/5, p.2487-2489 (1990).
- [Li 03] Y.F. Li, Z.G. Liu, Method for determining the probing points for efficient measurement and reconstruction of freeform surfaces, *Measurement science and technology*, 14/8, pp. 1280-1288 (2003).
- [Liang 96] T.-X. Liang, W.Z. Sun, L.-D. Wang, Y.H. Wang, H.-D. Li, Effect of Surface Energies on Screen Printing Resolution, *IEEE Transactions on components, packaging, and manufacturing technology - Part B*, 19/2 pp. 423-426 (1996).
- [Lide 98] D.R. Lide, *Handbook of Chemistry and Physics*, ISBN: 0849304792, CRC-Press (1998).
- [Lima 99] M.M. de Lima, R.G. Lacerda, J. Vilcarromero, F.C. Marques, Coefficient of thermal expansion and elastic modulus of thin films, *Journal of Applied Physics*, 86/9, p.4936-4942 (1999).
- [Loeb 58] L.B. Loeb, *Static Electrification*, Springer Verlag (1958).
- [Lonardo 02] P.M. Lonardo, D.A. Lucca, L. De Chiffre, Emerging Trends in Surface Metrology, *Annals of the CIRP*, 51/2, pp. 701-723 (2002).

- [Loon 97] R.J.A. van Loon, Ontwerp van een kalibratieopstelling voor precisietasters en ruwheidssensoren, Eindhoven University of Technology, Mechanical Engineering, Precision Engineering section, report number WPA-310081, *in Dutch*, December 1997.
- [Lorentz 81] H.A. Lorentz, *Annalen der Physik und Chemie*, 12, 127 (1881).
- [Lorrain 88] P. Lorrain, D.R. Corson, F. Lorrain, *Fields and Waves*, ISBN 0716718235, W.H. Freeman (1988).
- [Lowell 75] J. Lowell, Contact electrification of Metals, *Journal of Physics D: Applied Physics*, 8, p.53-63 (1975).
- [Lowell 80] J. Lowell, A.C. Rose-Innes, Contact electrification, *Advances in Physics*, 29/6, p.947-1023 (1980)
- [Lu 82] J.-C. Lu, N.A. Duffie, J.G. Bolinger, Two Dimensional Tracing and Measurement Using Touch-Trigger Probe, *Annals of the CIRP*, 31/1, p.415-419 (1982).
- [Maboudian 97] R. Maboudian, R.T. Howe, Critical Review: Adhesion in surface micromechanical structures, *Journal of Vacuum Science Technology B*, 15/1, p.1-20 (1997).
- [Maluf 04] N. Maluf, K. Williams, *An introduction to microelectromechanical systems engineering*, ISBN 1-58053-590-9, Artech House (2004).
- [Martins 90] J.A.C. Martins, J.T. Oden, F.M.F. Simões, A study of static and kinetic friction, *International Journal of Engineering Science*, 28, p. 29-92 (1990).
- [Marvin 82] A. M. Marvin, F. Toigo, Van der Waals interaction between a point particle and a metallic surface; I: Theory, *Phys. Rev. A*, 25/2, p.782802 (1982).
- [Mastrangelo 00] C.H. Mastrangelo, Suppression of stiction in MEMS, *Materials science of microelectromechanical systems (MEMS) devices II*, Materials Research Society (MRS) Symposium Proceedings, 605, p.105116 (2000).
- [Masuzawa 93] T. Masuzawa, Y. Hamasaki, M. Fujino, Vibroscanning method for nondestructive measurement of small holes, *Annals of the CIRP*, 42/1, pp. 589-592 (1993).
- [Masuzawa 00] T. Masuzawa, State of the art of micromachining, *Annals of the CIRP*, 49/2, pp. 473-488 (2000).
- [McCool 86] J.I. McCool, Comparison of Models for the Contact of Rough Surfaces, *Wear*, 107, p.3760 (1986).
- [McFarlane 50] J.S. McFarlane, D. Tabor, Adhesion of Solids and the Effect of Surface Films, *Proceedings of the Royal Society of London, Series A: Mathematical and Physical Sciences*, 202, p.224-243 (1950).
- [Medley 53] J.A. Medley, The dissipation of electrical charges generated by rollers, *British Journal of Applied Physics*, 4/2, p.S23-S27 (1953).
- [Meli 02] F. Meli, Roughness measurements according to existing standards with a metrology AFM profiler, *Proceedings of Euspen*, 2, pp. 533-536 (2002).
- [Meli 03] F. Meli, M. Fracheboud, S. Bottinelli, M. Bieri, R. Thalmann, J-M. Breguet, R. Clavel, High precision, low force 3D touch probe for measurements on small objects, *Proceedings of Euspen*, 2, pp.411-414 (2003).
- [Meli 04] F. Meli, A. Küng, Performance of a low force 3D touch probe on an ultraprecision CMM for small parts, *Proceedings of Euspen*, pp. 270-271 (2004).
- [Meli 07] F. Meli, A. Küng, AFM investigation of surface damage caused by mechanical probing with small ruby spheres, *Measurement Science and Technology*, 18, pp. 496-502 (2007).

- [Middelhoek 89] S. Middelhoek, S.A. Audet, *Silicon Sensors*, Academic Press, London, 1989.
- [Mikic 74A] B.B. Mikic, Thermal Contact Conductance: Theoretical Considerations, *International Journal of Heat and Mass Transfer*, 12, p.279300 (1974).
- [Mikic 74B] B.B. Mikic, R.T. Roca, A Solution to the Contact of Two Rough Spherical Surfaces, *Journal of Applied Mechanics*, ASME, 96, p.801-803 (1974).
- [Mittal 06] K.L. Mittal, *Contact Angle, Wettability and Adhesion*, ISBN 9067644366, VSP International Science Publishers, The Netherlands (2006).
- [Mizubayashi 99] H. Mizubayashi, J. Matsuno and H. Tanimoto, Young's Modulus of Silver Films, *Scripta Materialia*, 41, p.443-448 (1999).
- [Mohideen 98] U. Mohideen, A. Roy, Precision Measurement of the Casimir Force from 0.1 to 0.9 mm, *Physical Review Letters*, 81, pp. 4549-52 (1998).
- [Moon 98] S. Moon, Y.L. Shen, Errors in probe offset Vectors of multiple orientations in CMM measurements, *ASPE Proceedings*, 18, p.512-515 (1998).
- [Morel 2006] M.A.A. Morel, *Uncertainty Estimation of Shape and Roughness Measurement*, ISBN 90-386-2608-8, PhD. Thesis, Eindhoven University of Technology, Eindhoven, The Netherlands (2006).
- [Morita 90] M. Morita, T. Ohmi, E. Hasegawa, M. Kawakami, M. Ohwada, Growth of native oxide on a silicon surface, *Journal of Applied Physics*, 68/3, p.1272-1281 (1990).
- [Mossakovski 63] V.I. Mossakovski, Compression of elastic bodies under conditions of adhesion, *Journal of Applied Mathematics and Mechanics*, 27/3, p. 418-427 (1963).
- [Muralikrishnan 04] B. Muralikrishnan, J. Stone, S. Vemuri, C. Sahay, A. Potluri, J. Stoup, Fiber deflection probe for small hole measurements, *Proceedings of the ASPE Annual Meeting*, pp. 2427 (2004).
- [Nayfeh 85] N.H. Nayfeh, M.K. Brussel, *Electricity and Magnetism*, ISBN 047187681X, John Wiley & Sons Inc (1985).
- [Neugebauer 97] M. Neugebauer, F. Lüdicke, D. Bastam, H. Bosse, H. Reimann, C. Töpperwien, A new comparator for measurement of diameter and form of cylinders, spheres and cubes under clean-room conditions, *Measurement Science and Technology*, 8, pp. 849-856 (1997).
- [Neugebauer 01] M. Neugebauer, Uncertainty analysis for roundness measurements by the example of measurements on a glass hemisphere, *Measurement Science and Technology*, 12, pp. 68-76 (2001).
- [Neumann 79] A. W. Neumann, S. N. Omenyi, C. J. van Oss, Negative Hamaker coefficients; I: Particle engulfment or rejection at solidification fronts, *Colloid and Polymer Science*, 257/4, p.413-419 (1979).
- [Nicolaus 96] R.A. Nicolaus, G. Bönsch, Dimensional Measurements of a Silicon Sphere, *Conference on Precision Electromagnetic Measurements (CPEM)*, pp.167-168 (1996).
- [Nicolaus 97] R.A. Nicolaus, G. Bönsch, A Novel Interferometer for Dimensional Measurement of a Silicon Sphere, *IEEE Transactions of Instrumentation and Measurement*, 46/2, pp. 563-565 (1997).
- [Nishimura 01] K. Nishimura, K. Hidaka, N. Nishioki, US Patent No. 6,327,789 (11 December 2001).
- [Norton 03] M.P. Norton, D.G. Karczub, *Fundamentals of Noise and Vibration Analysis for Engineers*, ISBN 0521499135, Cambridge University Press (2003).

- [O'Connor 63] J.J. O'Connor, K.L. Johnson, The Role of Surface Asperities in Transmitting Tangential Forces Between Metals, *Wear*, 6, p.118139 (1963).
- [Oden 85] J.T. Oden, J.A.C. Martins, Models and computational methods for dynamic friction phenomena, *Computer Methods in Applied Mechanics and Engineering*, 52, p. 527-634 (1985).
- [Ohya 93] K. Ohya, M. Hachisuka, H. Tsumuraya, Y. Fujita, O. Arai, US Patent No. 5,247,751 (28 September 1993).
- [Opstal 06] S. van Opstal, Development of a Large area Automated Micro Assembler, MNSE-2006-009, Master thesis, Eindhoven University of Technology (2006).
- [Orr 75] F. M. Orr, L. E. Scriven and A. P. Rivas, Pendular rings between solids: meniscus properties and capillary force, *Journal of Fluid Mechanics*, 67/4, p.723-742 (1975).
- [Oss 79] C.J. van Oss, S.N. Omenyi, A.W. Neumann, Negative Hamaker coefficients; II: Phase separation of polymer solutions, *Colloid and Polymer Science*, 257/7, p.737 - 744 (1979).
- [Owens 67] J.C. Owens, Optical refractive index of air: dependence on temperature, pressure and composition, *Applied Optics*, 6, pp. 51-59 (1967).
- [Pakarinen 05] O.H. Pakarinen et al., Towards an accurate description of the capillary force in nanoparticle-surface interactions, *Modelling and Simulation in Materials Science and Engineering*, 13, p.1175-1186 (2005).
- [Patel 97] N. Patel, M.C. Davis, M. Lomas, C.J. Roberts, C.J.B. Tendler, M.W. Williams, STM of insulators with the probe in contact with an aqueous layer, *Journal of Physical Chemistry B*, 101/26, p.51385142 (1997).
- [Paul 81] R.P. Paul, *Robot Manipulators: Mathematics, Programming and Control*, ISBN 026216082X, MIT Press, MA (1981).
- [Peggs 99] G.N. Peggs, A.J. Lewis, S. Oldfield, Design for a compact high-accuracy CMM, *Annals of the CIRP*, 48/1, pp. 417-420 (1999).
- [Persson 00] B.N.J. Persson, *Sliding Friction: Physical Principles and Applications*, ISBN 3540632964, Springer, Berlin, Germany (2000).
- [Pham 04] D.T. Pham, S.S. Dimov, S. Bigot, A. Ivanov, K. Popov, Micro-EDM - Recent Developments and Research Issues, *Journal of Materials Processing Technology*, 149/1-3, pp. 50-57 (2004).
- [Picotto 91] G.B. Picotto, A. Sacconi, Nonlinearity analysis in heterodyne laser interferometers by using piezo-capacitive transducer, *Quantum Electronics and Plasma Physics*, 29, pp. 361-365 (1991).
- [Pinot 95] P. Pinot, Stability of Mass Standards Made of XSH Alacrite: Gravimetric Study of the Influence of Cleaning, *Metrologia*, 31/5, pp. 357-365 (1995).
- [Pornnoppadol 02] P. Pornnoppadol, S. Cao, M. Schmidt, R. Wilke, S. Bütetisch, V. Nesterov, U. Brand, Three-dimensional microprobe with reduced probing forces, *Proceedings of the 3rd Euspen International Conference*, Eindhoven, pp. 737-740 (2002).
- [Pornnoppadol 04] P. Pornnoppadol, *3D-Mikrotaster mit piezoresistiven Elementen*, ISBN: 3832232761, PhD Thesis, Technical University Braunschweig, in German (2004).
- [Pril 02] W.O. Pril, Development of High Precision Mechanical Probes for Coordinate Measuring Machines, ISBN 90-386-2654-1, PhD. Thesis, Eindhoven University of Technology, Eindhoven, The Netherlands (2002).

- [Rabe 02] U. Rabe, M. Kopycinska, S. Hirsekorn, W. Arnold, Evaluation of the Contact Resonance Frequencies in Atomic Force Microscopy as a Method for Surface Characterization, *Ultrasonics* 40, p. 49-54 (2002).
- [Rabinovich 02] Y.I. Rabinovich, J.J. Adler, M.S. Esayanur, A. Ata, R.K. Singh, B.M. Moudgil, Capillary forces between surfaces with nanoscale roughness, *Advances in Colloid and Interface Science*, 96, p.213-230 (2002).
- [Rabinowicz 04] E. Rabinowicz, *Friction and wear of materials*, ISBN 0471830844, Wiley-Interscience (2004).
- [Rajurkar 06] K.P. Rajurkar, G. Levy, A. Malshe, M.M. Sundaram, J. McGeough, A. DeSilva, X. Hu, R. Resnick, *Micro and Nano Machining by Electro-Physical and Chemical Processes*, *Annals of the CIRP*, 55/2, pp. 643-666 (2006).
- [Rao 03] S.S. Rao, *Mechanical Vibrations*, ISBN 0130489875, Prentice Hall (2003).
- [Renishaw 06A] Renishaw, Effects of continuous scanning on stylus balls; Three phenomena that can affect scanning accuracy, <http://www.renishaw.com/client/category/UKEnglish/CAT-1006.shtml> as it is on 08-2006 (2006).
- [Renishaw 06B] Renishaw, Renishaw scanning technology, www.renishaw.com/UserFiles/media/Renishaw_scanning.ppt as it is on 08-2006 (2006).
- [Ricco 92] A.J. Ricco, L.J. Kepley, R.C. Thomas, L. Sun, R.M. Crooks, Self-assembling monolayers on SAW devices for selective chemical detection, *Solid-State Sensor and Actuator Workshop*, p. 114-117 (1992).
- [Rijn 04] C.J.M. van Rijn, *Nano and Micro Engineered Membrane Technology*, Volume 10: *Membrane Science and Technology*, ISBN 0444514899, Elsevier Science (2004).
- [Roth 83] T. Roth, Antastverfahren mit Koordinatenmessgeraeten, *Feinwerktechnik & Messtechnik*, 91/4, p.177-179 (1983).
- [Ruan 94] J. Ruan, B. Bhushan, Atomic-scale and microscale friction studies of graphite and diamond using friction force microscopy, *Journal of Applied Physics*, 76/9, p.5022-5035 (1994).
- [Ruijl 01] T.A.M. Ruijl, *Ultra Precision Coordinate Measuring Machine: Design, Calibration and Error Compensation*, ISBN 90-6464-287-7, Delft University of Technology, Ph.D. Thesis (2001).
- [Ruud 94] J.A. Ruud, T.R. Jervis and F. Spaepen, Nanoindentation of Ag/Ni multilayered thin films, *Journal of Applied Physics*, 75, p.4969-4974 (1994).
- [Saito 03] A. Saito, U.S. Patent Application Publication No. 2003/0066354 (10 April 2003).
- [Sanfeld 00] A. Sanfeld, A. Steinchen, Surface Energy, Surface energy, stress, capillary-elastic pressure and chemical equilibrium constant in nanoparticles, *Surface Science*, 463/3, p.157-173 (2000).
- [Schellekens 98] P.H.J. Schellekens, et al., Design for Precision : Current Status and Trends, *Annals of the CIRP*, 47/1 (1998).
- [Schellekens 02] P.H.J. Schellekens, H. Haitjema, F.G.A. Homburg, *Metrologie voor W*, Lecture notes, 4C360, Eindhoven University of Technology, in Dutch (2002).
- [Schmitz 01] T. Schmitz, A. Davies, C. Evans, Uncertainties in interferometric measurements of radius of curvature, *Optical Manufacturing and Testing IV*, *Proceedings of SPIE*, 4451, pp. 432-447 (2001).
- [Schmitz 02] T. Schmitz, C.J. Evans, A. Davies, W.T. Estler, Displacement uncertainty in interferometric radius measurements, *Annals of the CIRP*, 51/1, pp. 451-454 (2002).

- [Schwartz 94] R. Schwartz, M. Gläser, Procedures for cleaning stainless steel weights, investigated by mass comparison and ellipsometry, *Measurement Science and Technology*, 5, pp. 1429-1435 (1994).
- [Schwenke 01] H. Schwenke, F. Wäldele, C. Weiskirch, H. Kunzmann, Opto-tactile Sensor for 2D and 3D Measurement of Small Structures on Coordinate Measuring Machines, *Annals of the CIRP*, 50/1, pp. 361-364 (2001).
- [Sciulli 97] D. Sciulli, Dynamics and Control for Vibration Isolation Design, Ph.D. thesis, Virginia Polytechnic Institute and State University (1997).
- [Seah 94] M.P. Seah, J.H. Qiu, P.J. Cumpson, J.E. Castle, Stability of Reference Masses II: The Effect of Environment and Cleaning Methods on the Surfaces of Stainless Steel and Allied Materials, *Metrologia*, 31/2, pp. 93-108 (1994).
- [Seggelen 05] J.K. van Seggelen, P.C.J.N. Rosielle, P.H.J. Schellekens, H.A.M. Spaan, R. Bergmans, G. Kotte, An elastically guided machine axis with nanometer repeatability, *Annals of the CIRP*, 54/1, pp. 487-490 (2005).
- [Seggelen 07] J.K. van Seggelen, NanoCMM: A 3D Coordinate Measuring Machine with low moving mass for measuring small products in array with nanometer uncertainty, ISBN 90-386-2629-0, Eindhoven University of Technology, Ph.D. Thesis (2007).
- [Selberg 92] L. Selberg, Radius measurement by interferometry, *Optical Engineering*, 31, pp. 1961-1966 (1992).
- [Sharma 03] R. Sharma, S. Trigwell, A.S. Biris, A. Sims, M.K. Mazumder, Effect of Ambient Relative Humidity and Surface Modification of the Charge Decay Properties of Polymer Powders in Powder Coating, *IEEE Transactions on Industry Applications*, 39/1, p.87-95 (2003).
- [Sharpe 01] W.N. Sharpe, K.M. Jackson, K.J. Hemker, Z. Xie, Effect of Specimen Size on Young's Modulus and Fracture Strength of Polysilicon, *Journal of Microelectromechanical Systems*, 10/3, p. 317-326 (2001).
- [Shashoua 58] V.E. Shashoua, Static electricity in polymers; I: Theory and measurement, *Journal of Polymer Science*, 33/126, p.65-85 (1958).
- [Shashoua 63] V.E. Shashoua, Static electricity in polymers; II: Chemical structure and antistatic behavior, *Journal of Polymer Science*, 1/1, p.169-187 (1963).
- [Shen 97] Y.L. Shen, X. Zhang, Pretravel compensation for vertically oriented touch-trigger probes with straight styli, *International Journal of Machine Tools and Manufacture*, 37/3, p.249-262 (1997).
- [Sheu 04] D.-Y. Sheu, Multi-Spherical Probe Machining by EDM: Combining WEDG Technology with One-Pulse Electro-Discharge, *Journal of Materials Processing Technology*, 149/1-3, pp. 597-603 (2004).
- [Sheu 05] D.-Y. Sheu, Micro-spherical probes machining by EDM, *Journal of Micromechanics and Microengineering*, 15, pp. 185-189 (2005).
- [Shull 96] A.L. Shull and F. Spaepen, Mechanical properties of thin films and multilayers, *Current Opinion in Solid State and Materials Science*, 1, p.679-683 (1996).
- [Singh 97] A. Singh, D.A. Horsley, M.B. Cohn, A.P. Pisano, R.T. Howe, Batch Transfer of Microstructures using flip-chip solder bump bonding, *Technical Digest, Transducers* (1997).
- [Slocum 92] A.H. Slocum, *Precision Machine Design*, ISBN 0872634922, Society of Manufacturing Engineers (1992).
- [Smith 92] S.T. Smith, D.G. Chetwynd, *Foundations of Ultra-Precision Mechanism Design*, ISBN 2881248403, Routledge (1992).

- [Smith 02] G.T. Smith, *Industrial Metrology: Surfaces and Roundness*, ISBN 1852335076, Springer-Verlag (2002).
- [Song 03] G. Song, et al., *Understanding Magnesium Corrosion: A Framework for Improved Alloy Performance*, *Advanced Engineering Materials*, 12/5: p. 837-858 (2003).
- [Spaan 06] H.A.M. Spaan, I. Widdershoven, M.A.A. Morel, *Novel calibration techniques and applications for touch probes with nanometre accuracy*, *Proceedings of Euspen* (2006).
- [Spence 75] D.A. Spence, *The Hertz contact problem with finite friction*, *Journal of Elasticity*, 5, p. 297-319 (1975).
- [Srinivasan 01] U. Srinivasan, D. Liepmann, R.T. Howe, *Microstructure to substrate self-assembly using capillary forces*, *Journal of Microelectromechanical Systems*, 10/1, p. 17-24 (2001).
- [Stifter 98] T. Stifter, E. Weilandt, S. Hild, and O. Marti, *Influence of the topography on adhesion measured by SFM*, *Applied Physics A*, 66, p.597-605 (1998).
- [Stifter 00] T. Stifter, O. Marti, B. Bhushan, *Theoretical investigation of the distance of capillary and van der Waals forces in scanning force microscopy*, *Physical Review B*, 62/20, p.667-673 (2000).
- [Stone 05] J.A. Stone, B. Muralikrishnan, J.R. Stoup, *A fiber probe for CMM measurements of small features*, *Proceedings of the SPIE*, 5879, pp. 254-264 (2005).
- [Stout 90] K.J. Stout, E.J. Davis, P.J. Sullivan, *Atlas of Machined Surfaces*, ISBN 0412377101, Chapman and Hall (1990).
- [Sugawara 93] Y. Sugawara *et al.*, *Effects of humidity and tip radius on the adhesive force measured with atomic force microscopy*, *Wear*, 168, p.13-16 (1993).
- [Sutton 87] C.M. Sutton, *Non-linearity in length measurement using heterodyne laser Michelson interferometry*, *Journal of Physics E: Scientific Instruments*, 20, pp. 1290-1292 (1987).
- [Syms 03] R.R.A. Syms, E.M. Yeatman, V.M. Bright, G.M. Whitesides, *Surface Tension-Powered Self-Assembly of Microstructures: the State of the Art*, *IEEE/ASME Journal of Microelectromechanical Systems*, 12/4, p. 1-31 (2003).
- [Sze 81] S.M. Sze, *Physics of Semiconductor Devices*, ISBN 0471056618, Wiley-Interscience (1981).
- [Tabor 51] D. Tabor, *The Hardness of Metals*, ISBN 0198507763, Oxford University Press (1951).
- [Tabor 81] D. Tabor, *Friction - the present state of our understanding*, *ASME Journal of Lubrication Technology*, 103, p. 169-179 (1981).
- [Tadmor 00] R. Tadmor, *The London-van der Waals interaction energy between objects of various geometries*, *Journal of Physics: Condensed Matter*, 13, p.L195-L202 (2000).
- [Takaya 99] Y. Takaya, N. Sato, S. Takahashi, T. Miyoshi, K. Saito, *Development of The Nano-CMM Probe based on Laser Trapping Technology*, *Annals of the CIRP*, 48/1, p. 421-424 (1999).
- [Takaya 00] Y. Takaya, N. Sato, S. Takahashi, T. Miyoshi, H. Shimizu, M. Watanabe, *The Laser Trapping Probe for Nano-CMM: Positional Detection Principle of The Laser Trapping Probe and Its Nature*, *Journal of the Japan Society for Precision Engineering*, 66/7, p. 1081-1086 (2000).

- [Takaya 04] Y. Takaya, K. Imai, T. Ha, T. Miyoshi, Vibrational Probing Technique for the Nano-CMM based on Optical Radiation Pressure Control, *Annals of the CIRP*, 53/1, p. 421-424 (2004).
- [Takaya 05] Y. Takaya, K. Imai, S. Dejma, T. Miyoshi, Nano-Position Sensing Using Optically Motion-controlled Micro probe with PSD Based on Laser Trapping Technique, *Annals of the CIRP*, 54/1, pp. 389-392 (2005).
- [Tang 90] W.C. Tang, et al., Electrostatic-Comb Drive of Lateral Polysilicon Resonators, *Sensors and Actuators A*, 21, pp. 328-331 (1990).
- [Taniguchi 83] N. Taniguchi, Current status in, and future trends of, ultraprecision machining and ultrafine materials processing, *Annals of the CIRP*, 32/2, p. 537 - 582 (1983).
- [Tas 96] N. Tas, T. Sonnenberg, H. Jansen, R. Legtenberg, M. Elwenspoek, Stiction in Surface Micromachining, *Journal of Micromechanics and Microengineering*, 6, p.385397 (1996).
- [Thalmann 05] R. Thalmann, J. Spiller, A primary roundness measuring machine, *Proceedings SPIE*, 5879, pp. 123-132 (2005).
- [Thomas 99] T.R. Thomas, *Rough Surfaces*, ISBN 1-86094-100-1, Imperial College Press (1999).
- [Tian 92] H. Tian, T. Matsudaira, Effect of relative humidity on friction behaviour of the head/disk interface, *IEEE Transactions on Magnetics*, 28/5, p.2530-2532 (1992).
- [Tian 93] H. Tian, T. Matsudaira, The role of relative humidity, surface roughness and liquid build-up on static friction behaviour of the head/disk interface, *Journal of Tribology*, 115, p.28-35 (1993).
- [Tichem 02] M. Tichem, B. Karpuschewski, Structuring of micro-assembly methods, *Proceedings of the 33rd International Symposium of Robotics* (2002).
- [Tichem 03] M. Tichem, et al., Self-Adjustment of Micro-mechatronic Systems, *Annals of the CIRP*, 52/1, p.17-20 (2003).
- [Tichem 04] M. Tichem, et al., A Classification Scheme for Quantitative Analysis of Micro-Grip Principles, *Assembly Automation*, 24/1, p.88-93 (2004).
- [Tongue 96] B.H. Tongue, *Principles of vibration*, ISBN 0-19-514246-2, Oxford University Press (2002).
- [Tori 94] A. Tori, M. Sasaki, K. Hane, S. Okuma, Adhesive force distribution on microstructures investigated by an atomic force microscope, *Sensors and Actuators A: Physical*, 44/2, p.153-158 (1994).
- [Trens 96] A. Trens, R. Denoyel, E. Guilloteau, Evolution of surface composition; porosity and surface area of glass fibres in a moist atmosphere, *Langmuir*, 12, p.1245-1250 (1996).
- [Trigwell 01] S. Trigwell, N. Grable, C.U. Yurteri, M.K. Mazumder, Effects of Surface Properties on the Tribocharging Characteristics of Polymer Powder as Applied to Industrial Processes, *Proceedings of IEEE/IAS Annual Meeting* (2001).
- [Tsuchitani 94] S. Tsuchitani, et al., Measurement of the Surface Force in Micro Structures and Its Reducion, *Transactions of the Society of Instrument and Control Engineers*, 30/2, p.136-142, in Japanese (1994).
- [Uhlmann 03] E. Uhlmann, D. Oberschmidt, G. Kunath-Fandri, 3D-analysis of microstructures with confocal laser scanning microscopy, *Proceedings of Machines and Processes for Micro-scale and Meso-scale Fabrication, Metrology and Assembly*, p.93-97 (2003).

- [Ungar 90] E.E. Ungar, D.H. Sturz, C.H. Amick, Vibration Control Design of High Technology Facilities, Sound and Vibration, July, p.20-27 (1990).
- [Vaccari 02] J.A. Vaccari, Materials Handbook, ISBN 007136076X, McGraw-Hill Professional (2002).
- [Verdonck 06] A.M. Verdonck, Adhesion forces in handling micro objects, Traineeship report, Eindhoven University of Technology (2006).
- [Vermeulen 64] P.J. Vermeulen, K.L. Johnson, Contact of non-spherical elastic bodies transmitting tangential forces, Journal of Applied Mechanics, Transactions of ASME, 31, p.338-340 (1964).
- [Vermeulen 99] M.M.P.A. Vermeulen, High-Precision 3D-Coordinate Measuring Machine: Design and Prototype-Development, ISBN 90-386-2631-2, Eindhoven University of Technology, Ph.D. Thesis (1999).
- [Vidic 98] M. Vidic, S.M. Harb, S.T. Smith, Observations of contact measurements using a resonance-based touch sensor, Precision Engineering, 22/1, p. 19-36 (1998).
- [Vigil 94] G. Vigil, Z. Xu, S. Steinberg, J. Israelachvili, Interactions of silica surfaces, Journal of Colloid and Interface Science, 165, p.367-385 (1994).
- [Visscher] A. Visscher, Optimisation of Damped Air Isolator, applied to Scanning Electron Microscopy, No. CTR 595-94-0098, Philips CFT, Eindhoven.
- [Visser 72] J. Visser, On Hamaker constants: A comparison between Hamaker constants and Lifshitz-van der Waals constants, Advances in Colloid and Interface Science, 3, p.331-363 (1972).
- [Vliet 96] W.P. van Vliet, W.P., et al., Accuracy limitations of fast mechanical probe, Annals of the CIRP, 45/1 (1996).
- [Vorburger 97] T.V. Vorburger, J.A. Dagata, G. Wilkening, K. Iizuka, Industrial uses of STM and AFM, Annals of the CIRP, 46/2, pp. 597620 (1997).
- [Wahlin 74] A. Wahlin, G. Backstrom, Sliding electrification of Teflon by metals, Journal of Applied Physics, 45, p.2058-2064 (1974).
- [Walpole 06] R.E. Walpole, R.H. Myers, S.L. Myers, K. Ye, Probability & Statistics for Engineers & Scientists, ISBN 0131877119, Prentice Hall (2006).
- [Wan 92] K.T. Wan, D.T. Smith, B.R. Lawn, Fracture and contact adhesion energies of mica-mica, silica-silica, and mica-silica interfaces in dry and moist atmospheres, Journal of the American Ceramic Society, 75/3, p.667-676 (1992).
- [Weckenmann 79] A. Weckenmann, G. Goch, H.D. Springborn, Korrektur der Taststiftbiegung bei Messungen mit Mehrkoordinaten-Messgeraeten, Feinwerktechnik & Messtechnik, 87/1, p.5-9 (1979).
- [Weckenmann 98] A. Weckenmann, B. Gawande, Koordinatenmesstechnik, Carl Hanser Verlag, Muenchen Wien (1998).
- [Weckenmann 04] A. Weckenmann, T. Estler, G. Peggs, D. McMurtry, Probe systems in Dimensional Metrology, Annals of the CIRP, 53/2 (2004).
- [Weckenmann 05] A. Weckenmann, G. Peggs, J. Hoffmann, Probing systems for dimensional micro- and nano-metrology, Measurement Science and Technology, 17, pp. 504-509 (2005).
- [Westphal 01] L.C. Westphal, Handbook of Control Systems Engineering, ISBN 0792374940, Springer (2001).

- [Wetzels 98] S.F.C.L. Wetzels, Laser Based Displacement Calibration with Nanometre Accuracy, Ph.D. thesis, ISBN 903860730X, Eindhoven University of Technology (1998).
- [Whitehouse 70] D.J. Whitehouse, J.F. Archard, The Properties of Random Surfaces of Significance in Their Contact, Proceedings of the Royal Society of London, Series A: Mathematical and Physical Sciences, 316, p.97121 (1970).
- [Whitehouse 94] D.J. Whitehouse, Handbook of Surface Metrology, ISBN 0750300396, Taylor & Francis (1994).
- [Widdershoven 04] I. Widdershoven, Calibration of a Precision Probe for Coordinate Measuring Machines; analysis and optimisation, M.S. report, PE 2004-131, Eindhoven University of Technology (2004).
- [Willett 00] C.D. Willett, M.J. Adams, S.A. Johnson, J.P.K. Seville, Capillary bridges between two spherical bodies, *Langmuir*, 16, p.9396-9405 (2000).
- [Williamson 68] J.B.P. Williamson, Topography of Solid Surfaces, in P.M. Ku, ed., *Interdisciplinary Approach to Friction and Wear*, NASA Special Publications, SP-181, p.85-142 (1968).
- [Williamson 69] J.B.P. Williamson, J. Pullen, R.T. Hunt, The Shape of Solid Surfaces, in F.F. Ling, ed., *Surface Mechanics*, ISBN 0471539058, New York, p.2435 (1969).
- [Window 92] A.L. Window, G.S. Holister, Strain gauge technology, ISBN 0853341184, Elsevier Science Publishing Company (1992).
- [Wong 03] H. Wong, Low-frequency noise study in electron devices: review and update, *Microelectronics Reliability*, 43, pp. 585-599 (2003).
- [Woody 03] S.C. Woody, S.T. Smith, A vector touch sensor probe: An experimental study, *Precision Engineering*, 27/3, p. 221-233 (2003).
- [Wortman 65] J.J. Wortman, R.A. Evans, Young's modulus, shear modulus and Poisson's ratio in silicon and germanium, *Journal of Applied Physics* 36(1), p.153-156 (1965).
- [Wozniak 02A] A. Wozniak, M. Dobosz, Metrological feasibilities of CMM touch-trigger probes, Part I: 3D theoretical model of probe pretravel, *Measurement*, 34/4, p.273-286 (2002).
- [Wozniak 02B] A. Wozniak, M. Dobosz, Metrological feasibilities of CMM touch-trigger probes, Part II: Experimental verification of the 3D theoretical model of probe pretravel, *Measurement*, 34/4, p.287-299 (2002).
- [Wu 99] J.J. Wu, Spectral analysis of the effect of stylus tip curvature on measuring rough profiles, *Wear*, 230, p.194200 (1999).
- [Wu 04] Y. Wu, M.A. Shannon, Theoretical analysis of the effect of static charges in silicon-based dielectric thin films on micro- to nanoscale electrostatic actuation, *Journal of Micromechanics and Microengineering*, 14, p. 989-998 (2004).
- [Yang 96] Q. Yang, C. Butler, P. Baird, Error compensation of touch-trigger probes, *Measurement*, 18/1, p.47-57 (1996).
- [Yeh 94] H. Yeh, J.S. Smith, Fluidic self-assembly for the integration of GaAs light-emitting diodes on Si substrates, *IEEE Photonics Technology Letters*, 6/6, p.706-708 (1994).
- [Young 02] W.C. Young, R.G. Budynas, Roarke's formulas for stress and strain, McGraw-Hill, London, 2002.
- [Yovanovich 03] M.M. Yovanovich, E.E. Marotta, Thermal Spreading and Contact Resistance, in A. Bejan, A.D. Kraus, eds., *Heat Transfer Handbook*, ISBN 9780471390152, John Wiley and Sons Inc, Hoboken, USA (2003).

- [Yu 89] Z.Z. Yu, P.K. Watson, Contact charge accumulation and reversal on polystyrene and PTFE films upon repeated contacts with mercury, *Journal of Physics D: Applied Physics*, 22, p.798-801 (1989).
- [Zahwi 01] D. Zahwi, A.M. Mekawi, Some effects of stylus force on scratching surfaces, *International Journal of Machine Tools and Manufacture*, 41/13, p.2011-2015 (2001).
- [Zanoni 88] C.A. Zanoni, High precision interferometric linear and angular displacement interferometry, Zygo Corporation document (1988).
- [Zimon 82] A.D. Zimon, *Adhesion of Dust and Powder*, ISBN 030610962X, Plenum Publishing Co., New York (1982).

Acknowledgement

It was a few weeks before my graduation that I had a talk with Professor Schellekens about my plans for the future. Amongst other things we spoke about the possibilities of doing a PhD. However, I told him that I was not really that interested because I wanted to work in industry as a preparation for starting my own company. The university environment seemed to be too static and unsuitable to do this. He did convince me though that this was also possible within the university.

The weeks after, I spoke with different PhD students and people from industry. One of these people was my uncle, Ad Smets, who always has a vivid way of making his point. I finally decided to give it a go, after all 'I could always quit'...

One of the things I really enjoyed while doing my work was guiding students. I was fortunate to have had a flying start with two graduation students, Ivo Widdershoven and Gerben van Eijk. Having just graduated myself this was a great experience, both to the project and for me personally. A total of 26 students contributed to this project and I greatly thank them for their efforts:

Hogeschool Utrecht, final projects: Roy van Ettehoven, Justin Rademaker, Roelof Jongeneel, Johan IJzerman and Jingfang Sun.

Technische Universiteit Eindhoven, final projects: Rob Heldens and Sander van Opstal.

Students who contributed in other projects, including practical traineeships: Tommie van Rijen, Frans de Nooij, Adnan Hasanovic, Luuk van Laake, Jack Chao, Maikel Huygens, Marco van Lierop, Martijn Verdonck, Roy Derks, Erik Manders, Jasper Simons, Niels de Kleijn, Johan Westerveld, Wouter Vandamme, Jasper Grasman, Rob van Haendel and Bas Versteeg.

After one and a half years into my PhD work, Professor Schellekens retired. After a turbulent period following this retirement, which gave me a much better sense of university dynamics, the section of Micro- & NanoScale Engineering emerged, led by Professor Dietzel. I am thankful that I was lovingly accepted there, which gave me the opportunity to experience the process of starting up a new research group.

Another great experience was the cooperation with different companies, especially the guiding committee of my project. Special thanks for their contributions go to: Concept 2 Volume (C2V), Mitutoyo, IBS Precision Engineering, NTS Mechatronics, Philips Applied Technologies and TNO Industry.

After completion of the tests with the first prototypes I started Xpress Precision Engineering. The goal was to facilitate my future plans for a startup. After a one-man-show of about 2 years, Ernst Treffers joined the company. He is a great person, both personally and commercially and I hope we will experience many good years working at Xpress.

The prototypes were manufactured at the technical department (GTD) at the Eindhoven University of Technology. Many people there did an impressive piece of work and I would like to make a special mention to Jos de Laat, Lucien Cleven, Jovita Moerel and Rinus Janssen for their help.

The project was financially supported by the Dutch Ministry of Economic Affairs (SenterNovem) in the framework of the IOP Precision Technology program. Future development of the probing sys-

tem is financially supported by the STW Valorisation grant program. Naturally, I am very grateful for their support.

During all this there are a few people that have greatly contributed to my work and they deserve a special mention. These are *Frank Delbressine*, *Han Haitjema*, *Erik Homburg*, *Gert-Jan Burger* and *Jan-Eite Bullema*. A warm thanks also goes to *Piet Schellekens*, who after his retirement seemed to have taken a hobby in my project. His insights and our many discussions were a privilege and an invaluable contribution to this work.

A final word of gratitude goes to my family and friends, whose regular company and encouragement is greatly appreciated, and my loving girlfriend Anouk.

This has truly been a great experience for me, thanks to all of you!

A handwritten signature in blue ink, appearing to be 'Edwin Bos', with a stylized, flowing script.

Edwin Bos

Eindhoven, November 2007

Curriculum vitae

- February 3, 1977 Born in Eindhoven, the Netherlands.
- 1989 - 1995 *Atheneum, Hertog Jan College, Valkenswaard*
Graduated cum laude¹ in 1995.
Award for best student in both Physics and Mathematics.
- 1995 - 2002 *Eindhoven University of Technology*
Department Mechanical Engineering, section Precision Engineering.
Received Master of Science degree with high honor.
Trainee ship at the National Research Council (NRC), Ottawa, Canada.
Master project on the design of a calibration setup for linear scales up to 300 mm with nanometer uncertainty.
- 2003 - 2007 *Eindhoven University of Technology*
Department Mechanical Engineering, section Micro- & Nanoscale Engineering.
Ph.D. on the design of a tactile 3D probing system for measuring MEMS with nanometer uncertainty.
- 2007 - today *Xpress Precision Engineering B.V., Eindhoven, The Netherlands.*
Director Research & Development, co-founder.
OEM of precision 3D tactile probes.
Winner of New Venture² 2007.
Obtained a 2-year funding by STW in their Valorisation Grant program.

¹Cum laude is the highest honor in Dutch education

²Competition for high potential startup companies, initiated by McKinsey & Company